



Terms and Conditions of Use of Digitised Theses from Trinity College Library Dublin

Copyright statement

All material supplied by Trinity College Library is protected by copyright (under the Copyright and Related Rights Act, 2000 as amended) and other relevant Intellectual Property Rights. By accessing and using a Digitised Thesis from Trinity College Library you acknowledge that all Intellectual Property Rights in any Works supplied are the sole and exclusive property of the copyright and/or other IPR holder. Specific copyright holders may not be explicitly identified. Use of materials from other sources within a thesis should not be construed as a claim over them.

A non-exclusive, non-transferable licence is hereby granted to those using or reproducing, in whole or in part, the material for valid purposes, providing the copyright owners are acknowledged using the normal conventions. Where specific permission to use material is required, this is identified and such permission must be sought from the copyright holder or agency cited.

Liability statement

By using a Digitised Thesis, I accept that Trinity College Dublin bears no legal responsibility for the accuracy, legality or comprehensiveness of materials contained within the thesis, and that Trinity College Dublin accepts no liability for indirect, consequential, or incidental, damages or losses arising from use of the thesis for whatever reason. Information located in a thesis may be subject to specific use constraints, details of which may not be explicitly described. It is the responsibility of potential and actual users to be aware of such constraints and to abide by them. By making use of material from a digitised thesis, you accept these copyright and disclaimer provisions. Where it is brought to the attention of Trinity College Library that there may be a breach of copyright or other restraint, it is the policy to withdraw or take down access to a thesis while the issue is being resolved.

Access Agreement

By using a Digitised Thesis from Trinity College Library you are bound by the following Terms & Conditions. Please read them carefully.

I have read and I understand the following statement: All material supplied via a Digitised Thesis from Trinity College Library is protected by copyright and other intellectual property rights, and duplication or sale of all or part of any of a thesis is not permitted, except that material may be duplicated by you for your research use or for educational purposes in electronic or print form providing the copyright owners are acknowledged using the normal conventions. You must obtain permission for any other use. Electronic or print copies may not be offered, whether for sale or otherwise to anyone. This copy has been supplied on the understanding that it is copyright material and that no quotation from the thesis may be published without proper acknowledgement.

Investigation of Low Voltage Fabry-Perot Modulators for Optical
Interconnect Applications

By
Declan James Byrne

A thesis submitted for the degree of
Doctor of Philosophy
in the University of Dublin

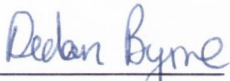
Under the supervision of
Prof. John Hegarty
Department of Physics
Trinity College Dublin
October 2000

TRINITY COLLEGE
12 MAR 2001
LIBRARY DUBLIN

*Thesis
6240*

Declaration

This thesis has not been submitted as an exercise for a degree at any other university. The work described herein is entirely my own, with the exception of the assistance mentioned in the acknowledgements and the collaborative work noted in the publications. I agree that Trinity College may lend or copy this thesis on request.



Declan James Byrne

Summary

Optical interconnect technology is one of the proposed solutions to the fast approaching communication bottleneck in electronic digital systems, arising from the bandwidth limitations of electrical interconnects. Optical modulators are a key technology in optical interconnect systems that can potentially provide the terabit (10^{12}) per second data rates required by future electronic systems. The optical technology used in such optical systems must fulfil many requirements for operation in what is a complex environment. One possible solution is an epitaxially grown semiconductor modulator structure, consisting of multiple quantum wells with an optical mirror or mirrors to form a modulator. Current devices with one back mirror operate sufficiently at current electronic supply voltages ($\approx 5\text{V}$) but operation at lower voltage required by falling electronic supply voltages ($\approx 1\text{V}$) does not produce the modulation depth required by digital systems to differentiate between digital logic values. The addition of a second mirror to this structure to form a Fabry-Perot modulator changes the physics of the device operation and has been shown to allow lower voltage operation to be possible.

The use of an resonant structure strongly influences the device characteristics such as its spectral bandwidth, angular range of operation, sensitivity to changing ambient temperature, optical saturation, and most importantly its sensitivity to variations in optical cavity thickness that determines the possible device arrays size. In this thesis the potential for low voltage operation of these modulator devices is explored particularly with reference to the InGaAs system and the resulting impact on the device operating tolerances is calculated. This work is part of a project to construct a working optical interconnect system and the operating tolerances are compared to the requirements of a real system. The approach taken is to develop a numerical model combined with experimental measurements to simulate the optical characteristics of the devices allowing the potential limits of operation of such devices to be explored.

Fabry-Perot modulators using a metal mirror and Bragg mirror are first examined revealing the main parameters that govern the modulation achievable in a cavity structure and the device structure required at lower voltage operation. This work also revealed the limitations on the modulation achievable using a metal coating as an optical mirror, especially when it must also function as an electrical contact. Fabry-Perot modulators using two Bragg mirrors to form the optical cavity are shown to be necessary at very low voltages and show the back mirror reflectivity is critical to these devices. Although very low voltage operation is shown to be possible, an investigation of the device tolerances reveals poor results due to the high cavity finesse and long optical cavity length. The poor tolerances are shown to be improved by the use of a short optical cavity, a so called 'microcavity modulator' device reveals the device tolerances and sensitivity to cavity thickness variation can be dramatically improved at very short cavity lengths of the order of a few wavelengths in size. The tolerances of these devices are examined with respect to the potential of existing technologies. Finally the lowest possible operating voltage using InGaAs modulator devices is concluded and an ideal device structure for low voltage operation is summarised.

Table of Contents:

Declaration	2
Summary	3
Table of Contents	4
Acknowledgements	8
Publications list	9

Chapter 1: Motivation and Thesis overview

1.1 Introduction	10
1.2 Electrical and optical interconnection	11
1.3 Optical interconnect technology	12
1.4 Optical interconnect devices	16
1.5 MQW Modulators	17
1.6 Thesis overview	20
1.7 References	21

Chapter 2: Fabry-Perot MQW Modulator: Physics and Basic Concepts

2.1 introduction	26
2.2 Low dimensional devices	27
2.3 Epitaxial Growth	28
2.4 Properties of quantum wells	28
2.4.1 Electron confinement in one dimension	29
2.4.2 Density of states	31
2.5 Excitons	32
2.6 Effect of an electric field on exciton absorption	34
2.7 MQW engineering	35
2.8 Strained MQW structures	36
2.9 The multiple quantum well <i>p-i-n diode</i>	37
2.10 Summary	39
2.11 The Fabry-Perot optical cavity	40
2.12 Fabry-Perot reflectance spectra	42
2.13 Optical cavity mirrors	45
2.14 Transfer Matrix Modelling	49

2.15 Assumptions made in modelling of modulator structures	53
2.16 Effect of light incident off-axis on Fabry-Perot resonance	54
2.17 Conclusions	56
2.18 References	56

Chapter 3: The Fabry-Perot Modulator Device

3.1 Introduction	60
3.2 Device requirements for use in optical interconnects	61
3.2.1 Reflectivity change ($R_{on}-R_{off}$) Vs. Contrast (R_{on}/R_{off})	61
3.2.2 Operation at CMOS voltages	65
3.3 Transfer Matrix modelling	65
3.3.1 InGaAs MQW QCSE absorption spectra	66
3.3.2 Optical cavity mirror choice	67
3.3.3 Transfer Matrix modelling results	67
3.3.3.1 Double-pass modulator modelling results	68
3.3.3.2 MQW Fabry-Perot modulator modelling results	70
3.3.3.3 Reflectance spectra	71
3.3.3.4 Optimum operating wavelength	72
3.3.3.5 Front Bragg mirror reflectivity	74
3.3.3.6 Optimum number of MQWs	75
3.3.3.7 Bias voltage operation	78
3.3.3.8 Lower voltage operation	79
3.3.4 Conclusions of transfer matrix modelling	80
3.4 Device Tolerances	82
3.4.1 Spectral Tolerance	82
3.4.2 Angular acceptance	84
3.4.3 MBE lateral growth tolerance	86
3.4.3.1 Absolute growth accuracy	87
3.4.3.2 Growth non-uniformity across a wafer	88
3.4.4 Temperature sensitivity	90
3.4.5 Optical saturation	93
3.4.6 Device speed	98
3.5 Conclusions for device tolerance	100
3.6 Conclusions of chapter 3	100
3.7 References	101

Chapter 4: Modulator measurements for 5V operation

4.1 Introduction	106
4.2 Device structure	106
4.3 Reflectivity measurements	109
4.3.1 Reflectometry as a diagnostic tool	109
4.3.2 Measurement system	110
4.3.3 Experimental error	114
4.4 Measured results	117
4.4.1 Electrical properties	118
4.4.2 Optical properties	119
4.4.2.1 Non-cavity structure	119
4.4.2.2 Optical cavity structure	124
4.4.2.3 Device results	125
4.5 Gold deposition on semiconductor material	133
4.5.1 Impact on Fabry-Perot modulator device	134
4.5.2 Modelling the optical properties of a gold /semiconductor interface	138
4.5.3 Measured optical reflectivities	138
4.6 Conclusions	141
4.7 References	142

Chapter 5: Alternative modulator structure

5.1 Introduction	144
5.2 Back mirror reflectivity	145
5.2.1 Limited Gold mirror reflectivity	145
5.2.2 Higher reflectivity back mirror	147
5.2.3 Impact on cavity resonance reflectivity	149
5.3 Modelled Fabry-Perot modulator results	151
5.3.1 Summary of results	153
5.3.2 Optical cavity formed using a Bragg stack front and back mirror	153
5.3.3 Modulation map of 1V modulator device	155
5.4 Maximum attainable reflectivity change	155
5.5 Operating tolerances	158
5.5.1 Spectral Bandwidth	158
5.5.2 MBE growth tolerances	163
5.5.2.1 Absolute growth accuracy	164
5.5.2.2 Growth non-uniformity across a wafer	164

5.5.2.3 Summary	169
5.5.3 Angular acceptance	170
5.5.4 Temperature sensitivity	172
5.5.5 Optical saturation	173
5.5.6 Device speed	174
5.6 Conclusions	175
5.7 References	175

Chapter 6: Impact of Microcavity regime on Fabry-Perot Modulators

6.1 Introduction	178
6.2 Benefits of a short optical cavity to LED emission	179
6.2.1 Spontaneous emission rate	179
6.2.2 Antinode factor	180
6.2.3 Extraction efficiency	181
6.2.3.1 Emission in bulk material	183
6.2.3.2 Optical cavity extraction	184
6.3 Impact of short optical cavity on Fabry-Perot modulators	186
6.3.1 Absorption rate	186
6.3.2 Antinode factor	186
6.3.3 Spectral and spatial properties	186
6.3.3.1 Cavity order	187
6.3.3.2 Fabry-Perot modulator cavity order	189
6.4 Impact of short cavity order	190
6.4.1 Spectral bandwidth	190
6.4.2 Angular acceptance	192
6.4.3 MBE Growth non-uniformities	194
6.4.4 Temperature sensitivity	197
6.5 Conclusions	198
6.6 References	199

Chapter 7: Conclusions

7.1 Conclusions	201
-----------------	-----

Appendix A

Appendix B

Acknowledgements

There are many people who have contributed to this thesis and remembering all of them after some tiring months of writing this thesis is going to be difficult, apologies to those I forget.

I thank my supervisor Professor John Hegarty for his encouragement and support, and for giving me the opportunity and freedom to be involved in this area of research. Many thanks to Dr. Paul Horan whose guidance, enthusiasm and knowledge was greatly appreciated.

To Louise, Stephen, David (DTF), Paul McEvoy and Tara for their warm welcome into a large research group and their willingness to help throughout my four years was much appreciated. To Tom and Fergal who got me started in those early days in the lab, allowing me to find my feet, many thanks. Also thanks to Brian Kelly for his 2-week crash course on Fabry-Perot modulators. Many thanks to Vincent Weldon for his many efforts amongst the hundreds of demands he handles at any one time. To Dr. James O’Gorman for his encouragement and willingness to share his knowledge. To Tara for her many efforts over the last 4 years (in keeping me up to date with developments), and saving me from the wire bonding nightmares. To Brendan for many useful discussions while searching for my golf ball. Thanks also to Alan for discussions both on microcavity physics and how to run Jordan GP.

I am also grateful to my international colleagues in the SPOEC project for their warm welcomes and willingness to share their knowledge on the vast area of optical interconnects. Special thanks to Prof. Colin Stanley, Dr. John Pearson and Dr. Adam Boyd for their many efforts in providing the devices for this thesis. I would like to thank the European union for their financial support under the ESPRIT MEL-ARI research program. Many thanks to Elaine and most recently Caroline for sorting out travel arrangements for yet another claims form. Thanks to James Egan and Dave Grouse for their technical assistance.

A big thank you to the many other group members, Fred, Pascal, Christophe, David McDonald, Cian, Andrea, John, Adrian, Shane, Mick, Gary, Paddy, Stephanie and Elaine for their friendliness and helpfulness. I must also mention Canice, if I think of something that he has contributed to this thesis before I get to the end I will thank him.

Finally thanks to my friends and flatmates who also contributed greatly to my well being over the last 4 years. To my family for their love and support, this thesis is also dedicated to them.

Publications list

1. Declan Byrne, Paul Horan and John Hegarty "Optimisation Modelling of InGaAs MQW Modulator Structures" presented at Semiconductor and Integrated Optoelectronics conference (Cardiff, April 1998)
2. Declan Byrne, Paul Horan and John Hegarty "Optimisation of InGaAs MQW modulator structures operating with 5V or less modulation" in Optics in Computing '98, Pierre Chavel, David AB Miller, Hugo Thienpoint, Editors, Proceedings of SPIE Vol 3490, 389-392 (1998)
3. SJ Fancey, MG Forbes, MR Taghizadeh, JAB Dines, GS Buller, AC Walker, MPY Desmulliez, G Pennelli, JH Marsh, CR Stanley, P Horan, D Byrne, J Hegarty, S Eitel, KH Gulden, A Gauthier, P Benabes and M Goetz "A free-space optoelectronic crossbar interconnect with Terabit/s communication to silicon electronics" presented at CLEO/Europe '98 (Glasgow, September 1998)
4. Declan Byrne, Paul Horan and John Hegarty "Design and characterisation of an Indium Gallium Arsenide Multiple Quantum Well modulator operating with 5 volts" presented at CLEO/Europe '98 (Glasgow, September 1998)
5. A.C. Walker, M.P.Y. Desmulliez, M.G. Forbes, S.J. Fancey, G.S. Buller, M.R. Taghizadeh, J.A.B. Dines, C.R. Stanley, G.Pennelli, A.R. Boyd, P. Horan, D. Byrne, J. Hegarty, S. Eitel, H.-P. Gauggel, K.-H. Gulden, A. Gauthier, P. Benabes, J.L.Gutzwiller, and M. Goetz, "Design and Construction of an Optoelectronic Crossbar Switch Containing a Terabit/s Free-space Optical Interconnect," " IEEE J. Selected Topics in Quant. Electron. as an Invited Paper for the Special Issue on Smart Photonic Components, Interconnects and Processing Vol. 5, No. 2, pp 236-249 (1999)
6. A.C. Walker, M.P.Y. Desmulliez, M.G. Forbes, S.J. Fancey, G.S. Buller, M.R. Taghizadeh, J.A.B. Dines, C.R. Stanley, G.Pennelli, A. Boyd, J.L. Pearson, P. Horan, D. Byrne, J. Hegarty, S. Eitel, H-P. Gauggel, K-H. Gulden, A. Gauthier, P. Benabes, J.L. Gutzwiller and M. Goetz "An Optoelectronic Crossbar Switch as a Demonstrator Test-Bed for Terabit/s i/o" in Optics in Computing, OSA Technical Digest (Optical Society of America, Washington DC, 1999), pp. 199-201
7. SJ Fancey, AC Walker, MR Taghizadeh, GS Buller, MG Forbes, MPY Desmulliez, J Pearson, AR Boyd, CR Stanley, S Eitel, H-P Gauggel, K-H Gulden, P Horan, D Byrne, J Hegarty, J-L Gutzwiller, M Goetz, P Benabes and A Gauthier "Terabit/s optoelectronic interconnection to silicon VLSI" presented at QE-14, September 1999
8. Declan Byrne, Paul Horan and John Hegarty " Impact of Microcavity regime on Low voltage InGaAs Fabry-Perot modulators " presented at CLEO/Europe 2000 (Nice, September 2000)
9. Declan Byrne, Paul Horan and John Hegarty, 'Investigation of low voltage InGaAs Fabry-Perot modulators for optical interconnect applications', to be submitted to journal of quantum electronics, November 2000.

To Tom, R.I.P.

Chapter 1: Motivation and Thesis overview

1.1 Introduction

Silicon integrated circuits (IC) have revolutionised our ability to process information and semiconductor optoelectronic devices have also had a major impact in information communications and storage, however it is only very recently that these complementary technologies have been integrated. Since the arrival of the first microprocessor in 1971 produced by Intel the processing capacity has grown exponentially with the number of instructions performed in one second, roughly doubling every 18 months [1]. In order to fully utilise this processing ability in digital electronic systems, information needs to be moved between ICs, ideally at a rate that avoids any latency. This interconnection is currently achieved using electrical metal lines but there are physical limitations to the amount of information these metal tracks can carry [2]. As the processing ability of IC increases there is a need for increased communication in/out of the IC achieved via input/output pins, which also must increase in number, taking up valuable areas of the silicon IC. Recent predictions by the semiconductor industry [3] on the 'interconnect technology' required in future systems show that up to the year 2005 electrical interconnects will continue to fulfil the interconnection role due to the use of higher conductivity metals and dielectric material of lower dielectric constant. Beyond 2005 a new approach for interconnection is necessary and research is required to find a solution. Opto-electronics interconnects are suggested as one of the possible solutions. In this field of research there has long been an interest in optical computing and since the development of crystal growth techniques much progress has been made in opto-electronic devices and in devices that perform logic functions optically [4]. Initial devices were not suitable for integration to electronic chips due to their high power consumption but advances in devices with low power consumption such a vertical cavity surface emitting lasers (VCSELs) and multiple quantum well (MQW) modulators means integration is now possible. A lot of current research in optical computing has moved towards using the communication advantages of optics that has long been exploited in optical fibre for long-distance communications (also developed due to the limitations of electrical wires) but now applied to shorter distance interconnection. The use of optics *in* computing could allow the processing abilities of electronics to continue to scale to higher speed and capacity avoiding the limits imposed by electrical interconnection.

In this thesis one of the opto-electronic devices currently favoured for use in optical interconnect, the MQW modulator device is investigated and developed with a view to lowering its operating voltage for compatible operation with future CMOS voltages [3] and future optical interconnects. In the remainder of this chapter the problems associated with electrical interconnects and the benefits of using light as the mode of communication are discussed. The approaches possible to implement optical interconnection are summarised as well as the various characteristics of devices short-listed for use in these systems. Finally following a brief history of the MQW modulator and an overview of the work presented in this thesis will be given.

1.2 Electrical and optical interconnection

The ability to integrate more transistors on a tiny piece of silicon IC has grown tremendously in the last two decades. Predictions for last year [3] were 21 million transistors rising to 1.4 billion in 2012. Correspondingly the on-chip clock frequency is predicted to increase from 1.2 Gbs⁻¹ to 3 Gbs⁻¹. This improvement in clock frequency is a result of shrinking feature size dramatically increasing the number of transistors. The reduced gate size results in faster switch times due to shorter device distances and thus a reduced signal travel time. The relationship between the number of transistors and the number of required input/output (I/O) pins on a chip is approximately given by Rent's rule [5] $C=(N/K)^n$ and the number of pins (N) required increases with the processing ability (C) of the chip where **K** is a constant, approximately 2.5 for high performance applications and **n** also a constant, ranges from 1.5 to 3.0. The predicted required number of I/O pins for 2012 is 5500 and the required off chip frequency prediction of 3 Gbs⁻¹ results in a total aggregate data rate of 4.1 Tbs⁻¹. It is currently unknown how this will be implemented, large chip sizes are unfavourable as increasing the interconnection delay affects the chip cost, performance and speed [6], opening the possibility to an alternative approach to the current electronic packaging technologies used.

The weakness of high density and functionality silicon ICs lies in its electrical interconnection and is only related to the silicon devices themselves through their increasing demand for higher bandwidth. The physical reasons for the limited bandwidth of electrical interconnects have been studied [7,8] and are related to the resistance and capacitance of the metal line as well as signal loss at high frequencies due to the skin effect. As a result there is a general formula that sets a fundamental limitation on the maximum number of bits B_{Max} a simple electrical line can carry before frequency dependent losses and distortion lead to interference between bits of information, given by

$$B_{Max} = B_0 \left(A/L^2 \right) \quad (1.1)$$

where A is the total cross sectional area of a line(s) of length L. B_0 is a constant $\approx 10^{16}$ bits s⁻¹ for on-chip lines and $\approx 10^{15}$ bits s⁻¹ for inter-chip lines. The ratio of the cross sectional area to the line length is known as the aspect ratio and means that using many small wires at low bit rates or large wires at higher bit rates leaves the total capacity unchanged. Scale invariance also means that miniaturisation does not bring any improvements. It is believed this limit will become problematic when data rates of Tbit s⁻¹ are required to and from IC. This limit is not a fundamental limit to electrical interconnects as repeaters could be used or other means such as frequency response line equalisation [9] to solve the

above limit of a simple digital wire. This allows the limit to be stretched but not overcome. There are also other problems encountered when using electrical interconnects.

Electrical cross talk becomes more significant at higher frequencies as the lines start to act like transmission and receiving antennas, termination resistors must be used for impedance matching to avoid reflections. There is also the problem of loss related distortion making extraction of timing signals more difficult and is problematic when communicating the system clock signal. Although these additional concerns are not fundamental limits they do have to be accounted for in the design of these lines.

The physical properties of light give it an advantage for use as an optical interconnect [10]. The high optical frequency of ≈ 500 THz compared to ≈ 10 MHz to 10 GHz for electronics means that there is no frequency dependent loss and there is no aspect ratio limit for optical interconnections. Because the carrier frequency is so high light can be modulated at much higher frequencies than is possible electrically. Impedance matching is relatively simple and can be achieved using anti reflection coatings. The short wavelength of light ≈ 500 nm compared to ≈ 3 cm to 30 m for electrical electronics means small waveguides (optical fibre) can be used for light guiding. It is also possible to image thousands of light beams in free space to sizes the order of the wavelength, passing through one another as there is no cross talk and immunity to electromagnetic interference, thus exploiting the parallelism of light. The short wavelength also means thousands of opto-electronic devices could be placed on the surface of an IC and occupying a much smaller area than occupied by an electrical I/O pin. The fact that light has a large energy quantum (1 eV compared to ≈ 40 neV to 40μ eV) means it is generated and detected quantum mechanically. There needs to be no direct electrical connection between emitter and detector in order to detect photons, allowing perfect electrical isolation. Due to the high capacitance and low impedance of electrical transmission lines high electrical power is consumed (10 – 100 mW per line) and they occupy a significant area of the chip. Opto-electronic devices are available with lower electrical power consumption [11] and once the optical signal is generated it can be sent large distance with little loss. The power consumed is used to drive the optical transmitters and receivers. The power consumption for an optical interconnect is expected to be an order of magnitude less compared to the electrical interconnect when used to connect CMOS ICs [12].

To summarise, as silicon integrated circuits increase in processing ability their communication requirements become more demanding and calculations show that significant limits exist to the electrical bandwidth possible without using a large area of the silicon. There is thus an expected communications bottleneck. The physical properties of light make it a favourable solution to this communications problem.

1.3 Optical interconnect technology

There are a number of technologies considered to implement optical interconnections to VLSI electronics and an overview can be found in [12]. At a cabinet to cabinet and board to board level, optical fibre based interconnections are already used in high performance systems using multiplexing to exploit the parallelism offered by optics to achieve high bandwidths. At a chip to chip level or

intermodule level within a board optical fibre technology is not suitable [13] although there has been some progress using plastic optical fibre [14]. The approach taken is to integrate optoelectronic interfaces directly with the chip itself using a large number of channels running at lower speeds in combination with free space optics. The surface of the chip itself can be used to integrate the optical inputs and outputs with the VLSI electronics. The optoelectronic interfaces can be integrated monolithically or in a hybrid fashion.

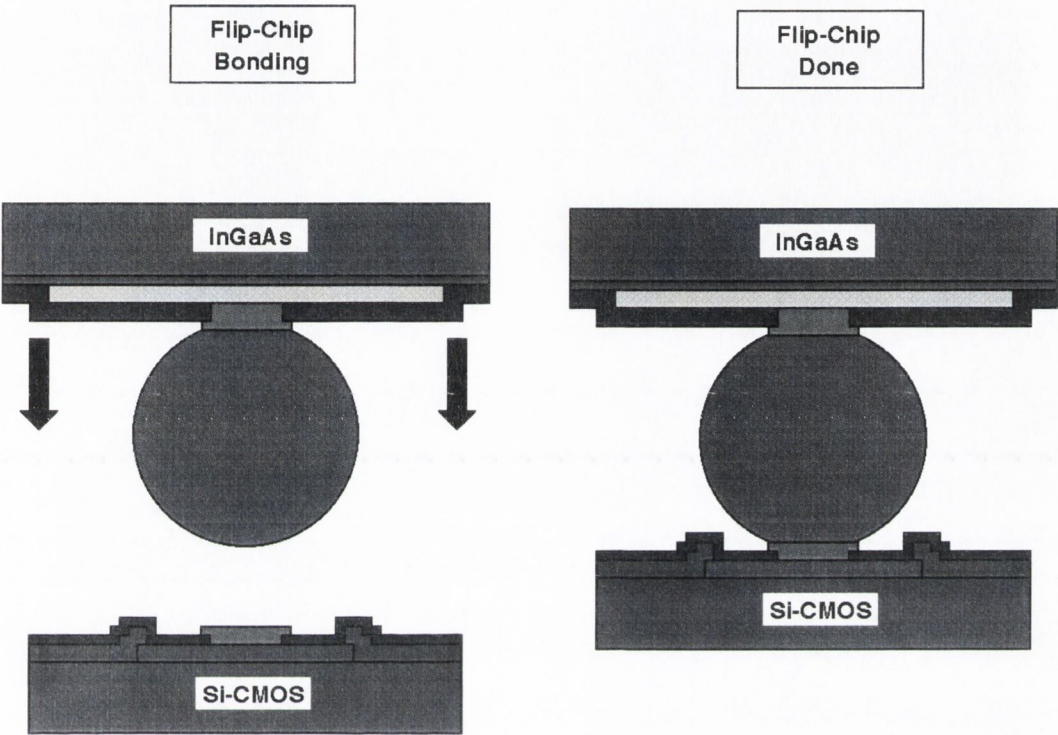


Figure 1.1: Flip-chip bonding of InGaAs optoelectronic devices to CMOS.

Silicon itself is an indirect band semiconductor and thus a very inefficient light emitter. It can be used as an optical detector and devices have been fabricated in silicon CMOS [15] but at the 850nm (or longer) emitter operating wavelengths currently being used for optical interconnects, the detector response is slow for devices made in silicon CMOS due to the long absorption length. Efforts to improve the speed generally result in reduced responsivity [16]. Another approach is to epitaxially grow the optoelectronic devices on silicon and has been achieved using modulators and light emitting diodes (LEDs) [17,18]. The higher growth temperatures of optoelectronic devices ($\approx 800^{\circ}\text{C}$) means that interconnect metalisation of the CMOS cannot occur before the growth of the optoelectronic devices as it results in degradation of the lines. This is invasive to the electronics and research into low temperature epitaxial growth [19] is being investigated to allow the electronics to be fully fabricated before integration. The ideal situation is where the electronics and optoelectronic interface can be developed and optimised separately and then integrated. This can be achieved in the case of hybrid integration. One of the most promising technique is flip-chip bonding. This has found wide application in electronics since first introduced by IBM [19,20]. Figure 1.1 shows the basis of the technique. A

controllable volume of solder is confined between a wettable pad on the IC and the optoelectronic interface being surrounded by a non-wettable region. When the temperature is raised to the melting point of the solder, surface tension brings the structures into alignment [21]. The melting point temperature is below $\approx 200^{\circ}\text{C}$ and does not affect the electronic interconnect lines. Figure 1.2 shows solder bumps on an optoelectronic interface containing arrays of detectors and MQW modulators on $20\mu\text{m}$ diameter bond pads prior to integration [22].

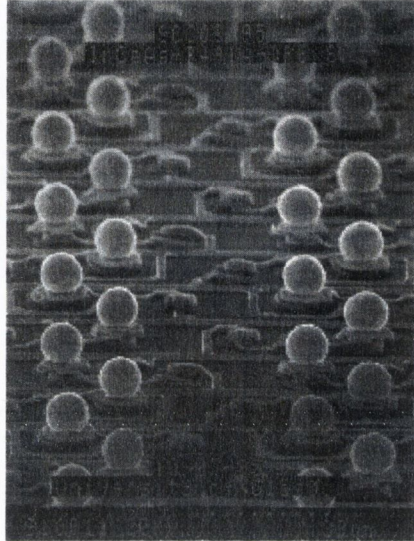


Figure 1.2: Scanning electron microscope image of solder bumps on an optoelectronic interface containing arrays of detectors and MQW modulators. The solder bond pad diameter is $20\mu\text{m}$ [22].

Good mechanical and electrical properties are achieved as well as very high yield generally greater than the device yield [23]. Bond pads are $\approx 20\mu\text{m}^2$ in size allowing thousands of optoelectronic devices to be integrated to the electronics. The work carried out in this thesis is part of a project to demonstrate Tbs^{-1} communication to silicon electronics using this technique. The primary objective of the Smart Pixel OptoElectronic connections (SPOEC) project is to investigate three-dimensional optical interconnects based on free-space connections. The functionality of the system involves an 8×8 optical crossbar in which the 64 inputs can be routed to any one of the 64 outputs. This has been achieved using a hybrid III-V semiconductor - Silicon CMOS flip-chip bonded technology as the main optical switching chip and this will have 4096 detectors (and 128 modulators) configured as a 64×64 array, each operating at $>200 \text{ Mbs}^{-1}$. Figure 1.3 shows the system schematic.

=====

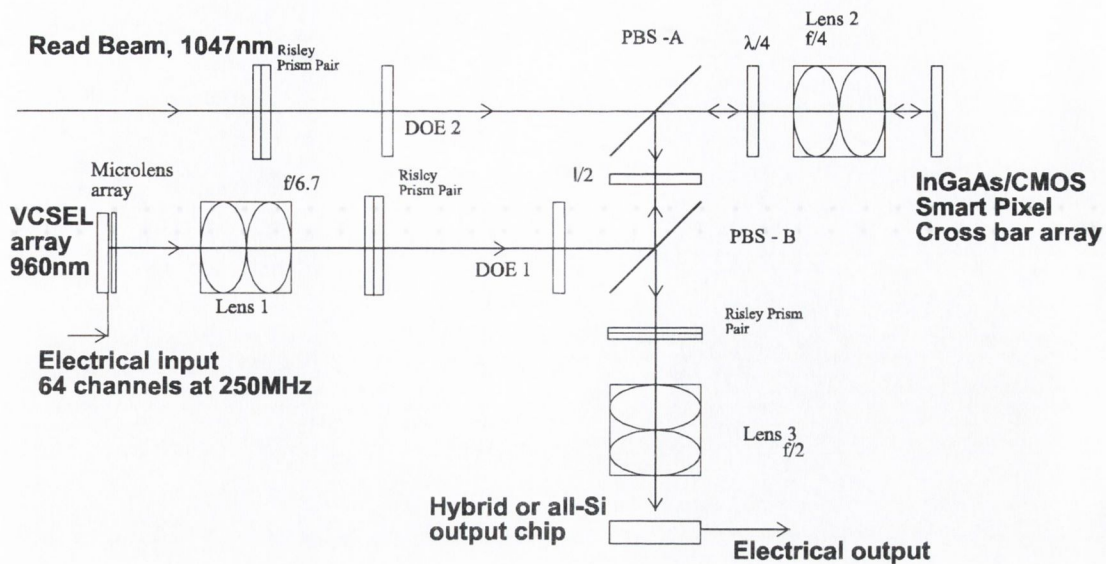


Figure 1.3: Optical scheme of SPOEC Demonstrator.

A detailed account of the system operation and components can be found in [24]. The modulator/detector optoelectronic devices on the switching chip are InGaAs-GaAs strain-balanced devices grown by molecular beam epitaxial (MBE). Arrays of detectors receive the input optical data via an 8x8 VCSEL array that has been optically fanned out 64 times using diffractive optical elements (DOE). The InGaAs/CMOS chip contains 8x8 blocks called 'super pixels' and each one receives all the input data. The underlying CMOS electronics convert the data to an electrical signal that will undertake path decoding before routing the signal that contains the address header of that 'super pixels' to its modulator output channel. The modulator then sends the data to its dedicated detector in an 8x8 detector array. In this way the 64 inputs can be routed to any one of the 64 outputs. In achieving this goal the system demonstrates $64 \times 64 \times 250 \text{ Mbps}^{-1} = 1 \text{ Tbs}^{-1}$ I/O to CMOS electronics. A number of experimental demonstrators have been constructed with potential terabit per second optical interfaces [25] but complete operation has not yet been achieved.

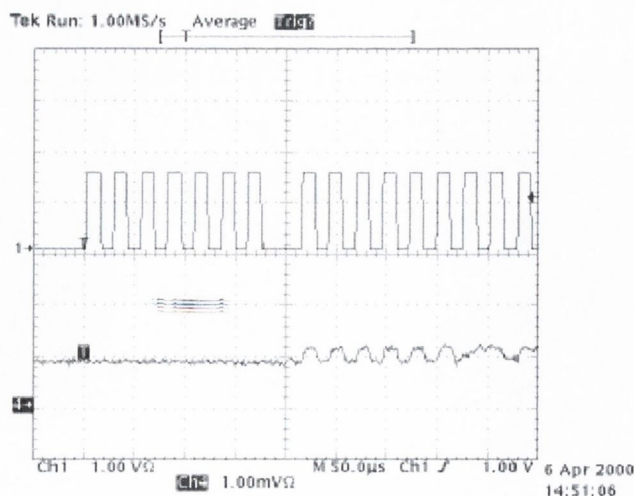


Figure 1.4: Data switch through the SPOEC system shown in figure 1.3.

Figure 1.4 shows one of the first measurements from the SPOEC system showing the input data on top with its address header and on the bottom, the data switched through the InGaAs/CMOS chip outputted by the 'super pixel' modulator with that address. The system is currently in the process of being tested and a data throughput of 0.2 Tbs^{-1} I/O to CMOS electronics has been demonstrated. A review of smart pixel technology can be found in [26] and a roadmap for optoelectronic-VLSI technology in [27]. The MQW modulator structures used in this technology is the subject of this thesis. The optoelectronic devices currently favoured for used in interconnect systems are now presented.

1.4 Optical interconnect devices

Optoelectronic interconnects naturally require both input and output devices. Large dense arrays of these devices are required and individual devices should be capable of at least running at the clock speed of the electronics. The detectors generally used are metal-semiconductor-metal (MSM) or p-i-n detectors due to the problems mentioned above in using silicon itself as the detection material. These detectors can achieve high speeds in the GHz range [28]. LEDs, Vertical Cavity Surface Emitting Lasers (VCSELs) and modulators are the three possible candidates for output devices, each one having its own advantages and disadvantages. Basic requirements include light emission from the top of the device (as oppose to edge emission) or 'surface normal' operation, as well as fabrication in large two-dimensional arrays (>1000 channels) with acceptable power dissipation ($<1\text{mW}$ per channel) and bandwidth $>1\text{Gbs}^{-1}$ [29].

LEDs: The main advantage of LEDs lie in their high temperature tolerance and low power consumption due to the absence of a threshold current. Large arrays are possible with high yields. Recent advances in microcavity LEDs [30] and non-resonant LEDs [31] have shown improved quantum efficiencies and modulation rates. A narrower emission pattern due to tailoring by the optical cavity improves the coupling efficiency to detectors by better matching to the numerical aperture of fibre or lens. Their main disadvantages lie in their relatively lower modulation speeds compared to VCSELs or modulators with a maximum of 1-2 GHz speeds predicted in the near future [29], and their relatively lower output powers ($\approx 400\mu\text{W}$).

VCSELs: are considered a promising emitter for use in optical interconnects but are still in a development stage and arrays have only very recently been flip-chip bonded and operated through CMOS [32]. Their main advantage lies in the fact that they can be modulated at high speeds with bias-free operation at 2.5 Gbs^{-1} demonstrated [33]. Low beam divergence allows efficient collection of the light. Output powers ($\approx 1\text{mW}$) are possible allowing optical fan-out to be achieved and individual oxide-confined devices with wall plug efficiencies greater than 50% at this output power have been demonstrated [34]. 64 to 144 element arrays having good uniformity and yield have been fabricated [24,35,36]. Their biggest issue is power dissipation and the resulting thermal problems especially when used in large dense arrays. Power dissipation in an individual device can be higher than an edge

emitting laser [37] and results in problems such as reduced power output, higher current thresholds and changes in emission wavelength.

Modulators: Multiple quantum well (MQW) modulators based on the Quantum Confined Stark Effect (QCSE) are a mature technology and have been extensively investigated in two dimensional arrays as large as 256x256 elements [38]. They have been used in a number of experimental systems involving optical interconnection to silicon [39,25]. The modulator device is essentially a pin diode and can also be used as a good detector, thus allowing arrays of modulators and detectors to be fabricated simultaneously. The modulator device has no threshold current and can potentially operate at voltages less than the material band-gap. Its speed of operation is largely dependent only on device and driver parasitic capacitance and individual devices have shown modulation bandwidths of 37GHz [40]. Reverse bias device operation results in small power dissipation (<1mW compared to \approx 14mW for VCSELs [29]) and thus very large arrays are possible. The modulator needs read beams to be aligned with it and the reflected light to be sent to a detector. This makes the system optics and optomechanics more bulky as can be seen in figure 1.3, and is one of the disadvantages of using modulator devices. Other disadvantages include the device sensitivity to temperature changes because of changes of the band-edge absorption wavelength and absorption saturation that can occur at high optical incident powers however this is not expected to be a major problem for the optical powers used in optical interconnects. The modulator contrast (the starting reflectivity value divided by the final reflectivity value) is also limited typically being \approx 2:1. There are two approaches to this issue. By using an optical cavity to create a Fabry-Perot modulator device, the contrast has been improved (22:1) and arrays have been fabricated and demonstrated [41]. The other method of dealing with low device contrast is to use pairs of modulators and operate differentially. In this case it is the signal difference that decides the logic state i.e. whether the first beam produces a larger voltage than the second at the detector. This has been the approach taken in the majority of the digital systems used to date [24,25,26,39,42]. Modulators operate sufficiently well at 5V but lower voltage operation is problematic for reasons intrinsic to the QCSE and MQW absorption. For lower voltage operation (compatible with future CMOS voltages) a new modulator structure will most likely be required. The issue of low device contrast and lower voltage operation for modulator devices operating in optical interconnect digital systems is the subject of this thesis and is introduced further in the following section.

Further information comparing modulators and VCSEL devices for use in optical interconnects can be found in [12,43,44].

1.5 MQW Modulators

Optical modulator devices 'print' information on light by changing the polarisation, phase or amplitude of the light. This can be achieved in many ways e.g. electro-optic, photorefractive, electro-absorption, magneto-optic and an overview of spatial light modulators can be found in [45]. Spatial light modulators can be fabricated from ferroelectric liquid crystals and 256x256 arrays have been fabricated on silicon [46] but their relatively low bandwidths as is the case with liquid crystal devices make them

unsuitable for optical interconnects. Semiconductor based devices have the advantage that a large number of well developed semiconductor processing techniques can be used for their fabrication and modern semiconductor growth can fabricate MQWs that have large absorption changes upon application of an electric field. An efficient way of applying an electric field across the MQW is by incorporating the MQW region into the intrinsic region of a *pin* diode. The optical absorption near the band-edge changes upon application of a reverse bias voltage allowing amplitude modulation of the incident light. The initial work was done by Miller et al. [47] and the initial devices operated in transmission through GaAs/AlGaAs quantum wells [48]. By adding a back mirror to these devices the interaction with the absorbing MQWs is doubled and improved contrast ratios were obtained for devices operating in reflection [49]. Typical contrasts of 2:1 and reflectivity changes 60% to 30% are achievable from double pass devices. Devices fabricated in GaAs/AlGaAs operated at 850nm and required the absorbing GaAs substrate to be removed. Due to the availability of high power laser sources at 1047nm (Nd:YLF) and 1064nm (Nd:YAG) that could be fanned out to large arrays of devices, fabrication was pursued in the InGaAs material system and had the benefit that the GaAs substrate was non-absorbing at these wavelengths. The recent impressive progress in high power laser diodes [50] means that future modulator devices in optical interconnects will most likely be fabricated using GaAs/AlGaAs materials where high optical powers are available.

Following the work by Miller et al. there was development of all optical devices called SEEDs (self electrooptic effect device) using MQWs *pin* diodes, where an incident light beam is used to generate the electric field which alters the device response to either the original or a secondary beam [51]. There were a wide variety of various functionality devices that evolved in incorporating MQW diodes for use in optical switching and computing systems and a review can be found in ref. [52]. The incorporation of the MQW *pin* diodes in an optical cavity by adding a second top mirror to the reflection modulator brought about a new device called a Fabry-Perot modulator. Device operation was due to interference between light reflected from the front and back mirrors, where the effective back mirror reflectivity could be controlled by changing the absorption in the optical cavity upon application of an electric field across the MQWs. When the reflected mirror amplitudes were close in value, extremely low reflectivity could be obtained and thus much higher contrasts were achieved (>100:1) [53,54] but initially operating voltages were high typically being >10V. The optical cavity effectively increases the interaction length of the light with the absorbing region and thus fewer MQWs could be used, allowing the optical cavity to compensate. The reduction in MQWs meant that lower voltages could be used to achieve the same electric field across the MQWs. Lower voltage operation was subsequently shown using GaAs/AlGaAs MQW Fabry Perot modulators, with the lowest operating voltage decreasing to $\approx 2V$ [55,56,57] but most had operating voltages $\approx 5V$. The trade-offs between the various operating parameters of these devices were explored mostly for GaAs/AlGaAs devices and can be found in [58,59,60]. Following these achievements modulator devices were fabricated in InGaAs/AlGaAs for operation at the 1047nm and 1064nm high power laser lines. Although good results were also achieved the performance generally was not as good as GaAs/AlGaAs devices and operating voltages of these devices remained quite high, typically >8V [61].

The work presented in this thesis investigates the possible low voltage operation of InGaAs/AlGaAs MQWs Fabry-Perot structures for use in optical interconnects. The starting point is the reflection modulator currently being used in the SPOEC system (figure 1.3) and by the addition of a front Bragg mirror a Fabry-Perot structure is created. The approach taken is to optimise the device structure for operation in differential pairs. Thus the device reflectivity change is optimised, not the device contrast that the majority of previous work has concentrated on, and has shown the device contrast to be very sensitive to cavity thickness changes and the production of large arrays of these devices to be difficult [62]. The fact that this work is part of a project to demonstrate a working interconnect system allows various tolerances for device operation in a real system to be assessed and benchmarks to be set. In this work the Fabry-Perot device tolerances are assessed and comparisons made either to the existing double-pass modulator used in the SPOEC system or to the tolerance set by the system itself e.g. the angular range that light is incident on the modulator by the system optics. The motivation for investigating low voltage operating is to assess compatibility with future CMOS operating voltages, which are predicted to fall to $\approx 1V$ by 2006 [3]. Work to date investigating lower voltage operation of MQW modulator structures based on the QCSE includes work done by Goossen et al. using a *nipin* (the MQWs placed in the intrinsic region) where the MQWs are stacked electrically in parallel and optically in series [63]. The MQW intrinsic regions use roughly half the number of MQWs normally used allowing lower voltages to be applied across the MQWs and there is no loss in absorption as the total number of MQWs in the structure has not changed. The results were good with reflectivity changes of 56% obtained at 0 to 6V operation and $\Delta R = 40\%$ for a 20nm range, but further work is required into this approach for operation at much lower voltages. Recent work by Ryvkin et al. into a novel device proposes using carrier heating to shift the absorption edge in bulk material and initial calculations predict that $< 1V$ operation with fast switching times may be possible [65]. There has also been some work into circuit design to give higher voltage swings using the CMOS supply voltages [66]. The approach taken in this thesis is to investigate the potential of low voltage operation using an optical cavity structure. A transfer matrix model is developed to model the device structure and combined with experimental measurements to strengthen and verify its predictions. Combining these methods of investigation allows the ultimate limits of operation to be examined. Given the complexity involved in fabricating large arrays of modulators devices and integrating them into an interconnect system, the approach taken was to always minimise changes to the existing single mirror modulator structure that has been used successfully. This is done in order to avoid adding any more processing steps than is already necessary, and to keep any changes within the capabilities of the existing device fabrication and processing abilities thus permitting modulator structures to be fabricated with existing technology. The work in this thesis, although specifically aimed at device operation using InGaAs/AlGaAs semiconductor material and for application in interconnect system, is kept as generic as possible in order to allow the results to be adopted to other material systems or applications.

1.6 Thesis overview

The work presented in this thesis was performed at Trinity College Dublin as part of the Smart Pixel OptoElectronic Connections project (SPOEC) which was a 42 month collaboration funded by the European union under the ESPRIT microelectronics advanced research initiative (MEL-ARI) Opto cluster. This collaboration brought together partners with a wide expertise in VCSEL and modulator devices, optical system architectures, diffractive optics and optomechanical assemblies, as well IC design and mixed (analogue and digital) circuit design. The principle goal was to build a demonstrator system that would show the capability of optical interconnects to communicate terabit per second data rates to silicon CMOS. The work performed in Trinity College and presented in this thesis involved investigating Fabry-Perot modulator devices for this system to obtain an improved performance over the existing 5V-reflection modulator and to explore the possibility of lower voltage operation. The results are presented in this thesis as follows.

In Chapter 2 the basic physics of MQWs showing large electroabsorption changes are presented as well as the differences in electroabsorption between InGaAs/AlGaAs and GaAs/AlGaAs quantum wells. The properties of an optical cavity are outlined and the different modes of device operation when a *pin* MQW diode is inserted into the cavity are presented. The transfer matrix model that is used to model the optical characteristics of these devices in this thesis is introduced along with the assumptions made and the data sources used in the model. Chapter 3 begins with an analysis of the device structure and requirements for maximising the device reflectivity change. The developed transfer matrix model is used to investigate the potential of InGaAs/AlGaAs MQW modulator devices. The double-pass reflection modulator is first investigated for operation with results confirming the limitations of these devices at lower voltage operation. An optical cavity device is then modelled formed by adding a front Bragg mirror to the device and using the existing gold coating as the back mirror of the cavity. This device showed low voltage operation but with limited modulation values. The impact of the optical cavity on the spectral bandwidth of this structure is calculated along with device tolerance to epitaxial growth changes, changes in ambient temperature and the device angular acceptance. The impact of the optical cavity on the device speed is examined as well as its sensitivity to the increase in optical power in the cavity. Based on the modelling results in this chapter a Fabry-Perot device structure was fabricated and measurements are presented in Chapter 4. Two separate wafers were fabricated, one consisting of a double-pass reflection modulator and the other a Fabry-Perot structure. Measurements from these wafers are presented and comparison is made with the modelling assumptions and predictions to validate the transfer matrix model developed in this work. Measurements from these devices showed various problems associated with using metal coatings on semiconductor material simultaneously as an optical mirror and an electrical contact. Measurements are presented on the optical properties of different gold deposition methods and the associated electrical properties are summarised. In Chapter 5 the strengthened model is used to investigate an alternative structure using a Bragg or Bragg/Au back mirror, allowing much larger back mirror reflectivities to be investigated and showing how critical this mirror is for very low voltage operation. The maximum

reflectivity change possible is examined and the optimum device structure presented. The operation tolerances of this alternative structure for use in a real system are also examined showing the potential problems of the device. Chapter 6 briefly presents some of the benefits of short optical cavities to light emitting diodes (microcavity LEDs) and the modelling results of the benefits of a short optical cavity to a microcavity modulator are examined, showing dramatic improvements to the device tolerance and sensitivity to growth non-uniformities. Finally Chapter 7 brings the results and conclusions of the previous chapters together to present the optimum Fabry-Perot structure permitting low voltage operation and use in an optical interconnect system.

1.7 References

- [1] MOORE GE, 'CRAMMING MORE COMPONENTS ONTO INTEGRATED CIRCUITS' (REPRINTED FROM ELECTRONICS, PG 114-117, APRIL 19, 1965), PROCEEDINGS OF THE IEEE, 86: (1) 82-85 JAN 1998.
- [2] MILLER DAB, OZAKTAS HM, 'LIMIT TO THE BIT-RATE CAPACITY OF ELECTRICAL INTERCONNECTS FROM THE ASPECT RATIO OF THE SYSTEM ARCHITECTURE', JOURNAL OF PARALLEL AND DISTRIBUTED COMPUTING, 41: (1) 42-52 FEB 25 1997
- [3] SEMICONDUCTOR INDUSTRY ASSOCIATION: THE NATIONAL TECHNOLOGY ROADMAP FOR SEMICONDUCTORS: TECHNOLOGY NEEDS', 1997 EDITION.
- [4] LENTINE AL, MILLER DAB, 'EVOLUTION OF THE SEED TECHNOLOGY - BISTABLE LOGIC GATES TO OPTOELECTRONIC SMART PIXELS', IEEE JOURNAL OF QUANTUM ELECTRONICS, 29: (2) 655-669 FEB 1993
- [5] 'INTRODUCTION TO MULTICHIP MODULES', SHERWANI N, QIONG Y, SANDEEP B, JOHN WILEY & SONS PUBLISHING, NY, 1996
- [6] KUNG SY, 'VLSI ARRAY PROCESSORS', PRENTICE HALL ENGLEWOODS CLIFFS, NJ, 1988
- [7] MILLER DAB, OZAKTAS HM, 'LIMIT TO THE BIT-RATE CAPACITY OF ELECTRICAL INTERCONNECTS FROM THE ASPECT RATIO OF THE SYSTEM ARCHITECTURE', JOURNAL OF PARALLEL AND DISTRIBUTED COMPUTING, 41: (1) 42-52 FEB 25 1997
- [8] B.J. SMITH, 'INTERCONNECTION NETWORKS FOR SHARED MEMORY PARALLEL COMPUTERS', PROC. 2ND INTERNATIONAL CONFERENCE ON MASSIVELY PARALLEL PROCESSING USING OPTICAL INTERCONNECTIONS (MPPPI), IEEE COMPUTER SOCIETY PRESS, PP. 255-256. (1995)
- [9] DALLY WJ, POULTON J, 'TRANSMITTER EQUALIZATION FOR 4-GBPS SIGNALING', IEEE MICRO, 17: (1) 48-56 JAN-FEB 1997
- [10] MILLER DAB, 'PHYSICAL REASONS FOR OPTICAL INTERCONNECTION', INTERNATIONAL JOURNAL OF OPTOELECTRONICS, 11: (3) 155-168 MAY-JUN 1997
- [11] WOODWARD TK, KRISHNAMOORTHY AV, LENTINE AL, GOOSSEN KW, WALKER JA, CUNNINGHAM JE, JAN WY, DASARO LA, CHIROVSKY LMF, HUI SP, TSENG B, KOSSIVES D, '1-GB/S TWO-BEAM TRANSMITTANCE SMART-PIXEL OPTICAL RECEIVERS MADE FROM HYBRID GAAS MQW MODULATORS BONDED TO 0.8- μ m SILICON CMOS', IEEE PHOTONICS TECHNOLOGY LETTERS, 8: (3) 422-424 MAR 1996
- [12] D.A.B. MILLER, 'DENSE TWO DIMENSIONAL INTEGRATION OF OPTOELECTRONICS AND ELECTRONICS FOR INTERCONNECTIONS', CRITICAL REVIEWS CONFERENCE AT SPIE'S SYMP. ON PHOTONICS WEST OPTOELECTRONICS '98, TO BE PUBLISHED

- [13] F.A.P. TOOLEY, 'CHALLENGES IN OPTICALLY INTERCONNECTING ELECTRONICS', IEEE JOURNAL OF SELECTED TOPICS IN QUANTUM ELECTRONICS, (2):1, 3-13, APRIL 1996
- [14] A. NEYER, B. WITTMANN AND M. JOHNCK, 'PLASTIC-OPTICAL-FIBER-BASED PARALLEL OPTICAL INTERCONNECTS', IEEE JOURNAL OF SELECTED TOPICS IN QUANTUM ELECTRONICS, (5):2, 193-200, MARCH/APRIL 1999
- [15] K. AYADI, M. KUIJK, P. HEREMANNS, G. BICKEL, G. BORGHS, R. VOUNCK, 'A MONOLITHIC OPTOELECTRONIC RECEIVER IN STANDARD 0.7 μ M CMOS OPERATING AT 180 MHZ AND 176-FJ LIGHT INPUT ENERGY', IEEE PHOTONICS TECHNOLOGY LETTERS,(9):1, 88-90, JAN 1997
- [16] T.K. WOODWARD AND ASHOK V. KARISHNAMOORTHY, '1 GB/S INTEGRATED OPTICAL DETECTORS AND RECEIVERS IN COMMERCIAL CMOS TECHNOLOGIES',IEEE JOURNAL OF SELECTED TOPICS IN QUANTUM ELECTRONICS, (5):2, 146-156, MARCH/APRIL 1999
- [17] K.GOSSEN, J.A. WALKER, J.E. CUNNINGHAM, W.Y. YAN, D.A.B.MILLER, S.K. TEWKSBUURY AND L.A. HORNAK, 'MONOLITHIC INTEGRATION OF GAAS/ALGAAS MULTIPLE QUATUM WELL MODULATORS AND SILICON METAL-OXIDE SEMICONDUCTOR TRANSISTOR', PROC. OSA TOP. MEETING, PHONTONICS IN SWITCHING, 16, P94-98, 1993
- [18] AHADIAN JF, VAIDYANATHAN PT, PATTERSON SG, ROYTER Y, MULL D, PETRICH GS, GOODHUE WD, PRASAD S, KOLODZIEJSKI LA, FONSTAD CG, 'PRACTICAL OEIC'S BASED ON THE MONOLITHIC INTEGRATION OF GAAS-INGAP LED'S WITH COMMERCIAL GAAS VLSI ELECTRONICS', IEEE JOURNAL OF QUANTUM ELECTRONICS, 34: (7) 1117-1123 JUL 1998
- [19] MILLER LF, 'CONTROLLED COLLAPSE REFLOW CHIP JOINING' (REPRINTED FROM IBM JOURNAL OF RESEARCH AND DEVELOPMENT, VOL 13, 1969), IBM JOURNAL OF RESEARCH AND DEVELOPMENT, 44: (1-2) 93-104 JAN-MAR 2000
- [20] WALE M, GOODWIN M, 'FLIP-CHIP BONDING OPTIMIZES OPTO-ICS', IEEE CIRCUITS AND DEVICES MAGAZINE, 8: (6) 25-31 NOV 1992
- [21] GOODWIN MJ, MOSELEY AJ, KEARLEY MQ, MORRIS RC, KIRKBY CJG, THOMPSON J, GOODFELLOW RC, BENNION I, 'OPTOELECTRONIC COMPONENT ARRAYS FOR OPTICAL INTERCONNECTION OF CIRCUITS AND SUBSYSTEMS', JOURNAL OF LIGHTWAVE TECHNOLOGY, 9: (12) 1639-1645 DEC 1991
- [22] COURTESY OF C.STANLEY, UNIVERSITY OF GLASGOW, SCOTLAND, UK.
- [23] KRISHNAMOORTHY AV, GOOSSEN KW, PROGRESS IN OPTOELECTRONIC-VLSI SMART PIXEL TECHNOLOGY BASED ON GAAS/ALGAAS MQW MODULATORS, INTERNATIONAL JOURNAL OF OPTOELECTRONICS,11: (3) 181-198 MAY-JUN 1997
- [24] A.C. WALKER, M.P.Y. DESMULLIEZ, M.G. FORBES, S.J. FANCEY, G.S. BULLER, M.R. TAGHIZADEH, J.A.B. DINES, C.R. STANLEY, G. PENNELLI, A.R.BOYD, P. HORAN, D. BYRNE, J. HEGARTY, S. EITEL, H-P. GAUGGEL, K.-H. GULDEN, A. GAUTHIER, P. BENABES, J.L. GUTZWILLER, AND M. GOETZ, 'DESIGN AND CONSTRUCTION OF AN OPTOELECTRONIC CROSSBAR SWITCH CONTAINING A TERABIT/S FREE-SPACE OPTICAL INTERCONNECT' IEEE J.SELECTED TOPICS IN QUANT. ELECTRON. SPECIAL ISSUE ON SMART PHOTONIC COMPONENTS, INTERCONNECTS AND PROCESSING,VOL. 5, NO. 2, PP 236-249 (1999)
- [25] LENTINE AL, GOOSSEN KW, WALKER JA, CHIROVSKY LMF, DASARO LA, HUI SP, TSENG BJ, LEIBENGUTH RE, CUNNINGHAM JE, JAN WY, KUO JM, DAHRINGER DW, KOSSIVES DP, BACON D, LIVESCU G, MORRISON RL, NOVOTNY RA, BUCHHOLZ DB,

'HIGH-SPEED OPTOELECTRONIC VLSI SWITCHING CHIP WITH >4000 OPTICAL I/O BASED ON FLIP-CHIP BONDING OF MQW MODULATORS AND DETECTORS TO SILICON CMOS', IEEE JOURNAL OF SELECTED TOPICS IN QUANTUM ELECTRONICS, 2: (1) 77-84 APR 1996

[26] HINTON HS, 'PROGRESS IN THE SMART PIXEL TECHNOLOGIES', IEEE JOURNAL OF SELECTED TOPICS IN QUANTUM ELECTRONICS, 2: (1) 14-23 APR 1996

[27] KRISHNAMOORTHY AV, MILLER DAB, 'SCALING OPTOELECTRONIC-VLSI CIRCUITS INTO THE 21ST CENTURY: A TECHNOLOGY ROADMAP', IEEE JOURNAL OF SELECTED TOPICS IN QUANTUM ELECTRONICS, 2: (1) 55-76 APR 1996

[28] HAYES EM, JURRAT R, PU R, SNYDER RD, FELD SA, STANKO P, WILMSEN CW, CHOQUETTE KD, GEIB KM, HOU HQ, 'FOUNDARY FABRICATED ARRAY OF SMART PIXELS INTEGRATING MESFETS/MSMS AND VCSELS', INTERNATIONAL JOURNAL OF OPTOELECTRONICS, 11: (3) 229-237 MAY-JUN 1997

[29] MEL-ARI TECHNOLOGY ROADMAP: OPTOELECTRONIC INTERCONNECTS FOR INTEGRATED CIRCUITS, EUROPEAN COMMISSION IST PROGRAMME: FUTURE AND EMERGING TECHNOLOGIES, 2ND EDITION SEPT 1999

[30] H. BENISTY, H. DE NEVE AND C. WEISBUCH, 'IMPACT OF PLANAR MICROCAVITY EFFECTS ON LIGHT EXTRACTION – PART I: BASIC CONCEPTS AND ANALYTICAL TRENDS', IEEE JOURNAL OF QUANTUM ELECTRONICS, 34: (9) 1612-1631 SEPT 1998

[31] WINDISCH RH, KNOBLOCH A, POTEMANS J, DUTTA B, DOHLER GH, BORGHS G, HEREMANS PL, 'LIGHT-EMITTING DIODES WITH 17% EXTERNAL QUANTUM EFFICIENCY AT 622 MB/S FOR HIGH-BANDWIDTH PARALLEL SHORT-DISTANCE OPTICAL INTERCONNECTS', IEEE JOURNAL OF SELECTED TOPICS IN QUANTUM ELECTRONICS, 5: (2) 166-171 MARCH/APRIL 1999

[32] KRISHNAMOORTHY AV, GOOSSEN KW, CHIROVSKY LMF, ROZIER RG, CHANDRAMANI P, HOBSON WS, HUI SP, LOPATA J, WALKER JA, D'ASARO LA, '16 X 16 VCSEL ARRAY FLIP-CHIP BONDED TO CMOS VLSI CIRCUIT', IEEE PHOTONICS TECHNOLOGY LETTERS, 12: (8) 1073-1075 AUG 2000

[33] SCHNITZER P, GRABHERR M, JAGER R, JUNG C, EBELING KJ, 'BIAS-FREE 2.5GBIT/S DATA TRANSMISSION USING POLYIMIDE PASSIVATED GAAS VCSELS' ELECTRONICS LETTERS, 34: (6) 573-575 MAR 19 1998

[34] JAGER R, GRABHERR M, JUNG C, MICHALZIK R, REINER G, WEIGL B, EBELING KJ, '57% WALLPLUG EFFICIENCY OXIDE-CONFINED 850NM WAVELENGTH GAAS VCSELS', ELECTRONICS LETTERS, 33: (4) 330-331 FEB 13 1997

[35] HIBBSBRENNER MK, MORGAN RA, WALTERSON RA, LEHMAN JA, KALWEIT EL, BOUNNAK S, MARTA T, GIESKE R, 'PERFORMANCE, UNIFORMITY, AND YIELD OF 850-NM VCSEL'S DEPOSITED BY MOVPE', IEEE PHOTONICS TECHNOLOGY LETTERS, 8: (1) 7-9 JAN 1996

[36] VAKHSHOORI D, WYNN JD, ZYDZIK GJ, LEIBENGUTH RE, '8X18 TOP EMITTING INDEPENDENTLY ADDRESSABLE SURFACE EMITTING LASER ARRAYS WITH UNIFORM THRESHOLD CURRENT AND LOW THRESHOLD VOLTAGE', APPLIED PHYSICS LETTERS, 62: (15) 1718-1720 APR 12 1993

[37] W. NAKWASKI, 'THERMAL ASPECTS OF EFFICIENT OPERATION OF VERTICAL CAVITY SURFACE EMITTING LASERS', OPTICAL & QUANTUM ELECTRONICS, 28: (4) 335-352, 1994

[38] T.L. WORCHESKY, K.J. RITTER, R.MATIN AND B.LANE, 'LARGE ARRAYS OF SPATIAL LIGHT MODULATORS HYBRIDIZED TO SILICON IC', APPLIED OPTICS LETTERS, VOL 35, P1180-1186, 1996

- [39] WALKER AC, GOODWILL DJ, RYVKIN BS, MCELHINNEY M, POTTIER F, VOGEL B, HOLLAND MC, STANLEY CR, 'THE SCOTTISH COLLABORATIVE INITIATIVE ON OPTOELECTRONIC SCIENCES (SCIOS) - DEVICES AND DEMONSTRATORS FOR FREE-SPACE DIGITAL OPTICAL-PROCESSING', OPTICAL COMPUTING, 139: 501-505 1995
- [40] C.C. BARRON, C.J. MAHON, B.J. THIBEAULT, G. WANG, W. JIANG, L.A. COLDREN, 'MILLIMETER-WAVE ASYMMETRIC FABRY-PEROT MODULATORS', IEEE JOURNAL OF QUANTUM ELECTRONICS, 31: (8) 1484-1493 AUG 1995
- [41] JENNINGS A, HORAN P, KELLY B, HEGARTY J, 'ASYMMETRIC FABRY-PEROT DEVICE ARRAYS WITH LOW INSERTION LOSS AND HIGH UNIFORMITY', IEEE PHOTONICS TECHNOLOGY LETTERS, 4: (8) 858-860 AUG 1992
- [42] MCCORMICK FB, CLOONAN TJ, LENTINE AL, SASIAN JM, MORRISON RL, BECKMAN MG, WALKER SL, WOJCIK MJ, HINTERLONG SJ, CRISCI RJ, NOVOTNY RA, HINTON HS, '5-STAGE FREE-SPACE OPTICAL SWITCHING NETWORK WITH FIELD-EFFECT TRANSISTOR SELF-ELECTRO-OPTIC-EFFECT-DEVICE SMART-PIXEL ARRAYS', APPLIED OPTICS, 33: (8) 1601-1618 MAR 10 1994
- [43] FAN C, MANSOORIAN B, VANBLERKOM DA, HANSEN MW, OZGUZ VH, ESENER SC, MARSDEN GC, 'DIGITAL FREE-SPACE OPTICAL INTERCONNECTIONS - A COMPARISON OF TRANSMITTER TECHNOLOGIES', APPLIED OPTICS, 34: (17) 3103-3115 JUN 10 1995
- [44] NAKAHARA T, MATSUO S, FUKUSHIMA S, KUROKAWA T, 'PERFORMANCE COMPARISON BETWEEN MULTIPLE-QUANTUM-WELL MODULATOR-BASED AND VERTICAL-CAVITY-SURFACE-EMITTING LASER-BASED SMART PIXELS', APPLIED OPTICS, 35: (5) 860-871 FEB 10 1996
- [45] J.A. NEFF, R.A. ATHALE AND S.H. LEE, 'TWO DIMENSIONAL SPATIAL LIGHT MODULATORS:A TUTORIAL', PROC. OF THE IEEE, 78: (5) 822-855 1990
- [46] MCKNIGHT DJ, JOHNSON KM, SERATI RA, '256X256 LIQUID CRYSTAL-ON-SILICON SPATIAL LIGHT MODULATOR', APPLIED OPTICS, 33:(14) P2775-2784, 1994
- [47] MILLER,D.A.B.,CHEMLA,D.S.,DAMEN,T.C.,GOSSARD,A.C.,WEIGMANN,W.,WOOD,T.H., AND BURRUS, C.A.(1985). 'BAND EDGE ELECTROABSORPTION IN QUANTUM WELL STRUCTURES: THE QUANTUM CONFINED STARK EFFECT' . PHYSICAL REVIEW LETTERS 52(22),2173-2176(1984)
- [48] T.H. WOOD, C.A. BURRUS, D.A. MILLER, D.S. CHEMLA, T.C. DAMEN, A.C. GOSSARD, AND W. WEIGMANN, 'HIGH SPEED OPTICAL MODULATION WITH GAAS/ALGAAS QUANTUM WELLS IN A PIN DIODE STRUCTURE', APPLIED PHYSICS LETTERS , 44: (1) 16-18 1984
- [49] G.D. BOYD, D.A. MILLER, D.S. CHEMLA, S.L. MCCALL, A.C. GOSSARD, AND J.H. ENGLISH, 'MULTIPLE QUANTUM WELL REFLECTION MODULATOR', APPLIED PHYSICS LETTERS, 50: (17) 1119-1121 1987
- [50] A.AL-MUHANNA, L.J.MAWST, D. BOTEZ, D.Z. GARBUZOV, R.U. MARTINELLI, AND J.C. CONNOLLY, 'HIGH POWER (≥ 10 W) CONTINUOUS-WAVE OPERATION FROM 100- μ M-APERTURE 0.97- μ M-EMITTING AL-FREE DIODE LASERS', APPLIED PHYSICS LETTERS, 73:(9) 1182-1184 31 AUG 1998
- [51] D.A.B. MILLER, D.S. CHEMLA, T.C. DAME, T.H. WOOD, C.A.BURRUS, A.C. GOSSARD, AND W.WIEGMANN, 'THE QUANTUM WELL SELF-ELECTROOPTIC EFFECT DEVICE:OPTOELECTRONIC BISTABILITY ANS OSCILLATION, AND SELF-LINEARIZED MODULATION',IEEE JOURNAL OF QUANTUM ELECTRONICS, 21: 1462-1475 1985

- [52] LENTINE AL, MILLER DAB, 'EVOLUTION OF THE SEED TECHNOLOGY - BISTABLE LOGIC GATES TO OPTOELECTRONIC SMART PIXELS' IEEE JOURNAL OF QUANTUM ELECTRONICS, 29(2) 655-669 1993
- [53] GERBER DS, DROOPAD R, MARACAS GN, 'A GAAS/ALGAAS ASYMMETRIC FABRY-PEROT REFLECTION MODULATOR WITH VERY HIGH CONTRAST RATIO', IEEE PHOTONICS TECHNOLOGY LETTERS, 5: (1) 55-58 JAN 1993
- [54] WHITEHEAD M, RIVERS A, PARRY G, ROBERTS JS, BUTTON C., 'LOW-VOLTAGE MULTIPLE QUANTUM WELL REFLECTION MODULATOR WITH ON:OFF RATIO >100:1', ELECTRONICS LETTERS, VOL.25, NO.15, PP.984-5 20 JULY 1989
- [55] PEZESHKI B, THOMAS D, HARRIS JS, 'OPTIMISATION OF MODULATION RATIO AND INSERTION LOSS IN REFLECTIVE ELECTROABSORPTION MODULATORS', APPLIED PHYSICS LETTERS, 57: (15) 1491-1492 OCT 8 1990
- [56] R.H. YAN, R.J. SIMES AND L.A. COLDREN, 'EXTREMELY LOW VOLTAGE FABRY-PEROT REFLECTION MODULATORS', IEEE PHOTONICS TECHNOLOGY LETTERS, 2: (2) 118-119 FEB 1990
- [57] WHITEHEAD M, RIVERS A, PARRY G, ROBERTS JS, 'VERY LOW-VOLTAGE, NORMALLY-OFF ASYMMETRIC FABRY-PEROT REFLECTION MODULATOR', ELECTRONICS LETTERS, 26: (19) 1588-1590 SEP 13 1990
- [58] YAN RH, SIMES RJ, COLDREN LA, 'SURFACE-NORMAL ELECTROABSORPTION REFLECTION MODULATORS USING ASYMMETRIC FABRY-PEROT STRUCTURES', IEEE JOURNAL OF QUANTUM ELECTRONICS, 27: (7) 1922-1931 JUL 1991
- [59] ZOUGANELI P, STEVENS PJ, ATKINSON D, PARRY G, 'DESIGN TRADE-OFFS AND EVALUATION OF THE PERFORMANCE ATTAINABLE BY GAAS-AL_{0.3}GA_{0.7}AS ASYMMETRIC FABRY-PEROT MODULATORS', IEEE JOURNAL OF QUANTUM ELECTRONICS, 31: (5) 927-943 MAY 1995
- [60] ZOUGANELI P, PARRY G, 'EVALUATION OF THE TOLERANCE OF ASYMMETRIC FABRY-PEROT MODULATORS WITH RESPECT TO REALISTIC OPERATING-CONDITIONS', IEEE JOURNAL OF QUANTUM ELECTRONICS, 31: (6) 1140-1151 JUN 1995
- [61] HU KZ, CHEN L, MADHUKAR A, CHEN P, KYRIAKAKIS C, KARIM Z, TANGUAY AR, 'INVERTED CAVITY GAAS/INGAAS ASYMMETRIC FABRY-PEROT REFLECTION MODULATOR', APPLIED PHYSICS LETTERS, 59: (14) 1664-1666 SEP 30 1991
- [62] LAW KK, MERZ JL, COLDREN LA, 'EFFECT OF LAYER THICKNESS VARIATIONS ON THE PERFORMANCE OF ASYMMETRIC FABRY-PEROT REFLECTION MODULATORS' JOURNAL OF APPLIED PHYSICS, 72: (3) 855-860 AUG 1 1992
- [63] GOOSSEN KW, CUNNINGHAM JE, JAN WY, 'STACKED DIODE ELECTROABSORPTION MODULATOR', IEEE PHOTONICS TECHNOLOGY LETTERS, 6: (8) 936-938 AUG 1994
- [64] FRITZ IJ, MYERS DR, VAWTER GA, BRENNAN TM, HAMMONS BE, 'NOVEL REFLECTANCE MODULATOR EMPLOYING AN INGAAS/ALGAAS STRAINED-LAYER SUPERLATTICE FABRY-PEROT CAVITY WITH UNSTRAINED INGAAS/INALAS MIRRORS', APPLIED PHYSICS LETTERS, 58: (15) 1608-1610 APR 15 1991
- [65] B.S. RYVKIN, A.C. WALKER AND E.A. AVRUTIN, 'ALGAAS HOT-ELECTRON OPTICAL MODULATOR', APPLIED PHYSICS LETTERS, 77:(13) 2060-2062 SEPT 2000
- [66] WOODWARD TK, KRISHNAMOORTHY AV, GOOSSEN KW, WALKER JA, TSENG B, LOTHIAN J, HUI S, LEIBENGUTH R, 'MODULATOR-DRIVER CIRCUITS FOR OPTOELECTRONIC VLSI', IEEE PHOTONICS TECHNOLOGY LETTERS, 9: (6) 839-841 JUN 1997

Chapter 2:

Fabry-Perot MQW modulator: Physics and Basic Concepts

2.1 introduction

The aim of this chapter is to present in a qualitative way the physics of the Fabry-Perot MQW modulator structure and to introduce how the device physics can be simulated. This quantitative understanding allows the physical device operation to be modelled using a computer program, permitting the boundaries of device operating to be explored much faster than would be possible solely with experimental exploration. This leads to Chapter 3 where the application of this model allows the principal goal of this thesis to be pursued. In Chapter 2 the electrical and optical properties of multiple quantum wells are first reviewed. The effect of an electric field on these properties then shows why these structures are used as devices for amplitude light modulation upon incorporation in a *p-i-n* structure. By including the *p-i-n* structure in an optical cavity yielding the Fabry-Perot modulator structure, increased sensitivity to changes in device reflectivity is obtained, achieving larger amplitude modulation. Finally the Transfer matrix model used to simulate these devices is detailed.

2.2 Low dimensional devices

Many of the successful applications of semiconductor multilayer heterostructures exploit the optical properties of quantum wells. Dramatic improvements in semiconductor materials, as well as a deeper understanding of the underlying physics due to extensive research into their optical properties [1] has led to a wide variety of devices including the Electro-absorption modulator. The optical properties of bulk semiconductors are due to the interaction of a continuum of electron states and a continuum of photon states having matching energy and momentum. The energy continuum of electron states or band structure is shown in Figure 2.1 for GaAs.

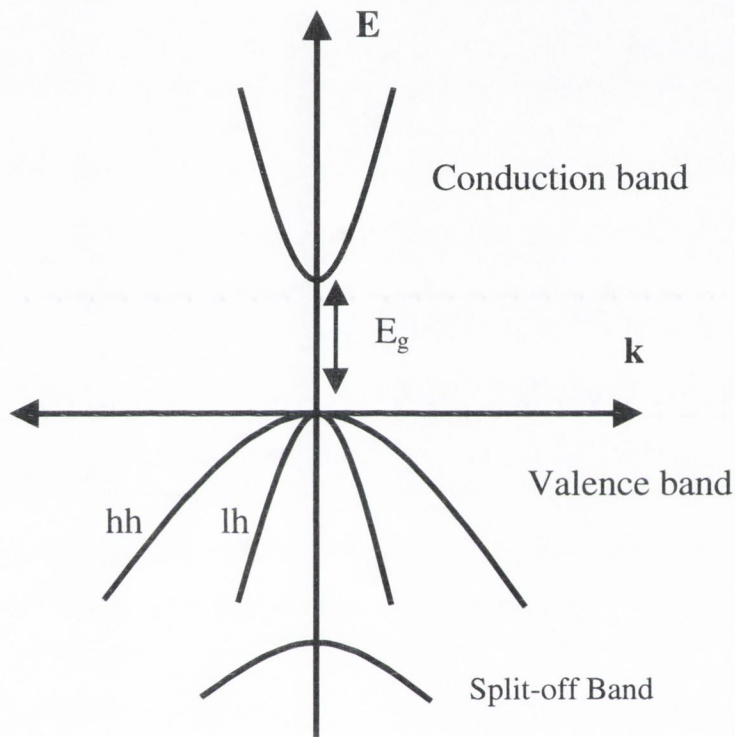


Figure 2.1: Energy-momentum plot of GaAs band structure

This continuum of electron states can be altered and made discrete by confining the electron in one direction to a region of space using a quantum well, thus changing the electron properties and the allowed electron energies. This approach is well established. Photons can also be confined in one dimension by a planar optical cavity allowing only certain optical energies to propagate. Additional modifications to the free space bulk semiconductor case result in interesting consequences and have been the subject of extensive research. Confinement of electrons in 2 dimensions (quantum wires) and 3 dimensions (quantum boxes), as well as optical confinement in 2 dimensions (waveguides) and 3 dimensions (photonic band gaps) is possible and produce interesting consequences. Technological problems in the fabrication of these devices have hindered research although much progress has been made in recent years [2]. The devices of interest in this thesis use confinement of electrons and photons to (quasi) two dimensions.

2.3 Epitaxial Growth

Large progress has been achieved in epitaxial growth of semiconductor crystals since the beginning of epitaxial growth techniques in the 1960s. The introduction of Molecular Beam Epitaxy (MBE) and Metal-Organic Chemical Vapour Deposition (MOCVD) allowed control of the chemical composition and the level of doping to thicknesses that approach an atomic monolayer. The semiconductor devices used in this work were grown by MBE by Prof. Colin Stanley at the University of Glasgow. This technique involves placing various semiconductor materials in various cells which are heated by an oven above their various melting points in a ultra high vacuum. Each cell has a shutter that can be opened and closed in less than 0.1s. The duration for which each shutter is open and the temperature of the cell determines the flux of atoms exiting and falling upon the growth substrate. The crystal integrity of the growing crystal can be monitored by *in-situ* techniques such as reflection high-energy electron diffraction (RHEED). In-situ optical reflectance monitoring can monitor the crystal layer growth rate. This technique is very important for the growth optical cavities and thickness accuracies of 0.2% of the desired thickness are currently achievable [3]. Using this growth technique layer thickness can be grown to accuracies of a few nanometers and hetero-interface widths of the order of a monolayer at growth rates typically $1\mu\text{m hr}^{-1}$. Wafer uniformity is reasonable with typical layer thickness fluctuations from the centre thickness of 1 to 1.5% across the majority of a 2-inch wafer [4]. It is this non-uniformity that currently limits the usable wafer area for fabrication of large arrays of devices incorporating an optical cavity. A more detailed account of MBE growth techniques can be found in [5]. This growth technique allows the growth of high quality thin films of semiconductor material having different energy band gaps allowing semiconductor quantum well structures to be grown with properties not seen in bulk material [6]. It also allows high quality distributed Bragg mirrors to be grown epitaxially with chosen reflectivities up to 99.9% [7]. Thus the interesting properties of photon and electron confinement can be monolithically integrated in one device.

2.4 Properties of quantum wells

An epitaxially grown multiple quantum well structure consisting of alternating high and low energy band gap semiconductor material is shown in Figure 2.2. Electrons (and holes in the valence band) in the lower band gap material are confined to a potential well due to the discontinuity in the conduction (and valence) band energy profiles at the different layer interfaces. The potential barrier can be engineered to be sufficiently large so a carrier cannot escape due to gained thermal energy or interaction with lattice vibrations. If the well width is then reduced so the electrons and holes are not in an infinitely thick material then the electron and hole are confined to a potential well in the growth direction. Quantum size effects now become important and have a large influence on the electronic and optical properties of the semiconductor. Their energies now become quantised and can be calculated from the quantum physics of a particle in a potential well. Since confinement only occurs in the growth

direction there is no confinement in the other two directions and the electron and hole properties remain similar to the bulk case in these directions.

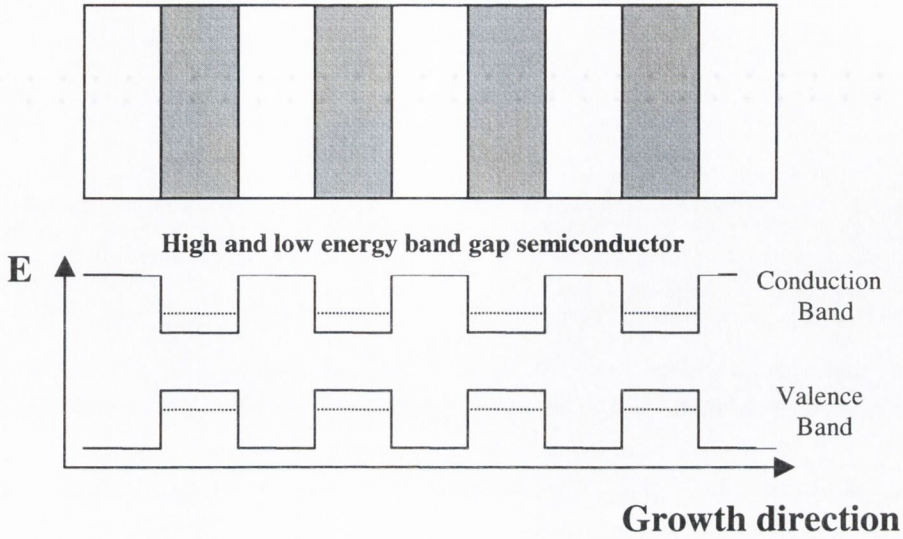


Figure 2.2: Multiple quantum well structure consisting of alternating high and low energy band gap semiconductor material.

2.4.1 Electron confinement in one dimension

As a first approximation the electron and hole confined in the quantum well can be considered as a particle in an infinite potential well [8]. Taking the potential energy inside the quantum well of length L_z to be zero and to be infinite at the well/barrier interface, the general solution to the time independent one dimensional Schrodinger equation

$$-\frac{\hbar^2}{2m_{eff}} \frac{d^2\psi(z)}{dz^2} + V(z) = E\psi(z) \tag{2.1}$$

is given by

$$\psi(z) = A\sin(kz) + B\cos(kz) \tag{2.2}$$

Where

$$k = \frac{\sqrt{2m_{eff}E}}{\hbar} \tag{2.3}$$

and A,B are constants. Assuming the centre of the quantum well is at $z=0$, then $\psi(z)=0$ at $\pm L_z/2$ from equation (2.2) this is possible when

$$2B \cos\left(\frac{kL_z}{2}\right) = 0 \qquad 2A \sin\left(\frac{kL_z}{2}\right) = 0 \qquad (2.4)$$

and gives solutions to the one dimensional Schrodinger equation in the form

$$\psi(z) = B \cos(kz) \qquad \cos\left(\frac{kL_z}{2}\right) = 0 \qquad (2.5)$$

and

$$\psi(z) = A \sin(kz) \qquad \sin\left(\frac{kL_z}{2}\right) = 0 \qquad (2.6)$$

The allowed values for k from equation (2.5) and (2.6) are thus

$$k_n = \frac{n\pi}{L_z} \qquad n=1,2,3,4,\dots \qquad (2.7)$$

Thus equation (2.3) and (2.7) give the allowed energy of an electron or hole inside a quantum well as

$$E_n = \frac{\hbar^2 k_n^2}{2m_{eff}} = \frac{\pi^2 \hbar^2 n^2}{2m_{eff} L_z^2} \qquad (2.8)$$

where m_{eff} is the effective mass of the electron or hole. The allowed electron and hole energies in the quantum well given by Equation (2.8) are shown in Figure 2.3 where there are a number of interesting points. Firstly the lowest allowed electron energy ($n=1$) is given by $E_C + (\pi^2 \hbar^2 / 2m_{eff} L_z^2)$ where E_C is the conduction band edge value. For $L_z=10\text{nm}$ and taking the electron effective mass in GaAs as $m_{eff}=0.067m_e$ the lowest electron energy level is $E_C + 56\text{meV}$. This comprises of $\sim 4\%$ of the GaAs bandgap. Thus absorption and emission is possible at energies greater than the bandgap and can be tuned by altering the thickness of quantum well as $E \propto 1/L_z^2$. There is of course a limit to the minimum barrier thickness below which tunnelling will occur. For a compound semiconductor with $E_g \sim 1\text{eV}$ this value is $\sim 5\text{nm}$ [9]. In the quantum well formed in the valence band quantised energies are also present. The degeneracy between the light and heavy hole seen in Figure 2.1 for the bulk case is lifted due to the difference in hole effective mass. For a GaAs quantum well with $L_z=10\text{nm}$ the energy separation is $\sim 10\text{meV}$. Thus as shown in Figure 2.3 we now have electron confined energies E_{e1} , E_{e2} and heavy hole and light hole confined states E_{hh1} and E_{lh1} . We will shortly see that it is absorption between these levels that dominate the absorption spectra of MQWs near the band gap energies. In reality the potential barrier is never infinite and the number of bound states in the quantum well decrease with decreasing

potential barrier. Since the quantum numbers of interest to us are small $n=1,2$ the infinite well approximation can be used for a quantum well with a finite potential barrier.

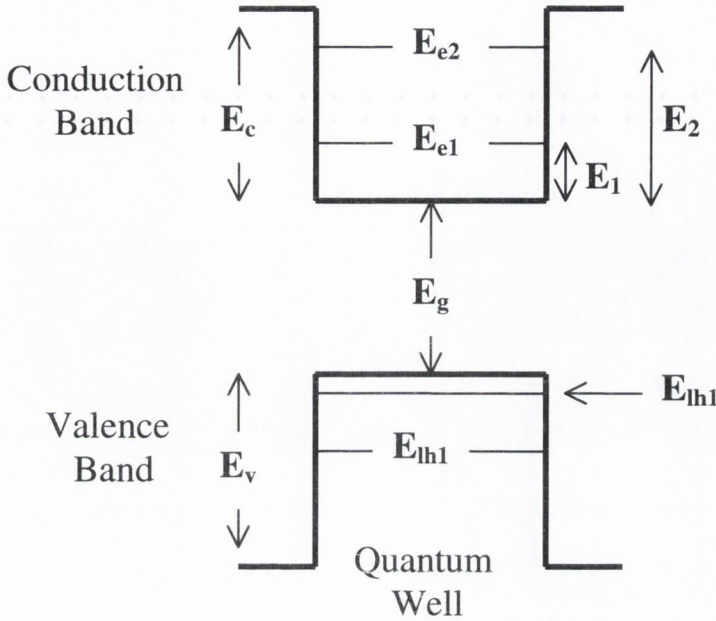


Figure 2.3: Allowed electron and hole energies in a quantum well given by equation (2.8)

2.4.2 Density of states

The absorption coefficient α for optical absorption between the valence and conduction band at a particular energy is directly proportional to the density of states. Thus any changes will directly be seen in the absorption spectrum of the MQWs. The confinement of an electron and hole in a quantum well also modifies the bulk three-dimensional density of states ρ_{3D} given by

$$\rho_{3D} = \frac{\sqrt{2} m_{eff}^{3/2}}{\pi^2 \hbar^3} \sqrt{E} \quad (2.9)$$

to a two-dimensional value $\rho(2D)$

$$\rho_{2D} = \frac{m_{eff}}{\pi \hbar^2} \quad (2.10)$$

for a quantised energy E_n in an infinite potential well. Both are plotted in figure 2.4.

The two dimensional density of states $\rho_{2D} = \rho_{3D}(E_n)L_z$ and are equal at energies E_n . It is important to note here that whereas the three dimensional density of states tends towards zero the two-dimensional case remains finite. This step like density of states is seen in the measured MQW absorption spectrum shown in Figure 2.5.

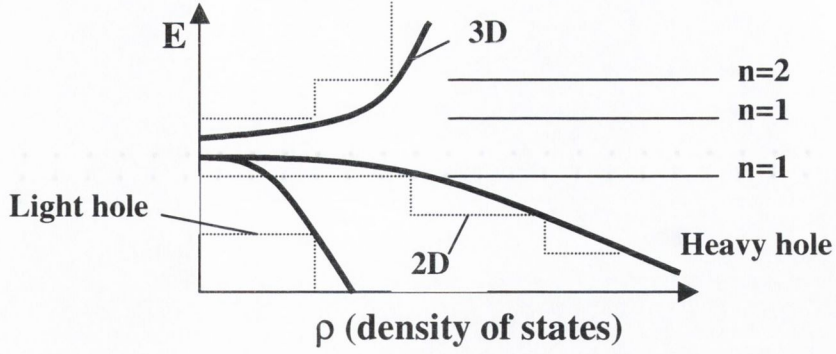


Figure 2.4: 2D step like density of states as seen in the measured MQW absorption spectrum shown in Figure 2.5.

2.5 Excitons

The absorption spectrum of a MQW would solely contain step-like optical transitions each consisting of the allowed transitions between the E_{lh1} , E_{hh1} and E_{e1} , as expected from Figure (2.3) and (2.4) but for the formation of excitons. Excitons are electron-hole pairs that have a hydrogen atom like structure, drawn together due to their coulomb attraction. Exciton formation in a quantum well and its reaction to an electric field form the basis of operation of a MQW Electro-absorption modulator. The exciton binding energy can be calculated by drawing an analogy with the Bohr atom and the 1S exciton state, the exciton binding energy in 3D is given by

$$R_{ex3D} = \frac{-m_{eff} e^4}{2(4\pi\epsilon_r \epsilon_o) a} \quad (2.11)$$

Where ϵ_r is the dielectric constant for the semiconductor material and a the Bohr radius of the exciton given by [1]

$$a = \frac{4\pi\epsilon_r \epsilon_o \hbar^2}{\mu e^2} \quad (2.12)$$

where μ is the reduced mass of the electron and hole.

When the exciton is confined to two dimensions as in a quantum well the exciton binding energy is given by [10]

$$R_{ex2D} = R_{ex3D} \left[\frac{1}{(n - 1/2)^2} \right] \quad (2.13)$$

Thus the binding energy of the 1S exciton is increased by a factor of 4 when confined to two-dimensions. In bulk GaAs the lowest exciton binding energy is $\sim 4.4\text{meV}$, having a Bohr radius of $\sim 20\text{nm}$. Thermal energy at room temperature is much greater than the binding energy so phonon scattering having energies $\sim 36\text{meV}$ can dissociate the exciton state. The absorption spectrum for the

bulk case at room temperature barely resolves the exciton absorption and appears part of the absorption continuum [11]. In bulk material the exciton only becomes clear at low temperatures. The situation is dramatically altered in a quantum well. The ideal 2D limit is never reached but as the quantum well width is reduced to the order of the exciton radius and smaller, the exciton radius decreases and the binding energy increases [1]. The increased overlap of the electron and hole wavefunctions also increases the oscillator strength and absorption coefficient [10]. The well width cannot be reduced infinitely due to penetration of the electron and hole wavefunction into the barrier thus decreasing their overlap and the absorption coefficient. Thus there is an optimum thickness, for GaAs this is for $L_z \sim 5\text{nm}$ and for $\text{In}_{0.53}\text{Ga}_{0.47}\text{As}$ $L_z \sim 8\text{nm}$. The corresponding exciton binding energy is normally a factor of 2-3 greater than the bulk case. This larger exciton binding energies in quantum wells allows exciton effects to dominate the room temperature optical properties [12]. This leads to some interesting applications such as four wave mixing and optical bistability.

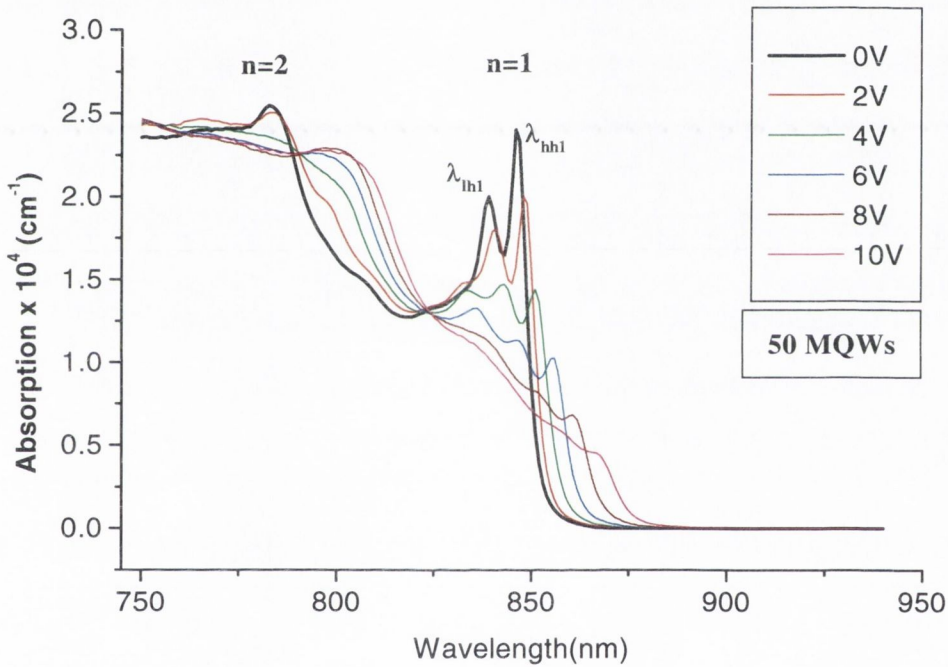


Figure 2.5: Room temperature absorption spectrum for 50 MQWs having a GaAs well thickness $L_w=8.5\text{nm}$ and a AlGaAs barrier thickness $L_B=6\text{nm}$ [13].

The room temperature absorption spectrum is shown (0V thick line) in figure 2.5 for 50 MQWs having a GaAs well thickness $L_w=8.5\text{nm}$ and an AlGaAs barrier thickness $L_B=6\text{nm}$. The absorption spectrum at energies close to the bandgap energy is dominated by 1S excitons formed by the E_{lh1} , E_{hh1} to E_{el} transitions ($n=1$ subband). The excitons formed by the $n=2$ subband have a large linewidth due to phonon scattering and fluctuations in quantum well width. This results in the excitons being broadened and unresolvable. The step like density of states ($n=1,2$) predicted in section 2.4.2 can clearly be seen.

2.6 Effect of an electric field on exciton absorption

In bulk semiconductors the change in absorption due to the presence of an electric field is known as the Franz-Keldysh effect. The semiconductor energy bands in the presence of an electric field are tilted and tunnelling of the electron and hole wavefunctions into the bandgap region results in light at energies less than the band gap energy being absorbed. At larger electric fields the spatial overlap of the electron and hole wavefunctions is decreased and this results in a smoothing of the absorption spectrum around the band edge [14]. The role of excitons in bulk material is small and thus this effect is limited in bulk material. In quantum wells the situation is quite different when an electric field is applied in the growth direction perpendicular to the quantum wells [15]. In this case the tilted energy bands in the quantum well cause the electron and hole states to move closer in energy (Figure 2.6).

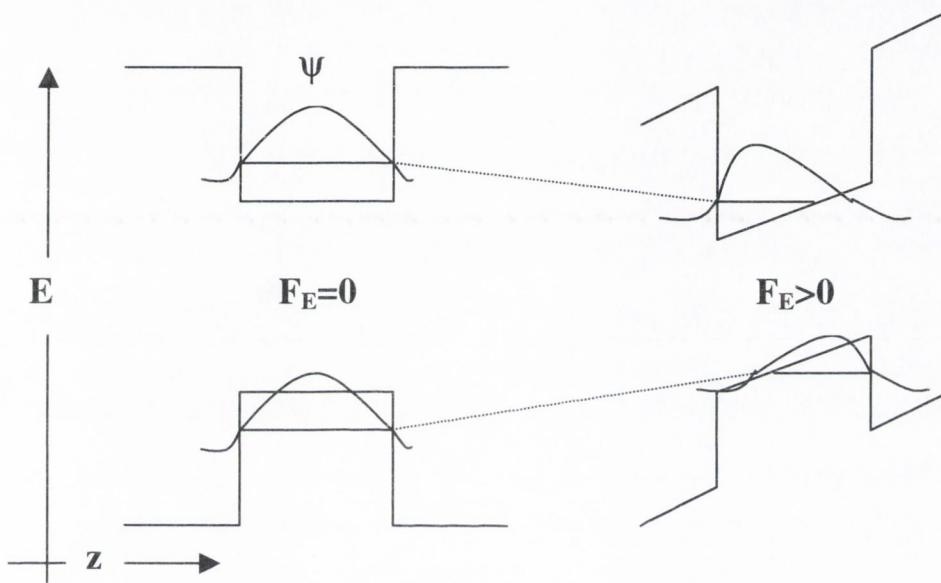


Figure 2.6: Tilted energy bands in the quantum well under the influence of an electric field cause the electron and hole states to move closer in energy. The electron and hole wavefunctions are also shown.

In the presence of an electric field the quantum well is far more effective at keeping the electron and hole in close proximity and although their wavefunctions move to opposite sides in the quantum well they remain overlapped and large exciton absorption is possible at much higher electric fields. Thus when an electric field is applied the MQW absorption spectrum consists of strong exciton absorption shifting to shorter wavelengths, this is the Quantum Confined Stark Effect (QCSE). This can be seen in Figure 2.5 for different voltages applied across the MQWs up to 10V. Exciton absorption can still be resolved at an electric field of $F_E = [10\text{V} / (50 \times 8.5\text{nm} + 6\text{nm})] \approx 1.4 \times 10^7 \text{ Vm}^{-1}$. There is a reduction in the overlap of the electron and hole wavefunction with increasing electric field resulting in the exciton absorption decreasing as seen in Figure 2.5 but exciton dissociation occurs at much higher fields compared to the bulk case. In bulk GaAs exciton features disappear at electric fields $\approx 10^5 \text{ Vm}^{-1}$. Exciton peak absorption changes up to 50 times greater are possible in MQWs. There is also a broadening of the exciton linewidth as an electric field is applied. This is most probably due to inhomogeneities in the electric field due to residual doping fluctuations or fluctuations in the quantum

well and barrier thickness. Surface roughness can also contribute as wavefunctions become localised towards the edges of the quantum wells. A full analysis of the effect of an electric field on MQWs can be found in [14,16].

2.7 MQW engineering

In using QCSE to form an electroabsorption device there are two operating positions in the wavelength spectrum in Figure 2.5. Large absorption changes occur at the hh1 exciton wavelength where an initially large absorption at zero bias decreases upon application of an electric field. This is normally called the λ_0 position. Large absorption changes also occur at longer wavelengths to the hh1 exciton wavelength (~860nm in Figure 2.5) where the initial absorption is small at zero bias and increases upon application of the electric field. This is known as the λ_1 position. It is this operation point which is chosen for the devices being considered in this thesis and the reasons why will become clearer in Chapter 3. For a weak electric field F_E and uniform symmetric wells the change in energy of the conduction and valence subband level E_1 (figure 2.3) is given by [17]

$$\Delta E_1 \approx m_{eff} F_E^2 L_Z^4 \quad (2.14)$$

The shift in wavelength seen in Figure 2.5 is thus quadratic with applied electric field. At much larger electric fields this quadratic behaviour weakens due to a build up of carriers in one side of the quantum well. Carriers will eventually escape through tunnelling at large fields. In designing MQW structures there are compromises between parameters. The wavelength shift is dependent on the well width L_Z , thus thicker wells produce larger shifts but also reduce carrier confinement so there is a compromise well thickness typically 5-15nm for III-V semiconductors. The exciton peak absorption in GaAs quantum wells was measured in ref. [18] for various well widths and was shown to increase for decreasing well widths down to ~5nm. Competing against this is the reduced wavelength shift at shorter well widths (Equation 2.14) and increased exciton linewidth proportional to $1/L_Z^2$ due to phonon broadening. The measured absorption change at the λ_1 wavelength position decreased as the exciton linewidth increased at thinner quantum wells <5nm.

Of principal concern in this thesis is the operation of these devices at low voltages (<5V) and there are a number of options available to reduce the operating voltage.

- a) The electric field F_E is inversely dependent on the total thickness t of the number of MQWs ($F_E = \text{Volt}/t$). Using short well widths ($\approx 10\text{nm}$) allows the operating voltage to be reduced. This results in a reduced exciton wavelength shift but relatively large absorption changes are still possible at λ_1 .
- b) The total number of MQWs can be reduced thus reducing the operating voltage. The reduction in absorption can be compensated by increasing the optical mirror reflectivities (Section 2.11) [19]. The disadvantage in this case is that high reflectivity mirrors reduce the device operating tolerances i.e. optical bandwidth, temperature sensitivity etc.

- c) Using wider well widths ($\approx 15\text{nm}$) results in a larger exciton wavelength shift but larger linewidth due to poorer confinement. By operating at the λ_0 position relatively large absorption changes (estimated from $\approx 1.3 \times 10^4 \text{ cm}^{-1}$ to $0.4 \times 10^4 \text{ cm}^{-1}$ [22]) are possible at relatively low electric fields and thus lower voltages.

The freedom allowed in MQW design summarised above is not enjoyed in the case of InGaAs wells grown on GaAs substrates. For the wavelength of interest in this work at 1047nm the $\text{In}_{0.22}\text{Ga}_{0.78}\text{As}$ well is lattice mismatched to GaAs by 1.7% for a 10nm well [21]. The strained active region is balanced by growing a buffer layer on top of the substrate and is discussed further in the next section. Thus the ease of lattice matched quantum well variations summarised above is not straightforward in strained material. The increased exciton linewidth due to alloy broadening and growth imperfections results in the absorption coefficient of longer wavelength MQWs being reduced by around a factor of two compared to the GaAs/AlGaAs system [22]. The strained active region increases the exciton linewidth further. The room temperature absorption spectrum for 95 MQWs having an $\text{In}_{0.22}\text{Ga}_{0.78}\text{As}$ well thickness $L_w=8.8\text{nm}$ and an $\text{Al}_{0.25}\text{Ga}_{0.75}\text{As}$ barrier thickness $L_B=5.54\text{nm}$ is presented in figure 2.7 [23]. Compared to Figure 2.5 the reduced and broadened exciton absorption is clear. In this thesis we have not investigated changes to the well and barrier thickness to maximise the absorption change possible. Earlier work was done by Stanley and Walker et al. [21] to balance the strain in these wells (section 2.8) and the absorption spectra measured from the best quality MQW structures were used (figure 2.7).

The absorption changes possible are much reduced compared to the GaAs/AlGaAs system due to the linewidth broadening and the lower absorption coefficient. For low voltage operation option b) was found to give the maximum reflectivity change at low voltage operation and will be addressed further in Chapter 3. The work presented in this thesis primarily concerns absorption changes due to InGaAs MQWs but results are generally applicable to other material systems.

2.8 Strained MQW structures

As mentioned above the wavelength of interest in this work at 1047nm requires an $\text{In}_{0.22}\text{Ga}_{0.78}\text{As}$ quantum well and is lattice mismatched to GaAs by 1.7% for a 10nm well [21]. In order to grow the active region on a GaAs substrate, an $\text{In}_z(\text{Al}_{0.15}\text{Ga}_{0.75})_{1-z}\text{As}$ buffer layer is grown on the GaAs where z is linearly graded from $z=0$ up to $z=0.17$. The active region having wells in compression and barriers in tension have an average lattice constant matching the top of the linearly graded buffer layer and are grown on this pseudo-substrate [24]. Lattice mismatch in the material generally reduces and broadens the exciton peak at high electric fields and produces a larger shift of the exciton peak, possibly due to defects arising from lattice relaxation [21]. The measured absorption data in Figure 2.7 shows a well defined exciton peak at 25V indicating the material quality is good and with no significant lattice mismatch or layer relaxation. The layer compositions for the Bragg mirror are chosen to have a lattice constant matching the graded buffer layer. The exciton line width in this material system is increased considerably relative to GaAs wells and is accompanied by a reduced absorption coefficient. The

increased linewidth is believed to be due to inhomogeneities such as alloy broadening and quantum well thickness variations and is also a natural result of a lower band-gap energy. In this case there is also a contribution due to strain non-uniformity that shifts the bandgap by varying amounts [24]. This results in smaller absorption changes in this material and thus it is expected that higher reflectivity mirrors may be required to compensate.

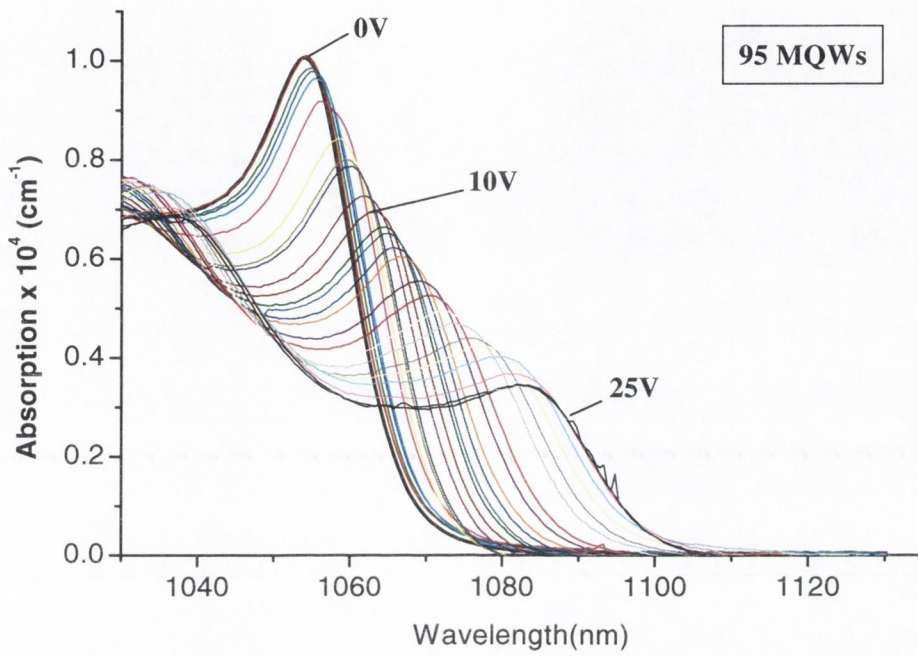


Figure 2.7: Room temperature absorption spectrum for 95 MQWs having an InGaAs well thickness $L_w=8.8\text{nm}$ and a AlGaAs barrier thickness $L_B=5.54\text{nm}$ [23].

2.9 The multiple quantum well *p-i-n* diode

An efficient way of applying an electric field across the MQWs is to incorporate the MQWs as the intrinsic region of a *p-i-n* diode [25]. By reverse biasing the diode, a large electrical field appears across the intrinsic MQWs and the QCSE allows light incident on the device to be variably attenuated. The device can operate in transmission [25], in reflection from a single back mirror, effectively doubling the MQW absorption (double-pass device) [26], or as an optical cavity device sandwiching the MQWs between two mirrors (section 2.10). In all these cases light is incident perpendicular to the growth direction as shown in figure 2.8 and large 2-dimensional arrays can be produced. Operation in a waveguide format is also widely used and often grown integrated to semiconductor laser sources [27]. For these devices operation at very low voltages is possible due to the larger interaction length. Unfortunately light coupling is more difficult and much larger arrays with easier light coupling are possible for surface normal incidence.

As the device operates in reverse bias, very small currents flow through the device thus allowing very large arrays with high efficiency, very low power dissipation and reduced thermal effects compared to light emitting devices. The device can also be operated as a detector facilitating the

production of large arrays of detectors and modulators on a single wafer. In reverse bias the intrinsic region is depleted of carriers and the photo-generated carriers are swept out and detected in an external circuit. High internal quantum efficiency (≈ 1) and responsivity is possible [14]. High-speed detection is limited by the sweep out time of the carriers and circuit capacitance [8]. Figure 2.8 shows the layer structure of the single back mirror reflection (double-pass) modulator being used in the SPOEC system (section 1.3). Gold metal contacts are deposited to form the electrical connection to the **p** and **n** doped layers. The gold metal contact on the **p**-doped layer also acts as the back mirror of the device.

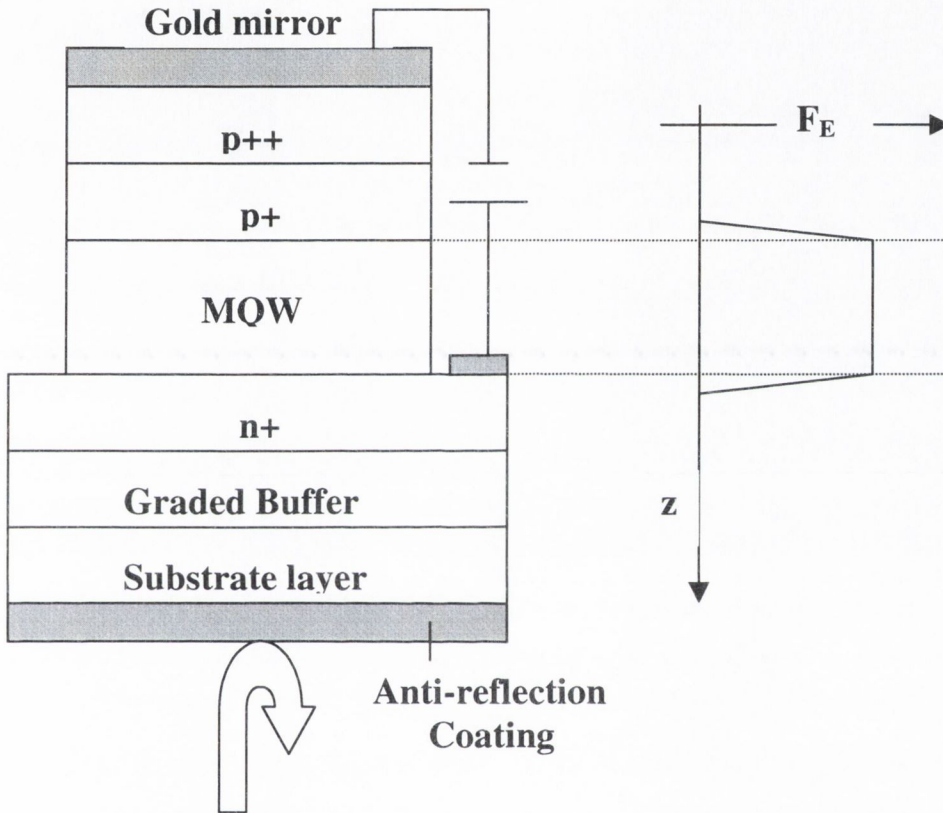


Figure 2.8: layer structure of a reflection (double-pass) modulator used in the SPOEC system (section 1.3). The gold metal contact on the **p**-doped layer also acts as the back mirror of the device. The average electric field F_E across the MQWs is also shown.

Also shown in figure 2.8 is a typical plot of the electrical field across the device. The reverse bias voltage is dropped across the intrinsic MQWs and the resulting average electric field F_E is given by

$$F_E = \frac{V + V_{Intrinsic}}{t_{Intrinsic}} \quad (2.15)$$

where V is the applied reverse voltage, $V_{Intrinsic}$ is the built in voltage across the intrinsic region and $t_{Intrinsic}$ is the thickness of the intrinsic region i.e. the total thickness of the MQWs. $V_{Intrinsic}$ is dependent on the p and n type doping concentrations and is typically 1-1.5V. The built in voltage will play an important role in low voltage operation of these devices. It could be used as a built in pre-bias or the

device could be forward biased by an amount equal to $V_{\text{Intrinsic}}$ to achieve modulation. The average electric field across the MQWs in figure 2.8 is shown as a flat line. In reality there is residual doping N_i in the intrinsic region which results in fluctuations in the electric field across the MQWs, depending on whether the impurity is p-type or n-type. Residual doping N_i will result in different quantum wells experiencing different electric fields and broadening of the exciton absorption [28]. High values of residual doping N_i also reduce the diode breakdown voltage.

2.10 Summary

So far in this chapter the effect of electron and hole confinement in quantum wells on the linear optical properties have been presented. The resulting large absorption change upon application of an electric field allows amplitude modulation to be achieved at wavelengths around the quantum well material bandgap. Devices can be formed by incorporating the MQWs in a *pin* diode structure. By placing the diode in an optical cavity, photon confinement is now also possible and the resulting optical properties of such a device called a Fabry-Perot modulator are presented next.

2.11 The Fabry-Perot optical cavity

The optical characteristics of a cavity formed by two parallel mirrors arise from multiple beam interference between light reflected from the back mirror interfering with light reflected from the front mirror. Figure 2.9 shows an optical cavity consisting of a back mirror of reflectivity R_B and a front mirror of reflectivity R_F separated by a spacer layer of thickness L_o having a refractive index n .

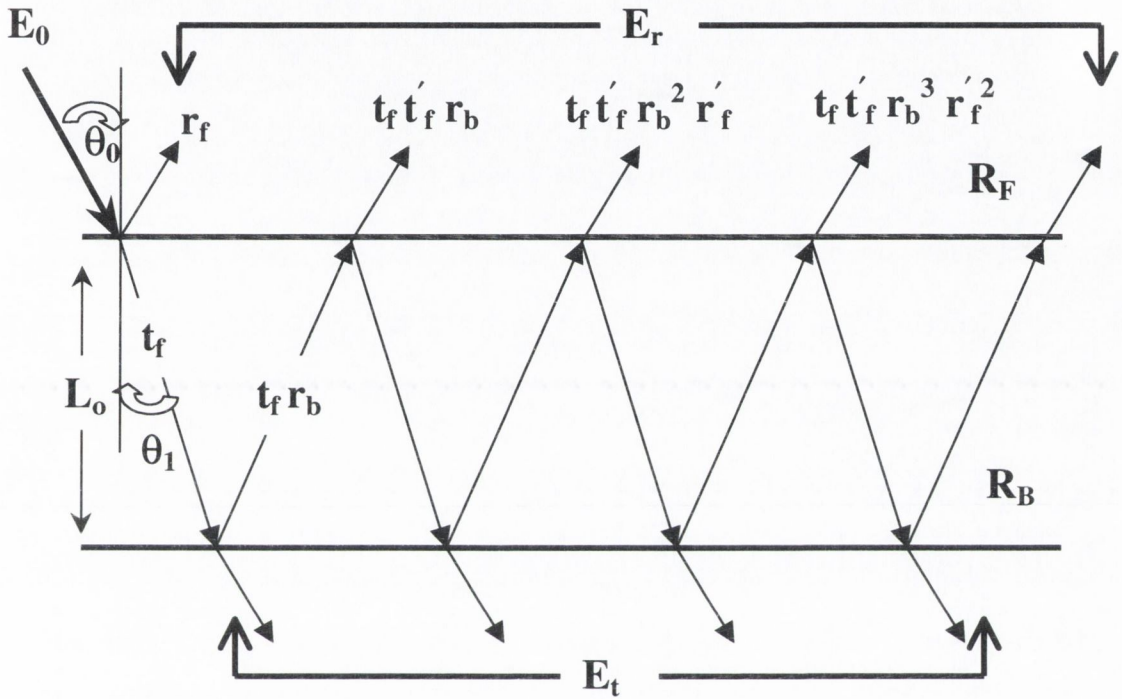


Figure 2.9: Fabry-Perot etalon of thickness L_o and refractive index n consisting of a front mirror of amplitude reflectance r_f and a back mirror of amplitude reflectance r_b . The incident reflected and transmitted waves are shown along with the amplitude coefficients for the reflected waves that are summed to find the total reflectance.

These characteristics can be found by considering a plane electromagnetic wave of amplitude E_0 incident upon the cavity at an angle θ_0 . A fraction of the incident amplitude r_f is reflected at the front mirror where r_f is the amplitude reflectance coefficient. The remaining fraction t_f is transmitted and undergoes multiple reflections inside the optical cavity from the front and back mirrors. Interference will occur if the coherence length of the incident light is long compared to the cavity length L_o . The resultant reflected wave amplitude E_R can be found by summing all the reflected waves as shown in Figure 2.9 where the Stokes relations [29,30] $r = -r'$ and $t' = 1 - r^2$ are used. It is assumed the cavity is absorbing and attenuates the light by $e^{-\alpha L}$ for each double pass and $L = L_o(\cos\theta_1)$ where θ_0 is related to θ_1 through Snell's law. The phase change of a wave is given by $e^{-i\delta}$ upon each traversal of the cavity where δ is the phase thickness given by

$$\delta = \frac{2\pi nL_o \cos\theta_1}{\lambda} \quad (2.16)$$

The resultant wave amplitude E_R is thus given by

$$E_R = E_0 (r_f + t_f t_f' r_b e^{-\alpha L} e^{-2i\delta} + r_f + t_f t_f' r_b^2 r_f' e^{-2\alpha L} e^{-4i\delta} + \dots + \dots + r_f + t_f t_f' r_b^m r_f'^{m-1} e^{-m\alpha L} e^{-2mi\delta}) \quad (2.17)$$

which is a geometric series that converges to give the reflected amplitude $r = E_R/E_0$

$$r = \frac{r_f + r_b e^{-\alpha L} e^{-2i\delta}}{1 - r_f r_b e^{-\alpha L} e^{-2i\delta}} \quad (2.18)$$

and the reflected intensity is given by $R = |r|^2$.

Using trigonometric identities [29,30,31] the reflected intensity can be written incorporating the Airy function

$$R = \frac{R_0 + F \sin^2 \delta}{1 + F \sin^2 \delta} \quad (2.19)$$

where

$$R_0 = R_F \left(\frac{1 - \frac{R_\alpha}{R_F}}{1 - R_\alpha} \right)^2 \quad (2.20)$$

$$R_\alpha = \sqrt{R_F R_B} e^{-\alpha L} \quad (2.21)$$

$$F = \frac{4R_\alpha}{(1 - R_\alpha)^2} \quad (2.22)$$

F is known as the coefficient of finesse. The cavity finesse \mathfrak{S} defined as the ratio of the separation of adjacent resonances to the half width of the individual resonance is given by

$$\mathfrak{S} = \frac{\pi\sqrt{F}}{2} \quad (2.23)$$

If the mirror reflectivities increase, the cavity finesse also increases according to Equation 2.22. For a fixed cavity length L_o the separation of adjacent resonances will be unchanged, thus as the finesse

increases the half width of an individual resonance will decrease. This has important implications for the spectral bandwidth of Fabry-Perot modulators.

Similarly the transmittance is given by

$$T = \frac{T_0}{1 + F \sin^2 \delta} \quad (2.24)$$

$$T_0 = \frac{(1 - R_F)(1 - R_B)e^{-\alpha L}}{(1 - R_\alpha)^2} \quad (2.25)$$

Some simple calculations using these equations give an insight into the properties of an optical cavity and are presented in the next section. Finally returning to Equation 2.16, resonant modes are achieved when $\delta = m\pi = (2\pi n L_o \cos\theta)/\lambda$, where m is an integer. Differentiating across, if the cavity thickness L_o changes by an amount ΔL due to error in growth, assuming a constant refractive index value and incident angle, then this leads to a change in the resonance position given by

$$\frac{\Delta\lambda}{\lambda} = \frac{\Delta L}{L_o} \quad (2.26)$$

As a result of this equation the percentage change in wavelength from the desired wavelength is given by the percentage change in cavity thickness from the required thickness. This equation has important consequences for the epitaxial growth of large arrays of Fabry-Perot devices.

2.12 Fabry-Perot reflectance spectra

Using Equation 2.19 the reflectance spectrum for an optical cavity over a short wavelength range is plotted in Figure 2.10. The reflectance spectrum is plotted for a cavity having equal ($R_F=R_B=40\%$) and unequal reflectivities ($R_F=40\%$, $R_B=95\%$). First the case where there is no absorption in the cavity is considered. From equation 2.19 resonances occur every time (Equation 2.16) $\delta=0$ or $m\pi$ where m is an integer called the cavity order or at wavelengths given by

$$\lambda = \frac{2nL_o \cos\theta_1}{m} \quad (2.27)$$

For the situation where $R_F=R_B=40\%$ the cavity is symmetric and at wavelengths given by equation 2.26 the light reflected from the back mirror and the front mirror is equal in amplitude and π out of phase and thus complete cancellation/destructive interference occurs. Since we assumed no absorption, all light at this wavelength is thus transmitted as $T+R+A=1$. For the situation where $R_F=40\%$, $R_B=95\%$ the cavity is asymmetric and light reflected from the back and front mirrors have unequal amplitudes resulting in only partial cancellation and about 80% of the light is reflected. The more asymmetric the mirror reflectivities the greater the amount of light reflected back. If absorption α is introduced into the optical cavity the effective back mirror reflectivity is given by

$$R_{B(\text{eff})} = R_B e^{-2\alpha L_o} \quad (2.28)$$

Thus if MQW absorption is introduced into the cavity and the cavity resonance wavelength is placed at λ_0 or λ_1 (section 2.7), the cavity reflectance can be controlled by the applied electric field across the MQWs.

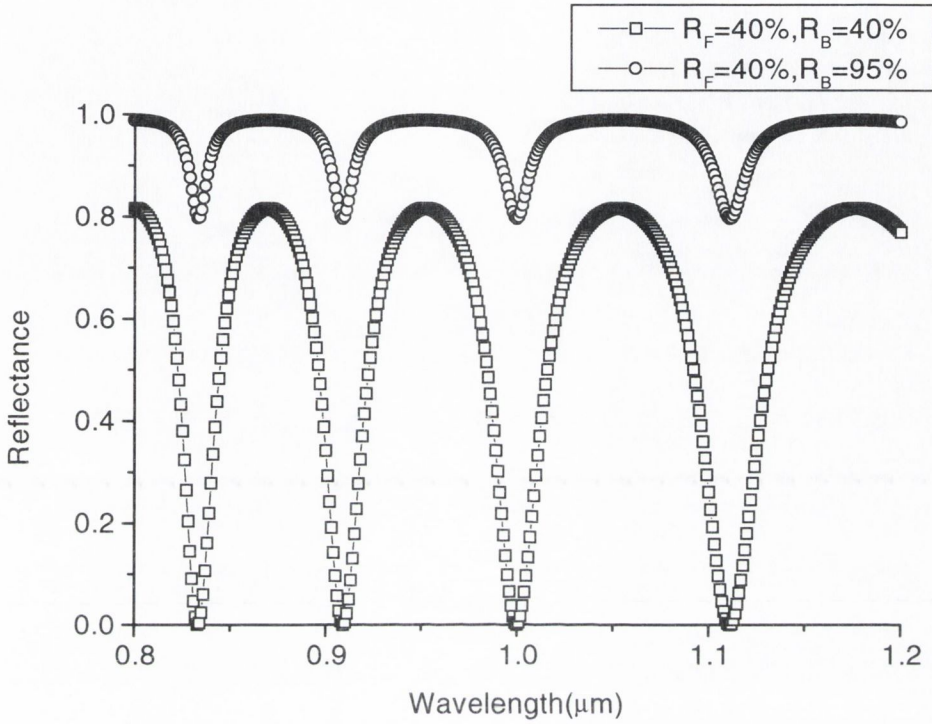


Figure 2.10: Reflectance spectrum plotted over a short wavelength range, using equation 2.19 for a cavity having equal ($R_F=R_B=40\%$) and unequal reflectivities ($R_F=40\%$, $R_B=95\%$) and no absorption in the optical cavity. $L_o=5000\text{nm}$, $n=1$ and $\theta_o=0$.

When $R_{B(\text{eff})}=R_F$ the cavity changes from being asymmetric to being symmetric and the cavity reflectance is zero due to complete destructive interference. This is known as the ‘impedance matching condition’ and occurs when

$$\alpha = \frac{1}{2L_o} \ln \left(\frac{R_B}{R_F} \right) \quad (2.29)$$

The advantage of using such a structure is that the interaction length of the light with the absorbing region can greatly be increased compared to a double-pass or transmission structure making the cavity reflectance far more sensitive to absorption changes. The reflectance from a double-pass modulator decreases only exponentially to zero as the absorption is increased. For low voltage operation Equation 2.15 requires the total absorption to reduce. Using an optical cavity can compensate for the reduced absorption and much lower voltage operation is expected for cavity devices.

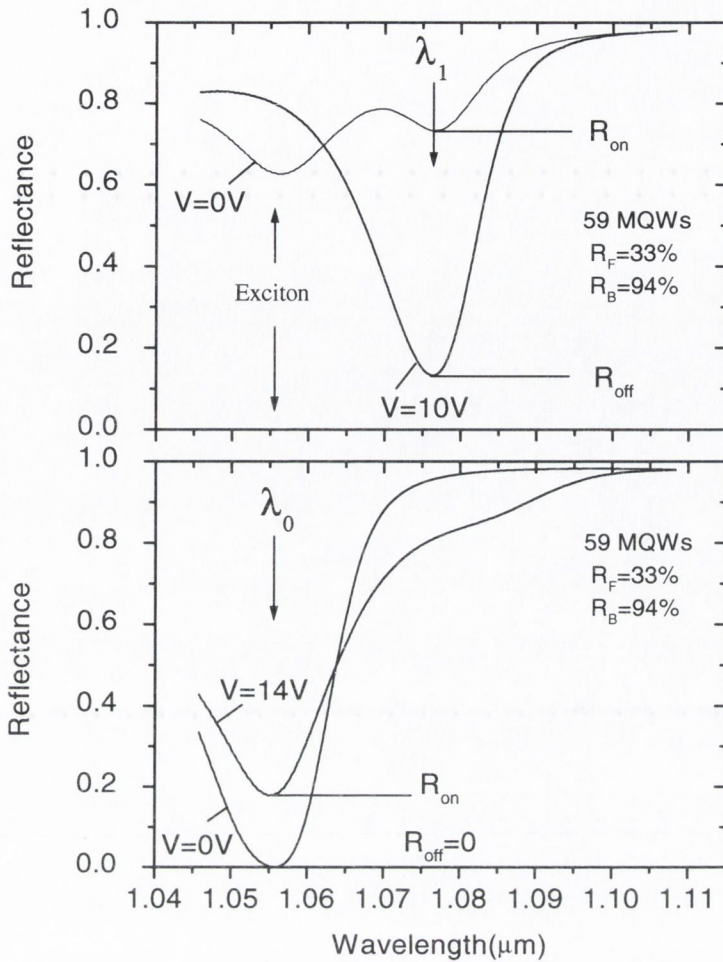


Figure 2.11: Reflectance spectra calculated using a transfer matrix model (see section 2.14) showing operation at the λ_0 and λ_1 operating positions.

Figure 2.11 shows the reflectance spectra calculated using a transfer matrix model (see section 2.14) showing operation at the λ_1 and λ_0 operating positions where device operation generally occurs. The absorption data from Figure 2.7 is used in the calculation. The top graph in figure 2.11 shows typical spectra when the Fabry-Perot resonance is placed at the λ_1 position. The absorption at λ_1 is initially small at 0V and the effective back mirror reflectivity is much higher than the front and thus the initial cavity reflectance is high/on. This is known as a normally 'on' device. When a voltage of 10V is applied the exciton shifts in wavelength and the absorption increases at λ_1 . The effective back mirror reflectivity is much closer in value to the front mirror and large cancellation occurs resulting in a low reflectance value from the optical cavity. Thus amplitude modulation is possible at λ_1 . The bottom graph shows operation when the Fabry-Perot resonance is at λ_0 . The front mirror reflectivity is chosen so the impedance matching condition (eqn.2.29) is fulfilled at λ_0 and the starting reflectivity is close to zero (symmetric cavity). This device is known as a normally 'off' device. When the voltage is turned on the exciton absorption shifts and reduces at λ_0 . The effective back mirror reflectivity increases

producing an asymmetric cavity and partial cancellation, making amplitude modulation possible at λ_0 . A detailed examination of these operating positions is presented in Chapter 3.

The device performance is normally evaluated in terms of the following parameters:

- (i) Contrast ratio $C = R_{on}/R_{off}$
- (ii) Reflectivity change $\Delta R = R_{on} - R_{off}$
- (iii) Insertion loss $IL = 1 - R_{on}$
- (iv) Spectral/optical bandwidth
- (v) Operating voltage V

All the above parameters will be addressed in the following chapters. This section is concluded by presenting the mode of operation of the modulator devices being investigated in this work. In the SPOEC optical interconnect system [32] the modulator devices are differentially paired due to the limited contrast achievable with a double-pass modulator, two modulators are used, one carries the data while the other carries its logical complement. In this case it is the signal difference that decides the logic state i.e. whether the first beam produces a larger voltage than the second at the detector. Single ended operation can result in logic errors if the received optical power unintentionally changes above or below certain logic levels. Differential operation guards against these optical power fluctuations, minimising the potential error and allowing logical levels to be decided correctly. For differential operation it is the signal difference which decides the logic level and thus in this thesis devices are optimised to produce maximum reflectivity changes $\Delta R = R_{on} - R_{off}$. The mirrors used to form the optical cavity for a Fabry-Perot device are presented next.

2.13 Optical cavity mirrors

Fabry-Perot modulator structures can be constructed using various different mirrors. Metal coatings make good mirrors and the coating is normally deposited after epitaxial growth of the semiconductor layers. For the wavelength of interest, 1047nm in this work, a gold metal mirror is most suitable having a reflectivity of 94%. The mirror formed by the Fresnel reflection from a semiconductor/air interface, typically around 30% for GaAs is also used in some devices. Both of these mirrors have the advantage that the reflected light has minimal penetration, they are 'hard' mirrors and their reflectivity is large over a very wide angular range. Unfortunately their reflectivities are not easily variable and metal mirrors are limited to a theoretical maximum of 95% due to absorption [33]. The third type of mirror commonly used is a monolithically grown mirror formed by alternating high and low refractive index layers called a distributed Bragg reflector. This mirror has the advantage that its reflectivity is controllable being dependent on the number of layers grown and very high reflectivities >99% are possible. The Bragg layers can be electrically conducting, doped p-type or n-type in many material systems. Its disadvantage is a natural consequence of its operation, the reflected light penetrates into the mirror thus increasing the optical cavity length making extremely small cavities of the order of a wavelength difficult to achieve.

A Bragg mirror in its simplest form consists of alternating high and low refractive index semiconductor layers of thickness $t_H = \lambda_{\text{Bragg}}/4n_H$, $t_L = \lambda_{\text{Bragg}}/4n_L$ as shown in Figure 2.12, where λ_{Bragg} is the wavelength of interest known as the Bragg wavelength. The layer order is given by S|(L(HL)^N|C where S denotes the substrate, C the cavity medium, L,H the low and high index layers and N the number of periods low and high index layers. The optical thickness of each layer is thus $\lambda/4$ and light is reflected at each interface due to the refractive index difference, travelling a phase thickness of $\pi/2$ for each single pass of a $\lambda/4$ layer. When the π phase change upon reflection of light incident from a medium of low refractive index to high refractive index is accounted for, all reflections are in phase and add constructively and the net phase change is zero in this case at the Bragg wavelength. The greater the number of Bragg periods the larger the reflectivity of the mirror. If the substrate refractive index is less than the refractive index of the first L layer ($n_S < n_L$) then a net phase change of π results. Thus layer order is important when designing an optical cavity to obtain destructive interference between the light reflected from the front and back mirrors.

The reflectance of this multi-layer structure can be calculated using the transfer matrix model (Section 2.14) and at normal incidence the reflectance of the layer structure shown in Figure 2.12 is given by

$$R = \left(\frac{n_S - (n_L^2/n_C)(n_L/n_H)^{2N}}{n_S + (n_L^2/n_C)(n_L/n_H)^{2N}} \right)^2 \quad (2.30)$$

The reflectance of the mirror is strongly dependent on the ratio of n_L/n_H . Thus the larger the difference in refractive index between the Bragg layers the fewer periods that are required to obtain a high reflectivity. Figure 5.3 in Chapter 5 shows the reflectance of an InAlAs / InGaAs Bragg mirror for different numbers of Bragg periods where $n_L = 3.12$ and $n_H = 3.42$. Due to the relatively poor contrast of the mirror $n_L/n_H=0.91$ and $\Delta n=0.3$, 30 periods are required to obtain a reflectance of 99%. The asymptotic increase in reflectance with increasing number of Bragg periods is typical of all Bragg mirrors. By using layers of better contrast the number of required periods can be considerably reduced. AlO_x/GaAs layers give the highest contrast mirrors currently used in semiconductor devices having $n_L \approx 1.7$ and $n_H \approx 3.5$ at 1050nm [34,35]. The upper reflectance value achievable is limited by absorption, scattering or diffraction losses.

The reflectivity spectrum for the Bragg mirror shown in Figure 2.12 using the above refractive index values with $n_S=3.5$ and $n_C=3.6$ is plotted in Figure 2.13 at a Bragg wavelength of 1000nm. High reflectivities are achievable but only over a certain wavelength range known as the stop band, clearly visible in Figure 2.13.

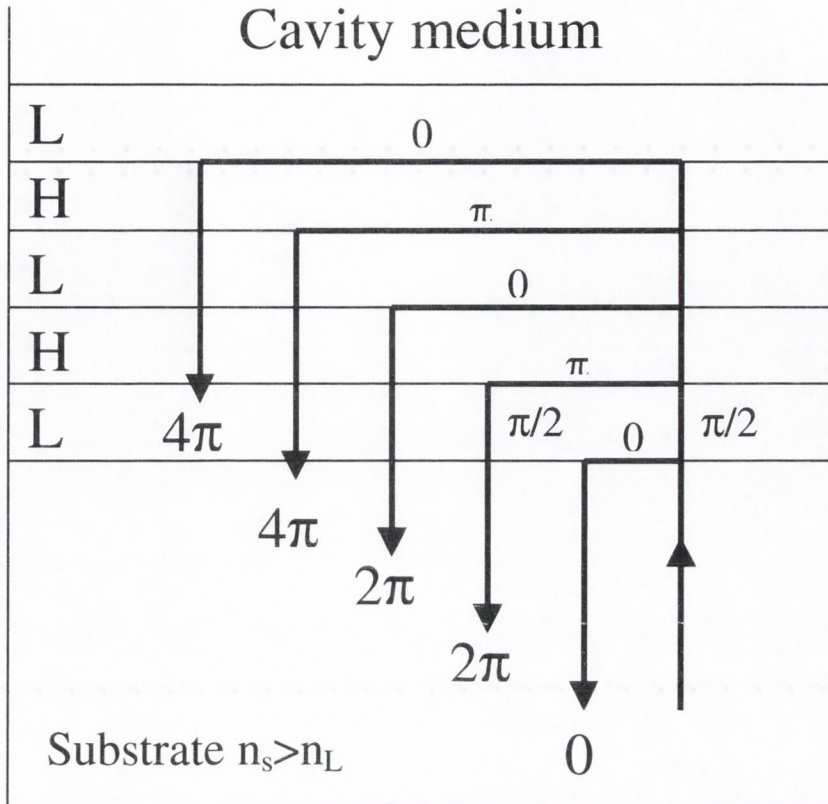


Figure 2.12: Bragg mirror in its simplest form consisting of alternating high and low refractive index semiconductor layers of thickness $t_H = \lambda_{\text{Bragg}}/4n_H$, $t_L = \lambda_{\text{Bragg}}/4n_L$. Operation is due to reflections from a series of interfaces adding constructively.

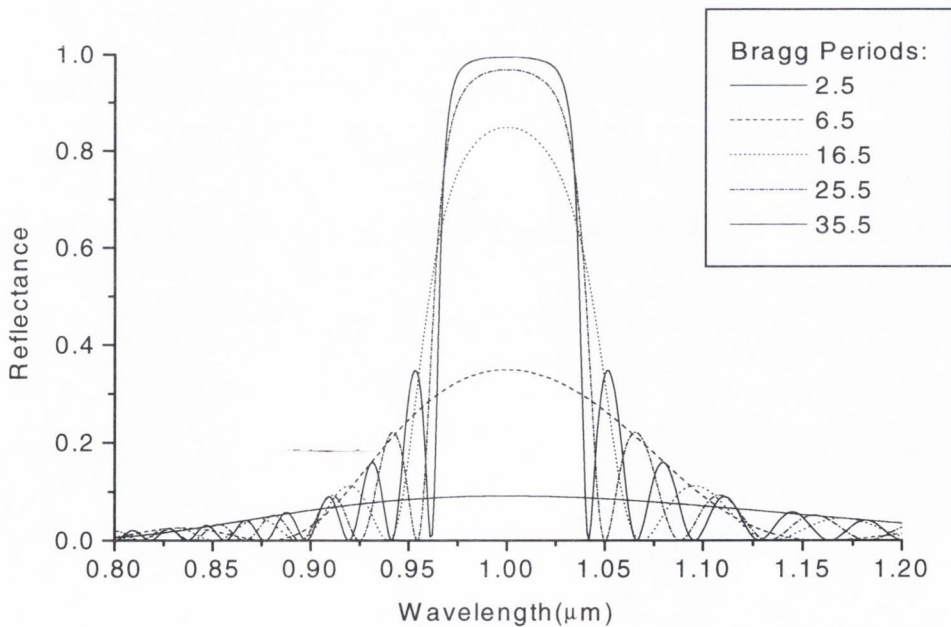


Figure 2.13: Reflectivity spectrum for the Bragg mirror shown in Figure 2.12 with refractive index values $n_L = 3.12$, $n_H = 3.42$, $n_S = 3.5$ and $n_C = 3.6$. $\lambda_{\text{Bragg}} = 1000\text{nm}$.

The spectral width of the high reflectance stop band is given by [38,39]

$$\Delta\lambda_{Bragg} = \frac{4\lambda_{Bragg}}{\pi} \sin^{-1} \left(\frac{n_H/n_L - 1}{n_H/n_L + 1} \right) \approx \frac{2}{\pi} \frac{\lambda_{Bragg} \Delta n}{n_{Average}} \quad (2.31)$$

where $n_{average}$ is the average refractive index of the Bragg mirror. Thus the width of the stop band increases as the refractive index difference of the Bragg mirror increases. The modulator structure can also be used as a photodetector operating side by side. In this case the resonant cavity detector will depend on the optical cavity to maintain high quantum efficiency due to the reduced number of MQWs and total absorption. Thus the stop-band must be sufficiently wide to give a high reflectivity at the detector wavelength as different modulator/detector operating wavelengths are used often used allowing wavelength dependent beam routing.

The reflectance of a Bragg mirror is also a function of incident angle. There are two principle factors involved. The Fresnel equations give the amplitude reflection coefficients for light incident at an angle θ and for different polarisations where n is the refractive index ratio the two media concerned [31].

$$\text{T.E.} \quad r = \frac{\cos\theta - \sqrt{n^2 - \sin^2\theta}}{\cos\theta + \sqrt{n^2 - \sin^2\theta}} \quad (2.32)$$

$$\text{T.M.} \quad r = \frac{n^2 \cos\theta - \sqrt{n^2 - \sin^2\theta}}{n^2 \cos\theta + \sqrt{n^2 - \sin^2\theta}} \quad (2.33)$$

Thus as light is incident off-axis the amplitude reflectance from the Bragg interfaces changes. The phase thickness also changes and is given by $\delta=(2\pi n t \cos\theta)/\lambda$ and the $\pi/2$ phase thickness changes as the incident angle increases. The apparent reduction in thickness due to $\cos\theta$ dependence at oblique incidence moves λ_{Bragg} to shorter wavelengths and the spectra shown in Figure 2.13 shifts to shorter wavelengths with increasing angle. The calculated angular dependence of the reflectance at λ_{Bragg} of the Bragg structure in Figure 2.13 is plotted in Figure 2.14. Similar to the wavelength case there is an angular stop-band of $\approx 17^\circ$, which is also dependent on the contrast of the Bragg layers.

For the Bragg mirror of interest in this work, light is incident from air and the structure is anti-reflection (AR) coated thus having a layer order AIR | AR | S |(L(HL)^N)|C. In this case the Fresnel reflection at the air-AR coating interface has a stronger contribution to the total reflectance and a large angular tolerance is achieved for the Bragg mirror [38]. The position of the dip in reflectivity for TM polarised light is dependent on the refractive indices of the Bragg mirror. The Bragg mirror used in the modulator structure will thus have a sufficiently large angular tolerance.

Finally in this section, the penetration depth of the light into the Bragg mirror can be given by [36,37]

$$L_P = \frac{\lambda}{2} \frac{n_L}{2n_{average} \Delta n} \quad (2.34)$$

Thus the penetration length for the Bragg mirror in Figure 2.13 is $\approx 800\text{nm}$ increasing the total length of the optical cavity as the mirror is effectively placed 800nm behind the first Bragg layer. In order to achieve short optical cavities where the behaviour of the cavity device is altered dramatically it is necessary to use high contrast mirrors (small Δn) reducing the effective cavity length.

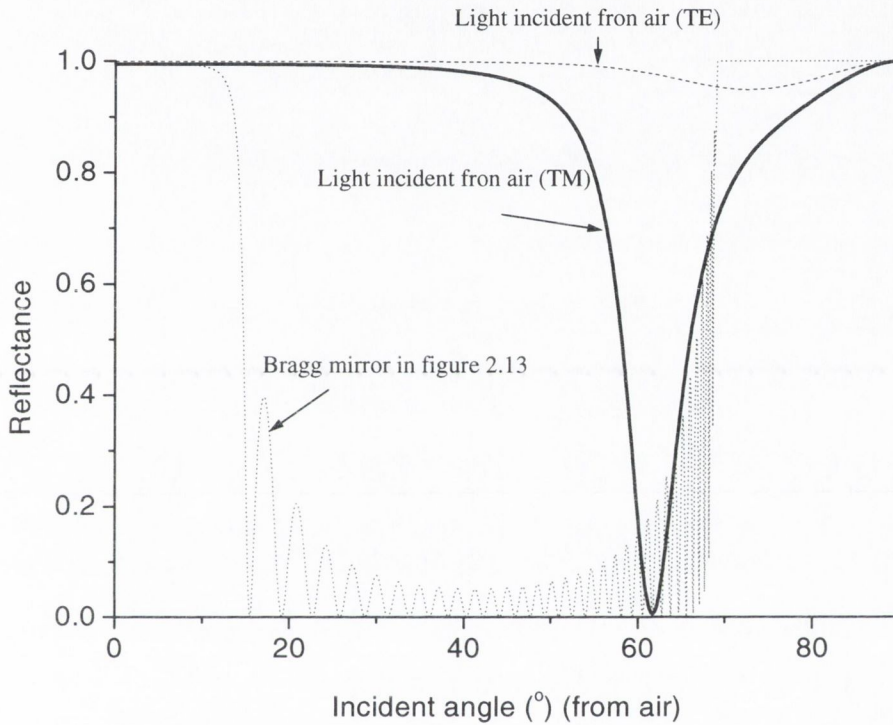


Figure 2.14: Calculated angular dependence of the reflectance at λ_{Bragg} of the Bragg structure in figure 2.12.

2.14 Transfer Matrix Modelling

The optical characteristics of a multilayer structure can be calculated using the approach taken in Section 2.11 where all the individual reflected and transmitted beams are summed. A more efficient approach is taken in the transfer matrix method where all the individual beams are considered to be already summed and the resultant electric and magnetic fields must satisfy the boundary conditions required by Maxwells equations. A summary of the approach in [29,30] is presented here. Figure 2.15 shows a beam of light incident on a single layer of thickness L and refractive index n_L surrounded by infinite media, a substrate of refractive index n_s and an incident medium of refractive index n_o . The transfer matrix approach to calculating the optical characteristics of this layer makes the following assumptions:

- (i) Each layer is homogeneous and isotropic.
- (ii) The incident medium is non-absorbing.
- (iii) The path difference between transmitted and reflected waves is small compared to the coherence length of the light.
- (iv) The width of the beam is large compared to any lateral displacement of the beam in the medium.

A beam of light is incident at an angle θ_1 with its electric field vector in a direction perpendicular to the plane of incidence. The magnitudes of the electric and magnetic fields can be related by

$$B = \frac{E}{v} = \frac{n}{c} E \quad (2.35)$$

The direction of energy flow is given by the Poynting vector

$$\vec{S} = \epsilon_0 c^2 \vec{E} \times \vec{B} \quad (2.36)$$

The inset boxes shown in Figure 2.15 represent the summed magnitudes of the electric fields at the layer boundaries. Thus E_{r1} represents the sum of all the reflected beams at interface **a**, E_{t2} represents the sum of all the transmitted beams moving into the substrate at interface **b**. In Figure 2.15, \mathbf{E} is everywhere tangent to the interfaces **a** and **b** but \mathbf{B} consists of a tangential component in y-direction and a perpendicular component in the x-direction.

By satisfying the boundary condition that the tangential components of the resultant electric and magnetic fields are continuous across interface **a** and **b** respectively we get

$$E_a = E_0 + E_{r1} = E_{t1} + E_{i1} \quad (2.37)$$

$$E_b = E_{i2} + E_{r2} = E_{t2} \quad (2.38)$$

and

$$B_a = B_0 \cos \theta_1 - B_{r1} \cos \theta_1 = B_{t1} \cos \theta_1 - B_{i1} \cos \theta_1 \quad (2.39)$$

$$B_b = B_{i2} \cos \theta_{i1} - B_{r2} \cos \theta_{i1} = B_{t2} \cos \theta_{t2} \quad (2.40)$$

Using the relation between electric and magnetic field in Equation 2.34, and using the fact that

$$E_{i2} = E_{t1} e^{-i\delta} \quad (2.41)$$

$$E_{i1} = E_{r2} e^{-i\delta} \quad (2.42)$$

where as before the phase thickness

$$\delta = \frac{2\pi}{\lambda} n_L L \cos \theta_{i1} \quad (2.43)$$

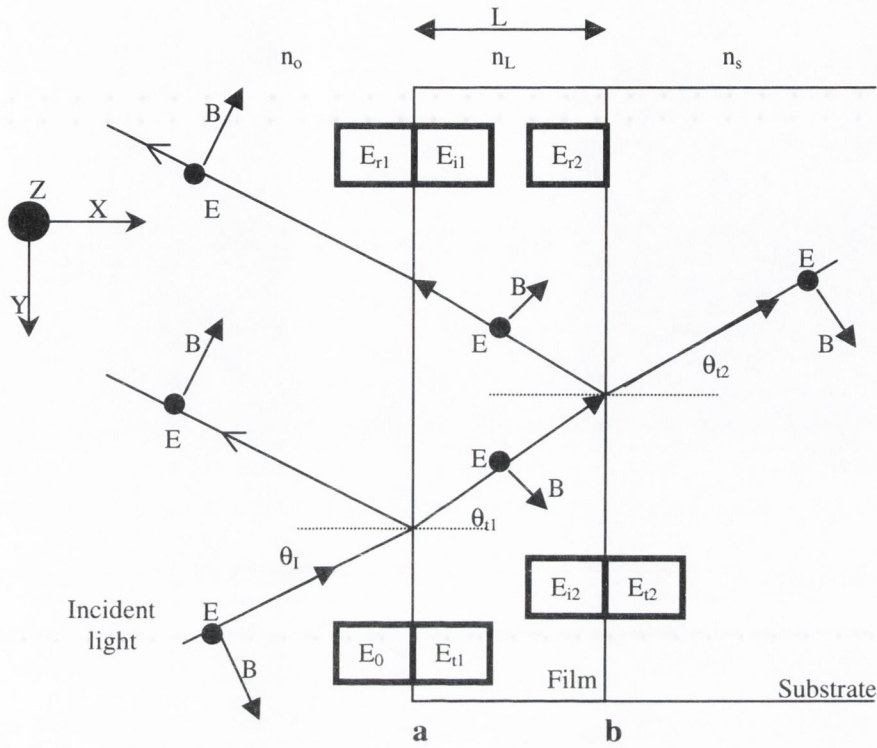


Figure 2.15: Light incident on a single layer of thickness L and refractive index n_L surrounded by infinite media, a substrate of refractive index n_s and an incident medium of refractive index n_0 . The electric and magnetic field vectors are indicated and each interface shows the sum of the electric fields for all the multiple reflected / transmitted light.

Equation 2.37 to 2.39 can be written respectively as

$$E_b = E_{t1}e^{-i\delta} + E_{i1}e^{i\delta} = E_{t2} \quad (2.44)$$

$$B_a = \gamma_0(E_0 - E_{r1}) = \gamma_L(E_{t1} - E_{i1}) \quad (2.45)$$

$$B_b = \gamma_L(E_{t1}e^{-i\delta} - E_{i1}e^{i\delta}) = \gamma_s E_{t2} \quad (2.46)$$

where the effective index is

$$\gamma_L = n_L \cos \theta_{t1} \quad \text{for TE polarisation (Figure 2.15)} \quad (2.47)$$

$$\gamma_L = n_L / \cos \theta_{t1} \quad \text{for TM polarisation} \quad (2.48)$$

Solving Equation 2.43 and 2.45 simultaneously yields

$$E_{t1} = \left(\frac{\gamma_L E_b + B_b}{2\gamma_L} \right) e^{i\delta} \quad (2.49)$$

$$E_{i1} = \left(\frac{\gamma_L E_b - B_b}{2\gamma_L} \right) e^{-i\delta} \quad (2.50)$$

and substituting these two equations into Equations 2.37 and 2.45 for boundary **a** gives the result

$$E_a = E_b \cos \delta + B_b \left(\frac{i \sin \delta}{\gamma_L} \right) \quad (2.51)$$

$$B_a = E_b (i\gamma_L \sin \delta) + B_b \cos \delta \quad (2.52)$$

where the following identities have been used $2\cos\delta = e^{i\delta} + e^{-i\delta}$ and $2i \sin\delta = e^{i\delta} - e^{-i\delta}$

These equations relate the fields at boundary **a** to the fields at boundary **b** and can be written in a matrix representation as

$$\begin{bmatrix} E_a \\ B_a \end{bmatrix} = \begin{bmatrix} \cos \delta & i \sin \delta / \gamma_L \\ i\gamma_L \sin \delta & \cos \delta \end{bmatrix} \begin{bmatrix} E_b \\ B_b \end{bmatrix} \quad (2.53)$$

This matrix is called the transfer matrix **M** of that layer. This can be generalised for many layers in a multilayer structure giving

$$\begin{bmatrix} E_a \\ B_a \end{bmatrix} = M_1 M_2 M_3 \dots M_N \begin{bmatrix} E_N \\ B_N \end{bmatrix}. \quad (2.54)$$

The multilayer structure can be represented by one matrix given by

$$M_T = M_1 M_2 M_3 \dots M_N \quad (2.55)$$

where the order of the matrices represents the order in which the incident light passes through them. The resulting matrix M_T will be of the form

$$M_T = \begin{bmatrix} m_{11} & m_{12} \\ m_{21} & m_{22} \end{bmatrix} \quad (2.56)$$

Further manipulation of Equations 2.37 and 2.44-2.46 produces the reflectance and transmission coefficients for the multilayer structure in terms of the transfer matrix elements in Equation 2.55, given by

$$t = \frac{2\gamma_0}{\gamma_0 m_{11} + \gamma_0 \gamma_s m_{12} + m_{21} + \gamma_s m_{22}} \quad (2.57)$$

$$r = \frac{\gamma_0 m_{11} + \gamma_0 \gamma_s m_{12} - m_{21} - \gamma_s m_{22}}{\gamma_0 m_{11} + \gamma_0 \gamma_s m_{12} + m_{21} + \gamma_s m_{22}} \quad (2.58)$$

and the intensity reflectance and transmission are given by

$$R = |r|^2 \quad \text{and} \quad T = \frac{n_s \cos \theta_s}{n_0 \cos \theta_i} \quad (2.59)$$

and the reflectance phase ϕ is given by $\phi = \arg(r)$.

To calculate the reflectance or transmittance of a multilayer structure the transfer matrix for each layer needs to be calculated. To do this the only information required is the layer thickness and refractive index and the angle that the light propagates in this layer, simply found from Snell's law. If one or more of the layers in a multilayer system are absorbing then the refractive index of that layer is written in its complex form

$$\tilde{n}_j = n_j - ik_j \quad (2.60)$$

where k_j is the extinction coefficient and is related to the absorption coefficient of the material at wavelength λ by $k_j = \alpha \lambda / 4\pi$. Thus MQW absorption is easily incorporated into the transfer matrix calculation. The biggest advantage of this method is the easy incorporation into a computer program and the ease of manipulation of the layers and layer information.

2.15 Assumptions made in modelling of modulator structures

Transfer matrix modelling is used to model the modulator structures of interest in this thesis. This numerical approach is very powerful. It allows all the reflectance dependent factors to be included in the model and the structure reflectance to be calculated accurately. The reflectance of the mirrors structures in Section 2.13 is naturally calculated and the penetration of the light into the Bragg which makes up the effective cavity length is a naturally inherent to the model. All phase information is accounted for and off-axis reflectance can easily be computed for both polarisation states.

The layer refractive index information is dependent on growth conditions as well as the layer structure and composition. Refractive index data is taken from various publications containing the optical constants of semiconductors [33,34,39,40] and each layer in the modulator structure includes dispersion data in the wavelength range of interest. The MQW absorption is measured (figure 2.7) and incorporated in the extinction coefficient using the complex refractive index ($\tilde{n}_j = n_j - ik_j$). The real refractive index value can be determined from the absorption coefficient [8] using the Kramers-Kronig relations and from published data. The strong exciton absorption peaks in MQWs result in similar peaks in real refractive index spectra around the exciton absorption wavelength. In the transfer matrix model used in this work the actual refractive index value was not calculated and the bulk value was used instead. This will introduce an inaccuracy into our model as the refractive index typically increases by $\approx 3\%$ in GaAs wells [41] around the exciton wavelength but is expected to be lower for

InGaAs wells. The main effect will be for the model to position the cavity resonance at a slightly longer wavelength. The further away from the λ_0 operating position the smaller the variation from the bulk value.

The change in refractive index with applied electric field (Electro-refraction) is also unaccounted for in the model. The change in refractive index can be as large $\approx 3\%$ in GaAs wells [42] but can be positive or negative depending on the choice of operating wavelength. The further away from the λ_0 operating position the smaller the change in refractive index value. Results have shown electrorefraction to have little effect on the reflectivity change from a device for operation at the λ_1 position [42] which will be the operating position of the devices considered here as discussed in Chapter 3. Thus these factors are not expected to have a major impact on the accuracy of the model at the operating wavelength. The main error that will cause a difference between the predicted and measured device optical characteristics will be error in layer thickness growth, placing the cavity resonance at the wrong wavelength. Highest accuracies are about 0.2% with in-situ monitoring [43], and 1% without. The strained MQW structure also brings an uncertainty to the absorption spectra and the real refractive index values. There are often significant differences between grown wafers. Thus having a calculated dispersion curve for the data in Figure 2.7 would not ensure accurate modelling results at the λ_0 wavelength region. The approach taken was to obtain the best possible data from published data books and to improve these values where possible from reflectivity measurements taken from grown structures. The numerical calculations in this thesis were performed in MATLAB and can be found in appendix A.

2.16 Effect of light incident off-axis on Fabry-Perot resonance

The transfer matrix model will be used to model the operation of the Fabry-Perot modulator structure for light incident off-axis in Chapter 3. The Fabry-Perot resonance position is dependent on the phase thickness given in Equation 2.16

$$\delta = \frac{2\pi L_o \cos \theta_1}{\lambda}$$

Thus as light enters the optical cavity off normal incidence the cavity length effectively becomes $L_o \cos \theta$ and effectively reduces in size with increasing incident angle. The result is a shift in cavity resonance to shorter wavelength. The important point to remember concerning a modulator device is that the operating wavelength is fixed, so it is the behaviour of the cavity reflectance at that wavelength that determines the modulator angular behaviour. To illustrate this the reflectance spectra of a typical optical cavity are shown in Figure 2.16 calculated using Equation 2.19. Data are shown for a cavity having $R_B=95\%$, $R_F=40\%$ and a cavity with $R_B=95\%$, $R_F=95\%$. The reflectivity is then plotted in Figure 2.17 plotted at the operating wavelength as a function of angle for the normal incidence resonance wavelength (1000nm). Figure 2.16 shows the data shifting to shorter wavelengths as expected from Equation 2.16 above. At the operating wavelength ($\lambda=1000\text{nm}$) the reflectance of the lower finesse cavity ($R_B=95\%$, $R_F=40\%$) increases in value at an incident angle of 10° . The relatively

narrower resonance of the higher finesse cavity means the reflectance increases at a much faster rate. The reflectance value at the operating wavelength of 1000nm moves along the side of the Fabry-Perot resonance with increasing angle and the characteristic resonance shapes can be seen in Figure 2.17. The reflectance plots in Figure 2.16 are also similar to those of a modulator device operating in the λ_1 position (see Figure 2.11). Thus subtracting the two curves in Figure 2.17 would yield a typical reflectivity change angular tolerance plot for this device. This example is thus allows some insight to the angular tolerance curves that will be presented later in Chapter 3. For small incident angles the tolerance is often flat due to the initial flat response in Figure 2.17. Then a sharp decrease occurs for larger angles until eventually the reflectivity change is zero occurring at 3° in Figure 2.17. This simple analysis shows how the angular tolerance is dependent on the spectral features and resonance widths of the device R_{on} and R_{off} reflectance curves.

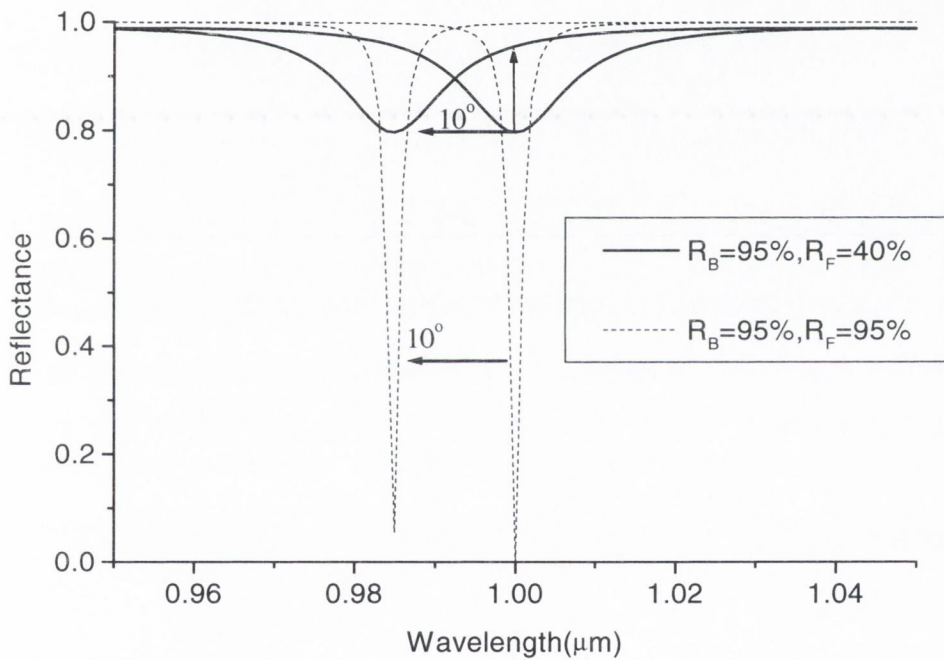


Figure 2.16: Reflectance spectra of a typical optical cavity calculated using Equation 2.19.

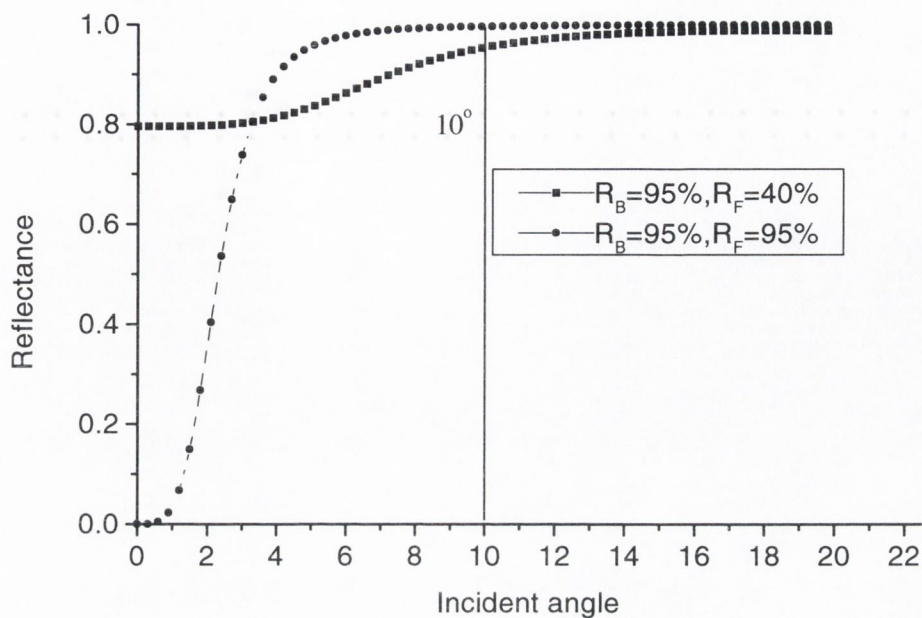


Figure 2.17: The reflectance value at the operating wavelength of 1000nm in figure 2.16 plotted with increasing angle.

2.17 Conclusions

In this chapter the basic physics behind the operation of a Fabry-Perot MQW modulator device has been presented. The device takes advantage of optical properties arising from electrical confinement in a quantum well and then uses optical confinement to make very efficient use of these properties. The basic optical characteristics of the device were presented with the intent of giving an insight into the device operation. When operating in a real system, there are many parameters that impact on device performance, due to changes in these basic properties. In later chapters the impact of these various parameters will be related back to the basic characteristics presented here. The highly useful transfer matrix model was introduced and an insight given in its operation. In Chapter 3 the possibility of low voltage operation of the Fabry-Perot modulator device is now investigated using this model along with the impact of the device structure on the device operating tolerances.

2.18 References

- [1] C.WEISBUCH AND B. VINTER, 'QUANTUM SEMICONDUCTOR STRUCTURES', ACADEMIC PRESS, BOSTON, 1991
- [2] C. WEISBUCH, H. BENISTY, R.HOUDRE, 'OVERVIEW OF FUNDAMENTALS AND APPLICATIONS OF ELECTRONS, EXCITONS AND PHOTONS IN CONFINED STRUCTURES', JOURNAL OF LUMINESCENCE, 85 271-293 2000.
- [3] J.F. KLEM, W.G. BREILAND, I.J. FRITZ, T.J. DRUMMOND, AND S.R. LEE, 'APPLICATION OF IN-SITU REFLECTANCE MONITORING TO MOLECULAR BEAM EPITAXY OF

VERTICAL-CAVITY STRUCTURES', J.VAC.SCI.technol.B 1, 16: (3) 1498 – 1501 MAY/JUN 1998

[4] LIN CH, GOOSSEN KW, SADRA K, MEESE JM, 'NORMALLY-ON GAAS/ALAS MULTIPLE-WELL FABRY-PEROT REFLECTION MODULATORS FOR LARGE 2-DIMENSIONAL ARRAYS', APPLIED PHYSICS LETTERS, 65: (10) 1242-1244 SEP 5 1994

[5] PARKER, E.H.C.(ED) (1985). 'THE TECHNOLOGY AND PHYSICS OF MOLECULAR BEAM EPITAXY'. PLENUM, NEW YORK

[6] MILLER DAB, CHEMLA DS, SCHMITT-RINK S, 'RELATION BETWEEN ELECTROABSORPTION IN BULK SEMICONDUCTORS AND IN QUANTUM WELLS: THE QUANTUM-CONFINED FRANZ-KELDYSH EFFECT', PHYSICAL REVIEW B-CONDENSED MATTER, VOL.33, NO.10, 6976-82 15 MAY 1986

[7] VAN DER ZIEL JP, ILEGEMS M., 'MULTILAYER GAAS-AL/SUB 0.3/GA/SUB 0.7/AS DIELECTRIC QUARTER WAVE STACKS GROWN BY MOLECULAR BEAM EPITAXY', APPLIED OPTICS, VOL.14, NO.11, 2627-30, NOV. 1975

[8] 'QUANTUM PHYSICS OF ATOMS, MOLECULES, SOLIDS...', R. EISBERG AND R. RESNICK, WILEY & SONS INC. 2ND EDITION ,1985

[9] BHATTACHARYA P, 'SEMICONDUCTOR OPTOELECTRONIC DEVICES', PRENTICE HALL INTERNATIONAL INC, NEW JERSEY, 1994

[10] S.SCHMITT-RINK, D.S. CHEMLA AND D.A.B. MILLER. 'LINEAR AND NON LINEAR OPTICAL PROPERTIES OF SEMICONDUCTOR QUANTUM WELLS" ADVANC. PHYS. 38 (1989)

[11] D.A.B. MILLER,CHEMLA,D.S..ET AL., 'LARGE ROOM TEMPERATURE OPTICAL NON-LINEARITY IN GAAS/ALGAAS MQW STRUCTURES, APPLIED PHYSICS LETTERS, 41,679-81.

[12] 'EXCITONS',E.I.RASHBA AND M.D.STURGE, EDS., NORTH HOLLAND PUBLICATIONS, AMSTERDAM (1982).

[13] COURTESY OF DR. GARETH PARRY, U.C.L. DIGITAL OPTICS GROUP.

[14] MILLER,D.A.B.,CHEMLA,D.S.,DAMEN,T.C.,GOSSARD,A.C.,WEIGMANN,W.,WOOD,T.H., AND BURRUS, C.A.(1985). 'ELECTRIC FIELD DEPENDENCE OF OPTICAL ABSORPTION NEAR THE BANDGAP OF QUANTUM WELL STRUCTURES'. PHYSICAL REVIEW B,32,1043-60

[15]CHEMLA,D.S.,DAMEN,T.C.,MILLER,D.A.B.,GOSSARD,A.C.,WEIGMANN,., 'ELECTROABSORPTION BY STARK EFFECT ON ROOM TEMPERATURE EXCITONS IN GAAS/ALGAAS MULTIPLE QUANTUM WELL STRUCTURES' . APPLIED PHYSICS LETTERS 42,864-866(1983)

[16] MILLER,D.A.B.,CHEMLA,D.S.,DAMEN,T.C.,GOSSARD,A.C.,WEIGMANN,W.,WOOD,T.H., AND BURRUS, C.A.(1985). 'BAND EDGE ELECTROABSORPTION IN QUANTUM WELL STRUCTURES: THE QUANTUM CONFINED STARK EFFECT' . PHYSICAL REVIEW LETTERS 52(22),2173-2176(1984)

[17] G.BASTARD,'WAVE MECHANICS APPLIED TO SEMICONDUCTOR HETEROSTRUCTURES', LES EDITIONS DE PHYSIQUE, PARIS 1988

[18] K.W.JELLEY, R.W.H. ENGELMANN, K.ALAVI AND H.LEE, 'WELL SIZE RELATED LIMITATIONS ON MAXIMUM ELECTROABSORPTION IN GAAS/ALGAAS MULTIPLE QUANTUM WELL STRUCTURES', APPLIED PHYSICS LETTERS, 55(1), 70-72 (1989)

- [19] R.H. YAN, R.J. SIMES AND L.A. COLDREN, 'EXTREMELY LOW VOLTAGE FABRY-PEROT REFLECTION MODULATORS', IEEE PHOTONICS TECHNOLOGY LETTERS, 2: (2) 118-119 FEB 1990
- [20] WHITEHEAD M, RIVERS A, PARRY G, ROBERTS JS, 'VERY LOW-VOLTAGE, NORMALLY-OFF ASYMMETRIC FABRY-PEROT REFLECTION MODULATOR', ELECTRONICS LETTERS, 26: (19) 1588-1590 SEP 13 1990
- [21] NEILSON DT, WILKINSON LC, GOODWILL DJ, WALKER AC, VOGELE B, MCELHINNEY M, POTTIER F, STANLEY CR, 'EFFECTS OF LATTICE MISMATCH DUE TO PARTIALLY RELAXED BUFFER LAYERS IN INGAAS/ALGAAS STRAIN BALANCED QUANTUM WELL MODULATORS', APPLIED PHYSICS LETTERS, 70: (15) 2031-2033 APR 14 1997
- [22] KEITH W. GOOSSEN, M.B. SANTOS, J.E. CUNNINGHAM AND W.J.JAN, 'INDEPENDENCE OF ABSORPTION COEFFICIENT-LINEWIDTH PRODUCT TO MATERIAL SYSTEM FOR MULTIPLE QUANTUM WELLS WITH EXCITONS FROM 850NM TO 1064NM', IEEE PHOTONICS TECHNOLOGY LETTERS, 5: (12) 1392-1394 DEC 1993
- [23] MEASUREMENTS COURTESY OF DR. LUCY WILKINSON, HERIOT-WATT UNIVERSITY, SCOTLAND, UK.
- [24] T.K. WOODWARD, THEODORE SIZER, D.L. SIVCO AND A.Y. CHO, 'INGAAS/GAAS MULTIPLE QUANTUM WELL OPTICAL MODULATORS FOR THE 1.02-1.07 μ M WAVELENGTH RANGE', APPLIED PHYSICS LETTERS, 57: (6) 548-550 AUG 6 1990
- [25] T.H. WOOD, C.A. BURRUS, D.A. MILLER, D.S. CHEMLA, T.C. DAMEN, A.C. GOSSARD, AND W. WEIGMANN, 'HIGH SPEED OPTICAL MODULATION WITH GAAS/ALGAAS QUANTUM WELLS IN A PIN DIODE STRUCTURE', APPLIED PHYSICS LETTERS, 44: (1) 16-18 1984
- [26] G.D. BOYD, D.A. MILLER, D.S. CHEMLA, S.L. MCCALL, A.C. GOSSARD, AND J.H. ENGLISH, 'MULTIPLE QUANTUM WELL REFLECTION MODULATOR', APPLIED PHYSICS LETTERS, 50: (17) 1119-1121 1987
- [27] KEITH W. GOOSSEN, M.B. SANTOS, J.E. CUNNINGHAM AND W.J.JAN, 'MULTIPLE QUANTUM WELL WAVEGUIDE MODULATORS', IEEE JOURNAL OF LIGHTWAVE TECHNOLOGY, 6: (6) 743-757 1988
- [28] D.J. NEWSON AND A.KUROBE, 'EFFECT OF RESIDUAL DOPING ON OPTIMUM STRUCTURE OF MULTIQUANTUM WELL OPTICAL MODULATORS', ELECTRONICS LETTERS, 23: (9) 439-440 1987
- [29] 'INTRODUCTION TO OPTICS', PEDROTTI F.L. AND PEDROTTI L.S., PRENTICE HALL INTERNATIONAL INC, NEW JERSEY, 1993
- [30] 'OPTICS', 2ND EDITION, HECHT EUGENE, ADDISON-WESLEY PUBLISHING, 1987
- [31] M.WHITEHEAD, G.PARRY, P. WHEATLEY, 'INVESTIGATION OF ETALON EFFECTS IN GAAS-ALGAAS MULTIPLE QUANTUM WELL MODULATORS', IEE PROCEEDINGS PART J, 136: (1) 52-58 1989

- [32] A.C. WALKER, M.P.Y. DESMULLIEZ, M.G. FORBES, S.J. FANCEY, G.S. BULLER, M.R. TAGHIZADEH, J.A.B. DINES, C.R. STANLEY, G. PENNELLI, A.R. BOYD, P. HORAN, D. BYRNE, J. HEGARTY, S. EITEL, H.-P. GAUGGEL, K.-H. GULDEN, A. GAUTHIER, P. BENABES, J.L. GUTZWILLER, AND M. GOETZ, 'DESIGN AND CONSTRUCTION OF AN OPTOELECTRONIC CROSSBAR SWITCH CONTAINING A TERABIT/S FREE-SPACE OPTICAL INTERCONNECT,' IEEE J. SELECTED TOPICS IN QUANT. ELECTRON. SPECIAL ISSUE ON SMART PHOTONIC COMPONENTS, INTERCONNECTS AND PROCESSING, VOL. 5, NO. 2, PP 236-249 (1999).
- [33] 'HANDBOOK OF OPTICS', OPTICAL SOCIETY OF AMERICA, MCGRAW-HILL, NY 1995
- [34] E.D. PALIK, 'HANDBOOK OF OPTICAL CONSTANTS OF SOLIDS I-III', ACADEMIC PRESS, BOSTON, 1998
- [35] M.H. MACDOUGAL, H. ZHAO, P.D. DAPKUS, M. ZARI AND W.H. STEIER, 'WIDE-BANDWIDTH DISTRIBUTED BRAGG REFLECTORS USING OXIDE/GAAS MULTILAYERS', ELECTRONICS LETTERS, 30:(14), 1147-1148, 1994
- [36] MACLEOD H.A., 'THIN FILM OPTICAL FILTERS', ADAM HILGER LTD, BRISTOL, 1986
- [37] H. BENISTY, H. DE NEVE AND C. WEISBUCH, 'IMPACT OF PLANAR MICROCAVITY EFFECTS ON LIGHT EXTRACTION - PART I: BASIC CONCEPTS AND ANALYTICAL TRENDS', IEEE JOURNAL OF QUANTUM ELECTRONICS, 34: (9) 1612-1631 SEPT 1998
- [38] T.H. DELONGE, F. MENKE AND H. FOUCKHARDT, 'OPTIMISATION OF WAVELENGTH DEPENDENT OPTOELECTRONICS MODULATORS AND REFLECTIVE OPTICAL INTERCONNECTS WITH OBLIQUE INCIDENCE MADE FROM ALGAAS/GAAS MULTILAYERS' OPTICS AND LASER TECH. , 25:(3), 187-192, 1992
- [39] 'PROPERTIES OF ALUMINIUM GALLIUM ARSENIDE', EDITED BY S. ADACHI, INSPEC EMIS DATAREVIEW SERIES NO.7, THE INSTITUTION OF ELECTRICAL ENGINEERS, LONDON, 1993
- [40] 'PROPERTIES OF LATTICE MATCHED AND STRAINED INDIUM GALLIUM ARSENIDE', EDITED BY PALLAB BHATTACHARYA, INSPEC EMIS DATAREVIEW SERIES NO.8, THE INSTITUTION OF ELECTRICAL ENGINEERS, LONDON, 1993
- [41] LIVESCU G, BOYD GD, MORGAN RA, CHIROVSKY LMF, FOX AM, LEIBENGUTH RE, ASOM MT, FOCHT MW, 'ROLE OF ELECTROREFRACTION IN QUANTUM-WELL FABRY-PEROT MODULATORS', APPLIED PHYSICS LETTERS, 60: (12) 1418-1420 MAR 23 1992
- [42] BOYD GD, LIVESCU G, 'ELECTROABSORPTION AND REFRACTION IN FABRY-PEROT QUANTUM-WELL MODULATORS - A GENERAL DISCUSSION', OPTICAL AND QUANTUM ELECTRONICS, 24: (2) S147-S165 1992
- [43] J.F. KLEM, W.G. BREILAND, I.J. FRITZ, T.J. DRUMMOND, AND S.R. LEE, 'APPLICATION OF IN-SITU REFLECTANCE MONITORING TO MOLECULAR BEAM EPITAXY OF VERTICAL-CAVITY STRUCTURES', J.VAC.SCI. TECHNOL. B 1, 16: (3) 1498 - 1501 MAY/JUN 1998

Chapter 3: The Fabry-Perot Modulator Device

3.1 Introduction

In this chapter the device design characteristics of InGaAs/AlGaAs Fabry-Perot Modulators, operating at low voltages and designed for maximum reflectivity change, are presented. Based on the device requirements for use in optical interconnects the optimum device structure is initially investigated using the Fabry-Perot equations (section 2.11). The InGaAs /AlGaAs MQW absorption spectrum is also examined revealing that for operation at a fixed voltage there is an optimum number of MQWs and operating wavelength. It also reinforces the view that operation with a pre-bias voltage may be advantageous. The benefits gained from using a structure incorporating a Au back mirror which make it a favourable first choice are discussed. Comprehensive transfer matrix modelling results for this structure are then presented revealing the optimum structure to achieve maximum reflectivity change and the modulation achievable for 5V to 1V operation. Since this device will be used in a real interconnect system, a full analysis of the device operating tolerances reveals the impact of the optical cavity and the lowest possible operating voltage for practical operation of this device structure.

3.2 Device requirements for use in optical interconnects

The important operating characteristics of MQW Fabry-Perot modulators are the reflectivity change $\Delta R = (R_{on} - R_{off})$, the contrast ratio $C = (R_{on} / R_{off})$, the insertion loss $IL = (1 - R_{on})$ and the operating voltage V . R_{on} or 'reflectivity on' is defined to be the high reflectivity of the device prior to the application of the operating voltage. R_{off} or 'reflectivity off' is defined to be the low reflectivity of the device after the application of the operating voltage. When operated in this mode the device is said to operate as a 'normally on' or 'starting reflectivity on' device as explained in Chapter 2. Optimisation of these parameters has a direct consequence on the device operating tolerances such as the spectral bandwidth, temperature sensitivity, MBE growth sensitivity, and angular acceptance. Much work has been done addressing these operating characteristics and tolerances both individually and collectively, in different material systems and for different device structures [1-5]. The relative importance and values of the above modulator characteristics and tolerances will be set by the system application. Thus the system application will dictate the device structure and design that is required.

There are two main operating characteristics that will shape the device design for modulators used in optical interconnects. The first is whether the device operates with maximum contrast or maximum reflectivity change. The second is compatibility with CMOS operating voltages. In this work the insertion loss is not considered to be a major issue as in the intended system the modulator output goes directly to an array of detectors and the optical data is converted to an electrical format. Thus there is no cascaded use of the optical signal, although a low insertion loss is important to minimise the required system input power. In Chapter 5 we will see that as a consequence of maximising the reflectivity change the insertion loss will also be minimised.

3.2.1 Reflectivity change ($R_{on} - R_{off}$) Vs. Contrast (R_{on} / R_{off})

When used in optical interconnects, Electro-Absorption modulators can function as transmitting and receiving components. These modulators currently operate in differential pairs due to the low device contrast and to guard against optical power fluctuations, under such operation the operating parameter to optimise is the reflectivity change. The output of this device is data in a binary format so it is the signal difference between the on and off state levels that is of prime importance. Much work to date on Fabry Perot modulators has been aimed towards design for high contrast [6]. The most important value to optimise for high contrast is the R_{off} value. These devices are normally designed to achieve the impedance matching condition which gives $R_{off} \approx 0$ and extremely large contrast ($C = R_{on} / R_{off}$). For large reflectivity changes the values of R_{off} and R_{on} are equally important, as high contrast does not necessarily result in the largest reflectivity change although large reflectivity changes are possible [7]. For $R_{off} = 0$ it is possible to have infinite contrast and still only have a few percent change in

reflectivity. For this reason, device design for maximum contrast is different to device design for maximum reflectivity change.

This difference in device design can be illustrated if the reflectance of the Fabry-Perot resonance is plotted using equation (2.19) for increasing absorption in the optical cavity as shown in Figure 3.1.

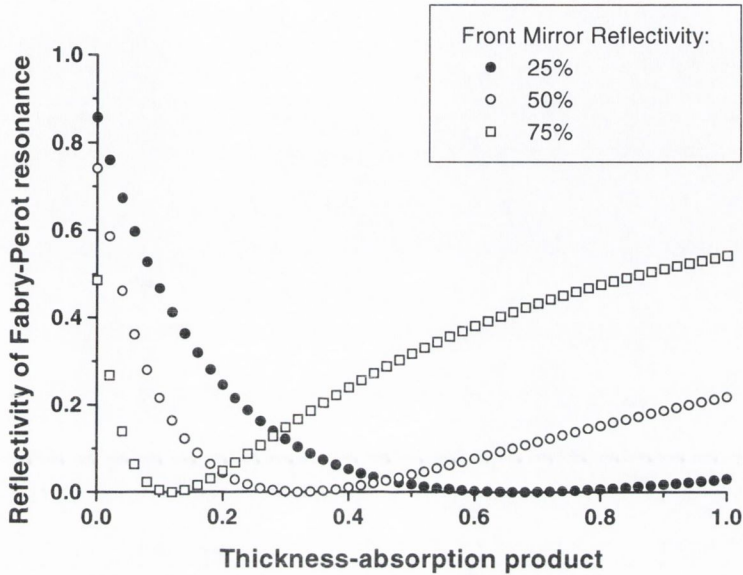


Figure 3.1: Reflectivity of the Fabry-Perot resonance is plotted using equation (2.19) for increasing absorption in the optical cavity and different values of R_f with $R_B=95\%$.

The back mirror reflectivity R_B is 95% and results are plotted for three different front mirror reflectance. These values typically represent a ‘normally on’ device where $R_B > R_f$ and the absorption increases when the operating voltage is applied to reduce the device reflectivity. Concentrating on the $R_f = 0.5$ curve, there is an initial rapid change in reflectance and the cavity reflectance is reduced as the absorption is increased. The rate of change reduces dramatically as the reflectance of the Fabry-Perot resonance approaches the impedance matching position. The initial thickness-absorption value of 0 to 0.2 changes the cavity reflectance by 0.7, the following thickness-absorption value of 0.2 (0.2 to 0.4) changes the cavity reflectance by 0.04. This is a consequence of the effective back mirror reflectance $R_{B(\text{eff})} = R_B e^{-2\alpha L}$ (equation 2.28) where αL is the thickness-absorption product, which decreases exponentially. At the impedance matching condition the resonance reflectance is zero as the effective back mirror reflectance equals $R_f = 0.5$. As the absorption is increased further, R_f is now greater than $R_{B(\text{eff})}$ and the resonance reflectance value increases. As $R_{B(\text{eff})}$ reduces exponentially, further increases in absorption reduce it by smaller amounts and the resonance reflectance increases accordingly in small amounts.

This data shows a number of important points. For device operation giving a large reflectivity change, absorption-thickness value changes below the impedance matching condition are most favourable. In this region the maximum reflectance changes are achieved when the absorption-thickness value changes from a value equal or close to zero to a value roughly one-half the impedance matching condition. In comparison device design for maximum contrast would require the impedance matching absorption-thickness value. The other point to note here, which we will return to shortly in Section 3.3.3 where the MQW absorption spectrum is discussed, is the cavity reflectance change when the thickness-absorption product has a value greater than the impedance matching value. Concentrating on the $R_f = 0.5$ curve there is roughly a linear change in cavity reflectance with thickness-absorption product. Thus device design will favour the initial change from zero in thickness-absorption product where the cavity reflectance changes in an exponential behaviour.

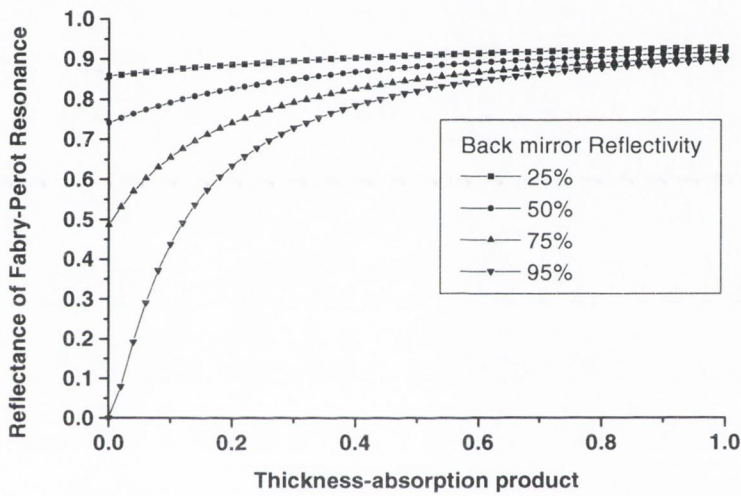


Figure 3.2: Reflectivity of the Fabry-Perot resonance is plotted using equation (2.19) for increasing absorption in the optical cavity and different values of R_B with $R_F=95\%$.

If the above mirror reflectivities are reversed i.e. the front mirror is 95% and the back mirror reflectivity is given the variable values of 25% to 95%, it is also possible to achieve modulation as shown in Figure 3.2. Here the cavity reflectance now increases as the thickness absorption product increases. The effective back mirror reflectance $R_{B(\text{eff})} = R_B e^{-2\alpha L}$ starts at a small reflectivity value R_B and decreases exponentially towards zero. Thus the cavity reflectance effectively approaches the reflectivity value of the front mirror. In this case the cavity reflectance changes most when the back and front mirror reflectivity values are high as seen in Figure 3.2 for the $R_B, R_F = 95\%$. The closer these values are to 100% the greater the change in cavity reflectance. The finesse of this optical cavity would be extremely large which reduces the device operating tolerances considerably and thus this structure is not favoured for the reflectivity change modulator. We conclude from the above results that the reflectivity change modulator structure should consist of a high R_B value and a lower R_F value, and the absorption should change ideally from zero to a value roughly half that of the impedance matching condition or vice versa.

The above issues can be summarised by looking at reflectivity curves typical of a device turned on and off. We will shortly see that when using MQW absorption, optimum operation occurs at a wavelength in the absorption spectrum where the absorption increases with applied voltage. Due to the fabrication of large arrays of these devices, the device will normally be turned off when not in use to conserve electrical power and thus the starting absorption will start from a low value. In this project the MQW absorption is measured experimentally and the optical cavity is then chosen to optimise the device modulation. Using the above conclusions the reflectivity of the Fabry-Perot resonance is plotted using equation (2.19) for increasing front mirror reflectance and is shown in Figure 3.3. The back mirror reflectivity is 95% and results are plotted for three different cavity absorption values. This is representative of the approach being taken in this project.

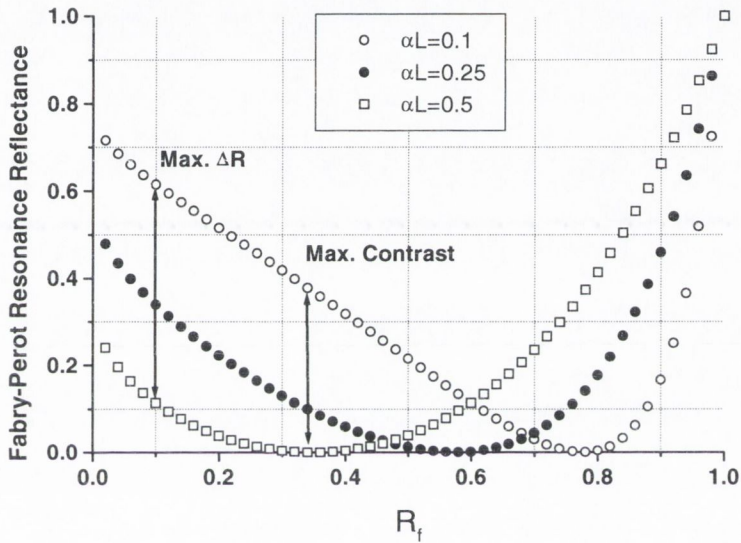


Figure 3.3: Reflectance of the Fabry-Perot resonance is plotted using equation (2.19) for increasing front mirror reflectance and different values of αL with $R_B=95\%$.

Concentrating on the $\alpha L = 0.1$ curve, this is representative of the Fabry-Perot modulator before its operating voltage is turned on and the absorption is low. The behaviour of the cavity reflectance is roughly linear up to the impedance matching condition at $R_F=78\%$. The $\alpha L = 0.5$ curve is representative of the Fabry-Perot modulator when the operating voltage is turned on and the absorption is high. The cavity reflectance reduces rapidly to zero at $R_F=34\%$. For maximum contrast design $R_F=34\%$ would be the chosen reflectivity of the front mirror, but for maximum reflectivity change $R_F=10\%$ gives the largest $\Delta R=50\%$. It is also interesting to note that a reflectivity change of 50% is also possible at $R_F=88\%$, in this case the reflectivity changes from a low value to a high value, a ‘normally off’ device. Once again the high reflectivity value of this front mirror makes it less attractive due to the negative impact on the device operating tolerances.

The above results from basic analysis using the Fabry-Perot equations have given an insight into the device structure designed for operation with maximum reflectivity change. It shows how this

device design differs from the device structure that gives maximum contrast. A full analysis using the transfer matrix model in the next section will reveal the optimum device structure.

3.2.2 Operation at CMOS voltages

The modulator operating voltage is the second operating characteristic that determines the modulator structure design. The MQW absorption for 95 MQWs for various applied voltages are shown in figure 2.7. The electric field F_E across the MQW region when a voltage V is applied across it is given by

$$F_E = \frac{V}{(t_w + t_B) \times N} \quad (3.1)$$

where N is the number of MQWs, and t_w, t_B the thicknesses of the well and barrier respectively. It follows from this that in order to shift the $0V$ (or 0 Vm^{-1}) exciton peak to longer wavelengths using the QCSE, the electric field across the MQWs must be increased. This can be done in two ways: by increasing the voltage or decreasing the thickness across which the voltage is being dropped. At lower voltage operation compatible with predicted future CMOS voltages [8], the voltage values will be fixed, thus in order to use the QCSE to achieve amplitude modulation, the number of MQWs must be reduced. There is an optimum electric field that gives maximum modulation. The aim is to find the voltage/thickness combination that achieves that electric field. The operating voltage will thus influence the device design in setting the number of MQWs that can be used, the lower the operating voltage the fewer the number of MQWs that can be used. The loss in absorption due to a reduced number of MQWs can be compensated by the optical cavity. This can be seen in the simple case shown in Figure 3.3. The cavities with less absorption require higher reflectivity front mirrors and thus higher finesse to lower the Fabry-Perot resonance reflectivity. Thus the operating voltage will set the number of MQWs which will thus set the finesse of the cavity required for modulation in the structure. The exciton linewidth and wavelength shift due to the QCSE also influence the device structure and are examined in detail next.

3.3 Transfer Matrix modelling

The transfer matrix model successfully used in [7,9,24] and described in Section 2.14 is used to investigate thoroughly the optimum structure and the potential modulation achievable from these devices. The response of these devices at low voltage operation is of particular interest in this work. In this section the MQW absorption is firstly discussed as well as the choice of device mirrors. The transfer matrix modelling results and optimum device structure are then presented.

3.3.1 InGaAs MQW QCSE absorption spectra

Compared to the (Al)GaAs system (see Figure 2.5 or [1]) the exciton absorption in the InGaAs system is intrinsically weaker and broader as detailed in Section 2.1 and shown in Figure 2.8, but shifts more under the QCSE. These intrinsic properties bring about a modulator design particular to these MQW absorption properties. The maximum absorption change is found by subtracting the 0V curve from the absorption curves at higher voltages (Figure 2.7). Figure 3.4 shows the resulting absorption changes.

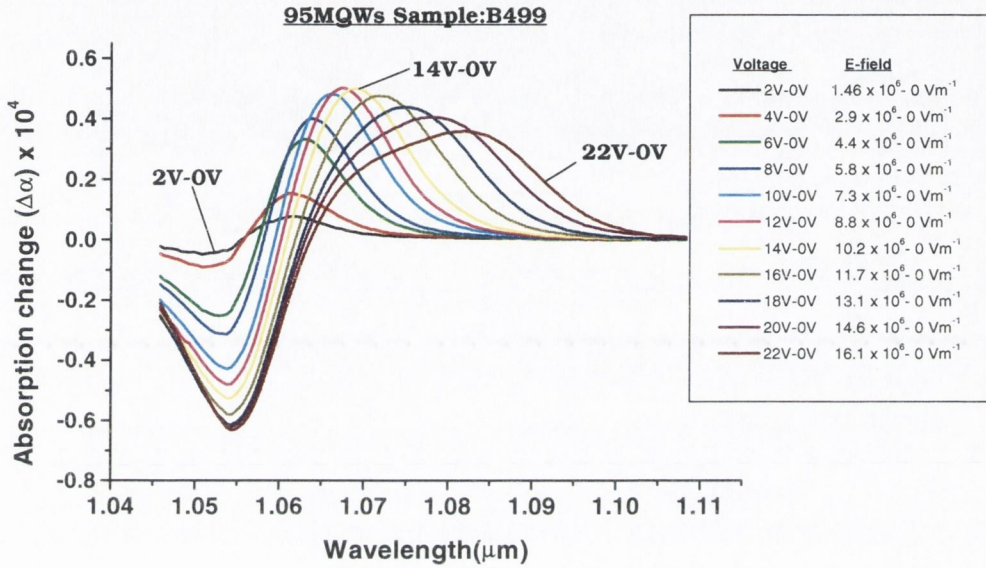


Figure 3.4: Maximum absorption changes found by subtracting the 0V curve from the absorption curves at higher voltages (Figure 2.7) for 95 MQWs.

The broad exciton and the large wavelength shift at higher electric fields result in the maximum absorption change occurring at large (voltage values) electric field values. For 95 MQWs the maximum reflectivity change would occur for 0 to 14V operation around $\lambda=1070\text{nm}$. Presuming the voltage available is limited to CMOS voltages (5V to 1V), to access the large absorption changes the use of a bias voltage is of possible benefit [10]. The current SPOEC system (Section 1.3) uses a 5V bias and 5V applied voltage for this reason, so operation is for a 5V to 10V voltage swing. The bias voltage and the applied voltage are the same and this will also be the approach taken here. Thus if a bias is used at 1V operation, the bias voltage will be 1V and the voltage swing will be from 1V to 2V. The larger absorption changes ($\Delta\alpha$) at higher electric fields can also be achieved by reducing the number of MQWs according to equation 3.1. Reducing the number of MQWs will allow higher electric fields across the MQWs and large absorption changes to be achieved but the total amount of absorption is reduced. Thus for any given operating voltage there will be an optimum number of MQWs at which the best modulation will be achieved. This number will be a balance between having sufficient total absorption and a sufficient absorption change ($\Delta\alpha$). Figure 3.4 also shows that the absorption change is

wavelength dependent; large changes occur at $\lambda=1070\text{nm}$ also at $\lambda=1055\text{nm}$. All these factors will be accounted for in the transfer matrix modelling of these devices.

3.3.2 Optical cavity mirror choice

Devices are initially designed with an optical cavity formed by a high reflectivity of 94% Au back mirror and Bragg stack front mirror. The Bragg stack front mirror consists of a $\lambda/4$ *InAlAs* / *InGaAs* layers. These layers are placed after the MQW strain balancing buffer layer (figure 2.8) to minimise the optical cavity length, which makes MBE growth of these devices easier (section 3.4.3). These material compositions are chosen so as to match the average lattice constant of the strained MQWs as explained in section 2.8. The back Au mirror deposited on the **p++** *InGaAs* layer gives theoretically a back mirror reflectivity of 94%. This structure is the most favourable as the Au back mirror functions as the electrical contact to the p-region as well as the back mirror of the optical cavity. The alternative would be to use another Bragg stack as the back mirror. The requirement of longer growth times, the added complexity of doping, or extra processing steps if direct contact is made to the p-region when a Bragg stack is used as the back mirror, make an Au mirror a preferred first option. From a systems point of view, for integration of the modulator to CMOS a ‘Flip-chip’ bonding technique is currently used successfully. This requires a metal deposition pad on the optical and CMOS surfaces and electrical contact is made through a tiny solder ball [11]. Using a gold mirror is also useful here for this process, acting as the metal pad on the modulator for this bridge. Thus for these reasons a device structure using a Au back mirror is first investigated as the preferred choice of structure from a fabrication and processing perspective.

3.3.3 Transfer Matrix modelling results

The transfer matrix model is used to investigate thoroughly the optimum structure and the potential modulation achievable from these devices. In Section 3.3.1 the *InGaAs* MQW QCSE absorption features were described. In modelling this active region of the modulator structure the operating voltage is fixed and the number of MQWs varied. The starting absorption data is from 95 MQWs at voltages from 0 to 25V (Figure 2.7). The absorption spectrum at a given field is extracted and we presume that the absorption coefficient for the 95 well structure can be linearly extrapolated down to fewer wells. The model thus uses the corresponding electric field absorption spectra and the absorption coefficient value for that number of MQWs. As the number of MQWs are reduced the physical length of the optical cavity shortens. The Fabry-Perot resonance is placed at the required wavelength by tuning the thickness of the *InGaAs* p+ layer inside the optical cavity, and in each case the physical length of the optical cavity is minimised. The optical cavity is formed using a front Bragg stack and back Au mirror. The reflectivity from the structure is first calculated for a double-pass device (no front mirror) and then for increasing Bragg stack periods/front mirror reflectivity. This is repeated at lower voltage values corresponding to future predicted CMOS operating voltages. Figure 3.4 also shows the wavelength dependence of the MQW absorption change. The optimum operating wavelength is investigated by

repeating the above process with the cavity resonance placed at various wavelengths. This is achieved by tuning the thickness of the InGaAs p+ layer inside the optical cavity. The model was also used to determine whether operation with or without a bias voltage was most beneficial. Thus the model can be thought of as working along a number of different paths summarised as follows:

- a) Active region: for a given applied voltage and the device in its off state, V_{off} , the number of MQWs N is varied, and the corresponding absorption spectrum and absorption coefficient are calculated from the measured data.
- b) Optical cavity: at each number of MQWs, N , the cavity reflectivity spectrum is calculated and this is repeated for various mirror reflectivities of the optical cavity.
- c) Operating wavelength: b) is repeated for the optical cavity resonances placed at various operating wavelengths in the optical spectrum shown in figure 2.7.
- d) a) b) c) repeated at the value of applied voltage for the device in its on state V_{on} .

Modelling results for the non-cavity double-pass modulator structure having no front mirror are first presented.

3.3.3.1 Double-pass modulator modelling results

The transfer matrix model is used to model the reflectance change from the double-pass modulator structure. This device has no optical cavity, only a back gold mirror. The read beam enters the device through the anti-reflection coating, reflects off the back Au mirror and exits passing only twice through the structure. The current SPOEC interconnect switch incorporates these device structures operating at 5V with a 5V bias voltage compatible with the 0.6 μm silicon process. If sufficient reflectance change were attainable from these structures they would be first choice for use in systems operating at lower voltages due to their proven record in real systems and relative ease of large array fabrication [12]. The devices were modelled as described above and the predicted reflectivity change at different numbers of MQWs is presented in figure 3.5 for operation down to 1V. In each case a bias voltage is used, the same as the operating voltage, and the results are at the optimum operating wavelength for that operating voltage. The actual R_{off} and R_{on} reflectivity spectra for the 5V and 1V modulator device at the optimum number of MQWs of 85 and 42, respectively, is shown in figure 3.6. The optimum operating wavelength $\lambda=1070.5\text{nm}$ for 5V operation and $\lambda=1064\text{nm}$ for 1V operation can be seen here. Using 95 MQWs at 5V operation, greater than 30% modulation is achieved and is consistent with values reported for similar structures in [13]. At this early stage our model predicts that a reduction to 85 MQWs can give a small improvement in device modulation. The 30% reflectivity change value is the minimum modulation specifically required for the SPOEC system in order to maintain a good signal to noise ratio and is used as an operational bench mark in this work. For zero bias (not shown here) a modulation of only 26% at 5V operation is predicted; thus the reason for using a bias voltage. At lower voltage operation (with a bias voltage) when the voltage drops to 3.3V, a reflectance change value of 22% is achievable. It decreases rapidly to a mere 6% by 1V operation. At fixed lower voltage operation

reducing the number of MQWs allows access to the larger absorption changes at higher electric fields (figure 3.4) that are required in order to achieve sufficient amplitude modulation.

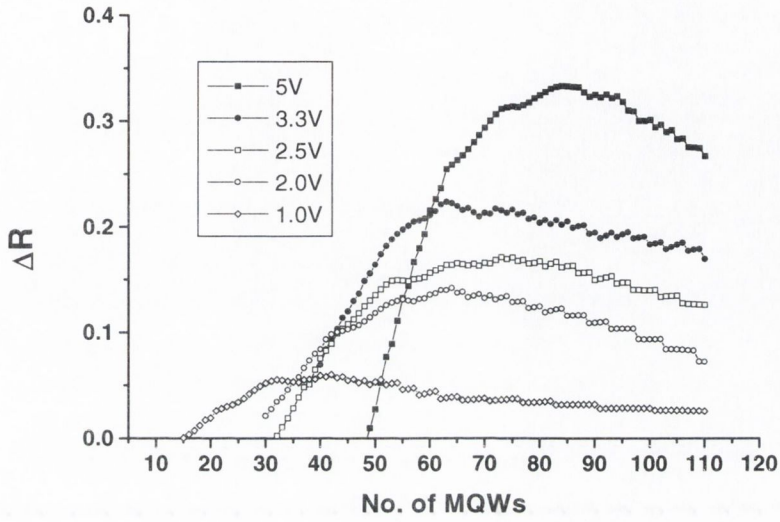


Figure 3.5: Transfer matrix modelling results for double pass modulators operating with a bias voltage.

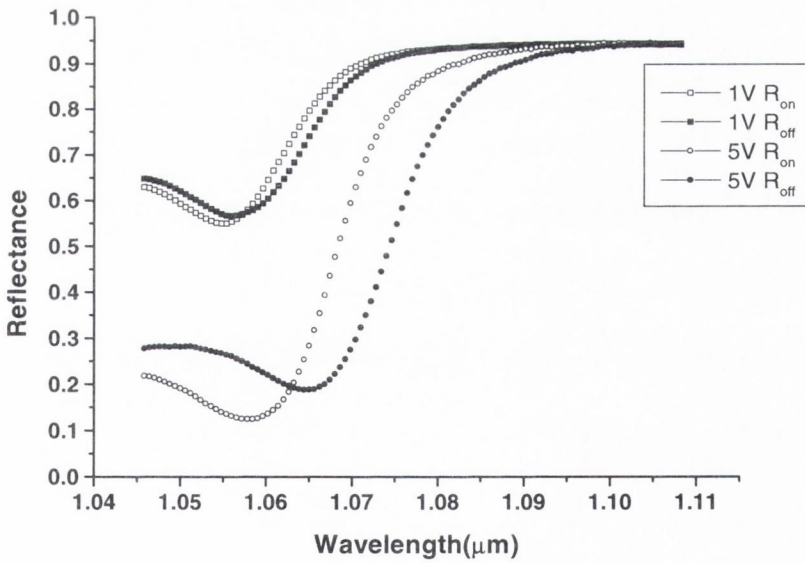


Figure 3.6: Reflectance values for 5V operation and 1V operation for the optimum number of MQWs 85 and 42 respectively.

But as the number of MQWs is reduced the total absorption is thus reduced and there is an optimum point reached between these two competing factors. This can be seen in figure 3.7 where the absorption change $\Delta\alpha$ for the 5V device, as calculated by the transfer matrix model and described in Section 3.3.3 above, is plotted for different numbers of MQWs. This optimum point is reached for 85 MQWs. The reflectivity change for the 5V device shown in Figure 3.5 above is also plotted for comparison. It is clear from Figure 3.7 that the device reflectivity change follows closely the absorption change values $\Delta\alpha$. Here as expected the maximum reflectivity change occurs at 85 MQWs. At lower voltage operation the reduction in the number of MQWs (and reduced total absorption) to achieve a sufficient change in absorption and amplitude modulation is fatal to these devices. The modulation thus diminishes rapidly and by 1V operation the modulation is very small and extinguished. It is clear from these results that an alternative device structure is required for lower voltage modulation.

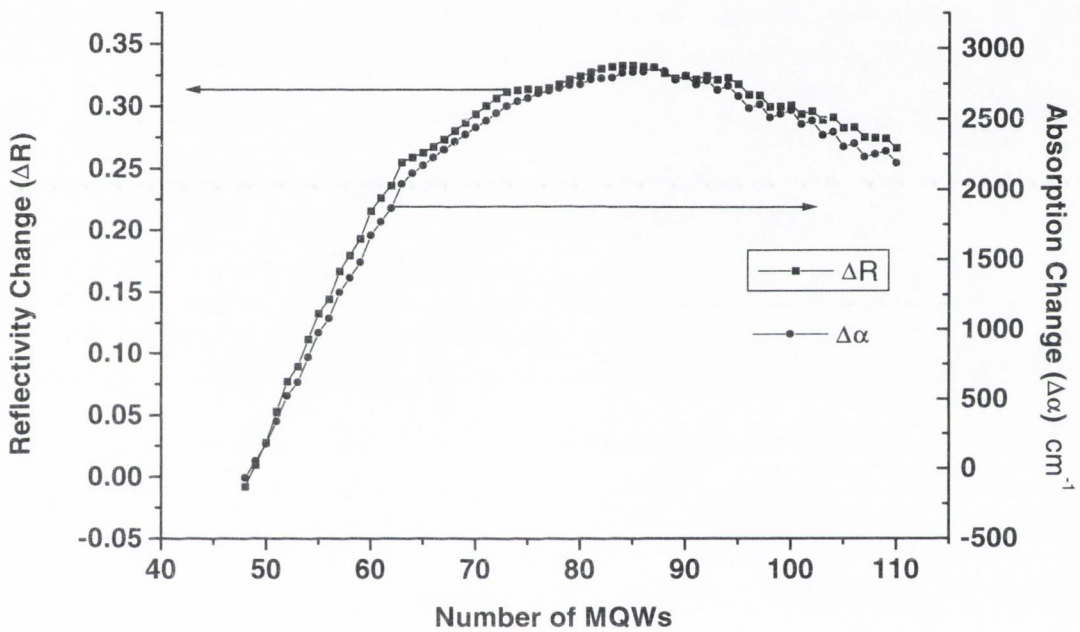


Figure 3.7: Absorption change $\Delta\alpha$ for the 5V device, as calculated by the transfer matrix model and described in section 3.3.3 above, plotted for different numbers of MQWs at the optimum operating wavelength $\lambda=1070.5\text{nm}$.

3.3.3.2 MQW Fabry-Perot modulator modelling results

The transfer matrix model is used to investigate thoroughly the optimum structure and the potential modulation achievable from these devices when the MQWs are incorporated in an optical cavity. The response of these devices at low voltage operation is of particular interest in this work. The model examines empirically the optimum number of MQWs, the optimum optical cavity structure and the optimum operating wavelength. It also examines the possible benefit of using a bias voltage. The modelling results of an immense amount of computational time are summarised in Table 3.1. At each operating voltage the optimum number of MQWs and the corresponding electric field across these

MQWs is tabulated. The optimum front mirror reflectivity and the maximum reflectivity change achievable for these optimised values are also presented. These values represent modelling results when a bias voltage is used. The values presented in round brackets in each case represent the values when a bias voltage is not used. For comparison the modulation values achievable at these operating voltages for the double-pass modulator device is presented in the final column. For operation with a bias voltage the optimum operating wavelength for the measured MQW absorption spectra used in the model was 1077nm, and without a bias voltage it was 1068nm. Before analysing these results generally the optimum device structure predicted by the model is presented and analysed. Factors such as the optical cavity, the optimum operating wavelength, and the number of MQWs, which influence the resulting MQW Fabry-Perot modulator reflectivity change, are examined in detail.

Voltage (and bias) V	No. of MQWs	E-Field Vm^{-1}	R_f %	Max ΔR Fabry-Perot Device %	Max ΔR Double Pass Device %
5	56 (45)	5.77×10^6	34 (45)	46 (44)	33
3.3	38 (29)	5.84×10^6	45 (52)	36 (31)	22
2.5	28 (24)	5.73×10^6	66 (75)	28 (25)	17
2	24 (23)	5.71×10^6	75 (75)	23 (18)	14
1.8	22 (15)	5.61×10^6	75 (79)	19 (16)	11
1	12 (13)	5.63×10^6	88 (88)	9 (6)	6

Table 3.1: Details of the required front mirror reflectivities ($R_B=94\%$), the number of MQWs, the electric field across the MQWs for each operating voltage for devices designed for maximum reflectivity change with a bias voltage. The values shown in brackets in each case is for operation without a bias voltage. For comparison the modulation predicted for a double pass modulators is also presented.

3.3.3.3 Reflectance spectra

Figure 3.8 shows the actual reflectance spectra for the optimally designed 5V and 2V modulator structures as summarised in Table 3.1, operating with a bias voltage. In the case of the 5V modulator R_{on} curve which represents the reflectivity before the device is turned on, the curve is a convolution of the Fabry-Perot dip at 1077nm and exciton absorption that has shifted in wavelength from 1054nm (figure 2.7) due to the 5V bias voltage to ~1065nm. When the voltage is turned on the QCSE shifts the exciton absorption peak towards the Fabry-Perot resonance and the resultant reflectivity is shown by the 5V R_{off} curve. Relative to the 2V modulator the lower finesse cavity of this 5V structure shows how strongly the exciton absorption influences the reflectivity spectra ‘pulling’ the cavity resonance towards it [14]. The R_{off} curve shows how the Fabry-Perot resonance appears to be closer to 1075nm than its true design position of 1077nm. The reflectivity at the operating wavelength changes from 60% to 14% giving $\Delta R = 46\%$ at the operating wavelength, as presented in Table 3.1. In direct contrast the 2V-modulator device has a higher front mirror reflectivity and thus a higher finesse cavity so the Fabry-

Perot resonance dominates the reflectivity spectra more. As a result the Fabry-Perot resonance is at the operating wavelength of 1077nm in both the R_{off} and R_{on} curves, and the reflectivity changes from 43% to 20% giving $\Delta R = 23\%$.

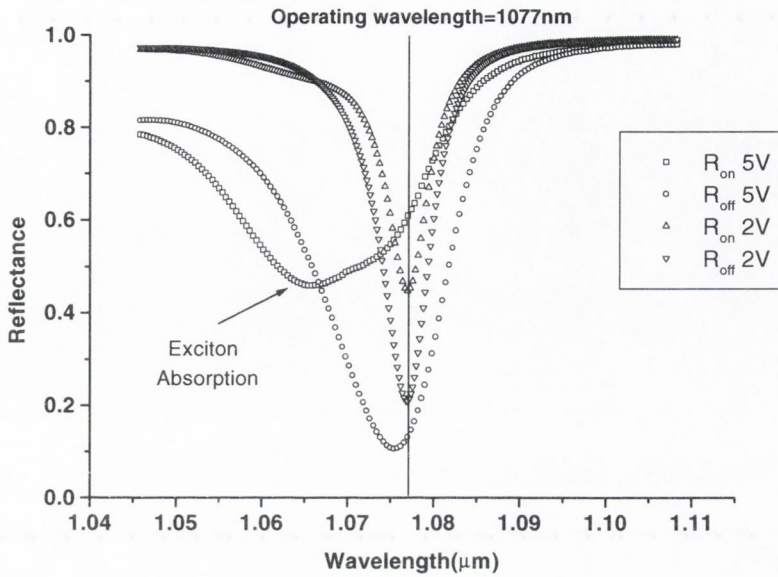


Figure 3.8: Reflectivity spectra for the optimally designed 5V and 2V-modulator structure.

3.3.3.4 Optimum operating wavelength

The optimum 5V-modulator MQW absorption spectra are shown in figure 3.9 at the 5V bias voltage and the 5V operating voltage. The absorption change $\Delta\alpha$ spectrum calculated by subtracting these two absorption curves is also shown. Looking closely at the $\Delta\alpha$ spectrum the choice of operating wavelength can be narrowed down to wavelengths around either 1060nm or 1075nm, which correspond to the two peaks in the $\Delta\alpha$ spectrum. The absorption change at 1060nm is roughly the same magnitude as at 1075nm but a larger reflectivity change is achieved at 1075nm. The main reason for this can be seen in figure 3.1. When the absorption value is large there is roughly a linear change in cavity reflectance with absorption change. This is the case here where the absorption coefficient changes from 5655cm^{-1} to 2995cm^{-1} at $\lambda=1060\text{nm}$. Device design favours a change to/from zero or close to zero in absorption where the cavity reflectance changes in an exponential behaviour (figure 3.1). This is the case at $\lambda=1075\text{nm}$. Of course there are more factors than the absorption coefficient alone that influence the reflectivity change of a MQW Fabry-Perot device but empirical modelling results have shown the maximum reflectivity change to be achieved at the operating wavelength of 1077nm, shown in figure 3.9.

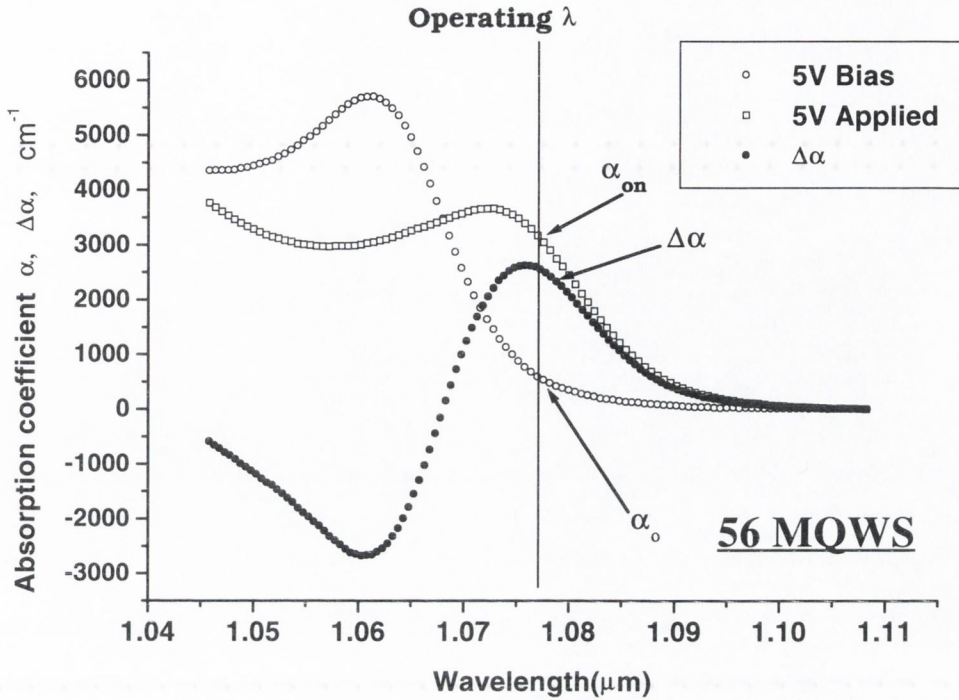


Figure 3.9: MQW absorption spectra at the 5V bias voltage and the 5V operating voltage. The absorption change $\Delta\alpha$ spectrum is also shown.

The optimum number of MQWs for operation at a given voltage can be seen in Table 3.1. At each operating voltage summarised in Table 3.1 the optimum number of wells for a given operating voltage corresponds to roughly the same electric field in each case. Thus the absorption spectrum shown in figure 3.9 is representative of the absorption spectrum at operating voltage (the absolute absorption change values on the y-axis being smaller at lower voltages). Thus systematic modelling reveals that there is an optimum electric field across the MQWs that gives the maximum modulation at each operating voltage.

At this optimum electric field the optimum operating wavelength was found empirically using the transfer matrix model to be at 1077nm. The $\Delta\alpha$ spectrum peaks at 1075nm. At 1077nm the $\Delta\alpha$ value is slightly smaller. Maximum modulation is achieved at this 1077nm because of the residual absorption value α_0 shown in figure 3.9. The residual absorption α_0 is the absorption that is present due to the bias voltage. This will determine the starting reflectivity R_{on} value for a 'normally on' device (starting reflectivity high). The broad exciton linewidth for InGaAs MQWs means that the α_0 value is significant and plays an important role in these devices. The absorption change $\Delta\alpha$ is the change in absorption from α_0 when the modulation voltage is turned on, and determines the final reflectivity R_{off} . The modulation depth or reflectivity change thus being $R_{on}-R_{off}$. The smaller the value of α_0 , the larger R_{on} , the larger $\Delta\alpha$ the smaller the value of R_{off} , thus maximising the $R_{on}-R_{off}$ value. The reflectivity value R_{on} is more sensitive to changes in α_0 than R_{off} is to changes in the $\Delta\alpha$ value. This is due to the exponential decrease in the effective back mirror reflectivity $R_{B(eff)}=R_B e^{-2\alpha L}$ of the device. Because α_0 is

a small value close to zero, the exponential dependence means that small changes in α_0 result in larger changes to $R_{B(\text{eff})}$ than similar changes in $\Delta\alpha$. Thus in Figure 3.9 changing the operating wavelength from 1075nm to 1077nm reduces the $\Delta\alpha$ value slightly but it also reduces the α_0 value and the gain in reflectivity change ($R_{\text{on}}-R_{\text{off}}$) is made through a larger increase in R_{on} value compared to a much smaller increase in R_{off} . This gain in reflectivity change is not hugely significant being of the order of 1% but it is important to understand why optimum operation is at 1077nm and not the maximum $\Delta\alpha$ value.

3.3.3.5 Front Bragg mirror reflectivity

The reflectance values for the optimum Fabry-Perot structure at 5V operation are shown in Figure 3.10 for increasing front mirror periods/reflectivity. The R_{on} corresponds to the reflectance value when the device is turned off. At the optimum 6 front Bragg periods $R_{\text{on}} = 60\%$ as stated previously, and the R_{off} value = 14%. This graph shows how the R_{off} and R_{on} values at the optimum operating wavelength as the front mirror reflectivity increases. Figure 3.8 is thus a snapshot of full reflectance spectra when the front mirror consists of 6 Bragg periods ($R_f=34\%$).

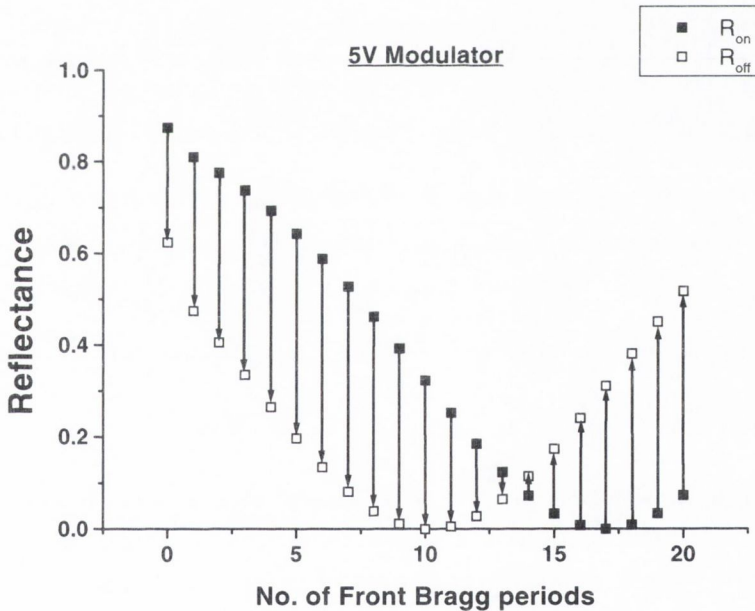


Figure 3.10: Reflectance values for the optimum Fabry-Perot structure at 5V operation for increasing front mirror reflectivity at $\lambda_{\text{op}}=1077\text{nm}$.

The R_{off} value and the R_{on} value decrease with increasing front mirror reflectivity similar to the behaviour of the optical cavity predicted by the Fabry-Perot equations in figure 3.3. The maximum reflectivity change occurs when the front mirror reflectivity has a value of 34% (6 periods). The maximum contrast ($R_{\text{on}}/R_{\text{off}}$) occurs when the number of front Bragg periods is 10 ($R_f\approx 70\%$) and $R_{\text{off}}\approx 0$. These modelling results confirm the conclusions drawn from the simple Fabry-Perot equation

results. The device structures for operation with maximum reflectivity change require lower reflectivity front mirrors compared to device designs for maximum contrast. As also predicted in Figure 3.3 large reflectivity changes are again possible at larger front mirror reflectivities $\approx 99\%$ (≈ 20 Bragg periods); here the device is operating as a 'normally off' device because the front mirror reflectivity is now becoming greater than the effective back mirror reflectivity. As mentioned earlier this device operation is not favourable as the higher front mirror reflectivity required results in a higher cavity finesse which impacts negatively on device operating tolerances as will be seen later. Figure 3.10 only shows data for 5V operation but similar results are achieved for lower voltage operation. Figure 3.10 shows the behaviour of the modulator device with various optical cavity front mirror reflectivities and how the transfer matrix model arrives at the optimum front mirror reflectivity in Table 3.1. The other critical parameters in the design of the optimum modulator structure are the MQW absorption.

3.3.3.6 Optimum number of MQWs

As mentioned above it has become clear from Table 3.1 that there is an optimum electric field across the MQWs that produced the maximum reflectivity change. There are many factors that determine this optimum electric field. The number of MQWs and its absorption spectrum are two of these principal factors. There is competition between the reducing number of MQWs that allows access to the larger absorption changes at higher electric fields (Figure 3.4) and the reduced total absorption due to the reduction in MQWs. The fact that we are using a bias voltage and the exciton linewidth is broad means the residual absorption α_0 has a strong influence and also means there is an optimum wavelength separation from the exciton absorption (Figure 3.9). Thus the optimum electric field must be a balance between all of the above. Similar to earlier work [15] an effort was made to extract a figure of merit from the absorption spectrum data to assess whether we may predict empirically the optimum number of wells and wavelength at a given operating voltage, thus avoiding the large amount of modelling required to produce table 3.1. A simple figure of merit such as $\Delta\alpha/\alpha_0$ could not be found although a more complex one may exist. The double-pass modulator device followed closely the absorption change values $\Delta\alpha$ at the operating wavelength for different numbers of MQWs (Figure 3.7). This is not the case when dealing with a MQW Fabry-Perot device. We have previously shown how the residual absorption α_0 value influences the reflectivity change value, the larger the cavity finesse the greater the influence the α_0 value has on the reflectivity change (see Section 5.4). Figure 3.10 shows how the reflectivity change is dependent on the cavity finesse and the strong influence of the exciton absorption on the Fabry-Perot resonance can clearly be seen in Figure 3.8 shifting it away from the device operating wavelength. Thus there are many more factors which contribute to the final reflectivity change when dealing with a MQW Fabry-Perot device. We conclude that a simple empirical model is difficult to achieve.

In the above analysis a correlation was found between the absorption change at the **optimum** operating wavelength 1077nm for different numbers of MQWs at 5V operation and the reflectivity change results of the optimum 5V structure. This data is shown in Figure 3.11. The influence of the changing $\Delta\alpha$ value at different numbers of MQWs in the optical cavity can be seen in the reflectivity

change curve. There is a large discrepancy at higher numbers of MQWs due to the influence of the exciton absorption on the Fabry-Perot resonance, which is stronger at larger numbers of MQWs due to the increased total absorption. At lower numbers of MQWs in Figure 3.11, the exciton absorption is shifted towards the operating wavelength and the reflectivity change follows more the change in absorption values $\Delta\alpha$. This is illustrated in Figure 3.12 where the reflectance curves are plotted for 56 MQWs as shown previously in figure 3.8 and for 68 MQWs. The important point here is that the stronger influence of the exciton absorption at 68 MQWs, which clearly shifts the Fabry-Perot resonance to shorter wavelengths, results in a reflectivity change at the operating wavelength of 1077nm much greater than expected if the absorption change value was solely considered (Figure 3.11). 56 MQWs gives the largest absorption change $\Delta\alpha$ at 1077nm, which also produces the largest reflectivity change. Figure 3.13 shows the absorption change $\Delta\alpha$ for operation at lower voltage operation with a bias voltage. Also in each case the number of MQWs at which the maximum $\Delta\alpha$ is achieved correlates with optimum number of MQWs giving the maximum reflectivity change in Table 3.1.

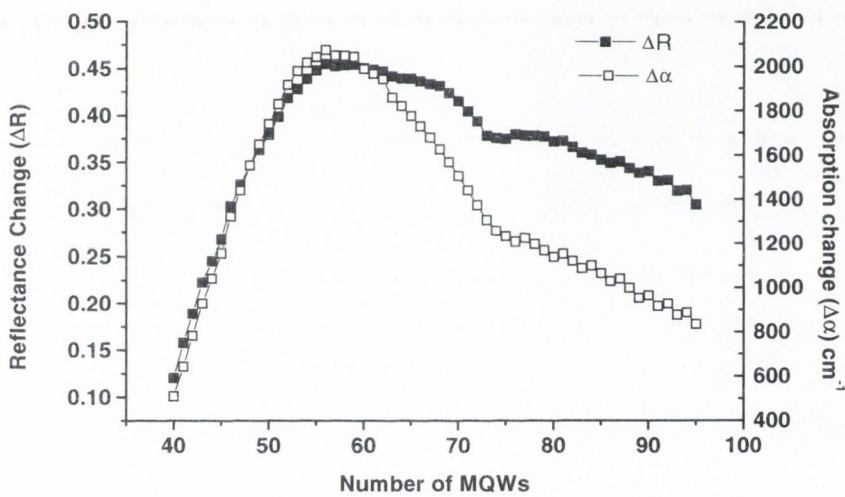


Figure 3.11: Absorption change at the operating wavelength 1077nm for different numbers of MQWs at 5V operation. The reflectivity change results at 1077nm for the optimum 5V structure are also shown for comparison.

We conclude here that there are many factors that influence the achievable reflectivity change value from a MQW Fabry-Perot modulator. The various intimate relationships between all these factors indicate how non-trivial it is to calculate the modulation achievable. All these intimate factors make an empirical understanding difficult. Thus the semi-empirical models developed in [16,17] optimising operation and tolerances of double-pass modulators would be difficult to produce in the Fabry-Perot case. Analysis of the device operation and tolerance requires more comprehensive modelling and is the subject of this thesis.

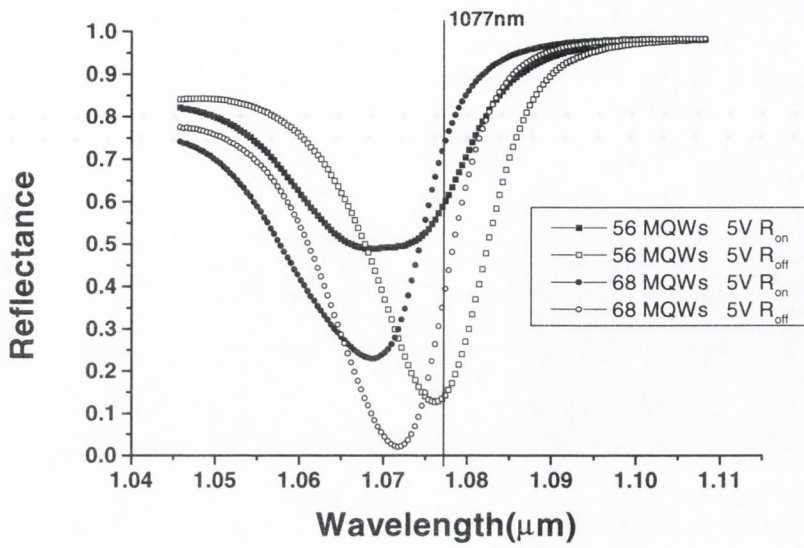


Figure 3.12: Reflectance curves plotted for 56 MQWs as shown previously in figure 3.8 and for 68 MQWs.

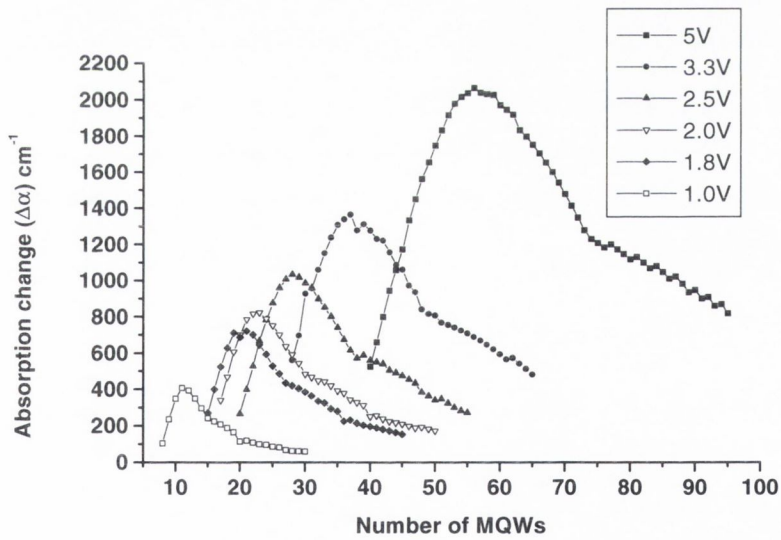


Figure 3.13: Absorption change $\Delta\alpha$ for operation at lower voltage operation with a bias voltage. In each case the number of MQWs at which the maximum $\Delta\alpha$ is achieved correlates with the maximum reflectivity change in Table 3.1.

3.3.3.7 Bias voltage operation

The factors that influence the reflectivity change of the MQW Fabry-Perot modulator just presented are for device operation with a bias voltage. For operation without a bias voltage the above conclusions also apply. The optimum operating wavelength is at a shorter wavelength of 1068nm as expected. The use of a bias voltage means the exciton hh peak starts at a longer wavelength. Thus without a bias voltage the optimum wavelength is expected to be at a shorter wavelength. The optimum number of MQWs will also be different to the bias case due to the voltage swing of 0V to 5V. The closer proximity of the Fabry-Perot resonance to the strong absorption of the 0V-exciton hh peak results in reflectivity spectra with behaviour similar to Figure 3.12, where the exciton absorption and Fabry-Perot resonance are strongly convoluted (68 MQWs). The reflectivity change results presented in Table 3.1 at various operating voltages indicate that roughly similar modulation values are achievable, with or without a bias voltage. Two of the main assumptions made in our transfer matrix model (Section 2.15) put a greater uncertainty upon the modelling results obtained for the no-bias case compared with the bias voltage case. When quantum wells are used, the exciton features give rise to a modification of their refractive index spectrum, both the real and imaginary parts, compared to their bulk spectrum [5,18]. The imaginary part we have measured experimentally but the real part was not. At wavelengths further away from the exciton peak wavelength this real refractive index modification is smaller and at longer wavelengths this value is similar to the bulk value. Using a bias voltage will eliminate this uncertainty but introduces an uncertainty due to electro-refractive effects [18]. The second assumption in our model concerns electro-refractive effects, the modification of the real refractive index with voltage. At longer wavelengths this effect is also minimised [5,18], thus operating with a bias voltage is favourable in this case. It is important to note here that it is very possible that modulation without a bias voltage could achieve the modulation values close to values predicted by the model or better. It is not being ruled out as a device structure, in fact it would be more favourable because of its lower electrical power consumption, especially when large arrays are involved. Electro-refraction effects can also be used in a positive way to increase the reflectivity change and spectral bandwidth [3]. To achieve more accurate modelling for operation without a bias voltage, further detailed dispersion measurements would be required from the quantum wells. Due to the strict timetable of the project an outside party was approached to do these measurements but no results were obtained. As the work done in this thesis is to explore the possibility and trade-offs associated with low voltage modulators, the findings and conclusions for bias operation will generally apply also to non-bias operation. The reason for choosing a bias voltage operation is to match the assumptions made in our transfer matrix model, which should yield more reliable and realistic predictions and allow the work to move forward.

3.3.3.8 Lower voltage operation

The performance of the MQW Fabry-Perot modulator at lower voltage operation is of principle interest in this project. The resulting reflectivity change and the optimum device details for 5V to 1V operation are summarised in Table 3.1 above.

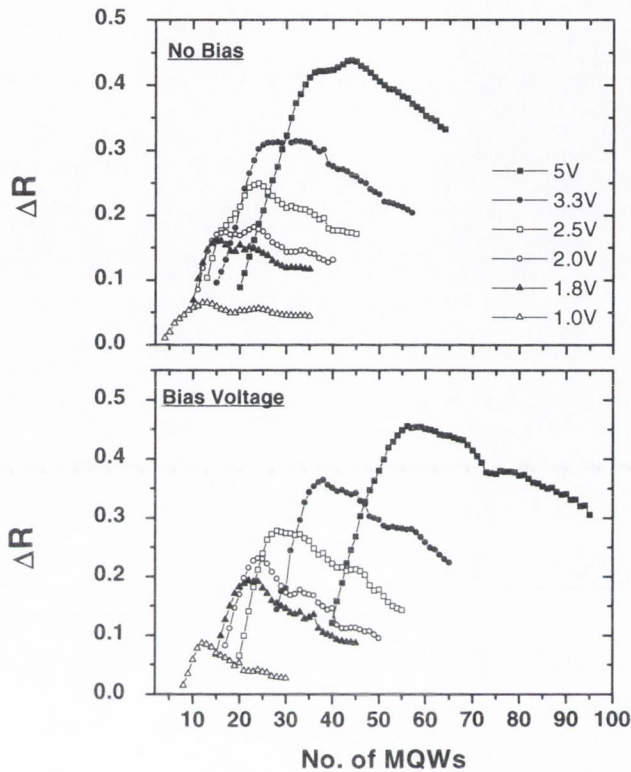


Figure 3.14: Reflectivity change at each operating voltage as a function of the number of MQWs in the optical cavity at the optimum front mirror reflectivity values and operating wavelength 1077nm.

Figure 3.14 shows the complete modelling results at each operating voltage as a function of the number of MQWs in the optical cavity at the optimum front mirror reflectivity values (Table 3.1) and operating wavelength. The factors that influence these curves have been discussed previously. Looking more closely at the predicted modulation from devices operating with a bias voltage, the first point to note is that the modulation achievable for a Fabry-Perot structure is better than that of a double pass structure at all operating voltages. At 5V operation there is a 40% improvement in modulation when an optical cavity is used which requires only the growth of a few extra Bragg layers. This improvement is due to the optical cavity making more efficient use of the MQW absorption. This improvement in signal to noise ratio could be important if the predicted very large arrays of devices (128x128) are required [19] and if optical fan-out is used to address all of these devices reducing significantly the incident optical read power per device. This extra modulation may also be traded for a gain in the device operating tolerances as will be shown in Chapter 5.

At lower voltage operation the number of MQWs is reduced to an optimum number to attain the optimum electric field discussed earlier. In the double-pass modulator structure this reduction in

overall absorption is fatal to the device modulation. In the case of the Fabry-Perot modulator, as the operating voltage is reduced the front mirror reflectivity is seen to increase as expected to compensate for the reduced total absorption. The light is trapped in the optical cavity to interact further with the reduced number of MQWs. Thus the optical cavity can compensate for the reduced absorption at lower voltage operation. This is consistent with experimental results for GaAs wells in [2,20]. Unfortunately modelling results show the reflectance change decreases with reduced operating voltage. The improved modulation compared to the double pass device is expected but the rapid fall in modulation with reduced voltage is not. It turns out and will be discussed in full detail in Chapter 5 that the falling modulation is due to the reflectivity of the front mirror having reflectivity values closer to the back Au mirror (94%) at lower voltage operation; thus the cavity reflectance value starts to approach zero. The back mirror reflectivity value is extremely critical to low voltage operation of these device structures. To keep a sufficient signal to noise ratio the reflectivity change specifically required for the SPOEC system is 30%, and this maybe achieved down to $\approx 2.5V$ operation for the favoured device structure using an optical cavity with an Au back mirror. Below this the modulation is not sufficient to meet the 30% requirement for this specific crossbar switch. Other systems may possibly operate at lower modulation values, for a reflectivity change of 20% modulation is possible for this structure down to 2V. For a double pass structure it should be noted that operation at 30% is only possible at 5V. 20% modulation is only possible at voltages greater than 3.3V.

3.3.4 Conclusions of transfer matrix modelling

Transfer matrix modelling to find the optimum structure for maximum reflectance change has confirmed earlier conclusions taken from some simple analysis using the Fabry-Perot equations and some simple analysis of the MQW absorption. Thorough device modelling has found the optimum Fabry-Perot device structure to achieve maximum reflectivity change. Modelling predictions have shown how the reflectivity change from the double-pass modulator structure diminishes at lower voltage operation. Only greater than 30% modulation is achievable at 5V operation with a bias voltage. 20% modulation is possible at 3.3V. At lower voltage operation the reflectivity change diminishes rapidly. Modelling results for the Fabry-Perot modulator structure indicate that the device performance can be improved at 5V operation to 46%. At lower voltage operation 30% modulation is achievable at operating voltages of 2.5V. Modulation changes of greater than 20% are predicted for operation down to 2V. It must be stressed that these values are for a modulator device with a gold back mirror (94%) and Bragg stack front mirror. This device structure is first investigated because of the advantages the structure brings to device fabrication and processing in large arrays. It is clear from the modelling results that this device structure cannot produce the required modulation when operating at future CMOS voltages [8] less than 2.5V. In Chapter 5 an alternative device structure is investigated where the back mirror reflectivity is not limited to 94%. The operation of these devices without a bias voltage may also be possible but more dispersion data is required for the model to confirm this. In this work the device structure operating with a bias voltage is investigated only due to the expected increased accuracy of the model predictions for this device. The modelling results are promising and operation at

near future CMOS operating voltages is predicted to be possible from a modulation point of view for this device structure and material system. Operation of these devices in a real optical interconnect means that the required modulation value must be achievable under different operating conditions. These conditions include changing ambient temperature and various incident angles. The increasing finesse of the optical cavity will also impact on the device MBE growth tolerance and spectral bandwidth. These tolerances are addressed in the following sections.

3.4 Device Tolerances

For practical operation of these Fabry-Perot modulator devices in a real system, a broad spectral bandwidth is required as well as good tolerances to MBE growth lateral non-uniformities for the production of large arrays. Operation must be possible at a range of incident angles due to the small device area and spot sizes required in large arrays. The optical cavity used in the Fabry-Perot structures above impacts on these operational parameters. The transfer matrix model is used to investigate these tolerances in detail to see if these devices could be used in a real working system. Comparison is made to the double-pass modulator device that has been used successfully in optical interconnect systems [12,21]. The impact of the cavity structure on the device electrical bandwidth, its sensitivity to optical power saturation and ambient temperature change are also presented.

3.4.1 Spectral Tolerance

The device spectral bandwidth is the wavelength range over which a desired reflectivity change is achievable. It is calculated by subtracting the R_{off} spectrum from the R_{on} spectrum. The wavelength range over which a precise ΔR value is achievable then defines the spectral bandwidth for this device. The spectral bandwidth impacts directly on the temperature sensitivity of the device, the angular acceptance of the device and most importantly the MBE growth of these devices. The larger the spectral bandwidth, the better the device tolerance to the above parameters. Each of these tolerances will be dealt with individually in this section. The spectral bandwidth also sets the spectral range within which the modulator read laser wavelength must remain if the required modulation is to be achieved. Solid state lasers have good temperature stability and a relatively stable lasing wavelength. The SPOEC system uses a Nd:Ylf solid state laser and has excellent temperature stability and high optical power. A high power semiconductor laser diode is a candidate for use in interconnect systems due to its small size but it has a poorer temperature stability. The change in bandgap energy with temperature will influence its lasing wavelength and thus is expected to require some temperature stabilisation such as a Peltier-cooler when used in a real system. Alternatively the semiconductor laser wavelength can be stabilised by using an external cavity. The larger the modulator spectral bandwidth the less sensitive it will be to changes of the read wavelength.

The reflectivity spectra for the optimum 5V and 2V modulator devices giving 46% and 23% reflection change respectively are shown in Figure 3.8. This shows clearly the reflectivity spectra narrowing at lower voltage operation. Higher finesse cavities result in a spectrally narrower Fabry-Perot resonance (Chapter 2) and $\overline{\text{much}}$ reduced spectral bandwidth when the R_{off} and R_{on} values are subtracted. For operation at lower voltages Table 3.1 shows how the front reflectivities and thus the cavity finesse, increase as the operating voltage decreases. Thus the narrowing of the Fabry-Perot resonance at lower voltage operation is expected to result in reduced spectral bandwidth. The spectral bandwidth was calculated for the devices summarised in Table 3.1 using the transfer matrix model and the resulting spectra are plotted in Figure 3.15. In each case the physical cavity thickness has been reduced to a minimum size while keeping the Fabry-Perot resonance at the required wavelength.

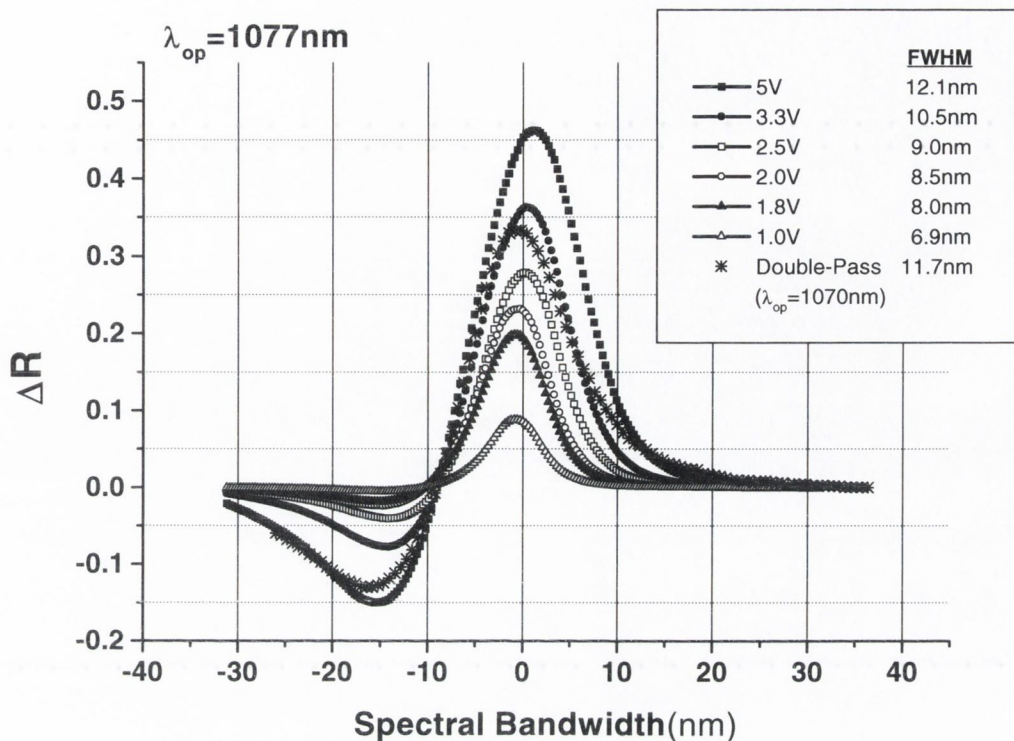


Figure 3.15: Spectral tolerance for 5V to 1V operation calculated using the transfer matrix model by subtracting the R_{on} and R_{off} reflectance curves plotted spectrally.

The predicted reduced spectral bandwidth at lower voltage operation is reflected in the full width half-maximum FWHM values in Figure 3.15. For a specific modulation of 30% required by the SPOEC interconnect a FWHM spectral bandwidth of 10nm is predicted for 5V operation and 5.6nm for 3.3V operation. For the double pass device operating at 5V the spectral bandwidth is 4.8nm. This is a significant result, it shows that an optical cavity does not necessarily reduce the spectral bandwidth of this structure but actually enhances it at 5V and 3.3V operation. At 2.5V operation the reflectance change is close to 30% and thus operation could be possible in the SPOEC system but for the fact that at wavelengths away from $\lambda_{op} = 1077\text{nm}$, the modulation falls off very quickly giving close to zero spectral tolerance. Thus operation of these structures at 2.5V is not practical which sets the minimum operation at 3.3V for this particular structure. The shape of the spectral bandwidth curve is influenced mainly by the Fabry-Perot resonance. Larger spectral tolerances are achieved when a reflectance change value somewhat greater than the required value (30%) is obtained at the operating wavelength. For lower ΔR values the corresponding spectral bandwidth values are much larger due to the shape of the Fabry-Perot resonance. For $\Delta R=20\%$ the spectral bandwidth increases to 13.3nm for the 5V Fabry-Perot device. The choice of ΔR for a system is important as the modulation value can be traded for spectral bandwidth and other device tolerances, as we will see later.

These modelling results have shown that the use of an optical cavity does not reduce the spectral bandwidth for operation at 5V and 3.3V at $\Delta R=30\%$. Although the 2.5V device produces

$\Delta R \approx 30\%$, practical operation of the device in a real system is not possible due to its poor spectral bandwidth at this modulation value. Other interconnect systems may tolerate lower ΔR operation and operation where $\Delta R = 20\%$ or less. In this case operation at 2.5V is possible and has a spectral bandwidth of 6.5nm. The spectral bandwidth is intrinsically related to the angular tolerance of these devices and is investigated next.

3.4.2 Angular acceptance

Electro-Absorption modulators traditionally operate at normal incidence and the majority of publications deal with only normal incidence operation. In optical interconnects like the one being assembled in SPOEC and others [12], large arrays of these devices are used. 128x128 array sizes are predicted for use in optical interconnects in the near future [19]. The device sizes on these arrays are small typically having an area of 20-35 μm^2 . These small device sizes require fast converging lenses to focus the read beam onto the device and light is incident at a range of angles off normal incidence. The lenses used to focus the light on the modulator devices in the SPOEC system lead to an angular width of $\pm 9^\circ$ [22]. This requires the modulator device to operate over this angular range i.e. $\Delta R = 30\%$ is required for light incident at angles as large as $\pm 9^\circ$.

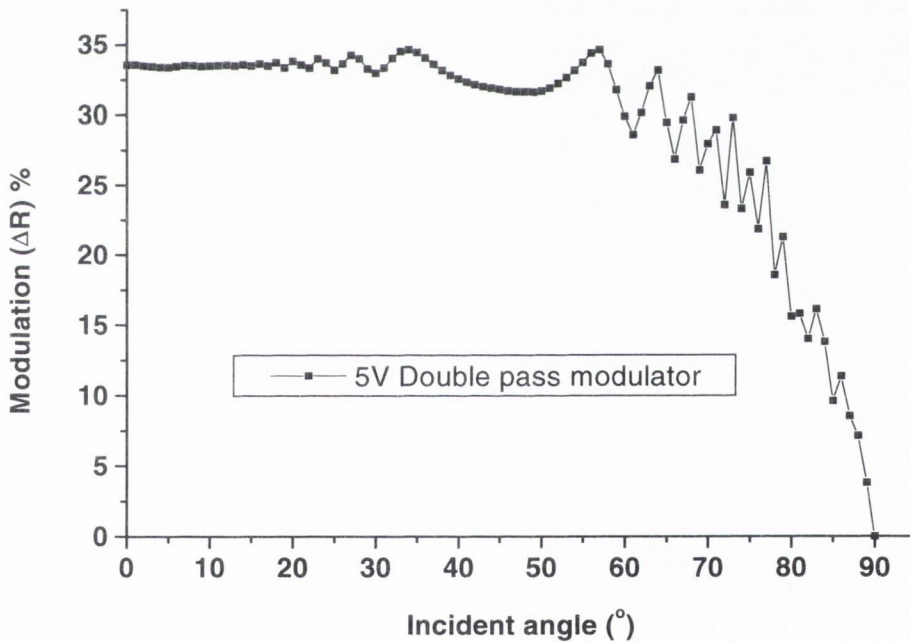


Figure 3.16: calculated angular response of the optimum 5V double-pass modulator structure.

Figure 3.16 shows the calculated angular response of the optimum 5V double-pass modulator structure. The angular response is principally determined by the angular properties of the semiconductor / gold interface and the deterioration of the anti-reflection coating at increasing incident angles. This produces the oscillations on the angular response curve as a large weak optical cavity ($\approx 10\mu\text{m}$) is formed between the front interface and the back gold mirror. The angular response of the double-pass structure

is very good having reasonably ‘flat’ response and $\Delta R > 30\%$ up $\approx 60^\circ$. The angular response of an optical cavity is very different to that of the double-pass structure and the reason is explained in Section 2.16. In this work our benchmark is to at least match the angular width of $\pm 9^\circ$ of the optics specifically used in the SPOEC system. The complex architecture of these systems puts tough design constraints on the design of the free-space digital optics for the interconnect systems [23]. These Fabry-Perot devices should have a large enough angular range so as not to add further constraints on the design of the system optics. This benchmark is of course specific to this interconnect; other systems or applications may not require an angular tolerance of this size. Thus the modelled results are presented in a general format.

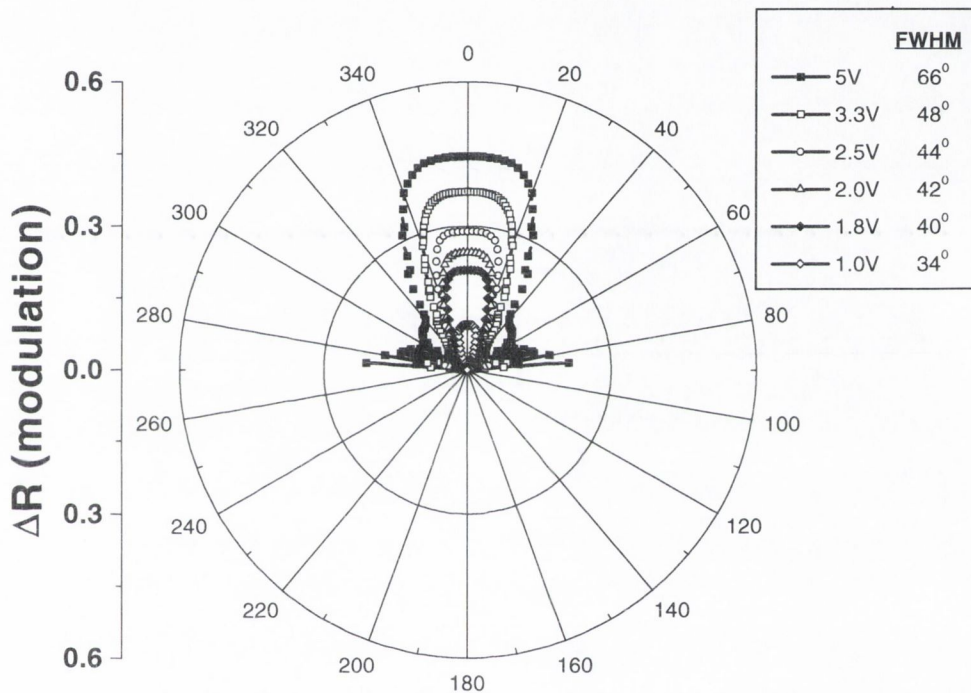


Figure 3.17: Modulation response for the optimum modulator designs at each voltage, a polar format is used with the reflectance change increasing radially from the centre.

Transfer matrix modelling can once again be used to calculate the angular response of these devices [24] at each operating voltage as outlined in section 2.14. These calculations allow for S and P type polarisation and the resultant reflectivity is found by taking the average of the TE and TM polarisation reflectivities. Figure 3.17 shows the modulation response at various incident angles for the optimum modulator designs at each operating voltage for the devices summarised in Table 3.1 plotted in a polar format. The reflectance change increases radially from the centre. The angular tolerance values were also calculated where the physical length of the cavity is minimised. As expected from Section 2.16 the increasing cavity finesse at lower voltage operation results in a decreasing angular acceptance. The reflectivity change in each case shows an initial ‘flat’ response to changing incident angle and then rapidly reduces to lower values. This makes the **total** modulation value easier to predict when light is

incident at a range of angles rather than calculating a convolution of changing modulation values weighted by the Gaussian profile of the lens. The angular acceptance for a specific $\Delta R=30\%$ is $\pm 27^\circ$ and $\pm 18^\circ$ for 5V and 3.3V operation respectively. At 2.5V the angular acceptance is also good. Due to the initial 'flat' response $\Delta R=28\%$ is predicted for $\pm 10^\circ$. For a reflectivity change of 20% the 2.5V, 2.0V and 1.8V devices have an angular response of $\pm 18^\circ$, $\pm 15^\circ$, $\pm 10^\circ$ respectively. These modelling results indicate that the 5V and 3.3V have large enough angular acceptance angles to match the angle tolerance of the free-space digital optics used in the current interconnect. Good angular tolerances are also predicted at lower voltage operation for operation at $\Delta R=20\%$.

3.4.3 MBE lateral growth tolerance

The biggest obstacle to the realisation of large arrays of low voltage Fabry-Perot modulators is their tolerance to MBE growth non-uniformities. In this method of crystal growth the substrate is held in a high vacuum while collimated beams of atoms are directed into the vacuum towards the substrate surface. The substrate is set spinning in order to allow a consistent thickness to be grown across the full wafer area, as the incident atom beam may not have an even distribution of atoms. Although this does improve the layer thickness distribution it is not perfect and the resulting thickness variation across a wafer is 'dome' shaped, relatively flat from the centre but toward the wafer edge the thickness normally reduces rapidly. Typical accuracies currently are $1 \rightarrow 1.5\%$ [25] variations from the centre thickness for the majority of the wafer, towards the edge the thickness variation from the centre thickness can be up to 2-3%. Experimental measurements of thickness variation across a wafer grown by MBE as part of this project can be found in Section 4.4.2.2. Thickness variations across the wafer result in the optical cavity thickness changing and thus the Fabry-Perot resonance will shift in wavelength from the operating wavelength. A large device tolerance to this thickness change is required to allow the fabrication of large device arrays and to ensure that a large area of the wafer can be used for device processing. In structures grown by molecular beam epitaxy (MBE) or MOVPE there are two issues. One is the absolute accuracy of the thickness grown in the centre of the wafer. This can be addressed by in-situ growth monitoring [26] and/or post-growth processing of the wafer [27]. The second is non-uniformity across a wafer mentioned above. This generally cannot be removed and must be tolerated. The double pass modulator structure has a very good tolerance to these thickness fluctuations. Once the quantum well/barrier thickness and composition are grown correctly and the exciton hh absorption peak is at the desired wavelength, devices can be processed from the majority of the wafer. The thickness fluctuations in well/barrier thicknesses are not cumulative (like the optical cavity) across the wafer and the shift of the exciton position in wavelength is small [28], measured to be 4nm across wafer 814 (Chapter 4). Thus it is possible to produce large arrays of these devices and to use the majority of the wafer for device processing.

3.4.3.1 Absolute growth accuracy

Without the use of in-situ growth monitoring the accuracy of a layer growth thickness at the centre of the wafer is close to $\pm 1\%$ of the thickness being grown, assuming the layer being grown is not larger than $\approx 1\mu\text{m}$ [29]. This accuracy is poor and produces a $\pm 1\%$ shift in wavelength (Eqn.2.26) of the Fabry-Perot resonance from the operating wavelength. When working with high finesse cavities and narrow spectral bandwidths this accuracy is not acceptable and makes growth of the device to the required wavelength difficult to achieve. In-situ growth monitoring dramatically improves the growth accuracy of the absolute thickness. The layer growth rate is measured using reflectivity measurements. Commonly used in VCSEL growth, accuracies of $\approx \pm 2\text{nm}$ of the target operation wavelength have typically been achieved [26]. With a VCSEL structure the wavelength at which the cavity resonance is placed at is normally the wavelength at which light emission occurs. When dealing with a modulator device the situation is different. Operation is fixed at a certain read wavelength. If the specific operating wavelength does not fall within the spectral bandwidth of the device, operation is only possible if the read wavelength is changed. This is problematic when working with other optical components such as microlenses and diffractive optical elements that are wavelength sensitive. Their efficiency and operation is largely reduced with small changes in the operating wavelength [30]. Using the VCSEL growth accuracy of $\pm 2\text{nm}$ of the target operation wavelength a minimum spectral bandwidth can be set. If the grown thickness of the optical cavity is such that the Fabry-Perot resonance is placed $+2\text{nm}$ (in wavelength) above the target operation wavelength, then the resonance must be spectrally wide enough so the required modulation value e.g. 30% is still achieved at the operating wavelength. This means that the spectral half-width must be 2nm at 30% modulation. The same argument holds when the Fabry-Perot resonance is placed -1nm from the target operation wavelength. Thus the overall full spectral bandwidth must be at a minimum of 4nm at the required modulation value based on current epitaxial growth accuracies. The larger the spectral bandwidth the better, but any smaller than this and it is most probable that device operation at the centre of a wafer at the desired operating wavelength would not be possible. Referring back to Figure 3.15 for $\Delta R=30\%$ the spectral bandwidth for the 5V and 3.3V operation is 10nm and 5.6nm respectively. At 2.5V the spectral bandwidth is 6.5nm for $\Delta R=20\%$. These values are larger than the minimum 4nm value set above and thus it should be possible to achieve accurate centre growth thickness for these devices.

Another important point that follows from this is related to the thickness non-uniformity across a wafer. Figure 4.15 in chapter 4 shows the percentage change in cavity thickness across the wafer for wafer B814. The cavity thickness generally decreases on moving away from the centre of the wafer, a result inherent to the growth process itself. Thus for this reason and for these devices it is advantageous to grow the cavity thickness too large, to a thickness which will still give the required modulation value. In doing this there will be a larger part of the wafer from which to process devices as the cavity thickness will decrease moving towards the edge of the wafer. Moving towards the wafer edge the shift in the exciton absorption wavelength across the wafer may be a concern but as mentioned earlier this shift is normally small, being only 4nm for wafer B814.

3.4.3.2 Growth non-uniformity across a wafer

To study the modulator growth tolerance, the modulation was calculated when the actual physical thickness deviated from the ideal optical cavity thickness for each modulator structure.

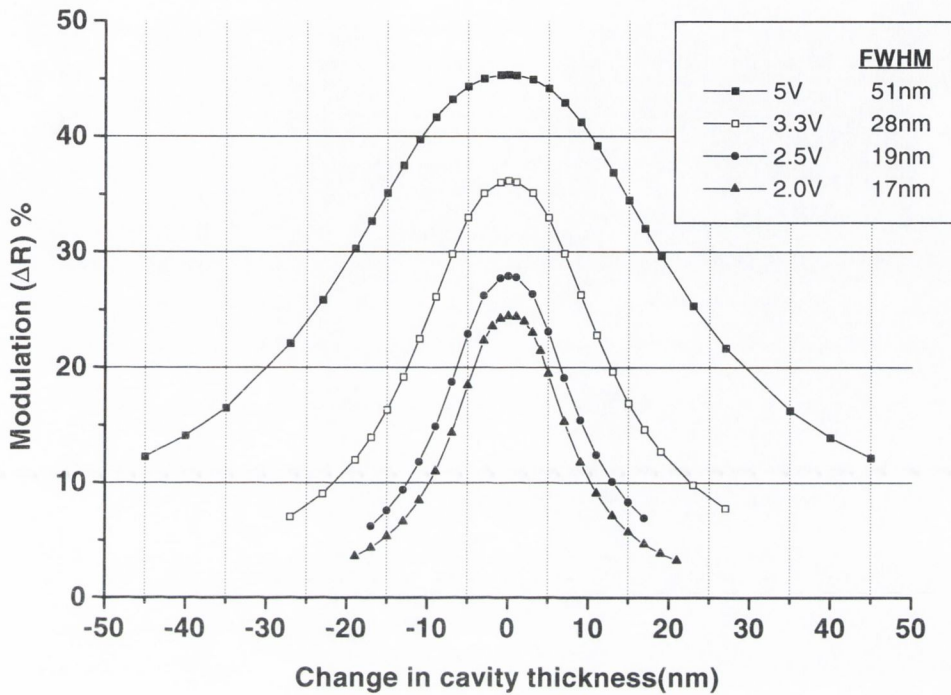


Figure 3.18: Resulting calculated modulation when the actual thickness deviated from the ideal cavity thickness for each modulator structure.

The modulation changes because the curves shown in Figure 3.15 above shift in wavelength from the fixed operating wavelength, as the cavity thickness increases or decreases from the ideal thickness (i.e. the thickness that places the resonance at the desired operating wavelength, 1077nm). Thickness fluctuations across the wafer also change the $\lambda/4$ layer thickness of the Bragg mirror and change the effective cavity length due to light penetration into the mirror, but have only a minor effect on the mirror reflectivity, shifting only the central wavelength of the Bragg mirror. The front mirror stop-band is spectrally wide so at the modulator operating wavelength the mirror reflectivity is relatively unchanged over the thickness fluctuations being considered here. In our modelling the physical cavity thickness has been reduced to a minimum size while keeping the Fabry-Perot resonance at the required wavelength. Figure 3.18 shows the resulting calculated modulation when the actual thickness deviated from the ideal cavity thickness of the modulator structure. These results show that the lower voltage cavities are more sensitive to cavity thickness changes, the modulation values fall more rapidly at lower voltage operation and this is reflected in the FWHM values shown in the inset figure 3.18. There are a number of factors that influence the resulting curves in Figure 3.18. These factors are addressed in detail in Section 5.5.2.2. As previously stated, the thickness change across a wafer varies as a

percentage of the centre wafer thickness. Thus more realistic picture of the device sensitivity to thickness change is presented if the data in figure 3.18 are presented as a percentage change in the physical cavity thickness of the modulator in question. The cavity thickness in each case is made up of **p** and **n** doped layers, each having a minimum value of 200nm, the total thickness of the number of MQWs, and the penetration length into the front Bragg mirror (equation 2.34). Figure 3.19 shows the data in figure 3.18 presented in this format. For 30% modulation there is a good tolerance of $\pm 1.0\%$ at 5V operation and $\pm 0.5\%$ at 3.3V operation. For a 20% modulation value there is a predicted tolerance of $\pm 0.5\%$ at 2.5V operation. Devices are normally processed from the central area of the wafer where a 1-1.5% variation in growth thickness exists. The above values mean that relatively large arrays of these Fabry-Perot devices can be fabricated from a large proportion of the useful area of the wafer. This assumes of course that in-situ monitoring can grow the correct cavity thickness at the centre of the wafer.

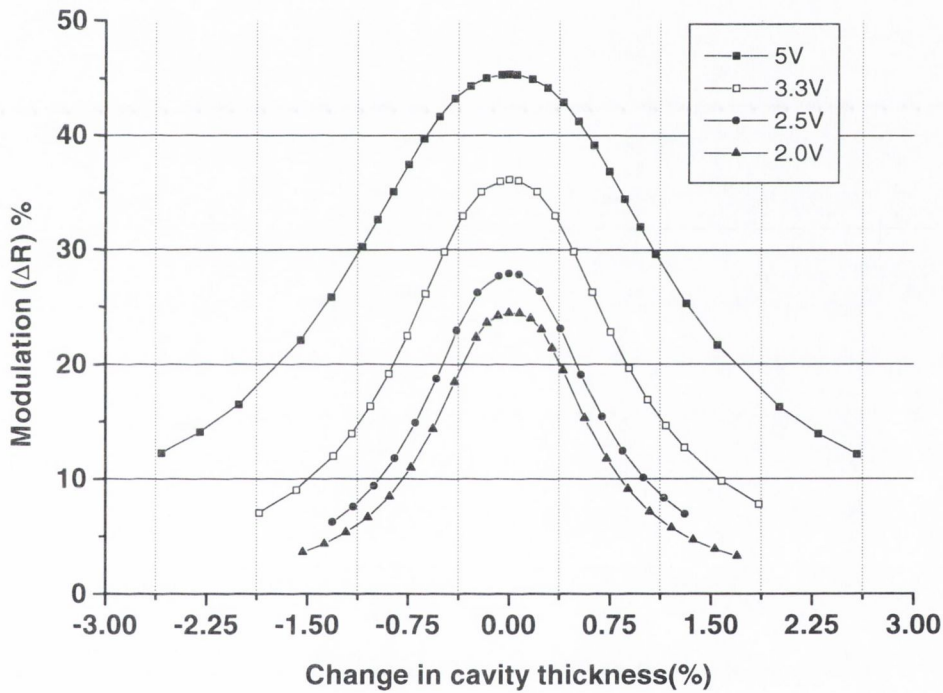


Figure 3.19: Cavity thickness variation presented in figure 3.18 as a percentage thickness change of the optical cavity thickness.

3.4.4 Temperature sensitivity

The resonant nature of the Fabry-Perot modulator structure makes it sensitive to environmental changes such as changes in the ambient temperature. The temperature change results in the exciton absorption peak and the Fabry-Perot resonance shifting in wavelength at different rates and thus the modulation at the operating wavelength changes. Experimental investigations into the temperature sensitivity of these devices can be found in [4,29,30]. Zouganeli et al. [4] examined in detail the effect of temperature change on both the on and off-state Fabry-Perot resonance and estimated its value from experimental measurements for AlGaAs/GaAs MQWs. As the temperature **increases** the following is expected:

- a) The reflectivity on-state resonance (R_{on}) red shifts by a value larger than the thermo-optic effect [36] value of $0.083\text{nm}/^\circ\text{C}$. The increased real refractive index value of the MQW region as the exciton-resonance separation decreases, causes the on-state resonance (R_{on}) to shift by a larger value. From measurements the on-state resonance is estimated to change by $0.14\text{nm}/^\circ\text{C}$.
- b) The reflectivity off-state resonance (R_{off}) red shifts by a smaller value than the on-state resonance with temperature. This is due to the increasingly negative QCSE induced refractive index change (electro-refraction) as the exciton-resonance separation decreases. From measurements the off-state resonance is estimated to change by $0.07\text{nm}/^\circ\text{C}$.
- c) The exciton measured red shift due to the material band-gap dependence on temperature [32] was $0.4\text{nm}/^\circ\text{C}$.

For decreasing temperature it was assumed the device temperature dependence was a function of the band edge dependence only. Due to the difficulty in finding published material with these values for InGaAs/GaAs MQWs and the short lifetime of this project not permitting experimental measurement of these values, the above values are used in the transfer matrix model as an approximation of how the device would behave to temperature changes. The temperature coefficient of the band edge is approximately equal for both material systems. The values for the resonance shift are expected to be slightly different for InGaAs/GaAs MQWs. Without accurate values for InGaAs/GaAs MQWs the AlGaAs/GaAs values will allow us to model the device behaviour approximately and to see what effect lower voltage operation will have on the temperature sensitivity of the device. The modelling results using the AlGaAs/GaAs values are not expected to be largely different to that for InGaAs/GaAs MQWs.

The reflectivity change with temperature is investigated using the transfer matrix model by shifting the exciton hh peak and the on and off-state resonance according to the above values from the optimum exciton-resonance separation. The on and off-state resonances are shifted in wavelength by increasing or decreasing the cavity thickness. The R_{off} , R_{on} and thus the ΔR value are then calculated for a range of temperature changes at the operating wavelength. Figure 3.20 shows these modelling results for the temperature sensitivity of the 5V and 2V modulator devices. The results for the 5V-

modulator device show the reflectivity change decreasing as the ambient temperature increases or decreases from the chosen operating temperature. The operating temperature of these devices must be predetermined before device growth due to the band gap dependence on temperature. The quantum well/barrier thickness and composition are then chosen so the exciton hh peak will be placed at the operating wavelength at this chosen operating temperature. The temperature change shown in Figure 3.20 is the temperature change from this predetermined operating temperature.

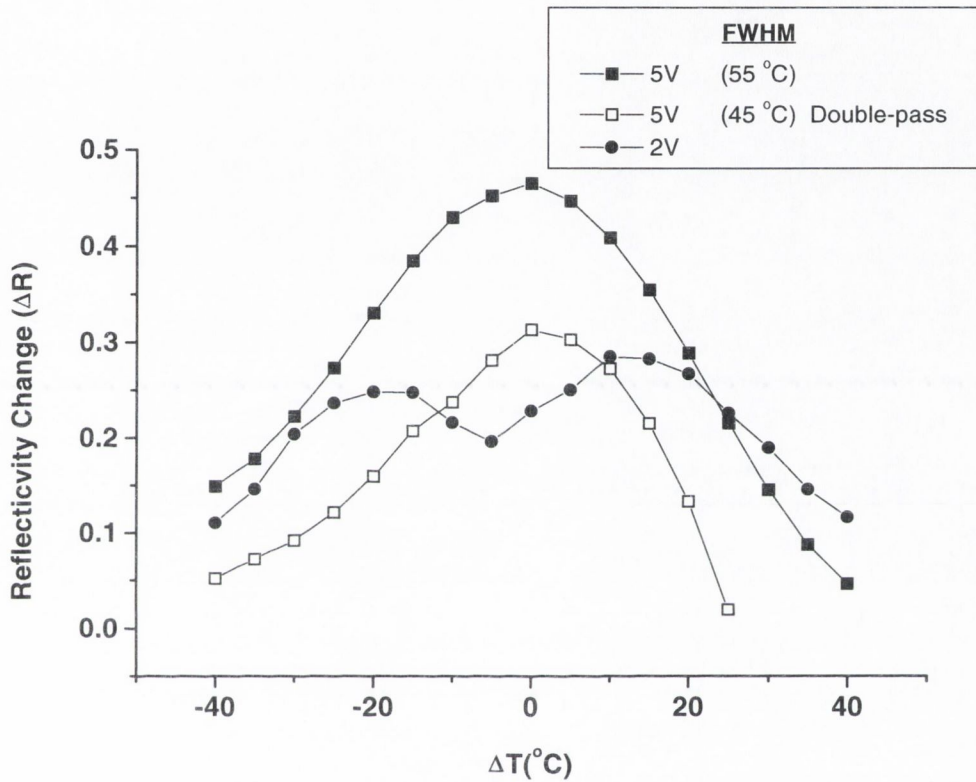


Figure 3.20: Modelled modulation change at the device operation wavelength due to changing ambient temperature for 5V and 2V operation. The calculated temperature sensitivity of the 5V Double-pass modulator is also shown for comparison.

As the ambient temperature decreases the modulation value also decreases at the operating wavelength. This is due to the exciton shifting to shorter wavelengths and moving away from the Fabry-Perot resonance and thus the R_{off} and R_{on} value increase at the operating wavelength. Thus the reflectivity change $\Delta R = (R_{\text{on}} - R_{\text{off}})$ slowly decreases in value, as seen in Figure 3.20. As the ambient temperature increases the modulation value again decreases. In this case the exciton shifts to longer wavelengths towards the off-state resonance at a much faster rate than to the on-state resonance. The R_{off} value does not change significantly at the operating wavelength due to this increased absorption as it is already at a low reflectivity value as expected from Figure 3.1. The on-state resonance and exciton relative separation decreases and thus the R_{on} value decreases due to the increased exciton absorption. Thus the falling R_{on} value results in the reflectivity change $\Delta R = (R_{\text{on}} - R_{\text{off}})$ decreasing as seen above. The

modelled behaviour of the 5V-modulator device is similar to the behaviour found experimentally in [4]. The behaviour of the 2V modulator is somewhat different than the 5V modulator and gives an interesting result. Figure 3.8 shows the R_{off} and R_{on} reflectivity curves for these modulator devices. The R_{off} reflectivity has a value much higher than the 5V modulator case. This is the reason the temperature sensitivity initially increases from the 23% modulation value and then decreases similar to the 5V curve. At increasing temperature the R_{off} value decreases significantly unlike in the 5V modulator case and thus the reflectivity change $\Delta R = (R_{\text{on}} - R_{\text{off}})$ increases initially. When the R_{off} value reaches lower reflectivity values it then behaves like the 5V modulator and the ΔR value decreases. The temperature range investigated here is larger than that studied in [4]. Thus the accuracy as mentioned previously is not expected to be perfect but the data in Figure 3.20 should give a reasonable indication of the temperature behaviour. The device tolerance to temperature changes is predicted to be relatively large from the above modelling results for both the 5V and 2V modulator devices. The low finesse cavity and the broad exciton result in a large temperature tolerance for the 5V device, predicted to be 55°C. Unfortunately the temperature range is not large enough to operate in a standard electronics environment (-30°C to +50°C) and operation with a temperature control unit such as a Peltier-cooler is required. Specifically in the SPOEC interconnect the Fabry-Perot modulators are the optical interface to the silicon integrated circuit. The silicon electronics must operate in required temperature range for optimum performance and thus require a temperature control system to handle the large electrical power dissipation to remove the generated heat. The Silicon IC in the SPOEC system is integrated to a Peltier-cooler for operation at the optimum temperature [29] and thus the integrated modulator devices will also be temperature stabilised by the Peltier-cooler. Thus once the modulator devices are fabricated to operate at the required temperature the temperature sensitivity indicated by the above modelling is good enough for operation with a Peltier-cooler. The device should be tolerant to normal ambient temperature changes and the time delay for the Peltier-cooler to adjust to the optimum operating temperature.

For comparison the temperature sensitivity of the 5V double-pass modulator device is calculated using the transfer matrix model. In this case it is only the band-gap dependence on temperature that causes the modulation at the operating wavelength to change. The device modelled is the optimum 5V device shown in Figure 3.6 above and the operating wavelength is 1070.5nm where the maximum reflectivity change occurs. Modelling results show the modulation decreasing with changing temperature as expected. The device is less sensitive to negative temperature change due to the exciton shifting to shorter wavelengths and the reflectivity at the operating wavelength (1070.5nm) moving along the absorption tail of the exciton where the absorption changes more gradually as shown in Figure 3.6. This influence of the exciton absorption on the temperature sensitivity curve can also be seen in the 5V Fabry-Perot modulator curve although not as strongly. These results indicate that using an optical cavity at 5V operation does not make the modulator device more sensitive to temperature changes relative to the double-pass structure. In fact it improves the temperature sensitivity. For operation at 30% reflectivity change the sensitivity is dramatically improved from 7.5°C to 41°C. At $\Delta R = 20\%$ the predicted temperature range is 30°C for the 5V double-pass device. This value compares

well to the measured value of 27°C for InGaAs/AlGaAs MQWs in [13]. The predicted temperature range for the Fabry-Perot device is a factor of two greater at $\Delta R= 20\%$.

3.4.5 Optical saturation

The exciton absorption in these modulator devices is saturated or ‘bleached’ at high laser intensities. The principle physical sources of this ‘bleaching’ of the MQWs, which reduces the exciton oscillator strength, are band filling and renormalisation of the band gap [35]. Band filling arises from the Pauli exclusion principle. Carriers that are created in the quantum well will occupy the states at the bottom of the conduction band and the top of the valence band. The Pauli exclusion principle implies that these states are now no longer available for further optical transitions. Under conditions of high laser intensities this becomes continually the case. The exciton wavefunction is made up from these free particle states near the band edge (Chapter 2) and when these states become unavailable the result is a reduction in exciton oscillator strength. Band gap renormalisation is a renormalisation of the energy of the free particle states due to the presence of electrons and holes that are generated at high laser intensities. This results in a reduction of the band gap. Exciton formation is extremely difficult because of the excess number of free carriers and large local electric fields present. This results in a dramatic reduction in exciton absorption. In a normally ‘on’ Fabry-Perot device the above mechanism as well as other effects such as field screening due to charge build-up and thermal effects modify the reflectivity change achievable at various optical powers prior to the exciton saturation power [36]. We assume here that the limit of operation of the device is set by the occurrence of exciton saturation.

A saturation irradiance value of 80 kW/cm² for GaAs MQWs is used [37]. Thus for a current interconnect device area of 121µm² [19] the saturation limit is 100 mW. For the double pass modulator structure the saturation limit is halved to 50mW as the reflection from the back mirror effectively doubles the light intensity incident on the MQWs. When an optical cavity is used the light intensity also increases inside the MQWs, the higher the finesse of the cavity the higher the intensity of the light inside the cavity. The electric field intensity at any point inside the optical cavity is a sum of rays reflected from the front and back mirrors that interfere with each other. This produces a spatial variation in field amplitude inside the optical cavity. By summation of electric field amplitudes inside the cavity in the same manner as in equation 2.18 a useful formula for calculating the ratio of in cavity intensity to incident intensity can be obtained [38]. The terms used are all defined in section 2.11.

$$\frac{I_{Cavity}}{I_o} = \frac{1}{\alpha L_o} \frac{(1 - e^{-\alpha L_o})(1 + R_B e^{-\alpha L_o})}{(1 - \sqrt{R_F R_B} e^{-\alpha L_o})^2} \frac{(1 - R_F)}{1 + F \sin^2(\delta)} \quad (3.2)$$

This formula can thus be used to find the average increase in electric field intensity inside the optical cavity. This information can then be used to find the saturation limit of the modulator devices in Table 3.1. The transfer matrix model can also be used to calculate the increase in intensity inside the optical cavity and thus to investigate the reduction in the saturation limit due to the higher finesse cavities of the low voltage modulator structures. In the transfer matrix approach for calculating the reflectivity

from a multi-layer structure [39], the electric (\mathbf{E}) and magnetic field (\mathbf{B}) at interface ‘a’ is related to the electric and magnetic field at interface ‘b’ (see figure 3.21) by the following matrix

$$\begin{bmatrix} E_a \\ B_a \end{bmatrix} = \begin{bmatrix} \cos(\delta) & \frac{i \sin(\delta)}{\gamma_1} \\ i \gamma_1 \sin(\delta) & \cos(\delta) \end{bmatrix} \begin{bmatrix} E_b \\ B_b \end{bmatrix} \quad (3.3)$$

Where the phase difference is given by

$$\delta = \left(\frac{2\pi}{\lambda_o} \right) n_1 d \cos \theta \quad (3.4)$$

and

$$\gamma_1 = n_1 \cos \theta \quad (3.5)$$

n_1 being the refractive index and d the thickness of the layer, λ_o the free space wavelength of the incident light.

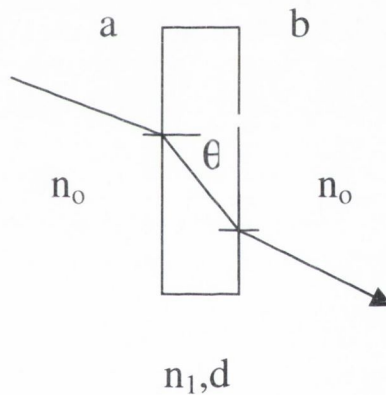


Figure 3.21: light incident at interface ‘a’, entering a layer of thickness t and refractive index n_1 .

It can easily be shown that $\mathbf{E}_b = \mathbf{E}_t$ and $\mathbf{B}_b = \gamma \mathbf{E}_t$, \mathbf{E}_t being the amplitude of the electric field transmitted at interface ‘b’. Letting $\mathbf{E}_t = 1$ allows the electric and magnetic field to be calculated at interface ‘a’. The fields can then be normalised by multiplying by the amplitude transmission coefficient ‘ t ’ at interface ‘b’, which can be calculated quite easily using the transfer matrix. To plot the fields through the entire layer, the layer of thickness t is divided into smaller thicknesses of the same refractive index and the above procedure repeated. Figure 3.22 shows the Electric field intensity calculated using the transfer matrix plotted through a 5V Fabry-Perot modulator device which was fabricated in this project (Chapter 4). The individual MQWs have been omitted here, and only the cavity region of the device plotted, for reasons of clarity. The figure clearly shows the expected exponential penetration into the metal gold mirror and the expected node/antinode at each interface of the $\lambda/4$ layer Bragg stack mirror. The MQW region is zoomed in on and shown in Figure 3.23. The lines of larger separation represent a

quantum well layer while the lines of shorter separation are barrier layers. The predicted positioning of the standing wave node/antinode in the MQW region using this approach can be tested by systematically placing the quantum wells at **either one** of these predicted node or antinode of the standing wave of the incident light. This is done using the transfer matrix and modelling results confirmed the absorption to be enhanced when the quantum wells were placed at the above predicted antinodes and suppressed when placed at a node. These small tests indicate that this method of calculating the electric field of the incident light inside the structure to be successful. We also found that the absolute value of the electric field value did not give the expected absolute value but the relative values through the device structure were changing in the expected manner. The data in Figure 3.22 tells us the electric field intensity value inside the optical cavity and relates to electric field intensity value incident on the device. This allows the relative increase in intensity inside the optical cavity to be calculated and the saturation limit of the MQWs also to be calculated. The electric field intensity is calculated for the device structures presented in Table 3.1 at each operating voltage using the transfer matrix method and also equation 3.2 above. The results were found to be comparable and the saturation limit for each operating voltage was then calculated. The results are presented in Table 3.2.

In the transfer matrix approach the above values are calculated by first calculating the electric field intensity for the double-pass modulator structure whose saturation limit is known to be half that of the bare MQWs. This is used as our reference point. The increase in intensity in the optical cavity is then calculated relative to the double-pass modulator device. The values obtained for the increase in cavity intensity relative to the incident intensity I_0 gave good agreement with Equation 3.2. The saturation limit at lower voltage operation was calculated for a device area of $60\mu\text{m}^2$, assuming the expected minimum spot size the light would be focussed to is half the device area. The results summarised in Table 3.2 decrease as expected. The saturation limit is predicted to be a factor of 22 lower than the double pass modulator device at 2V operation and a factor of 30 lower at 1V operation. Thus the optical power of the incident read beam would be required to decrease to 2.25 mW and 1.6mW respectively. The effect of these lower saturation limits are specific to each individual interconnect system. In the current SPOEC interconnect system the optical power incident on the 5V modulator devices is predicted to be 2.12 mW [30]. This value is smaller than the predicted saturation limit for the 2V device of 2.25mW above.

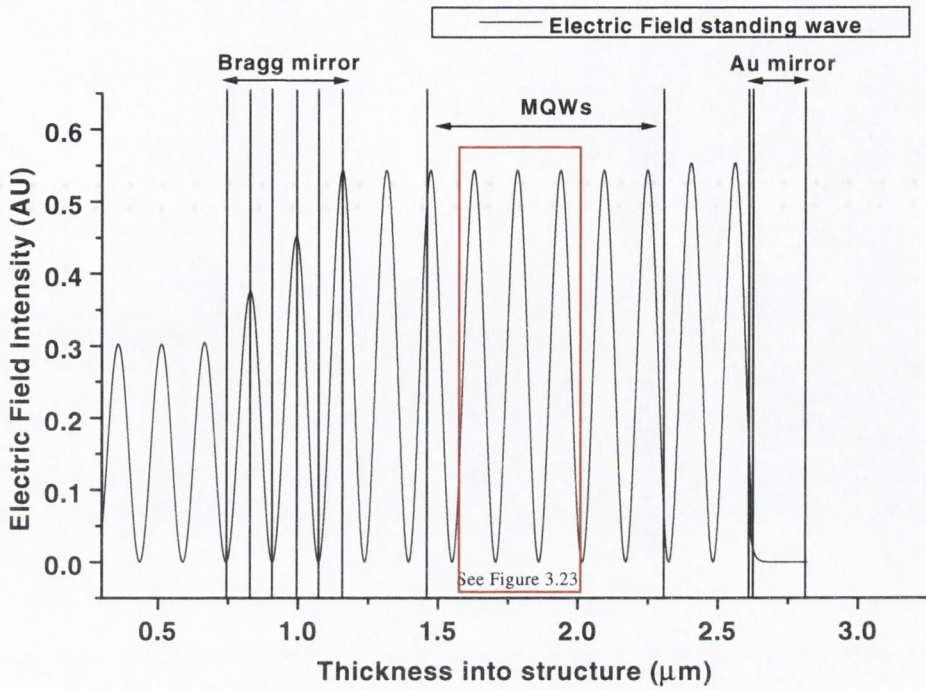


Figure 3.22: Electric field intensity calculated using the transfer matrix plotted through the 5V Fabry-Perot modulator device fabricated in this project (chapter 4).

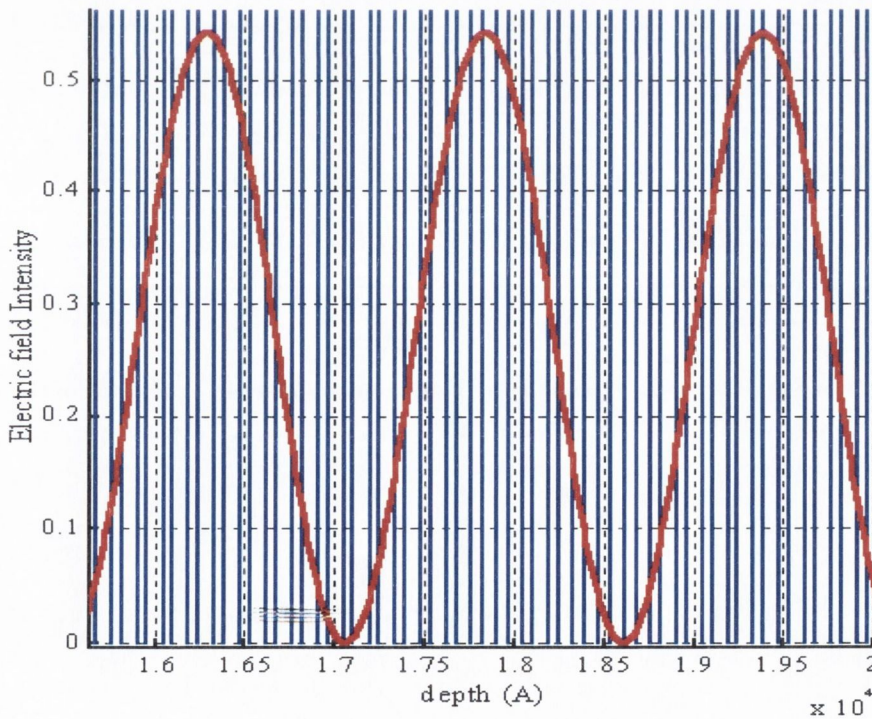


Figure 3.23: Electric field intensity zoomed in on part of the MQW section of the 5V device shown in figure 3.22 above. The solid lines of wider separation represent the InGaAs quantum well, narrower solid lines represent the AlGaAs barrier.

Voltage (and bias) V	Cavity Finesse	I_{Cavity}/I_0	Saturation Limit (mW)
5	5.4	7.6	6.5
3.3	9.3	13.2	3.75
2.5	13	19.2	2.65
2	15.4	22.2	2.25
1.8	15.4	22.6	2.2
1	21	30.8	1.6

Table 3.2: Details of the reduction in optical saturation power as the optical cavity finesse increases at low voltage operation for a spot size of $60\mu\text{m}^2$.

The Micro Electronics-Advanced Research Initiative (MEL-ARI) Opto-Electronic interconnect roadmap [19] summarises the expected changes to these devices in future interconnect systems. Modulator device area is predicted to reduce to $49\mu\text{m}^2$ for 1V operation. Assuming the expected minimum spot size the light would be focussed to is half the device area, this reduces the above saturation values in Table 3.2 by more than one half. Counteracting this change array sizes are also expected to increase to 128×128 from 64×64 , thus optical fan-out of the read-laser to these device is expected to reduced the incident power by a factor of four. This leaves Table 3.2 approximately unchanged. At this stage it would be useful to calculate a minimum value of required optical power incident on these modulator devices. In an interconnect system it is assumed that the modulated signals taken from the modulator devices would be coupled to an array of detectors. These detectors are most likely to be semiconductor-based detectors integrated to silicon electronics to convert the data into an electrical format. If MQW detectors are used similar to those in the SPOEC switching-chip, the optical power reaching these detectors is of critical importance to ensure sufficient photocurrent is available for the silicon receivers to operate correctly. An incident optical power of $8.6\mu\text{W}$ is currently believed to be a sufficient value to stay above this minimum value and to permit operation of the silicon drivers. This value is dependent on the photocurrent amplifier sensitivity and future design may allow even less optical incident power [40]. The optical power incident on the modulator devices is 2.12mW and when coupled to the detector at the output arm the optical power is predicted to drop to 0.3mW due to losses from the interconnect routing optics. If the minimum incident power on the detector is $8.6\mu\text{W}$ this allows the minimum incident power on the modulator itself to be $61\mu\text{W}$. Thus the incident read power must not be smaller than this value or larger than the values shown in Table 3.2. We conclude that the reduction in saturation limit shown in Table 3.2 should not have a major impact on the device operation even at low voltage operation. The incident optical power on the modulator devices can be reduced without infringing on the operation of the modulator device or the interconnect system.

3.4.6 Device speed

The factors that influence the modulation bandwidth of the Fabry-Perot *pin* detector can be divided into an intrinsic factor and an extrinsic factor. The intrinsic factor depends on the carrier dynamics of the material, particularly the exciton formation and dissociation time as well as the time taken to remove the electrons and holes from the quantum well. The external factor is the device RC time constant. The modulator case is quite different since the photogenerated carriers do not have to be collected in order for the device to function and the intrinsic factor is not a fundamental factor to the device speed. The speed of operation has been shown to be limited solely by its parasitic RC time constant [41] and device electrical bandwidths up to 37 GHz has been demonstrated. It is the RC time constant of the modulation bandwidth that is affected when the Fabry-Perot modulator structure is altered for lower voltage operation. The modulator device is a p-i-n diode and can be treated as a simple capacitor. Its total capacitance is normally made up of the intrinsic layer capacitance given by

$$C_{\text{intrinsic}} = \frac{\epsilon_s A}{d_s} \quad (3.6)$$

(where A is the device area and d_s is the thickness of the intrinsic region) and the bond-pad capacitance which is given by

$$C_{\text{bond}} = \frac{\epsilon_{\text{ox}} A_{\text{bond}}}{d_{\text{ox}}} \quad (3.7)$$

A_{bond} is the bond-pad area and d_{ox} is the thickness of the oxide layer between the contact pad and semiconductor surface. In the SPOEC interconnect the modulator devices are Flip-Chip bonded to analog silicon circuitry which are the drive electronics used to charge the modulator capacitance. Here it is the time taken to charge the modulator capacitance by the drive electronics that actually limits the speed of the modulator device. Modulation bandwidths limited by measurement equipment were measured up to 500Mbit/s for the MQW modulators used in the optical interconnect which are similar to those in the SPOEC system [21].

The modulator intrinsic capacitance is calculated using equation 3.5 for a decreasing number of intrinsic MQWs (well=8.8nm, barrier =5.54nm) and a dielectric constant value of 13 [34]. Figure 3.24 shows the resulting capacitance increase for the current SPOEC modulator device. The device intrinsic capacitance for the 5V double-pass structure that contains 95 MQWs is calculated to be 83 fF. The Fabry-Perot 5V structure has a capacitance of 131fF (56 MQWs). For operation at 2V whose structure contains 22 MQWs the capacitance has increase by over a factor of 4 to 353 fF. At 1V operation the increase is a factor of 8 to 638fF for the Fabry-Perot device. The predicted reduction in device area in future interconnect systems predicted by the interconnect roadmap [19] must also be considered here. The device capacitance is again calculated but at the predicted reduced device area. The resulting capacitance is shown in figure 3.25. A device area of $15\mu\text{m}^2$ is predicted to operate at 3.3V. The device capacitance is predicted here to be 47 fF for 39 MQWs. The device area of $7\mu\text{m}^2$ is predicted to operate at 1.0V and here the device capacitance is expected to be 33 fF. In both cases the

predicted capacitance is lower than the calculated capacitance of the current 5V double-pass modulator structure being used in the SPOEC system.

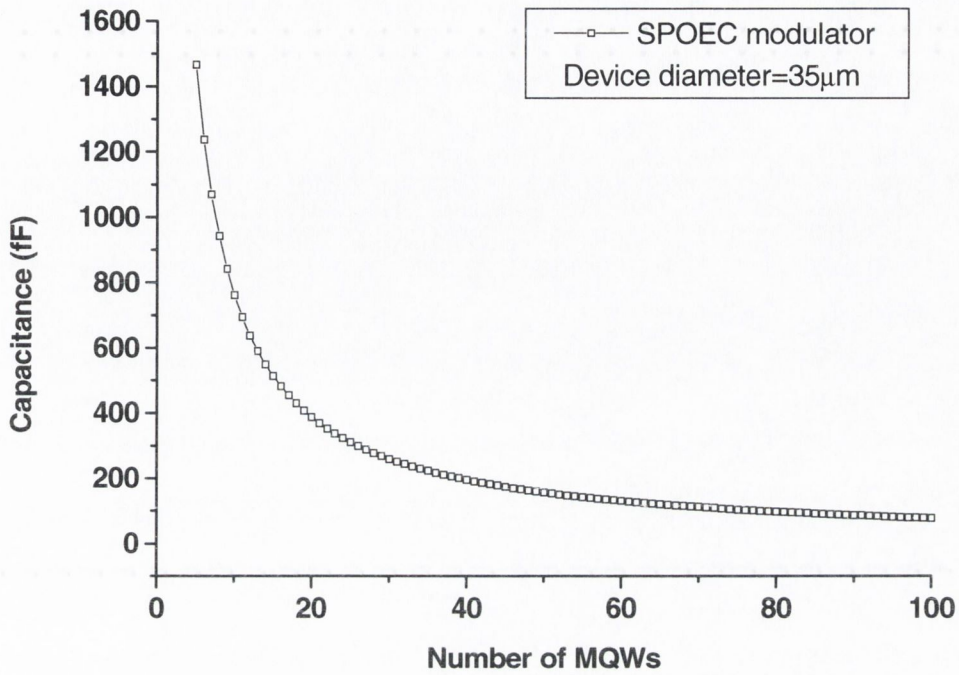


Figure 3.24: Resulting capacitance for the current SPOEC modulator device calculated using equation 3.5, for different number of MQWs.

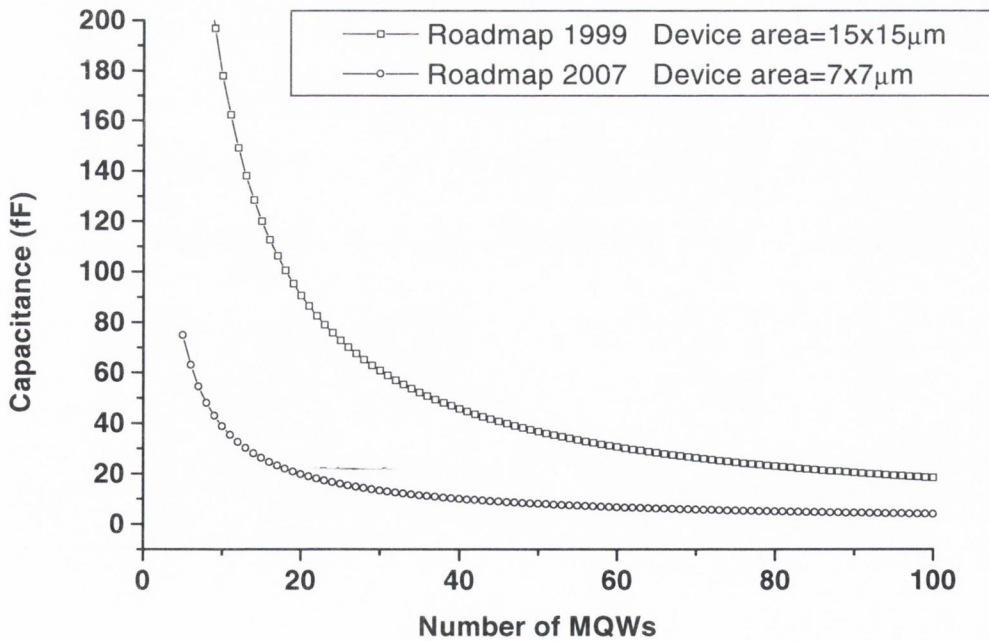


Figure 3.25: Device capacitance for a modulator structure calculated using equation 3.5, using the predicted future device area [19].

If the device area scales down in size according to the interconnect roadmap then the device capacitance is not expected to increase at lower voltage operation and the modulation bandwidth will not be affected. In the SPOEC system the diffractive optical element used to fan-out the 8x8 VCSEL array onto the 64x64-detector array was found to be one of the main factors after the lens spot-size that determined the device area. Changes in VCSEL emission wavelength across the array of $\Delta\lambda = 0.3\text{nm}$ resulted in the $20\mu\text{m}$ spot size moving by a maximum of $5\mu\text{m}$. The device diameter was chosen to be $35\mu\text{m}$ after allowing for other factors such as manufacturing tolerances. The important point here is that the modulator and detector devices are fabricated on the same wafer and thus if the device area cannot be reduced the capacitance of the detector scales according to Figure 3.24. To fully see the impact of this increase in capacitance the full device capacitance must be considered. The full device capacitance of the current double-pass modulator, including bonding and drive circuitry capacitance is estimated to be at least 10pF [42]. At 1V operation the 555fF increase in capacitance is only a 6% increase in the total capacitance. The capacitance seems likely to be dominated by the bond pad capacitance. Such a small percentage increase is not expected to impact on modulator bandwidth significantly.

3.5 Conclusions for device tolerance

In this section the consequent changes to various device parameters due to the device alteration for operation at lower voltage operation were investigated. The optical cavity effects on the device spectral bandwidth, angular tolerance and MBE growth tolerance were calculated using the transfer matrix model. Predicted results indicate that the optical cavity does not seriously impede any of these parameters. Devices still have tolerances that are within the limits required for use in a real interconnect system. The increase in optical power for this structure is not expected to limit device operation. The device temperature sensitivity is not expected to be increased to a detrimental level and the increased device capacitance is not expected to seriously impact on its electrical modulation speed.

3.6 Conclusions of chapter 3

In this chapter the main operating characteristics which shape the InGaAs Fabry-Perot modulator design for use in optical interconnects were investigated. The parameters that dictate the device structure are found to be the device reflectance change ($R_{\text{on}} - R_{\text{off}}$) and operating voltage V . Initial modelling of a double pass modulator structure showed why these structures have poor operation at lower voltage operation. Some simple analysis of a Fabry-Perot modulator indicating the optimum mode of operation and device structure was verified by thorough modelling using the developed transfer matrix model. Analysis of these modelling results showed the many factors that are considered by the model and the difficulty in trying to predict empirically the expected modulation and optimum device structure. Modelling results for this preferred cavity structure using an Au back mirror revealed

that there is an optimum electric field at a given voltage to be applied across the MQWs. The reduction in absorption at lower voltage operation is compensated by the optical cavity. Operation with a pre-bias voltage is chosen as modelling results are expected to be most accurate in this case. Modelling results predict that the modulation prerequisite of 30% or more is obtainable for operation at 5V, 3.3V and 2.5V. At lower voltage operation the modulation reduces considerably but may be of use in other applications. This is investigated fully in chapter 5 where results will show the failure of the optical cavity to compensate the reduced absorption, due to the low reflectivity of the back Au mirror. For a non-cavity double pass structure 30% reflectance change is only possible at 5V operation. Modulation at lower voltage operation is reduced dramatically. With modulation predicted to be possible at lower voltages, sensitivity to device tolerances and operation that are critical for implementation in an operational system showed positive results. For 5V and 3.3V operation, spectral bandwidth and angular acceptance are of very acceptable values for practical operation. MBE growth tolerances for 5V operation are good but are reduced somewhat for 3.3V operation but still good enough for the fabrication of large arrays. 2.5V operation is problematic due to zero spectral tolerance but possible maybe for other systems with more tolerant systems parameters. Initial modelling of Fabry-Perot structures using specifically an Au back mirror, potential operation and systems operation down to 3.3V is predicted to be possible.

In the following chapter experimental results are taken from devices based on the above modelling results to test and strengthen the developed transfer matrix model. This work revealed some interesting consequences of using Au mirrors in these devices. Following the insights gained in Chapter 4, in Chapter 5 further modelling exploring will be presented looking at the potential limits of operation of these devices.

3.7 References

[1] CUNNINGHAM JE, 'RECENT DEVELOPMENTS AND APPLICATIONS IN ELECTROABSORPTION SEMICONDUCTOR MODULATORS', MATERIALS SCIENCE & ENGINEERING R-REPORTS, 25: (5-6) 155-194 AUG 31 1999

[2] R.H. YAN, R.J. SIMES AND L.A. COLDREN, 'EXTREMELY LOW VOLTAGE FABRY-PEROT REFLECTION MODULATORS', IEEE PHOTONICS TECHNOLOGY LETTERS, 2: (2) 118-119 FEB 1990

[3] M.G. XU, T.A. FISHER, J.M. DELL, AND A. CLARK, 'WIDE OPTICAL BANDWIDTH ASYMMETRIC FABRY-PEROT REFLECTION MODULATOR USING THE QUANTUM CONFINED STARK EFFECT', JOURNAL OF APPLIED PHYSICS VOL.84 (10) 5761-5 NOV. 1998

[4] ZOUGANELI P, PARRY G, 'EVALUATION OF THE TOLERANCE OF ASYMMETRIC FABRY-PEROT MODULATORS WITH RESPECT TO REALISTIC OPERATING-CONDITIONS', IEEE JOURNAL OF QUANTUM ELECTRONICS, 31: (6) 1140-1151 JUN 1995

[5] ZOUGANELI P, STEVENS PJ, ATKINSON D, PARRY G, 'DESIGN TRADE-OFFS AND EVALUATION OF THE PERFORMANCE ATTAINABLE BY GAAS-AL_{0.3}GA_{0.7}AS ASYMMETRIC FABRY-PEROT MODULATORS', IEEE JOURNAL OF QUANTUM ELECTRONICS, 31: (5) 927-943 MAY 1995

- [6] GERBER DS, DROOPAD R, MARACAS GN, 'A GAAS/ALGAAS ASYMMETRIC FABRY-PEROT REFLECTION MODULATOR WITH VERY HIGH CONTRAST RATIO', IEEE PHOTONICS TECHNOLOGY LETTERS, 5: (1) 55-58 JAN 1993
- [7] LIN CH, MEESE JM, CHANG YC, 'A LOW-VOLTAGE, HIGH-REFLECTANCE-CHANGE NORMALLY OFF REFRACTIVE GAAS/AL_{0.2}GA_{0.8}AS MQW REFLECTION MODULATOR', IEEE JOURNAL OF QUANTUM ELECTRONICS, 30: (5) 1234-1240 MAY 1994
- [8] SEMICONDUCTOR INDUSTRY ASSOCIATION: THE NATIONAL TECHNOLOGY ROADMAP FOR SEMICONDUCTORS: TECHNOLOGY NEEDS', 1997 EDITION.
- [9] FRITZ IJ, HAMMONS BE, HOWARD AJ, BRENNAN TM, OLSEN JA, 'FABRY-PEROT REFLECTANCE MODULATOR FOR 1.3 MU-M FROM (INALGA)AS MATERIALS GROWN AT LOW-TEMPERATURE', APPLIED PHYSICS LETTERS, 62: (9) 919-921 MAR 1 1993
- [10] B.PEZESHKI, D. THOMAS AND J.S. HARRIS JR, 'LARGE REFLECTIVITY MODULATION USING INGAAS-GAAS', IEEE PHOTONICS TECHNOLOGY LETTERS, 2: (11) 807-809 NOV 1990
- [11] GOODWIN MJ, MOSELEY AJ, KEARLEY MQ, MORRIS RC, KIRKBY CJG, THOMPSON J, GOODFELLOW RC, BENNION I, 'OPTOELECTRONIC COMPONENT ARRAYS FOR OPTICAL INTERCONNECTION OF CIRCUITS AND SUBSYSTEMS', JOURNAL OF LIGHTWAVE TECHNOLOGY, 9: (12) 1639-1645 DEC 1991
- [12] LENTINE AL, GOOSSEN KW, WALKER JA, CHIROVSKY LMF, DASARO LA, HUI SP, TSENG BJ, LEIBENGUTH RE, CUNNINGHAM JE, JAN WY, KUO JM, DAHRINGER DW, KOSSIVES DP, BACON D, LIVESCU G, MORRISON RL, NOVOTNY RA, BUCHHOLZ DB, 'HIGH-SPEED OPTOELECTRONIC VLSI SWITCHING CHIP WITH >4000 OPTICAL I/O BASED ON FLIP-CHIP BONDING OF MQW MODULATORS AND DETECTORS TO SILICON CMOS', IEEE JOURNAL OF SELECTED TOPICS IN QUANTUM ELECTRONICS, 2: (1) 77-84 APR 1996
- [13] WILKINSON L.C., 'INDIUM GALLIUM ARSENIDE MULTIPLE QUANTUM WELL DEVICES FOR OPTICALLY INTERCONNECTED SMART PIXELS', PH.D THESIS, HERIOT WATT UNIVERSITY, UK, 1998
- [14] 'MICROCAVITIES AND PHOTONIC BANDGAPS: PHYSICS AND APPLICATIONS', P11-P32, J. RARITY AND C.WEISBUCH (EDS.), KLUWER ACADEMIC PUBLISHERS, NETHERLANDS, 1996
- [15] STOHR A, HUMBACH O, ZUMKLEY S, WINGEN G, DAVID G, JAGER D, BOLLIG B, LARKINS EC, RALSTON JD, 'INGAAS/GAAS MULTIPLE-QUANTUM-WELL MODULATORS AND SWITCHES', OPTICAL AND QUANTUM ELECTRONICS, 25: (12) S865-S883 DEC 1993
- [16] NEILSON DT, 'OPTIMISATION AND TOLERANCE ANALYSIS OF QCSE MODULATORS AND DETECTORS', IEEE JOURNAL OF QUANTUM ELECTRONICS, 33: (7) 1094-1103 JUL 1997
- [17] GOOSSEN KW, CUNNINGHAM JE, JAN WY, LEIBENGUTH R, 'ON THE OPERATIONAL AND MANUFACTURING TOLERANCES OF GAAS-ALAS MQW MODULATORS', IEEE JOURNAL OF QUANTUM ELECTRONICS, 34: (3) 431-438 MAR 1998
- [18] LIVESCU G, BOYD GD, MORGAN RA, CHIROVSKY LMF, FOX AM, LEIBENGUTH RE, ASOM MT, FOCHT MW, 'ROLE OF ELECTROREFRACTION IN QUANTUM-WELL FABRY-PEROT MODULATORS', APPLIED PHYSICS LETTERS, 60: (12) 1418-1420 MAR 23 1992
- [19] MEL-ARI TECHNOLOGY ROADMAP: OPTOELECTRONIC INTERCONNECTS FOR INTEGRATED CIRCUITS, EUROPEAN COMMISSION IST PROGRAMME: FUTURE AND EMERGING TECHNOLOGIES 2ND EDITION SEPT 1999

- [20] WHITEHEAD M, RIVERS A, PARRY G, ROBERTS JS, 'VERY LOW-VOLTAGE, NORMALLY-OFF ASYMMETRIC FABRY-PEROT REFLECTION MODULATOR', ELECTRONICS LETTERS, 26: (19) 1588-1590 SEP 13 1990
- [21] WALKER AC, GOODWILL DJ, RYVKIN BS, MCELHINNEY M, POTTIER F, VOGEL B, HOLLAND MC, STANLEY CR, 'THE SCOTTISH COLLABORATIVE INITIATIVE ON OPTOELECTRONIC SCIENCES (SCIOS) - DEVICES AND DEMONSTRATORS FOR FREE-SPACE DIGITAL OPTICAL-PROCESSING', OPTICAL COMPUTING, 139: 501-505 1995
- [22] PRIVATE COMMUNICATION WITH DR. STUART FANCY, PHYSICS DEPARTMENT, HERIOT-WATT UNIVERSITY, SCOTLAND, UK.
- [23] SJ FANCEY, MR TAGHIZADEH, GS BULLER, MPY DESMULLIEZ AND AC WALKER "OPTICAL COMPONENTS OF THE SMART-PIXEL OPTO-ELECTRONIC CONNECTION (SPOEC) PROJECT" JOURNAL OF THE EUROPEAN OPTICAL SOCIETY A - PURE AND APPLIED OPTICS 1(2) PP304-306, (1999)
- [24] FRITZ IJ, BRENNAN TM, HAMMONS BE, HOWARD AJ, WOROBAY W, VAWTER GA, MYERS DR, 'LOW-VOLTAGE VERTICAL-CAVITY TRANSMISSION MODULATOR FOR 1.06 MU-M', APPLIED PHYSICS LETTERS, 63: (4) 494-496 JUL 26 1993
- [25] LIN CH, GOOSSEN KW, SADRA K, MEESE JM, 'NORMALLY-ON GAAS/ALAS MULTIPLE-WELL FABRY-PEROT REFLECTION MODULATORS FOR LARGE 2-DIMENSIONAL ARRAYS', APPLIED PHYSICS LETTERS, 65: (10) 1242-1244 SEP 5 1994
- [26] J.F. KLEM, W.G. BREILAND, I.J. FRITZ, T.J. DRUMMOND, AND S.R. LEE, 'APPLICATION OF IN-SITU REFLECTANCE MONITORING TO MOLECULAR BEAM EPITAXY OF VERTICAL-CAVITY STRUCTURES', J.VAC.SCI.TECHNOL.B 1, 16: (3) 1498 - 1501 MAY/JUN 1998
- [27] FOBELETS K, KELLY B, HORAN P, HEGARTY J, 'CONTROLLED SHIFT OF THE OPTICAL RESONANCE OF FULLY PROCESSED ASYMMETRIC FABRY-PEROT MODULATOR ARRAYS', SEMICONDUCTOR SCIENCE AND TECHNOLOGY, 11: (4) 582-586 APR 1996
- [28] LAW KK, MERZ JL, COLDREN LA, 'EFFECT OF LAYER THICKNESS VARIATIONS ON THE PERFORMANCE OF ASYMMETRIC FABRY-PEROT REFLECTION MODULATORS', JOURNAL OF APPLIED PHYSICS, 72: (3) 855-860 AUG 1 1992
- [29] PRIVATE COMMUNICATION WITH DR. ADAM BOYD, DEPARTMENT OF ELECTRONIC AND ELECTRICAL ENGINEERING, UNIVERSITY OF GLASGOW, SCOTLAND, UK.
- [30] A.C. WALKER, M.P.Y. DESMULLIEZ, M.G. FORBES, S.J. FANCEY, G.S. BULLER, M.R. TAGHIZADEH, J.A.B. DINES, C.R. STANLEY, G. PENNELLI, A.R. BOYD, P. HORAN, D. BYRNE, J. HEGARTY, S. EITEL, H.-P. GAUGGEL, K.-H. GULDEN, A. GAUTHIER, P. BENABES, J.L. GUTZWILLER, AND M. GOETZ, 'DESIGN AND CONSTRUCTION OF AN OPTOELECTRONIC CROSSBAR SWITCH CONTAINING A TERABIT/S FREE-SPACE OPTICAL INTERCONNECT' IEEE J. SELECTED TOPICS IN QUANT. ELECTRON. SPECIAL ISSUE ON SMART PHOTONIC COMPONENTS, INTERCONNECTS AND PROCESSING, VOL. 5, NO. 2, PP 236-249 (1999)
- [31] R.H. YAN AND L.A. COLDREN, 'EFFECT OF TEMPERATURE ON THE OPERATING CHARACTERISTICS OF ASYMMETRIC FABRY-PEROT REFLECTION MODULATORS', APPLIED PHYSICS LETTERS, 57: (3) 267-269 16 JULY 1990
- [32] ZOUGANELI P, WHITEHEAD M, STEVENS PJ, RIVERS A, PARRY G, 'TEMPERATURE SENSITIVITY OF ASYMMETRIC FABRY-PEROT MODULATORS', ELECTRONICS LETTERS, 26: (17) 1384-1386 AUG 1990

- [33] J.S. BLAKEMORE , 'SEMICONDUCTOR AND OTHER MAJOR PROPERTIES OF GALIUM ARSENIDE' JOURNAL OF APPLIED PHYSICS, VOL. 53 R123-181 1982
- [34] 'PROPERTIES OF LATTICE MATCHED AND STRAINED INDIUM GALLIUM ARSENIDE' EDITED BY PALLAB BHATTACHARYA, INSPEC EMIS DATAREVIEW SERIES NO.8, THE INSTITUTION OF ELECTRICAL ENGINEERS, LONDON, 1993
- [35] S.SCHMITT-RINK, D.S. CHEMLA AND D.A.B. MILLER. 'LINEAR AND NON LINEAR OPTICAL PROPERTIES OF SEMICONDUCTOR QUANTUM WELLS' ADVANC. PHYS. 38 (1989)
- [36] MOTTAHEDEH R, PARRY G, WHITEHEAD M, ROBERTS JS, BUTTON CC, 'HIGH-POWER PERFORMANCE OF ASYMMETRIC FABRY-PEROT MQW MODULATORS', IEEE PHOTONICS TECHNOLOGY LETTERS, 6: (6) 703-705 JUN 1994
- [37] GOOSSEN KW, CUNNINGHAM JE, JAN WY, 'GAAS 850-NM MODULATORS SOLDER-BONDED TO SILICON', IEEE PHOTONICS TECHNOLOGY LETTERS, 5: (7) 776-778 JUL 1993
- [38] YOKOYAMA H, 'A SIMPLIFIED ANALYSIS OF THE OPTICAL BISTABILITY OF MULTIPLE QUANTUM WELL ETALONS' , IEEE JOURNAL OF QUANTUM ELECTRONICS, 25: (3) 1190-1195 1989
- [39] 'THIN FILM OPTICAL FILTERS', MACLEOD HA, ADAM HILGER LTD, BRISTOL, 1986
- [40] FORBES MG, 'ELECTRONIC DESIGN ISSUES IN HIGH-BANDWIDTH PARALLEL OPTICAL INTERFACES TO VLSI CIRCUITS', PH.D THESIS, HERIOT WATT UNIVERSITY, UK, MARCH 1999
- [41] C.C. BARRON, C.J. MAHON, B.J. THIBEALT, G. WANG, W. JIANG, L.A. COLDREN, MILLIMETER-WAVE ASYMMETRIC FABRY-PEROT MODULATORS, IEEE JOURNAL OF QUANTUM ELECTRONICS, 31: (8) 1484-1493 AUG 1995
- [42] PRIVATE COMMUNICATION WITH DR. MARK FORBES, PHYSICS DEPARTMENT, HERIOT-WATT UNIVERSITY, SCOTLAND, UK.

Chapter 4: Modulator measurements for 5V operation

4.1 Introduction

In this chapter measurements from modulator devices fabricated by molecular beam epitaxial growth are presented. The device structure is fabricated based on theoretical modelling using the transfer matrix model for operation at 5V as presented in Chapter 3 previously. Two types of structures are grown, one with an optical cavity and the other a double-pass structure (single back mirror). Experimental reflectivity measurements are taken from these structures for comparison with modelling predictions to examine the accuracy of the model and to develop it further. Problems encountered with gold-semiconductor interfaces during this work lead to some additional work looking more closely at the electrical, optical and adhesive properties of this interface for various gold deposition methods. Experimental results from these interfaces are presented. The methods used to model such an interface as well as their impact on modulator performance are discussed.

4.2 Device structure

In Chapter 3 transfer matrix modelling results for 5V operation predicted improved device performance for a Fabry-Perot modulator structure relative to a double pass modulator device. The modelled device tolerances such as the angular acceptance and spectral bandwidth indicated that practical operation in an optical interconnect architecture is possible. Good MBE growth tolerances also allows the growth of large arrays (see Chapter 3). A device structure with 59 MQWs, a gold back mirror and a 16% front mirror was chosen. Although this is not the structure which will give the maximum reflectance change of 46% when the front mirror reflectivity is 34% (Table 3.1), a 16% front mirror reflectivity will theoretically give a large modulation of 42% but also better growth tolerances due to its lower finesse (Section 3.4.3). The device schematics shown in Figure 4.1(a) and (b) were grown by molecular beam epitaxial growth on wafers B813 and B814 respectively. These labels refer to the University of Glasgow categorising scheme.

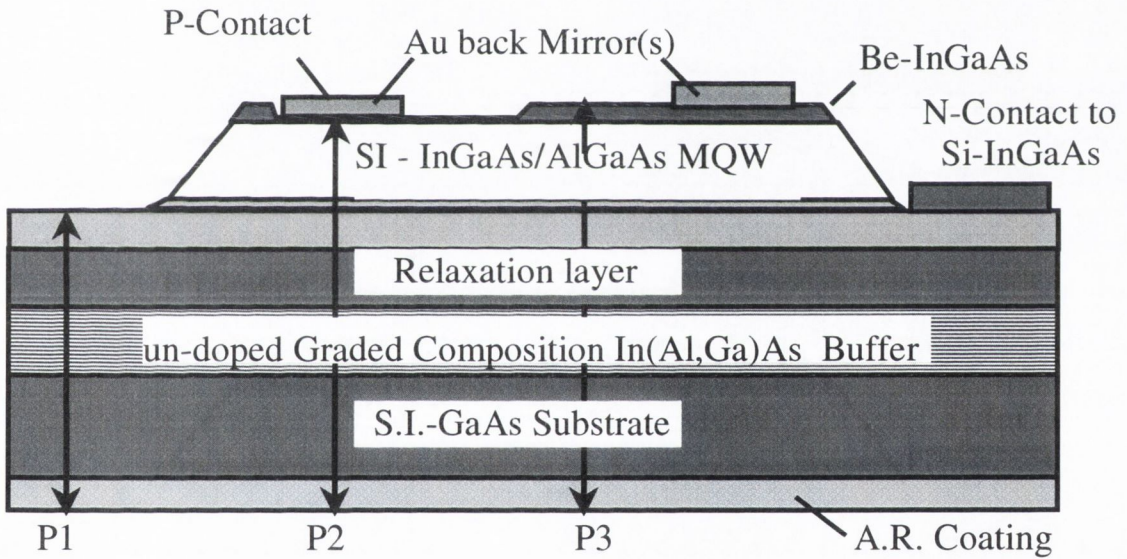


Figure 4.1(a): Double pass 5V modulator structure (wafer B813).

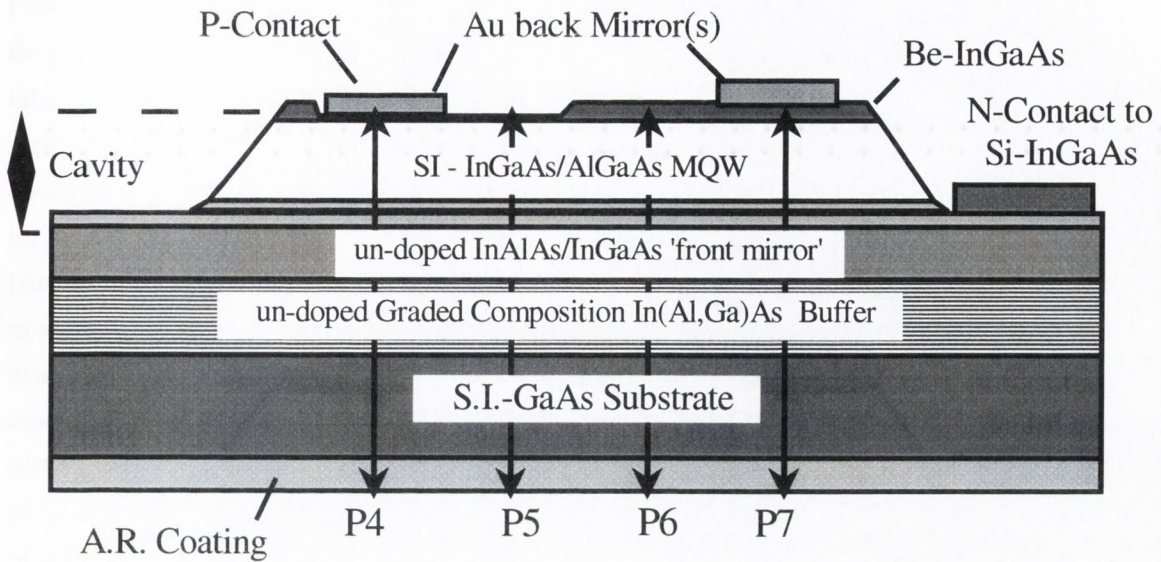


Figure 4.1(b): Fabry Perot 5V modulator structure (wafer B814).

The two structures are identical except that the first structure on wafer B813 does not have a front Bragg mirror and thus is a double-pass modulator structure, light enters through the anti-reflection coating reflects off the back mirror and exits (see position P2). The optical cavity is clearly shown in Figure 4(b). There are two optical cavities possible, one formed by the front Bragg mirror and the Au back mirror (P4 & P7) and the other by the front Bragg and the back mirror formed by the Be doped InGaAs-air interface which has a reflectivity of $\approx 31\%$ (P5 & P6). Devices were processed having windows of $50\mu\text{m}^2$ for both of these optical cavities so measurement from both cavities could be possible. Wet etching has been used to remove a small amount of the p+ InGaAs cap layer in selected areas (P4 & P5). This will allow two cavities with slightly different optical thicknesses to be evaluated.

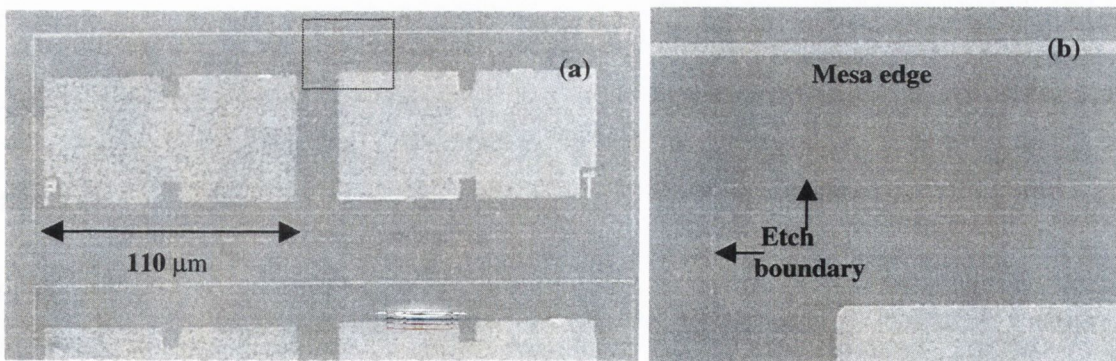


Figure 4.2(a): SEM of mesa plateaux with different metallisations; sputtered gold (denoted by 'P' and evaporated gold (denoted by 'T'). The area defined by the dashed rectangle is shown in greater detail in (b).

Figure 4.2 shows a SEM image of wafer B814 whose schematic is shown in Figure 4.1(b). In this part of the processed wafer there are four gold back mirror pads ($50 \times 50 \mu\text{m}$) whereas only two are shown in the schematic. The shallow etch boundary of the P+ Be doped InGaAs layer is shown in Figure 4.2(b). Also highlighted is the mesa edge where the P+ layer and the MQWs are etched away forming a sloping sidewall down to the N+ layer. The device processing steps are summarised in Appendix A of this thesis. The reason for using two different deposition types of gold for the back mirror will be dealt with later in this chapter. Useful measurements can also be taken from these two interfaces for B813 double pass structure (P2 & P3) as well as the air-n+ semiconductor interface (P1) as indicated in Figure 4.1(a). The primary purpose of these measurements is to test the accuracy of the transfer matrix model predictions and to strengthen its input parameters such as the semiconductor refractive indices where possible. The double-pass structure B813 will act as a benchmark against which any improvements in performance resulting from the inclusion of the Fabry-Perot in B814 can be gauged. The measurements indicated above should maximise the amount of information that can be obtained from these wafers. Of course successful of course these devices could also be used in the interconnect system.

4.3 Reflectivity measurements

Direct measurements of the thickness of the optical layers grown and of the layer refractive indices is possible but difficult. The modulator device can be cleaved and an electron microscope could be used to measure the thickness of each layer. The refractive indices can be measured using ellipsometry. Knowing these values precisely would of course allow the reflectivity and positions of the Fabry-Perot resonances to be calculated. By Anti-reflection coating the as-grown wafer on both sides the MQW absorption could also be assessed. The reflectivity change can be found by measuring directly the optical power reflected at the on and off device states. These different measurement methods are difficult, expensive and can take a long time to complete. The approach taken here is to combine reflectivity measurements at a broad wavelength range from various parts of the device mesa shown in Figure 4.1 above; and using this gathered information with the transfer matrix model, a more complete picture of the optical characteristics of the device can be produced.

4.3.1 Reflectometry as a diagnostic tool

Reflectance measurements are used to explore the differences between model predictions and grown structures. Initial measurements are taken from areas on the device mesa such as P1 & P3, which provides real information for our model allowing the material refractive indices values to be fine-tuned to more realistic values. Measurements are also taken to find the refractive index contrast (Δn) and thus the reflectivity of the front Bragg mirror on wafer B814 from positions P5 & P6. When this information is obtained the model parameters are strengthened and the model predictions for the Fabry-Perot device can

then be compared to measurements taken from these devices at positions P4 & P7. The measured reflectance spectrum will contain features resulting mainly from the exciton absorption and Fabry-Perot resonances. These resonances will be very nearly equally spaced in the spectral range of interest. At wavelengths below the hh exciton peak absorption features will dominate the spectrum. At longer wavelengths the Fabry-Perot resonances are less influenced by the exciton absorption which reduces exponentially at longer wavelengths. Here reflectance values at resonance become dependent only on the front and back mirror reflectivities. If one of the mirror reflectivities is known the other can easily be found. This is the case for measurements taken from the cavity formed by the air-InGaAs semiconductor interface on wafer B814 (P5 & P6), its reflectivity is known (as the refractive index of the InGaAs layer is known to reasonable accuracy) so the reflectivity of the front Bragg stack can be found. The number of Bragg mirror periods grown is known so the mirror reflectivity is adjusted in the model by changing the refractive index period difference/contrast (Δn) of the mirror. This is done until a satisfactory fit to the measured data is obtained. The starting point is of course the originally calculated device structure. The Fabry-Perot resonance is placed at the required operating wavelength by adjusting the thickness of the P+ layer essentially a spacer layer in the optical cavity. The mirror reflectivities are then found and set as an independent variable in our model from then on.

If the zero bias hh exciton is grown to the wrong wavelength but not too far (within $\approx 20\text{nm}$) from the measured absorption spectrum used in the model, the absorption spectrum is shifted in wavelength to the measured wavelength. It is assumed that this is done physically by changing the MQW layer compositions and that the same electric field spectrum is attainable. The choice of zero bias hh exciton wavelength is important, as once it is set, it will be the reference point from which reflectivity predictions are made at larger voltages. The zero bias value is chosen to avoid electro-refraction whose effects could result in the exciton position wavelength being slightly wrong. The modified MQW refractive index spectrum at 0V [1] may also produce an uncertainty in the true exciton wavelength. These uncertainties can occur due to the Fabry-Perot resonance being close in wavelength to the exciton causing the reflectivity spectrum to be convoluted and leading to a false choice of exciton wavelength. However, this should not be a major problem with optimum operation at a wavelength separation of 23nm. The MQW region is then set as an independent variable in our model. Now that our modelling parameters are optimised the measured reflectivity at different applied voltages can then be compared to the model predictions at these operating voltages allowing the accuracy of the transfer matrix model to be tested.

4.3.2 Measurement system

The reflectometer measurement system used in this work which is fundamentally a Michelson interferometer is outlined in Figure 4.3.

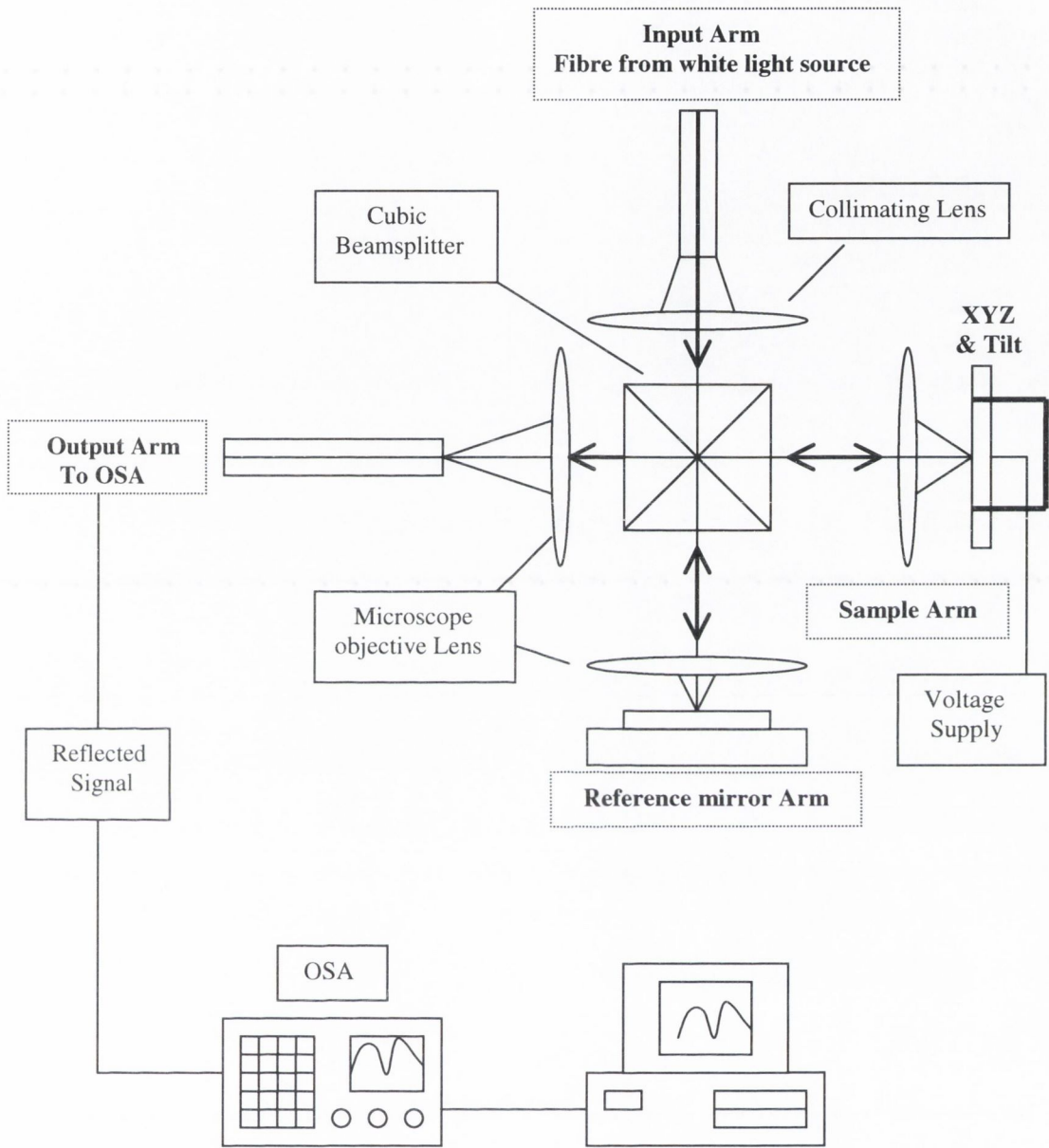


Figure 4.3: Reflectometer measurement system

The light source used is a 100W OSRAM tungsten-halogen lamp that is focused into a 50 μ m core diameter silica fibre. This fibre is then the input to the reflectometer. The light exiting this fibre is collimated in free space using a x10 microscope objective with a focal length of 8.3mm and a matching numerical aperture. A cubic beamsplitter, which is essentially two combined prisms, is used to split the collimated beam into two arms at 90° to each other, a reference arm and the sample arm. To calculate the absolute reflectivity an optical power spectrum is taken from a reference mirror with a known reflectivity (a Newport protected silver metal mirror ER.2 which has a relatively flat reflectivity of 97.5% over the wavelength range of

interest) while light reflected in the sample arm is blocked out. A spectrum is then taken from the sample arm while the reference arm reflection is blocked out and is normalised by the reference measurement to give the absolute reflectivity value. Both arms contain a x20 microscope objective with a focal length of 14.8mm to focus the light to a theoretical spot size of $28\mu\text{m}$ ($8.3/14.8 \times 50\mu\text{m}$). Using identical lenses in both arms ensures both arms suffer the same losses.

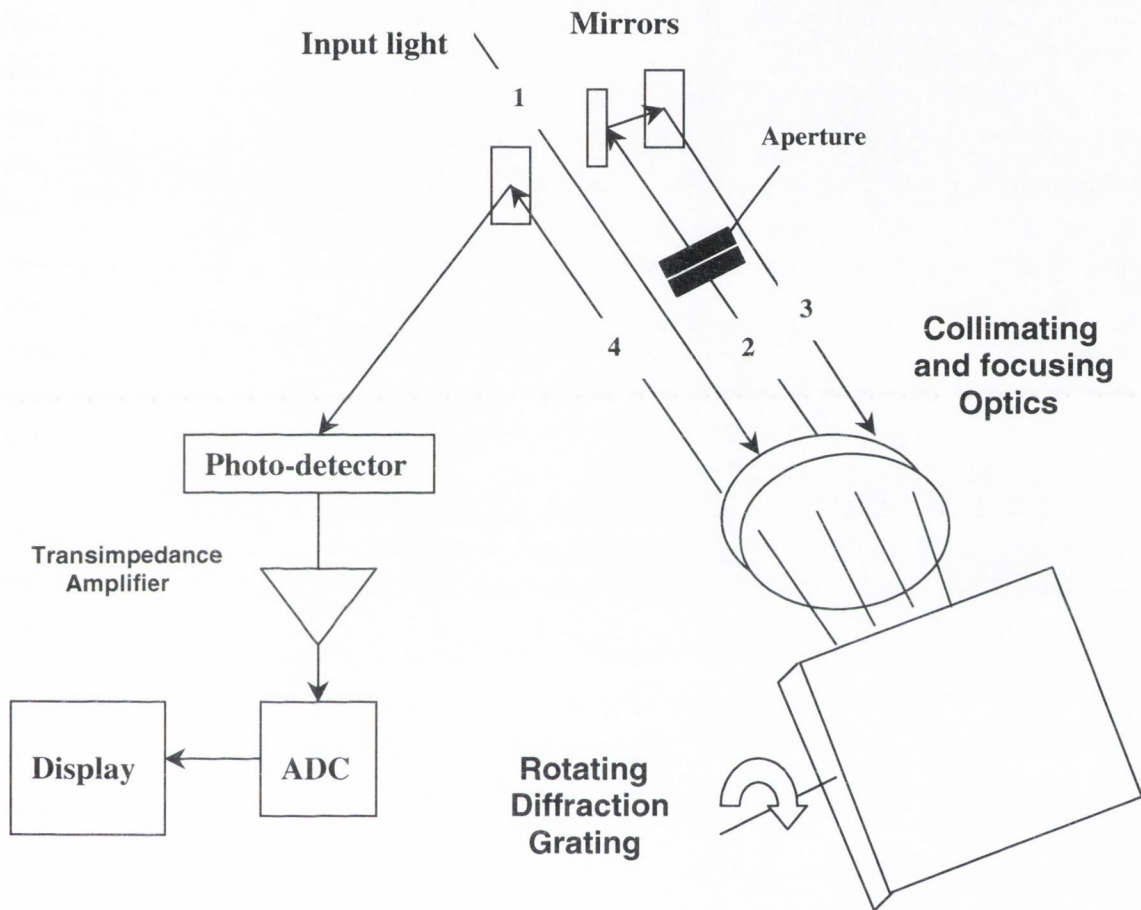


Figure 4.4: Diagram showing the basic layout of the Hewlett Packard HP 71450 optical spectrum analyser. The above diagram and all quoted data are taken from the HP 71450 instrument reference book.

Prior to reflectivity measurements being taken identical reference mirrors are placed in both arms and an optical power spectrum is measured in each arm. This allows the unequal splitting by the beamsplitter to be calculated and is taken into account when the final absolute reflectivity is calculated. The optical power is typically a few nano-Watts in each arm, small enough to prevent intensity dependent optical nonlinearities or optical power saturation of the exciton absorption.

The optical spectrum and power is measured using a Hewlett Packard HP 71450 optical spectrum analyser (OSA). This device is essentially a double-pass monochromator and a basic block diagram is shown in Figure 4.4. The input light is first collimated by the optical element and dispersed by the diffraction grating according to $m\lambda = d\sin\theta$ where d is the grating spacing, m the diffraction order and θ the incident angle. This results in a spatial distribution of the light based on wavelength. The diffraction grating is positioned such that the desired wavelength λ passes through the aperture. The width of this aperture determines the bandwidth of the wavelengths allowed to pass through to the detector. Various apertures are available allowing various resolution bandwidths between 0.08nm and 10nm to be achieved. Following the monochromator is the photo-detector, which acts as a power detector converting the optical power to an electrical current. This is converted to a voltage using a transimpedance amplifier and digital signal processing converts the signal to a digital format where it can be displayed and manipulated. The device operating range is from 600nm to 1700nm with an absolute wavelength accuracy of ± 0.5 nm. As mentioned above the device FWHM wavelength resolution ranges from 0.08nm to 10nm, in this work measurements were taken at a resolution of 1nm. This OSA can detect pico-Watts of power so our measurements have a good signal to noise ratio but the background signal is measured and accounted for in the absolute reflectivity calculation.

The optical power output from the white light source is very stable and the short coherence length of this source means that interference effects in the measured signal due to reflections from different optical surfaces in the measurement system are avoided. The input to the optical spectrum analyser is by 62.5 μ m core diameter silica fibre, thus the reflected signals from the sample or reference mirror are finally focussed down into this fibre by a x10 microscope objective. If a He-Ne laser is used, an interference pattern formed by the reflection in each arm can be observed on a screen placed just before this final lens. This is a useful alignment tool ensuring both collimated beams overlap precisely before being focussed into the collection fibre. This also ensures that light is incident normally on the sample being measured. The particular device that is selected for measurement is initially aligned by forward biasing the device. Light emission is collected and collimated by the lens in the sample arm and enters the OSA. The sample is moved using its XYZ translator until the signal received by the OSA is maximised. Finer adjustments are then made using the observed device reflection spectra displayed by the OSA and to the tilt of the device using the interference pattern mentioned above. The devices are addressed optically and electrically from opposite sides. This is achieved by mounting the processed devices in a plate with a window for optical access and electrical contact is made using individual needle probes from the other side of the plate. The plate is then mounted on the translational stage, which has 3-dimensional movement and tilt adjustment.

Other light sources were also explored such as an Oriel 75W Xenon arc lamp and a GEC-Marconi LED whose output was centred at 1050nm. The Oriel Xenon arc lamp had many sharp emission peaks in the wavelength region of interest and thus the OSRAM tungsten-halogen lamp, which gave a relatively flat spectrum, was preferred. Measurements were also taken using the LED source having a FWHM of 50nm. These measurements are a useful comparison to the tungsten-halogen lamp as it allows a check of the

second order contribution of the diffraction grating to the measured data. Due to the broad emission of the tungsten-halogen lamp at shorter wavelengths these wavelengths can appear in the wavelength range of interest (1000-1100nm) due to the second order effect of the diffraction grating. Because the LED does not have any emission in the 500-550nm range, measurements taken using this source do not suffer from this second order effect. Almost identical results were obtained in both cases indicating that the second order contribution to be negligible. Of course an optical filter can also be used but this would reduce the already small optical power of the white light source further. For a broader spectrum range the tungsten-halogen lamp is preferable to the LED source.

4.3.3 Experimental error

There are a number of sources of experimental error in the reflectivity measurements. These errors include errors in the wavelength measurement by the OSA due to a possible miscalibration, and errors in the reference mirror reflectivity quoted by Newport. These errors are small with wavelength accuracy being quoted to $\pm 0.5\text{nm}$ when the device is calibrated using the device internal calibration system, and mirror reflectivity quoted as $\pm 0.5\%$. We have found the main source of error to come from chromatic dispersion in the microscope objective lens, which is used to focus the light onto the reference mirror and wafer sample. Microscope objective lenses are normally designed to counteract chromatic aberration in the visible spectrum. They consist of multiple refracting elements of opposite refracting power, convex and concave lenses of different glasses can be used, all cemented together to form a compound lens that has a net focal length but a reduced dispersion over a certain portion of the visible spectrum [2]. The wavelengths of interest in our measurements are in the near infrared, this spectral region is on the outer edge of the visible spectrum where the chromatic dispersion in these lenses is not corrected and becomes stronger at these and longer wavelengths. This is illustrated by measurements taken using different lenses placed only in the reference arm of the reflectometer in Figure 4.3. The light from the white light source is focussed onto the mirror of a constant reflectivity value over the wavelengths of interest, and a wavelength of $1.060\mu\text{m}$ is brought into focus i.e. the optical power value at this wavelength is maximised. The lens distance from the mirror is controlled by an XY translator, which is manually adjusted until the chosen wavelength is brought into focus. The resulting measurements are shown in Figure 4.5. As a comparison the white light spectrum is also shown measured directly by the OSA, not passing through the reflectometer lens. The white light spectrum measured directly is relatively 'flat' so the 'shaping' of the white light spectrum due to chromatic dispersion in the lenses can clearly be seen in figure 4.5. In the OSA arm there is also of course a final lens that focuses the light into the fiberised input of the OSA arm. This lens is common in all cases so differences between the lenses in the reference arm can still be observed.

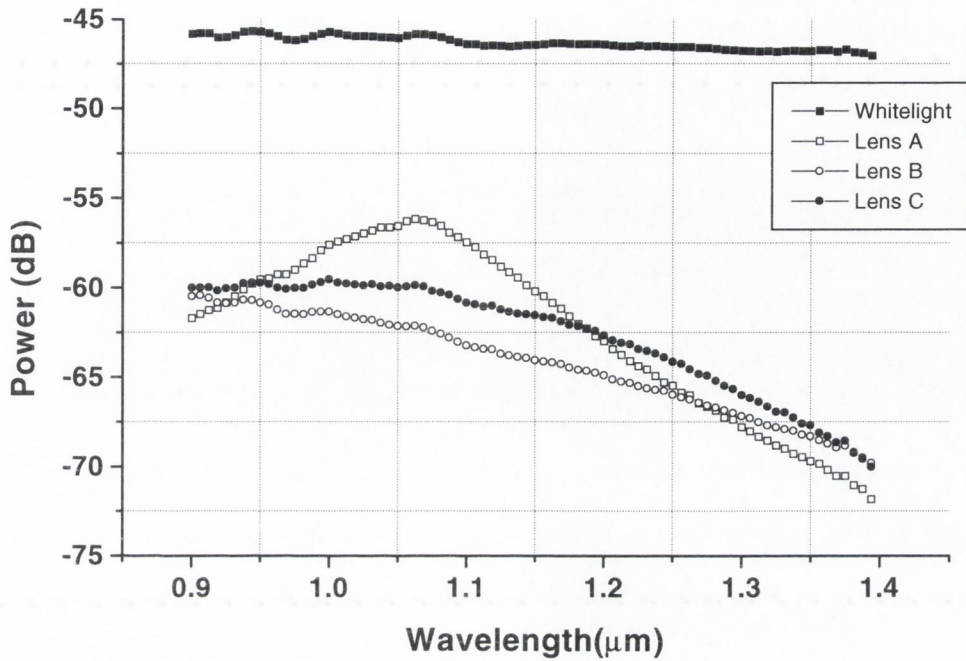


Figure 4.5: Spectral measurements taken from different lenses placed in the reference arm of the reflectometer. The relatively ‘flat’ white light spectrum is shown as a reference.

Lens A is an Elliot Scientific C110TM-B with a design wavelength of 780nm and a focal length of 6.24mm. At wavelengths either side of 1060nm there is a steep slope indicating strong aberration which is possibly due to chromatic dispersion and/or spherical aberration. Lens B is a x20 Leitz Wetzlar microscope objective taken from a Leitz Wetzlar optical microscope and C is a Newport M-20X x20 microscope objective with a focal length of 8.3mm. Both show a more flat wavelength response relative to lens A but at longer wavelengths it gets progressively worse. Lens C has a slightly lesser slope to B and is thus used in the reflectometer measurement system.

The problem with such aberrations when the wavelength response is not flat is that it makes measuring absolute reflectivity values more difficult. For example if a spectrum is taken from the reference mirror in the reference arm focused to 1060nm, and then a spectrum is taken from the same reference mirror placed in the sample arm. Ideally the same signal should have been measured in both arms and the absolute reflectivity should be a constant flat value and the calculated absolute reflectivity should be equal to the reference mirror reflectivity value, 97.5% at all wavelengths. But a difficulty arises in bringing a particular wavelength into focus, the optical power at this wavelength is maximised but it tends to act like a ‘saddle’ point. As the lens is moved slightly closer and further away the optical power at this wavelength has a maximum value and keeps a constant value while the optical powers at wavelengths above and below are still changing, oscillating about this point. Thus if the lens in the sample arm is not focussed/positioned

at 1060nm identically to the reference arm then the curve seen in Figure 4.5 changes. This normally results in wavelengths on one side of the focal wavelength having less optical power and the other having more and the resulting absolute reflectivity having a lower value and a higher value respectively. (Of course the opposite can also be true). This error due to chromatic dispersion in the lens was found to be the principal source of error in our measurements. The purchase of an alternative lens designed for operation in near-infra red was considered but not carried out due to the large expense of these specialised lenses. Thus much care was taken to minimise this error experimentally, but it is extremely difficult to eliminate. To measure this error the reflectometer was used to take a spectrum from the reference mirror in the reference arm and from an identical reference mirror in the sample arm as mentioned above. In the sample arm the lens was focused to the identical wavelength as the reference arm at 1080nm and it was ensured that all wavelengths had equal optical powers in each arm. This is done using software to divide the spectra in real time and when both arms are focused identically a perfectly flat spectral response is obtained.

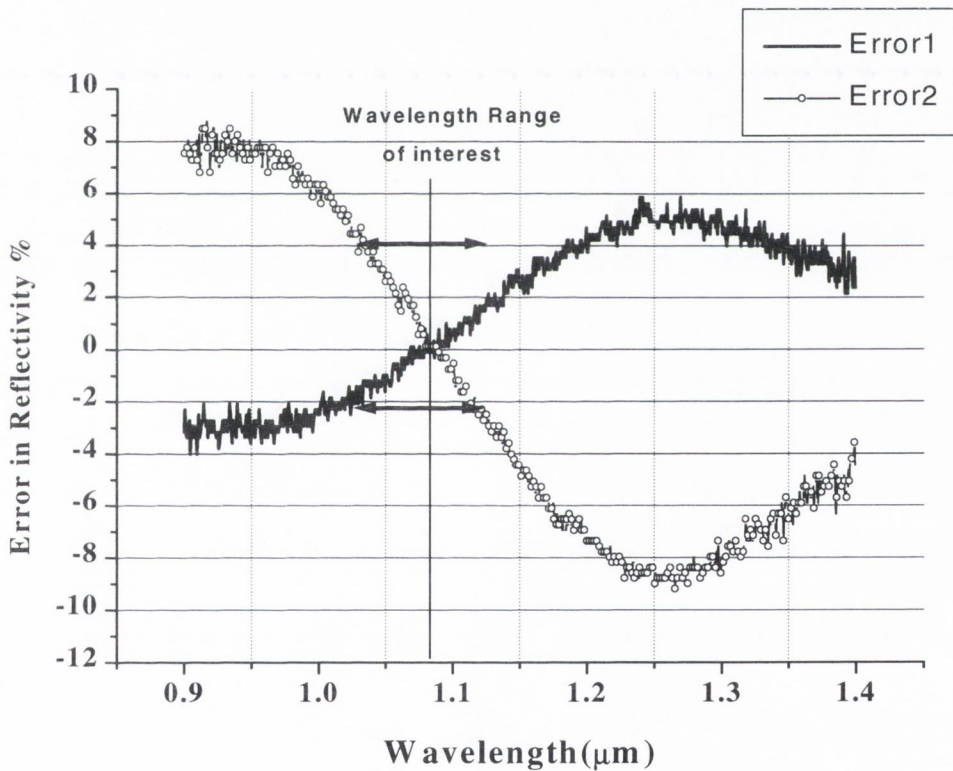


Figure 4.6: Measured experimental error for the reflectometer measurement system.

The sample lens is then moved slightly **away** (error 1), and **towards** (error 2) the mirror by an amount depicting the accuracy believed to be possible under experimental conditions i.e. it is believed that the lens can be experimentally brought to position/focus between these two limits. The difference between these two spectra and the ideal perfectly flat spectrum can then be plotted as an experimental error and is shown

in Figure 4.6. The increased and decreased error around the focal wavelength (1080nm) is clear as expected from above. Around the modulator wavelength range of interest, 1030 to 1130nm, the experimental error is of an acceptable value. At 1030nm the error is -1.9% to $+4\%$ an average of $\pm 3\%$ and at 1130nm it is -3% to $+2\%$, an average of $\pm 2.5\%$. At longer and shorter wavelength, either side of this window, experimental error increases rapidly. It is assumed that the two arms when a measurement is being taken can be focussed to within this predicted error and these are the largest errors that any absolute reflectivity measurement will have due to chromatic dispersion in the lenses within this wavelength range of interest. The presentation of reflectivity results from wafers B813 and B814 will not show the experimental error for reasons of clarity to keep the presentation of data comprehensible.

4.4 Measured results

The electrical properties of these *pin* diodes measured at the University of Glasgow are first summarised and then reflectivity measurements taken from wafers B813 and B814 at prime positions indicated previously in figure 4.1 are presented. Figure 4.7 shows the grown device layer structure with details of the intended growth thicknesses and refractive indices at the operating wavelength as used in the transfer matrix model. As well as giving detailed layer growth information this data is useful when analysing the reflectivity data from various parts of device structures on wafers B813 and B814.

4x 2.5nm $\text{In}_{0.135}\text{Ga}_{0.865}\text{As}$ /Be δ -doping= $1 \times 10^{13}\text{cm}^{-2}$	3.43
275.85nm $\text{In}_{0.135}\text{Ga}_{0.865}\text{As}:\text{Be}(2 \times 10^{18}\text{cm}^{-3})$	3.43
59x 5.54nm $\text{Al}_{0.25}\text{Ga}_{0.75}\text{As}$ / 8.8nm $\text{In}_{0.22}\text{Ga}_{0.78}\text{As}$ +1x 5.54nm $\text{Al}_{0.25}\text{Ga}_{0.75}\text{As}$	3.32 / 3.55
300nm $\text{In}_{0.135}\text{Ga}_{0.865}\text{As}:\text{Si}(2 \times 10^{18}\text{cm}^{-3})$	3.43
88.28nm $\text{In}_{0.135}\text{Al}_{0.865}\text{As}$ /75.78nm $\text{In}_{0.135}\text{Ga}_{0.865}\text{As}$	3.01 / 3.5
1 μm $\text{In}_{0.135}\text{Al}_{0.15}\text{Ga}_{0.715}\text{As}$	3.51
2 μm $\text{In}_x(\text{Al}_{0.15}\text{Ga}_{0.85})_{1-x}\text{As}$ linear graded buffer layer ($x=0$ to 0.17)	3.47
S.I. - GaAs substrate	3.46

Figure 4.7: Detailed layer Structure for B814; B813 is identical except for the omission of the mirror stack. The real refractive index values used to model the structure are also shown.

4.4.1 Electrical properties

The measured diode I - V characteristics show good electrical properties. Figure 4.8 shows the typical diode I - V characteristics for both thermally evaporated and sputtered gold P-contact layers with a thickness of 200nm on wafer B814.

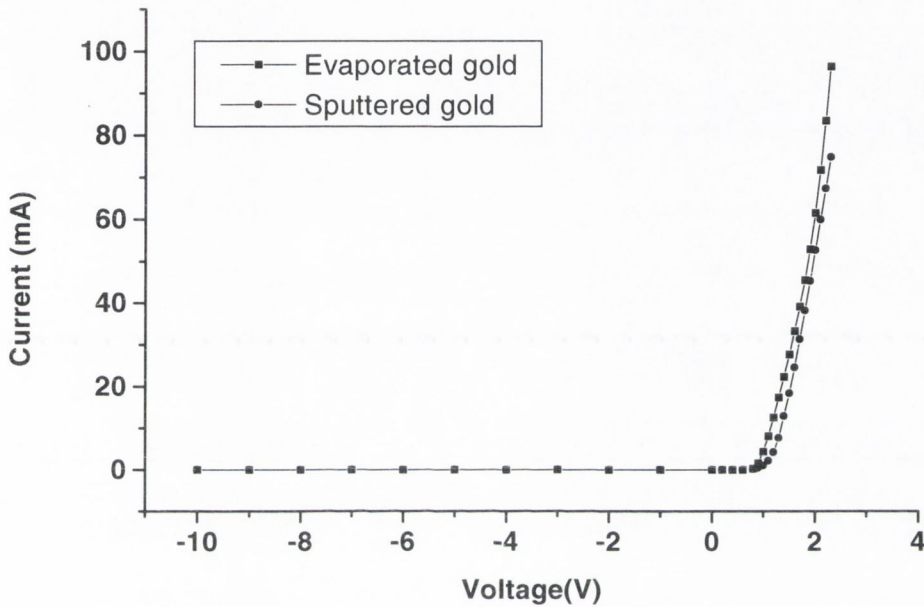


Figure 4.8: I-V diode characteristics for B814 with sputtered and evaporated gold p-contacts.

These two types of gold depositions were chosen in order to compare their electrical, mechanical and optical properties and will be dealt with later in this chapter. The “turn-on” voltage is about +0.8 V for thermally evaporated gold and for sputtered gold it is slightly greater at +0.9 V. Reverse currents are generally about -1400nA at -10V in both cases. The contact resistance of the unalloyed metal-p+-semiconductor have also been measured. A low contact resistance is important, as the modulation bandwidth is determined by the device RC time constant, as explained in Section 3.4.6. The resistance is measured from N+ and P+ gold contact pads of varying separation. Resistance vs pad separation measurements are shown in Figure 4.9. The contact resistance is calculated by extrapolating the curves in Figure 4.8 back to zero separation and is estimated to be about an acceptable value of 25Ω for both evaporated and sputtered gold contacts.

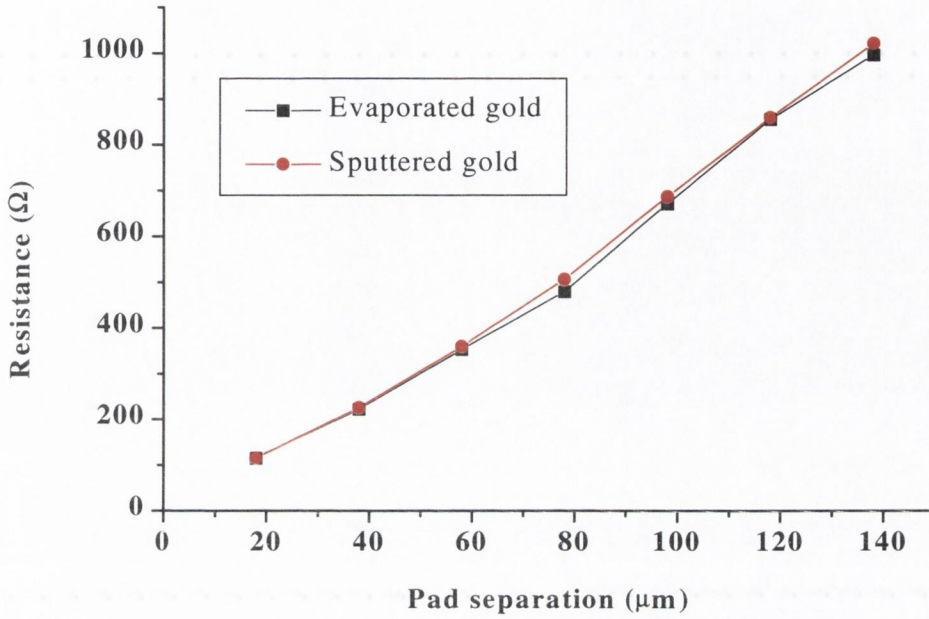


Figure 4.9: Resistance characteristics of B814, extrapolating to the contact resistance at a pad separation of zero give a contact resistance of 25Ω for both gold deposition methods.

4.4.2 Optical properties

4.4.2.1 Non-cavity structure

Referring back to Figure 4.1(a) reflectivity spectra were obtained from the three positions indicated, the n+ semiconductor / air interface (P1), the p+ semiconductor / air interface (P3) and the full device structure from the high reflectivity back mirror p+ semiconductor / gold interface (P2). Figure 4.10 shows the measured reflectivity spectrum and the predicted reflectivity spectrum from the transfer matrix model for the n+ semiconductor / air interface (P1). The modelled data is plotted from 1040nm onwards as the measured MQW absorption data used in the model to predict the reflectivity spectrum was measured from this wavelength. The reflectivity data is measured from 900nm and initially increases in value with increasing wavelength due to absorption below the band gap wavelength of the InGaAs ($\approx 1030\text{nm}$) and GaAs ($\approx 900\text{nm}$) layers. The reflectivity levels off above this, being dependent only on the wavelength dependent refractive index values. The experimental error previously presented in Figure 4.6 is of course applicable to these values. The measured data ideally should be smooth but clearly has a modulation imprinted upon it. The source of this modulation is due to an optical cavity formed by refractive index differences between layers. The primary reflections that cause this interference come from the n+

semiconductor / air interface and the interface between the GaAs substrate layer and the graded buffer layer (see Figure 4.7).

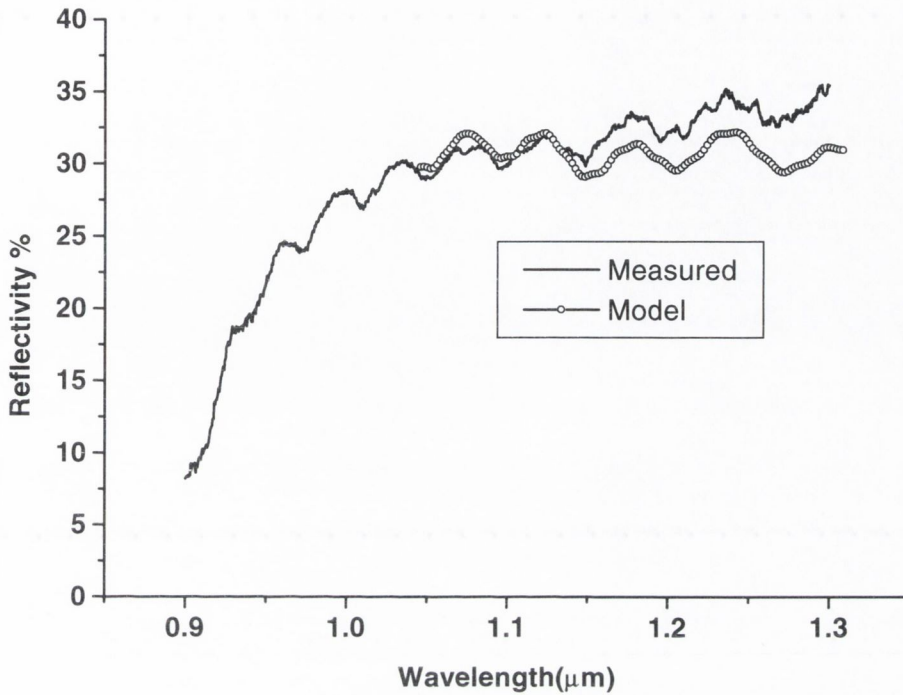


Figure 4.10: Measured reflectivity spectra and the predicted transfer matrix model reflectivity spectra from the n+ semiconductor / air interface.

These are easily found using the transfer matrix model. The depth of modulation is found to be sensitive mainly to the refractive index step between the GaAs and graded buffer layer. The resonance separation is sensitive to the combined thickness of the graded buffer and relaxation layers (the present optical cavity), and the reflectivity level (y-axis) is sensitive to the refractive index of the n+ layer only. The initial starting layer thicknesses and refractive indices shown in Figure 4.7 had to be adjusted slightly to achieve the optimum fit to the measured data using the above information. The refractive index of the buffer layer was changed from a value of 3.47 to 3.56, a change of only 2.5%. This is not surprising due to its complicated layer structure composition and estimation of its refractive index value from the literature [3]. The refractive index of the n+ layer was unchanged indicating that its estimated value is possibly close to the real value. The relaxation layer thickness was increased by 130nm to give the optimum resonance separation, this error in thickness growth is not unexpected for such a thick layer. The fit to the experimental data is very acceptable and deviations from the model predictions are within the expected experimental error.

This measurement is useful as it allows the fine-tuning of the layer thicknesses and refractive indices values closer to their real values, thus strengthening the model predictions.

Measurements taken from the p+ semiconductor / air interface (P3) on B813 which pass through the MQW region are now presented in Figure 4.11 below.

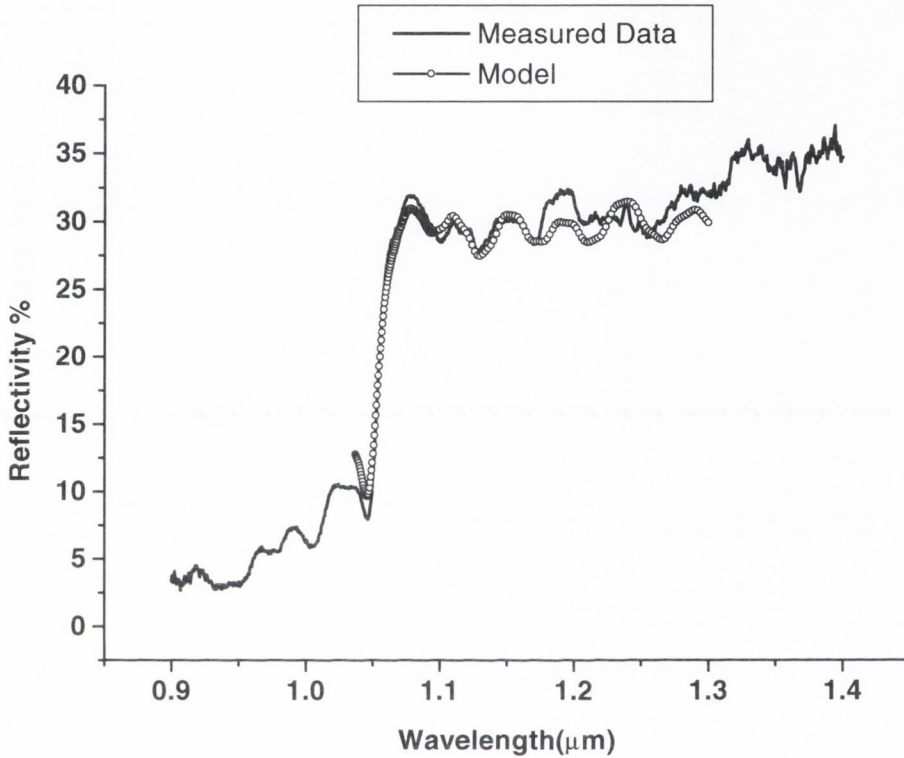


Figure 4.11: Measured reflectivity spectra and the predicted transfer matrix model reflectivity spectra from the p+ semiconductor / air interface through the MQW region.

The exciton absorption is clearly seen from the data at with the hh exciton peak at 1046nm. The model fit to the measured data indicates that the predicted absorption value for 59 MQWs is close to what was expected. To be complete in our model analysis, the amount of absorption in the cavity was varied, but this did not yield any improvement and generally produced a worse fit to the data. The measured data once again has a modulation imprinted upon it. The principal source of this modulation is the interference formed by reflections from the GaAs μ -graded buffer interface and the p+ semiconductor / air interface. To obtain the best fit to the data, the thickness of the p+ layer was adjusted by 10nm to align the interference resonances. Small adjustments of the refractive index of the p+ layer do not influence the data fit. It is difficult to know when taking this measurement whether it is from the etched or unetched region of the p+ InGaAs layer, so no additional information is gained regarding the model parameters here. Measurements

taken from the full device structure on B813 from the back Au mirror (P2) are shown in Figure 4.12. It became clear from these measurements that there was a problem with this interface.

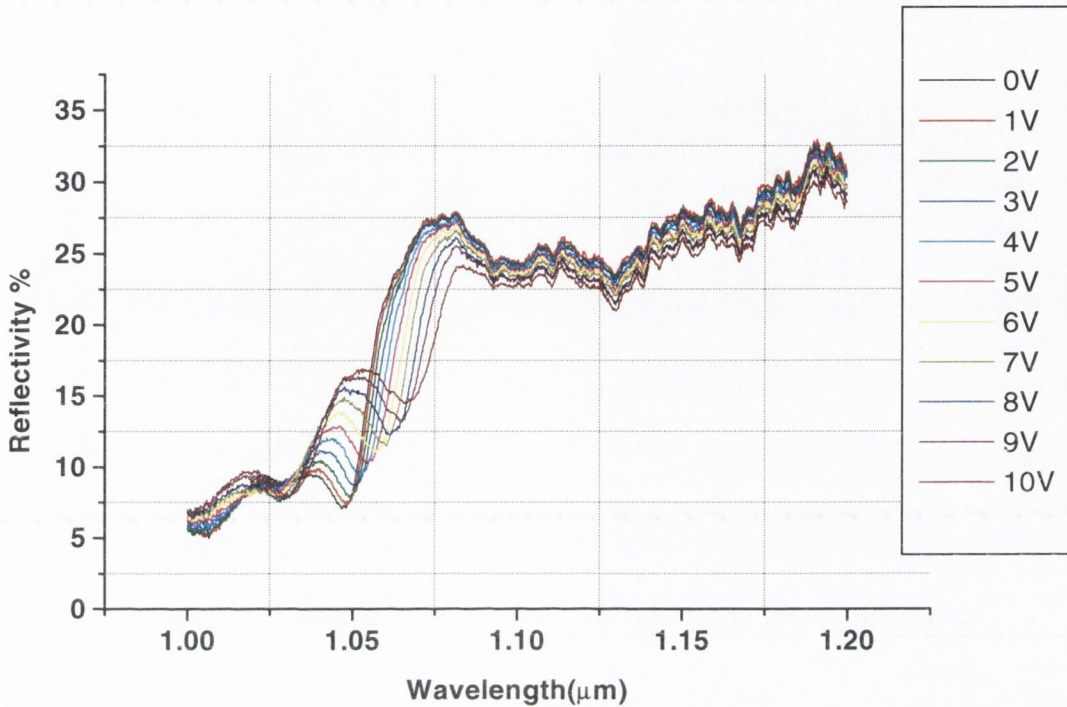


Figure 4.12: Measured reflectivity spectra from the double-pass structure on wafer B813 at various voltages.

This result is typical of all devices on B813. The low reflectivity values indicate that the light does not reflect from a gold interface at all. At longer wavelengths away from the exciton absorption ($>1100\text{nm}$) the reflectivity values should be that for reflection from an Au / semiconductor interface which is expected to be 94%. It is clear that this is not the case, with reflectivity values being even less than that seen in Figure 4.11 for the p+ semiconductor / air interface. Having spoken with Dr. Adam Boyd at the University of Glasgow who processed these devices. In his opinion the fact that all contacts failed indicates that it was not the contact anneal that damaged the devices (this is done to improve the mechanical robustness of the contact), but the treatment before metalisation. During this process the devices may have been contaminated from resist and not cleaned properly, it is a difficult trade off between cleaning the surface and damaging it. As a result of this there was a closer investigation of the optical and electrical properties of Au deposited on (In)GaAs, the results of which are presented later in this chapter in Section 4.5.

The measured results do indicate the quantum well material is of good quality and shows a good QCSE (Quantum Confined Stark Effect) shift. The exciton is 8nm short of where we expected it to be from wafer B499 as both MQW compositions should be identical (Figure 2.7). Whether this arises from a

compositional change in the material and/or a growth error in the well/barrier thickness is unknown. In the transfer matrix model the starting absorption data is from 95 MQWs at voltages from 0 to 25V as outlined in Chapter 3. The absorption spectrum at a given electric field is extracted from this data. Thus the assumption is made that the shift of the exciton hh peak in wavelength should be similar for similar electric fields applied across the MQW region. Comparing the exciton hh peak shift of the original 95 MQW data with the above 59 MQW data can test this assumption. Figure 4.13 shows the exciton hh peak shift in wavelength for 59MQWs measured from Figure 4.12 above and for 95 MQWs measured from Figure 2.7. This is plotted at the corresponding electric field value across the MQW region, calculated using Equation 3.1.

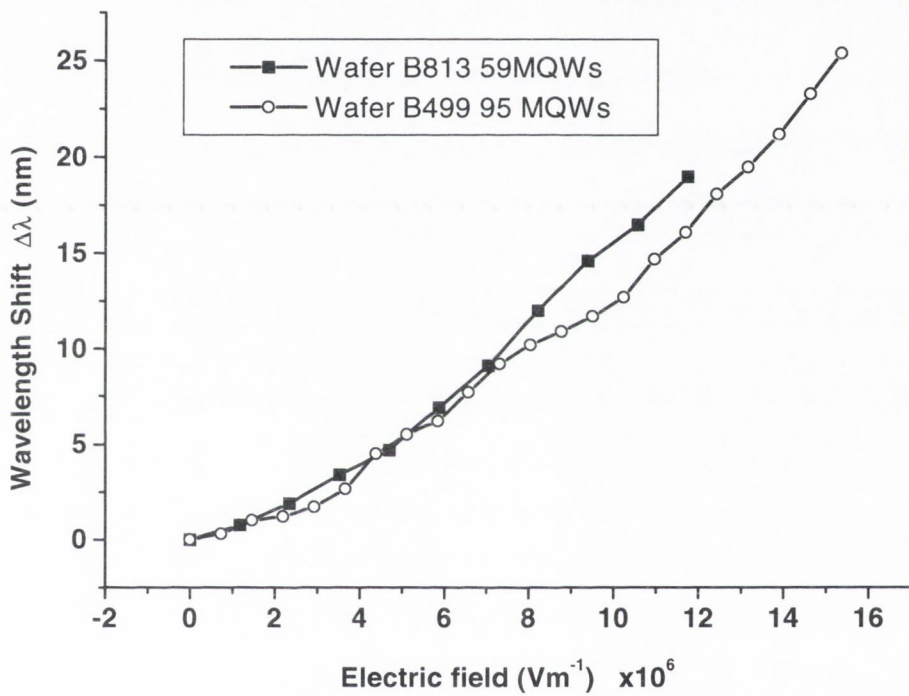


Figure 4.13: Exciton hh peak shift in wavelength for 59MQWs measured from figure 4.12 above and for 95 MQWs measured from figure 2.7. This is plotted at the corresponding electric field value across the MQW region calculated using equation 3.1.

The resulting shift in wavelength of the exciton hh peak is comparable for both sets of MQWs justifying the assumption made in our model at this reduced number of MQWs. The slightly greater Stark shift for B813 at higher electric fields may possibly be due to a number of factors. i) More accurate layer thickness growth due to a reduced number of MQWs or ii) different well and barrier compositions in both wafers producing different exciton confinement. It is most likely due to the larger influence of the built-in junction voltage that results in a larger field across the reduced number of MQWs. Despite the problems encountered with wafer B813 some useful results have been obtained from it, indicating that the developed transfer matrix

model is valid and has been improved further by these measurements. This gives a good indication that model reflectivity predictions for the Fabry-Perot devices on wafer B814 should be close to the expected values. The problems encountered with the gold interfaces on B813 were also present for the Fabry-Perot devices on B814. Thus a new piece of the B814 wafer was then processed and Au mirrors deposited successfully. Reflectivity spectra from these devices are presented next.

4.4.2.2 Optical cavity structure

The biggest obstacle to the fabrication of large arrays of Fabry-Perot modulators lies in the device tolerance to MBE growth non-uniformities as outlined in Section 3.4.3. Thickness variations across the wafer result in the optical cavity thickness changing and thus the Fabry-Perot resonance will shift in wavelength from the operating wavelength. The equation that governs the shift $\Delta\lambda$ in wavelength from an operating wavelength λ when the cavity thickness t changes by Δt , which is given by Equation 2.26, is given by

$$\frac{\Delta\lambda}{\lambda} = \frac{\Delta t}{t} \quad (4.1)$$

The percentage change in cavity thickness causes the same percentage change in the resonance position wavelength from the operating wavelength λ . By measuring the shift in wavelength $\Delta\lambda$ from the wafer edge to the wafer centre across wafer B814 the percentage change in cavity thickness across the wafer can be calculated. Figure 4.14 shows the reflectivity spectra measured from a piece of the unprocessed B814 wafer. The spectra were measured at the edge of the wafer and at different positions moving towards the centre of the 2-inch wafer. The Fabry-Perot resonances are of course not at the expected operating wavelength due to the absence of the back gold mirror. Unfortunately the piece of the wafer from which these measurements were taken was only 18mm long and is short of the wafer centre. Figure 4.15 plots the resonance position wavelength marked in Figure 4.14 as it shifts when moving away from the wafer edge towards the wafer centre. From this data the resonance at the very centre of the wafer at 25.4mm from the wafer edge is extrapolated to be 1130nm. Using Equation 4.1 above, the percentage change in wavelength from this centre wavelength is calculated and presented also in Figure 4.15. As mentioned above this value also represents the percentage change in cavity thickness from the wafer centre to the wafer edge. These values have only been measured from one part of the wafer but generally MBE growth results in similar fluctuations across all parts of the wafer. Generally non-cavity devices are processed from the area of the wafer where less than 1% to 1.5% thickness changes occur [4]. For the above wafer this represents 41% to 62% of the wafer area. Section 3.4.3.2 shows how the device modulation changes as a function of percentage thickness fluctuations across the wafer. The above values are useful as they give an indication of the area of the wafer that would be available for processing to these modulator structures. This available area will of course decide the number of possible array modules or the maximum possible array size that could be processed assuming the centre wafer thickness can be grown correctly.

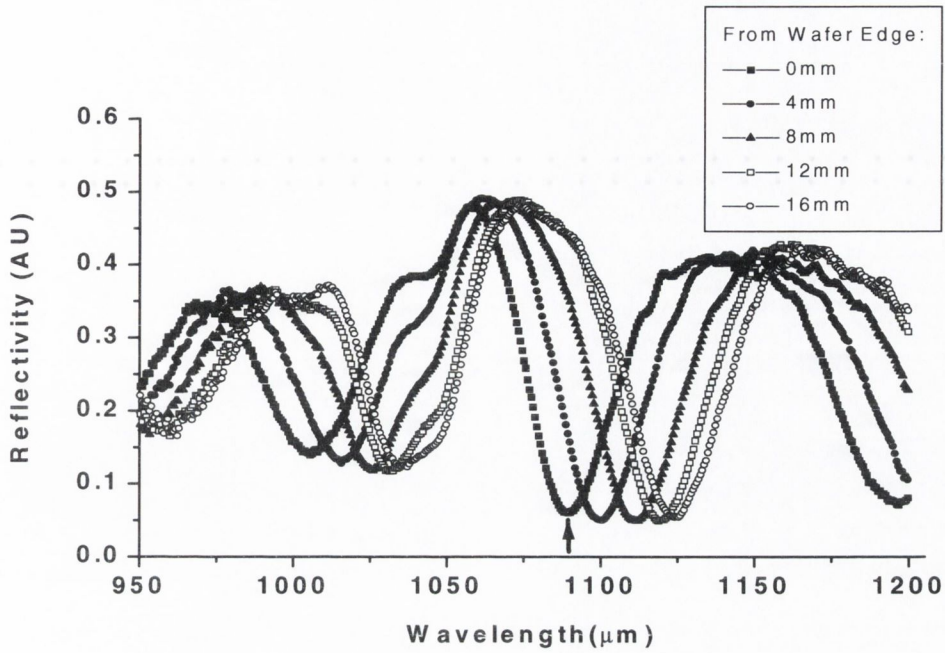


Figure 4.14 shows the reflectivity spectra measured from a piece of the unprocessed B814 wafer. The spectra were measured at the edge of the wafer and at different positions moving towards the centre of the 2-inch wafer.

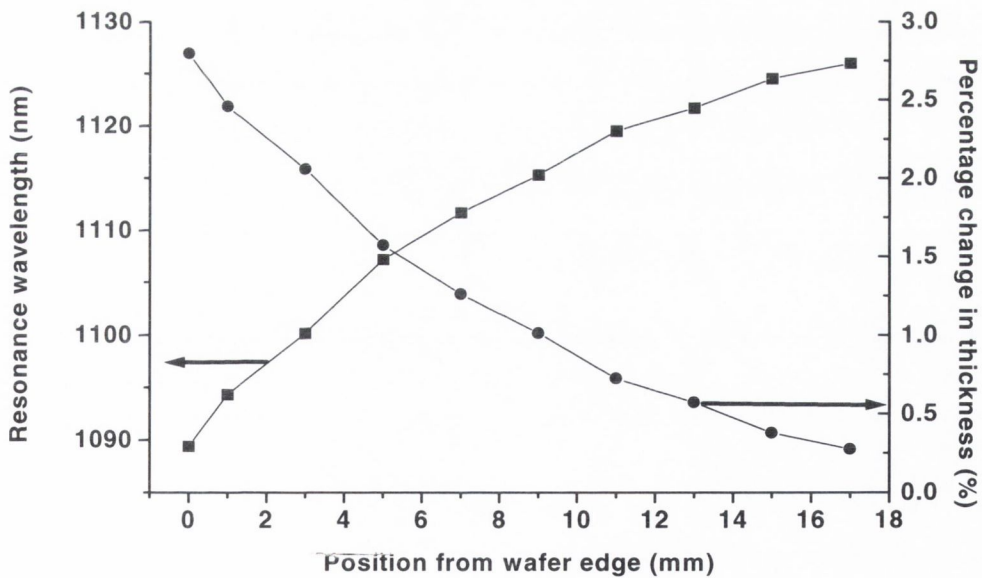


Figure 4.15: Plot of the resonance position wavelength from the wafer edge marked in Figure 4.14 and the percentage change in wavelength (thickness) calculated from the predicted centre wavelength of 1030nm and Equation 4.1.

4.4.2.3 Device results

Reflectivity spectra were obtained from the positions (P4-P7) indicated in Figure 4.1(b). The reflectivity spectra from the etched (P5) and unetched (P6) optical cavities formed by the p+ semiconductor / air interface and the Bragg front mirror are shown in Figure 4.16 along with the model fit to this data.

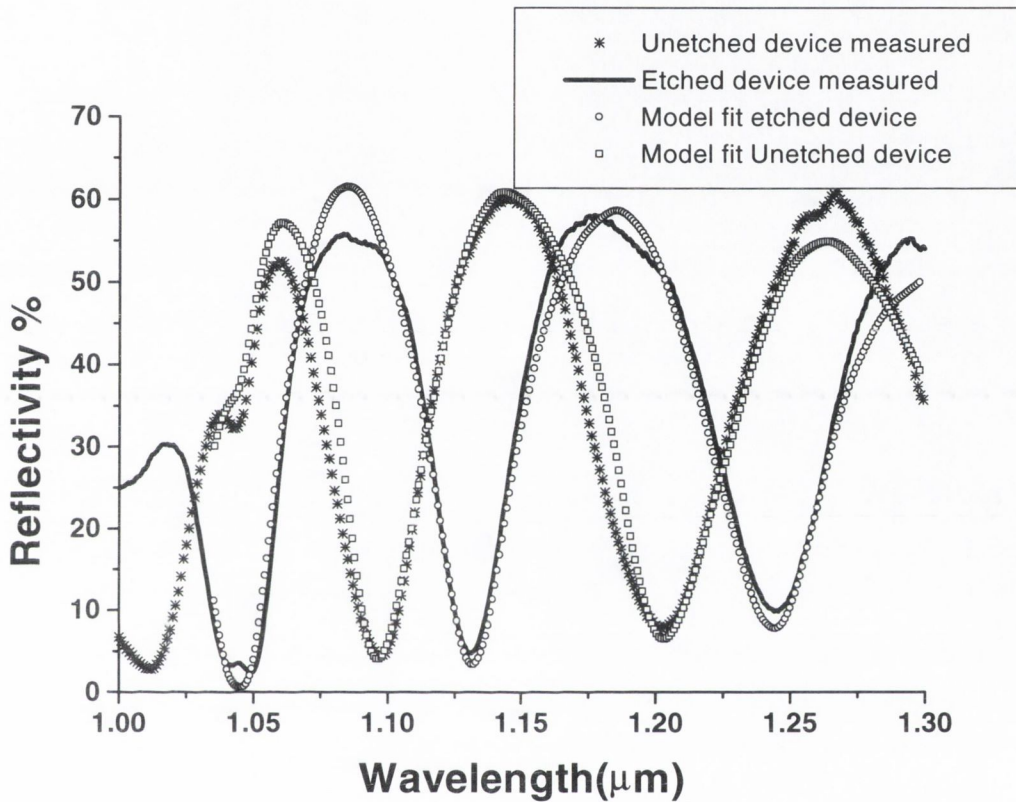


Figure 4.16: Reflectivity spectra from the etched and unetched optical cavities formed by the p+ semiconductor / air interface and the Bragg front mirror as indicated in Figure 4.1(b). The transfer matrix model fit to this data is also shown with corrected data.

The measured reflectivity spectra show a large modulated signal that is dominated by the optical cavity resonances. The reflectivity of the back mirror is low $\approx 31\%$ and the reflectivity of the front mirror in fact, as we will shortly see is $\approx 8\%$ (not 16% as expected). The broad Fabry-Perot resonances seen here are caused by this low finesse cavity and the large modulation and interference is due to the mirror reflectivities being small and close in value.

To compare the model prediction to this measured data the starting point is of course the originally calculated device structure. This data fit had the correct shape in wavelength but the maximum and

minimum reflectivity values were found to be too large and too low, respectively. As the optical cavity dominates the reflectivity spectra shown in Figure 4.16, this discrepancy is thus most likely due to an error in the mirror reflectivities. The back mirror reflectivity is dependent on the refractive index of the p+ layer only, the refractive index of air being well known. This value taken from the literature [3] may not be perfectly known but is expected to be close to the real value and small differences will largely not influence the reflectivity of this interface (30.5%). Thus the most likely cause for the large difference is the reflectivity of the Bragg front mirror. The front mirror consisted of a 2.5 period *InAlAs* / *InGaAs* Bragg mirror. The refractive indices of both layers were varied systematically to give the best fit to these two measurements (Figure 4.16) and a much better match to the experimental data was achieved. The best fit was obtained when the refractive index of the *InAlAs* layer was increased by only 3% and the refractive index of the *InGaAs* layer was decreased by only 2.25%. However this has the effect of nearly halving the internal reflectivity of the mirror as the refractive index step per period is significantly reduced from 0.49 to 0.3. The internal reflectivity of the front mirror falls in reflectivity from the expected 16% to 8%. Figure 4.16 shows the best fit achievable when adjusting the refractive indices to match both sets of experimental data simultaneously.

The refractive index change of the front mirror layers is small, only a few percent. It is quite possible that these changes are due to both strain effects [5] and to the source of our refractive index data being slightly different to the actual values, which were measured from samples grown by Vapour-Phase Epitaxy. The modelled data gives an acceptable fit to the experimental data, because the changes in the refractive index values are so small and the fit to the experimental is good. It is believed that these new values are closer to the true values for our particular material. This result does not impact on previously modelled reflectivity change results as presented in Chapter 3, only the number of periods of front Bragg mirror will be required to increase to achieve the required front mirror reflectivity. It does impact on the reflectivity change achievable with this grown cavity structure. The original 16% front mirror reflectivity was expected to give a 42% reflectivity change. The actual front mirror reflectivity of 8% when modelled predicts a lower reflectivity change of 37%. This is an unfortunate outcome but the principal purpose of these measurements is to test the accuracy and validity of the transfer matrix model predictions and to strengthen its input parameters such as the semiconductor refractive indices where possible. This is achieved and tested with measurements from this device.

Reflectivity spectra measured from the full Fabry-Perot modulator structure formed by the back gold mirror and the Bragg front mirror (P7) are now presented. As shown in Figure 4.16, different areas of the wafer have Fabry-Perot resonances at different wavelengths. Figure 4.17 shows reflectivity spectra at various voltages taken from a device on wafer B814 close to the centre of the wafer. The optimum operating wavelength separation predicted by our model is 23nm to the longer wavelength side of zero bias *hh* exciton wavelength. At this position on the wafer the Fabry-Perot resonance is much further than this away at 1095nm, a detuning of about 50nm. Thus large modulation is not expected. In Figure 4.17 two cavity orders/resonances are clearly visible one at 1015nm and the next at 1095nm (free spectral range).

The zero bias hh exciton wavelength is slightly shorter than wafer B813 at 1043.5nm which is most likely due to slight compositional variation between wafers. The measured results do indicate that the quantum well material is of high quality, showing good exciton absorption and a good QCSE (Quantum Confined Stark Effect) shift.

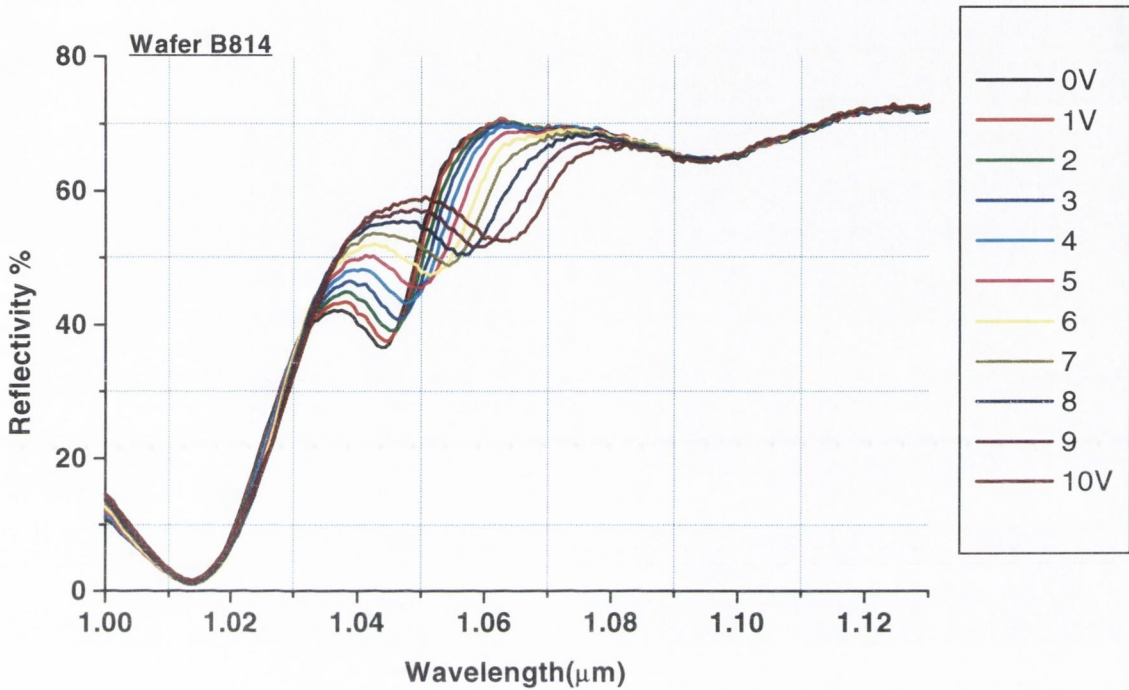


Figure 4.17: Reflectivity spectra at various voltages taken from a device on wafer B814 processed close to the wafer centre.

This data shows clearly the importance of placing the Fabry-Perot resonance at the optimum operating wavelength. The Fabry-Perot and exciton are not close enough in wavelength to take advantage of the optical cavity. At 10V the exciton wavelength is too far away from the Fabry-Perot resonance at 1095nm to change the effective back mirror reflectivity ($R_{B(eff)}$) and thus the cavity reflectivity does not change at that wavelength. At higher voltages it is possible to shift the exciton absorption closer to 1095nm but it will have a further reduced absorption value and operation is at a fixed voltage of 5V bias and 5V applied i.e. 5V and 10V. Modulation of $\approx 16\%$ is achieved at 5V operation at 1066nm, which is roughly the optimum operating wavelength predicted by the model (exciton wavelength +23nm). This device is essentially operating as a double-pass modulator as the exciton is between Fabry-Perot modes where the cavity reflectivity is flat. The reflectivity values are representative of the exciton absorption and looking closely at the 5V reflectivity curve the reflectivity is high at 1066nm indicating a relatively low α_0 value. The reflectivity at 10V shows the exciton peak shifted to 1066nm, which indicates that the absorption change

$\Delta\alpha$ is largest around this wavelength. Both of these results indicate that the model prediction of using 59 MQWs when designed to operate at 5V with a bias is correct.

As mentioned above the optimum operation is expected when the Fabry-Perot resonance is placed close to 1066nm. Figure 4.18 shows reflectivity spectra at various voltages taken from a device on wafer B814 closer to the wafer edge where the optical cavity is close to the optimum thickness and the cavity resonance \approx 1066nm.

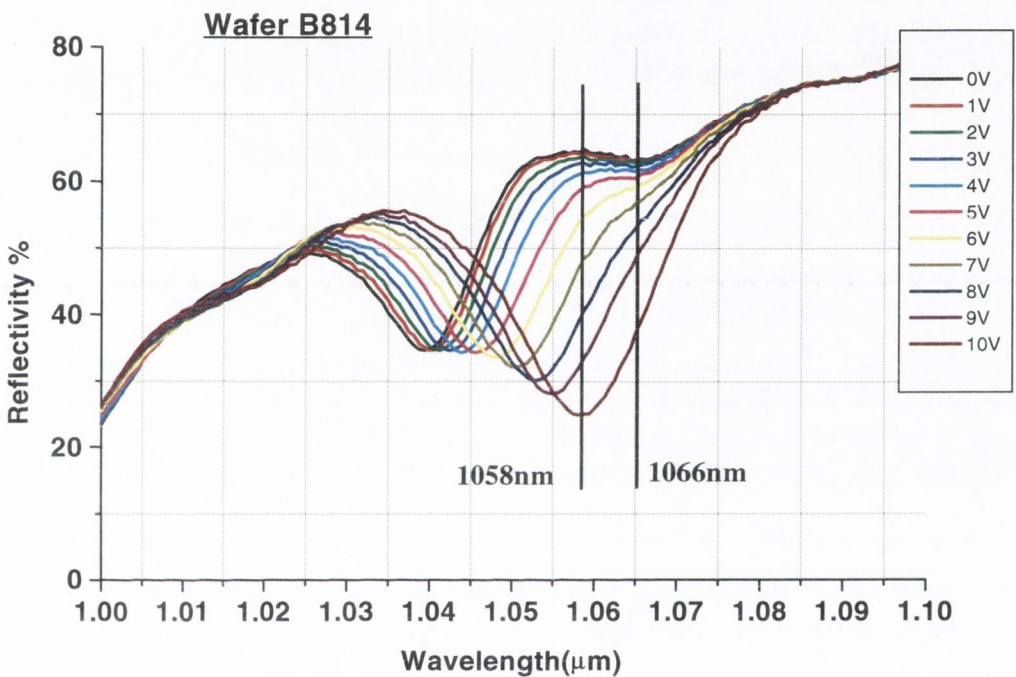


Figure 4.18: Reflectivity spectra at various voltages taken from a device on wafer B814 where the cavity resonance is near the optimum wavelength of 1066nm.

The change in reflectivity at the Fabry-Perot resonance at increasing voltages and thus increasing absorption values can clearly be seen, demonstrating the operating principle of these devices. The device from which these measurements were taken was processed from near the wafer’s edge, a region where the MBE lateral growth non-uniformities are at their greatest and layer thicknesses change most rapidly. Thus the *hh* exciton peak wavelength has shifted to a wavelength of 1039nm from 1043.5nm in Figure 4.17 which was measured closer to the centre of the wafer. This means the optimum operating wavelength should be around 1062nm. This is not what is observed in Figure 4.18. The Fabry-Perot resonance is ‘pulled’ towards the exciton absorption and optimum operation occurs at 1058nm. The reason for this is once again due to a problem with the gold back mirror reflectivity and will be discussed further shortly. It is difficult to achieve the theoretical 94% and for the above device turns out to be around 78%. This reduced

optical cavity finesse allows the exciton to have a greater influence on the Fabry-Perot resonance and thus is 'pulled' to shorter wavelengths. The optimum operating wavelength thus shifts to 1058nm. The shortest wavelength position of a Fabry-Perot resonance on wafer B814 is 1057nm and data measured from such a device is presented later. The current Fabry-Perot resonance at 1066nm gives good modulation as shown in Figure 4.18 and fitting the model predictions to these spectra will equally test the model validity.

Figure 4.19 shows the above measured reflectivity for reverse bias voltages of 0V, 5V and 10V only and the predicted model reflectivity spectra for these voltages. The model has been adjusted to take account of the lower back mirror reflectivity. How this is done will be discussed shortly. The model gives a satisfactory fit to the measured data. Discrepancies between the model prediction and measured data at shorter wavelengths are most likely due to variations in the MQW material composition and width for this device, compared to the MQWs the absorption data used in the model was taken from. These variations impact on the absorption coefficient and the linewidth of the exciton. Even with sample to sample variations the model gives a reliable prediction of the Stark shift and absorption coefficient.

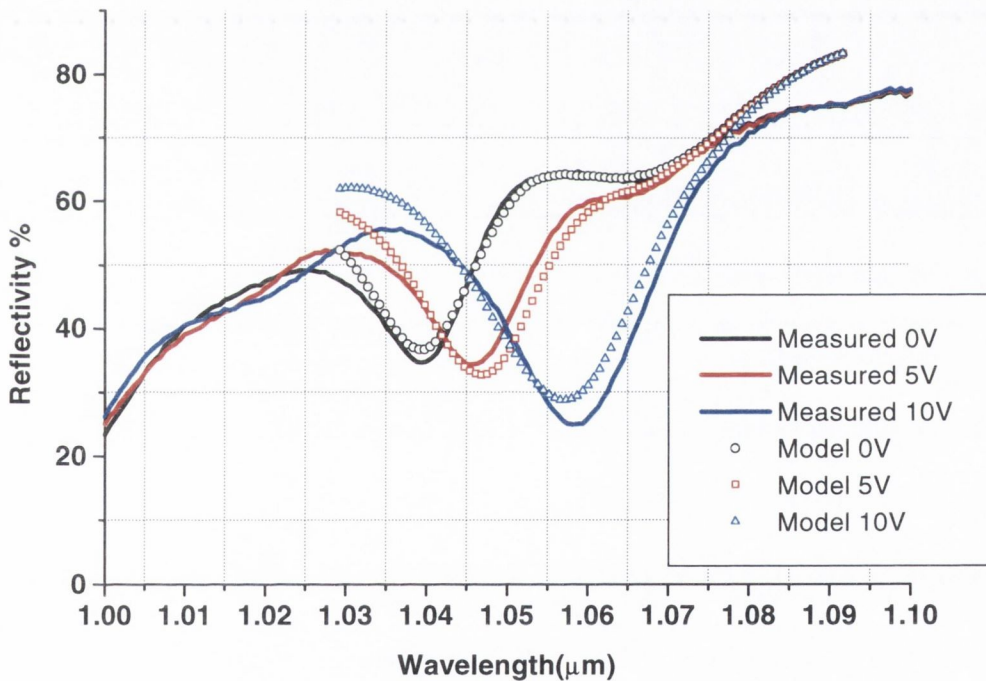


Figure 4.19: Measured reflectivity for reverse bias voltages of 0V, 5V and 10V only and the predicted model reflectivity spectra for these voltages.

There are two main factors that are unaccounted for in the transfer matrix model, which will contribute to the spectra of the measured data and cause discrepancies between the measured and modelled data. These factors are Electro-refraction (the change in refractive index with electric field) and the increase in the real refractive index value of the MQWs around the exciton wavelength. The model fit at 0V is good. When

there is no voltage applied there are no electro-refractive effects. Thus the fit to the measured data at wavelengths longer than 1050nm is good. The discrepancy at wavelengths around the exciton wavelength is most likely due to the unaccounted increase in refractive index value of the MQWs at 0V. The model uses the bulk refractive index value for the quantum well, but the real value around to the exciton wavelength for a quantum well is normally a few percent different [1][6] to the bulk value. This would mostly affect the optical path length and thus the resonance position. The combination of the resonance position being far from the exciton wavelength at 0V and the absence of Electro-refractive effects may explain the best data fit at a 0V bias. At 5V electro-refractive effects are present and the overestimation of the QCSE by our model is a normal consequence of not including this effect [1,6], the data fit is still acceptable at this applied voltage. At 10V the change in refractive index due to electro-refraction would be considerably reduced around the resonance wavelength. Thus a better fit is expected at this voltage than the fit presented in Figure 4.19. The model seems to underestimate the QCSE at 10V. The reason for this is possibly due to the stronger QCSE shift shown in Figure 4.13 for wafer B814 which results in the exciton shifting further in wavelength, compared to B499 whose data is used in the transfer matrix model. The model gives a good prediction of the coupling between the exciton and Fabry-Perot at the modulation voltages, thus yielding a satisfactory prediction of the modulation achievable as shown in Figure 4.20.

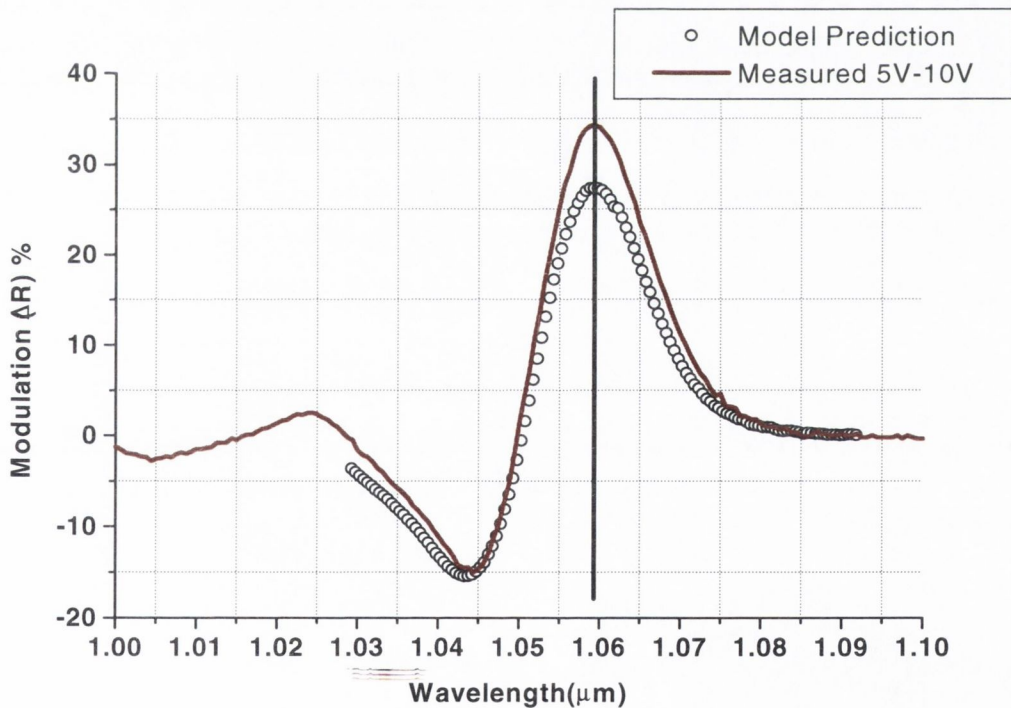


Figure 4.20: Modulation (ΔR) for 5V \rightarrow 10V (5V bias and 5V applied voltage). The curve shown is achieved by subtracting the 5V and 10V curves shown above in Figure 4.19.

The modulation (ΔR) for this device for the design voltage of 5V \rightarrow 10V (5V bias and 5V applied voltage) is presented here. The curve shown is achieved by subtracting the 5V and 10V curves shown above in Figure 4.19. Although the model fit to the 5V and 10V measured data was not perfect, there is good agreement between the predicted and measured modulation shown in Figure 4.20. The slightly over and under estimation of the data fit at these voltages results in the measured modulation being greater than what was predicted by our model.

Reflectivity measurements from a device processed close to the device in Figure 4.19, whose Fabry-Perot resonance at 1057nm is closer to the exciton hh peak, is presented in Figure 4.21. In this case the device reverse breakdown voltage was 8V so data up to 7V could only be obtained. The model parameters used to fit to the data are identical to Figure 4.19 above, the thickness of the p+ layer is reduced slightly to shift the Fabry-Perot resonance to 1057nm. The model fit to the data is reasonably good but not as good as Figure 4.19. The reason for this is most likely due to electro-reaction effects and the modified refractive indices values around the exciton peak at 0V, which are unaccounted for in the model. The closer proximity of the Fabry-Perot resonance to the exciton hh peak means greater discrepancies are expected between the measured and modelled data, particularly at wavelengths closer to the Fabry-Perot resonance as seen in Figure 4.21. This data indicates that our choice of operation with a bias voltage, which requires the operating wavelength to be further away from the exciton wavelength, yielding more accurate model predictions, is justified.

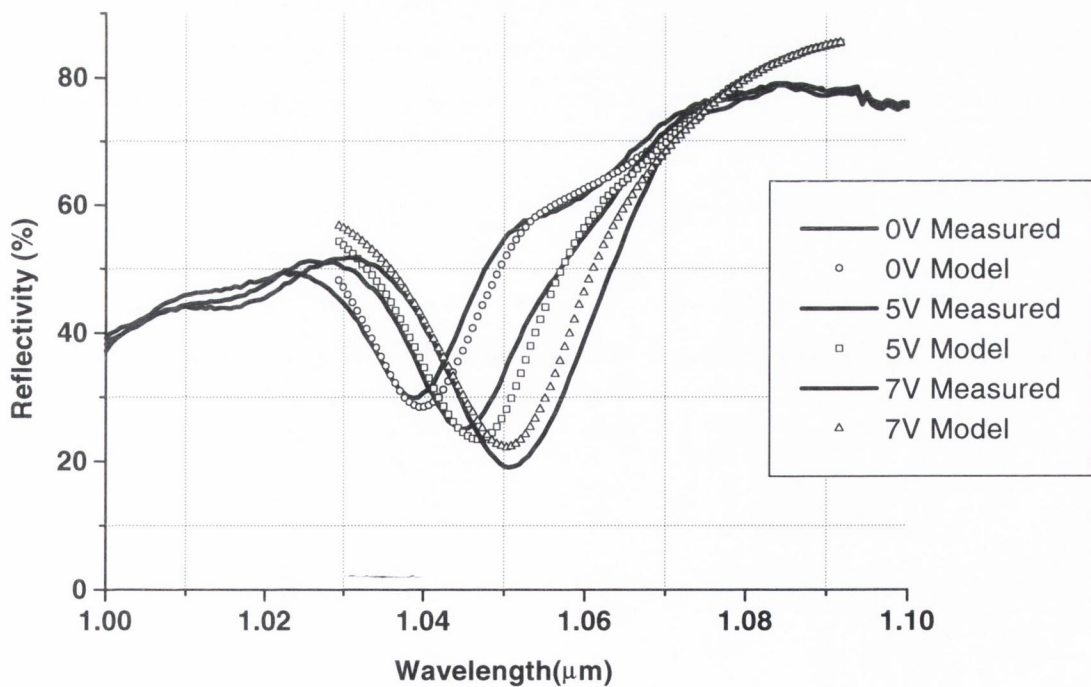


Figure 4.21: Measured and modelled reflectivity spectrum for a device processed close to the device presented in figure 4.19 but with its Fabry-Perot resonance at 1057nm.

Measured data from the devices shown in Figure 4.1 from various positions and interfaces have strengthened and validated the transfer matrix model developed in this work. Data from the double-pass devices on wafer B813 has helped to improve the estimated refractive indices closer to their actual values and shows how the model can predict the interference effects from interfaces which produce small reflections as seen in Figure 4.7. Measurements have also confirmed some of the model assumptions made in chapter 3 to be true for a device with 59 MQWs. The absorption coefficient for 95 MQWs can be linearly scaled down to fewer wells. The electric field spectrum at 95 MQWs can be extracted and similar spectra are achieved at similar fields for 59 MQWs. Measurements from the cavity structures on Wafer B814 with the semiconductor/air back mirror indicate the model can give a good prediction of the interference effects when the back mirror reflectivity is small and close in value to the front mirror reflectivity. Data from the full Fabry-Perot device gives a good prediction of the coupling between the exciton and Fabry-Perot and thus the modulation achievable. Working with a bias voltage appears to be a good choice as results indicate that not including electro-refraction effects in our model introduces an uncertainty to the model predictions. This uncertainty is greater if the Fabry-Perot resonance is closer in wavelength to the exciton hh peak wavelength, using a bias voltage allows this uncertainty to be minimised. At 5V operation the measured and modelled difference are currently acceptable when using a bias voltage. It follows from these results that the transfer matrix model developed has been validated. It is fair to say that its predictions are not absolutely perfect but these results indicate a high level of accuracy. The main assumptions made in Chapter 3 for designing a modulator to operate at low voltages have also been verified. The model can be used with a just degree of confidence in its modulation prediction capabilities to explore the possibility of low voltage Fabry-Perot modulators.

As stated in Chapter 3 the back gold mirror acts as an electrical contact and a high reflectivity mirror. The processing steps undertaken to achieve an ohmic contact with good, mechanically robust properties often result in a gold/semiconductor interface with a lower reflectivity than the expected ideal value of 94%. The fit to the data for the full 5V-modulator devices shown previously in both cases can only be achieved if the reflectivity of the back Au mirror is reduced to 78%. This is achieved in our model simply by increasing the real part of the complex refractive index value of the gold layer. The model originally assumes a perfect interface between the Au and semiconductor which in reality is difficult to achieve. Modelling of such an interface and further issues related to this interface are now addressed in the following section.

4.5 Gold deposition on semiconductor material

There are a number of ways of depositing gold on a semiconductor surface. The two most common methods are sputtered gold deposition and evaporated gold deposition. The gold/semiconductor interface functions as an electrical contact as well as a mirror and achieving both simultaneously is not trivial. Very

often it is a trade off, achieving a good electrical contact may mean sacrificing some of the mirror's reflectivity. The processing steps undertaken to achieve an ohmic contact with good 'adhesive' properties often results in the gold/semiconductor interface with a lower reflectivity than the expected ideal 94%. The problems encountered with this gold/semiconductor interface early in this work led to some additional research alongside the main goal of this project. In coalition with the University of Glasgow the electrical and optical properties of various depositions of gold on semiconductor were assessed. The main results from these measurements are presented in Section 4.5.3. Firstly the reflectivity spectra from evaporated Au on semiconductor material, which impacts on the modulation results previously presented are discussed.

4.5.1 Impact on Fabry-Perot modulator device

Reflectivity measurements from evaporated Au/semiconductor interfaces will be shown in Figure 4.25 in Section 4.5.3. The measurements are taken from three different samples incorporating simply an AR coating deposited on one side of a GaAs or InGaAs layer; evaporated, non-annealed gold was deposited on the opposite side identical to the gold deposited on the modulator devices measured above. These results are typical of the reflectivity measured, for the majority of interfaces across each sample in question. The results show a large variation in reflectivity from this interface for different samples, ranging from an almost perfect 92% to as low as 26%. The reason for the variations in reflectivity from sample to sample is at present unknown but is inherent to the gold deposition/device fabrication process itself.

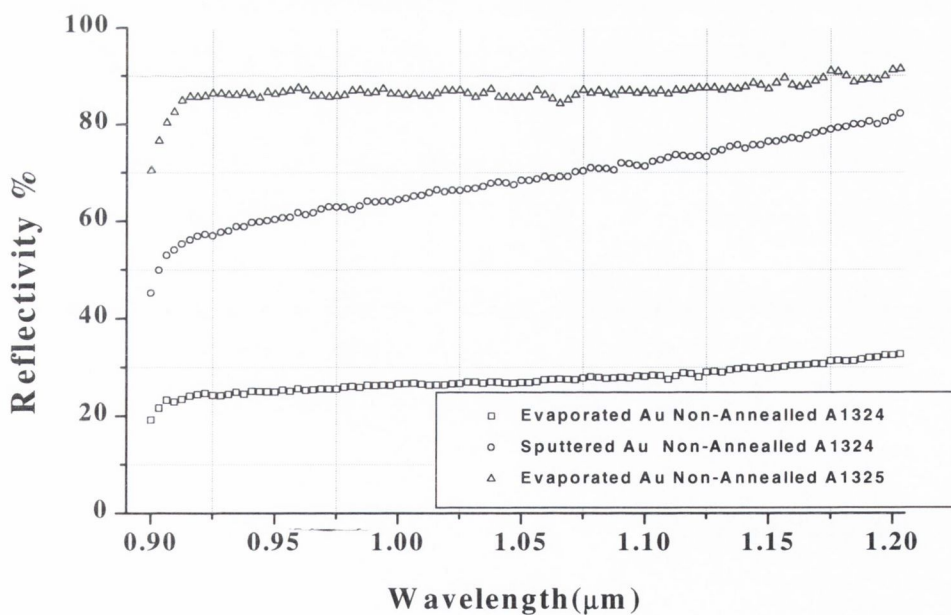


Figure 4.22: Measurements taken over a broad spectrum from Gold/GaAs interfaces

These results indicate that the ideal mirror reflectivity assumed by the model is not always present which was also the case for measurements taken from B814 above, where the interface reflectivity is thought to be 78%. Measurements taken over a broader spectrum from these interfaces are shown below in Figure 4.22, revealing a stronger than expected reflectivity dependence on wavelength. In this wavelength range the reflectivity from this interface is theoretically expected to be relatively constant. The reflectivity values decrease sharply around 900nm due to GaAs band-gap absorption. Measurements from the evaporated gold/GaAs interfaces indicate there is a small increase in reflectivity with increasing wavelength. This small increase could be due to experimental error (Figure 4.4), thus this data from the evaporated Au interfaces does not give clear evidence for this wavelength dependence. Data measured from the sputtered Au/GaAs interface demonstrate clearer evidence and the reflectivity is seen to increase very quickly in the wavelength region where the experimental error is smallest.

Reflectivity measurements taken from wafer B814 that contains the Fabry-Perot modulator devices also suggest a reflectivity wavelength dependence for a sputtered gold interface. Data are taken from devices with sputtered and evaporated gold back mirrors that are processed side by side on B814 and is shown in Figure 4.23 below. It must be stressed that the data here and in Figure 4.22 are measured from different wafers and their only relation is that they have evaporated and sputtered Au interfaces.

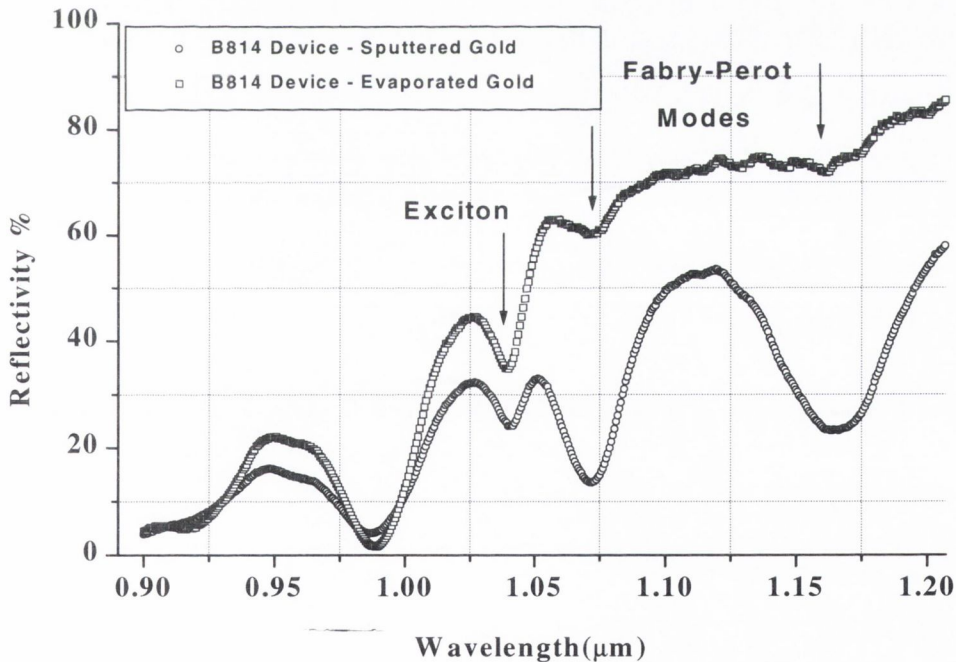


Figure 4.23: Data taken from devices with sputtered and evaporated gold back mirrors that are processed side by side on B814.

The difference in absolute interface reflectivity between these two gold depositions is clear from this data. The sputtered gold mirror reflectivity has a much lower value. The resulting Fabry-Perot modes are very clear and have lower reflectivity values compared to the evaporated gold. This is due to the back mirror reflectivity being closer in value to the front mirror and the reflectivity spectrum resembles more the data shown in Figure 4.16 for a low reflectivity back mirror. When the back mirror reflectivity has a high value and the difference in front and back mirror reflectivities is large, the Fabry-Perot dip is less pronounced as seen in the data for evaporated gold. The reflectivity values at the Fabry-Perot minima show large increases in value at longer wavelengths for the sputtered Au devices. This indicates that the back mirror reflectivity is increasing in value with increasing wavelength. If the back mirror reflectivity were relatively flat, the reflectivity values at the Fabry-Perot minima would also reflect the almost equal reflectivity behaviour seen at the Fabry-Perot minima in Figure 4.16. The data from the evaporated gold mirror indicates that the mirror reflectivity is lower than the expected 94%. If the back mirror had this value the reflectivity values at wavelengths above the exciton absorption would be extremely high. These data do not allow us to conclude anything about the back mirror reflectivity dependence on wavelength.

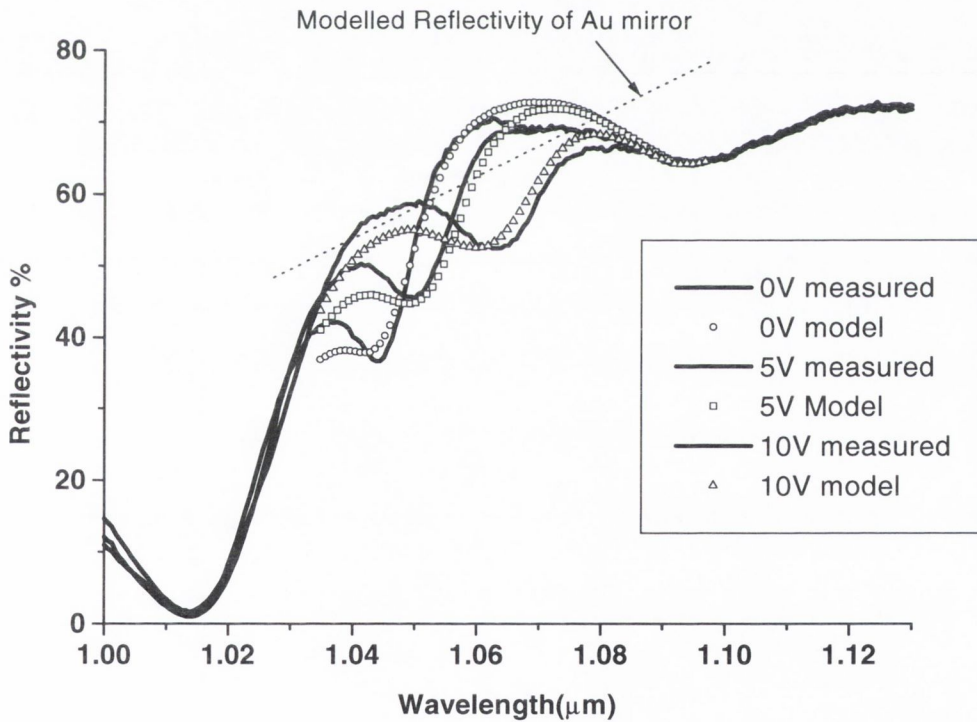


Figure 4.24: Experimental data from Figure 4.17 along with the model fit to the data where the gold reflectivity is linearly increased from 50% at 1035nm to 76% at 1097nm.

The majority of measurements for evaporated gold indicate that its reflectivity does not have strong wavelength dependence. The model fit to the experimental data in Figures 4.19 and 4.21 was achieved

using a reduced but constant reflectivity value of 78%. These measurements were taken from devices, which were processed at the same time on the same piece of wafer (B814) close to the edge of the wafer. Data shown in Figure 4.12 were taken from a separately cleaved piece from the centre of B814 processed at a different time. In this case it is not possible to obtain an acceptable fit to the measured data using a constant back mirror reflectivity value. A satisfactory data fit is only obtained if the gold reflectivity is linearly increased from 50% at 1035nm to 76% at 1097nm, the wavelength range of the model data. The experimental data from Figure 4.17 is shown in Figure 4.24 along with the model fitted to the data using these wavelength dependent reflectivity values. There was no real indication from basic interface measurements that the evaporated gold interface reflectivity is strongly wavelength dependent. These results strongly suggest this is the case here and maybe unique to this processing run. The sputtered gold measurements from the above processed sample from the centre of the wafer and the other processed sample from the wafer edge show similar wavelength dependent reflectivity behaviour as figure 4.23 above.

The reflectivity results above show the possible problems that can be encountered when using gold deposited on semiconductor material as an electrical contact and an optical mirror. The absolute reflectivity value can be reduced significantly and it can also be strongly wavelength dependent. The reason for this outcome seems to be inherent to the gold deposition/device fabrication processes themselves. The resultant reflectivity change from a Fabry-Perot modulator device will be affected by the altered back mirror reflectivity. The data in Figure 4.23 indicate that the phase change of the light upon reflection is unaffected as the Fabry-Perot positions occur at the same wavelengths in both cases. Thus it is only the reduced absolute back mirror reflectivity that results in the overall device reflectivity being reduced. The reflectivity change is calculated from $(R_{on}-R_{off})$ and the reduced overall device reflectivity will affect mostly the R_{on} value. The higher the front mirror reflectivity, the more sensitive this value to back mirror reflectivity changes will be. Modelling of the optimum 5V modulator design which has a relatively low front mirror reflectivity of 40%, predicts that the 45% modulation achievable with a perfect 94% back mirror reflectivity halves in value, falling to 25% for a back mirror reflectivity of 78% (Figure 4.20). At 55% reflectivity the modulation is a mere 8%. In the case where the reflectivity of the back mirror is changing with wavelength it is the reflectivity at the operating wavelength which is of most importance and the same behaviour predicted above applies. The modulation results shown in Figure 4.20 are quite good despite the back mirror reflectivity being only 78%, this is a result of the front mirror reflectivity being very low in value at only 8% and thus the cavity reflectivity is less sensitive to back mirror reflectivity changes. For lower voltage operation where much higher front mirror reflectivities are required, the uncertainty with this interface becomes a very serious problem. The above predictions indicate the highly sensitive and critical nature of the back mirror reflectivity to these devices. It is extremely important when using Fabry-Perot devices that a high and predictable back mirror reflectivity can be produced.

4.5.2 Modelling the optical properties of a gold /semiconductor interface

The lower reflectivity Au back mirror is modelled by changing the refractive index value of the Au layer. Both real and imaginary parts that account for absorption in the layer are altered. The magnitude of the refractive index change is significant; being changed from an ideal value taken from the literature of $0.2903-7.463i$ to $0.9203-6.263i$ which corresponds to a reflectivity change of 95% to 78%. More dedicated research [7] investigating this specific problem suggests that the interface may be composed of a granular makeup of the Au atoms, embedded as particles in the semiconductor crystal. Results indicate that the interface can be modelled if the layer is represented as a mixture of Au and a void [8]. Taking this into consideration, altering the refractive index in such a significant manner may not be an unreasonable first approach for representing this interface.

4.5.3 Measured optical reflectivities

The three main characteristics required from a metal/semiconductor interface when used as an optical mirror and electrical contact are

- a) High reflectivity
- b) Ohmic I - V characteristics with low contact resistance
- c) High mechanical robustness

Earlier results have shown the implications of reduced back mirror reflectivity on Fabry-Perot modulator devices. Ohmic I - V characteristics with low contact resistance are essential for electrical operation of the device, high currents reduce the device lifetime and low contact resistance is necessary to achieve high electrical bandwidths. The adhesion of the gold to the semiconductor is also critical, these devices must be able to survive a number of processing cycles [9] and even more so if the devices are 'flip-chip' mounted to drive electronics. The gold adhesion is tested by the removal of a piece of 'scotch tape' placed on the gold contact. The adhesion and electrical properties were tested at the University of Glasgow.

Three different gold depositions on GaAs/InGaAs with an anti-reflection coating on the opposite side were investigated. The first of these depositions is evaporated pure gold deposited by thermally evaporating Au and deposition occurs at a rate of about 2 nm/sec. Evaporated gold contacts typically showed good electrical properties but poor adhesion. The sputtered gold deposition method is achieved by high-energy bombardment of the gold releasing clusters of gold atoms and is deposited on the semiconductor surface at a rate of about 50 nm/min. Measurements showed this contact to have good electrical and adhesive properties and it is currently the preferred deposition for the double-pass modulators/detectors in the SPOEC project. The third deposition method is a thermally evaporated mixture

of gold nickel and chromium. Alloying of a metal-semiconductor junction is normally required to produce Ohmic $I-V$ characteristics but the University of Glasgow has produced good Ohmic $I-V$ characteristics without alloying using sputtered deposition. The alloyed contacts typically also showed good electrical and adhesive properties. Additional wafers were also processed with each of these depositions but the contacts were thermally annealed after the metal deposition. This is done as previous results have shown this to improve the adhesive and electrical properties. Reflectivity measurements taken from each of these depositions for annealed and unannealed devices are shown in the following Figures 4.25 to 4.27. These results are typical of the reflectivity measured, for the majority of interfaces across each sample in question. Wafer number A1324 and A1325 are GaAs wafers, B837 and B838 are GaAs wafers with InGaAs quantum wells. The reflectivity results in each case show a large variation in reflectivity for different wafer samples. The evaporated gold contacts show reflectivities ranging from an almost perfect 92% to as low as 26%.

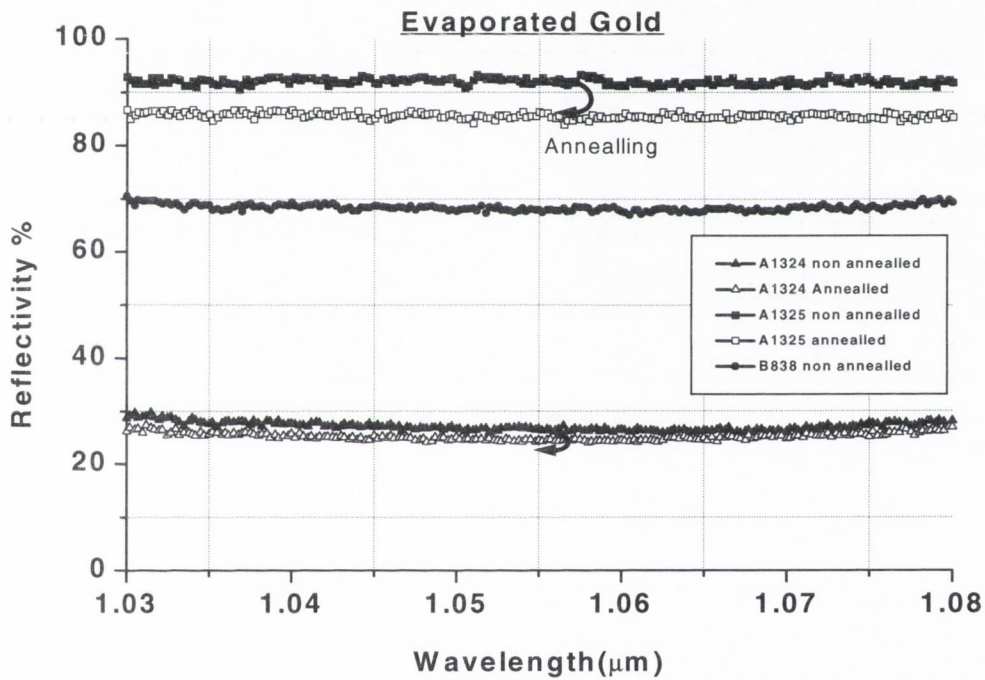


Figure 4.25: Reflectivity measurements taken from gold contacts/mirrors produced from evaporated gold deposition for annealed and unannealed devices.

The Au/Ni/Cr contact shows similar fluctuations in reflectivity while the sputtered gold contacts are more consistent in reflectivity. The reason for the variations in reflectivity from sample to sample is at present unknown but are inherent to the gold deposition/device fabrication process itself. The effect of annealing the samples typically reduces the interface reflectivity by about 10%.

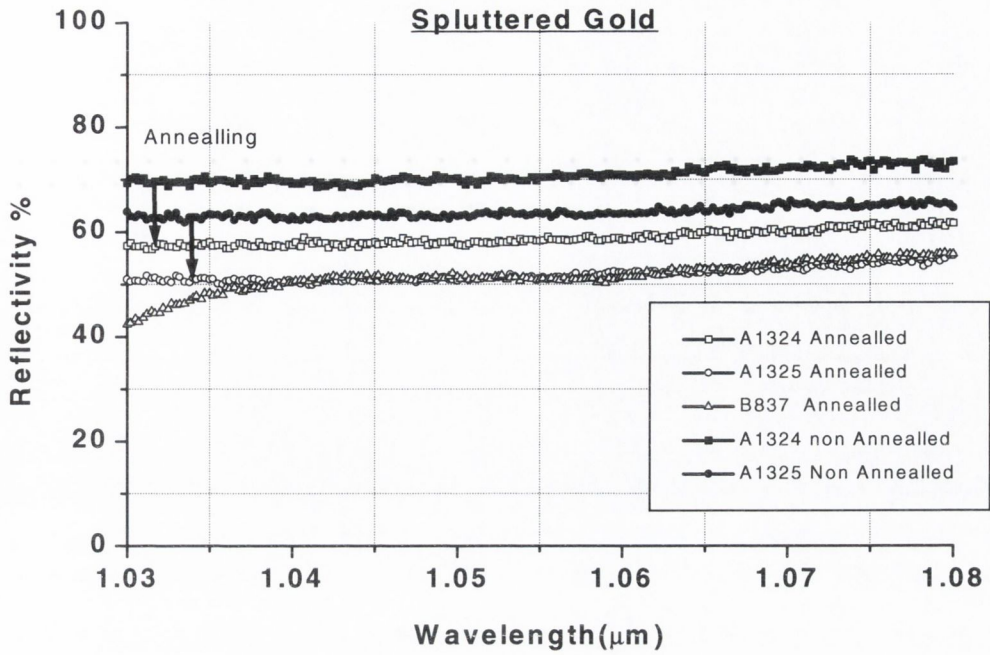


Figure 4.26: Reflectivity measurements taken from gold contacts/mirrors produced from sputtered gold deposition for annealed and unannealed devices.

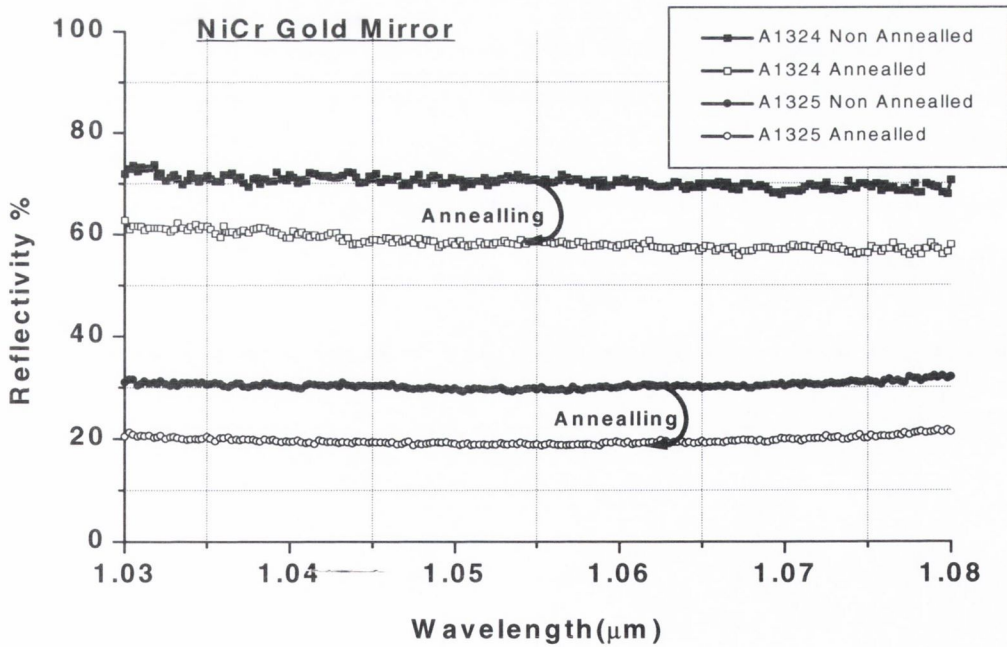


Figure 4.27: Reflectivity measurements taken from gold contacts/mirrors produced from evaporated Au/Ni/Cr deposition for annealed and unannealed devices.

Evaporated gold shows the highest reflectivity value at 92%, as might be expected from pure evaporated gold, but results also show that when the process goes wrong it results in extremely small reflectivity values (26%). This was also experienced for devices processed on wafer B813 reported earlier in Section 4.4.2.1 where the back mirror reflectivity appears to be about 26%, also from Figure 4.12. The Au/Ni/Cr combination shows a lower maximum reflectivity of 70%. This reflectivity is expected to be lower than pure gold, due to the theoretically lower reflectivity of Ni and Cr at these wavelengths. When combined with gold the resulting reflectivity is expected to be lower. Sputtered gold shows a maximum value of 70% and minimum of 50%. The reflectivity of this interface is more reproducible in this set of measurements. The reduced reflectivity is believed to come from the deposition process itself where the impact of the more energetic Au atoms results in more damage to the optical interface. This may also produce the good adhesive qualities shown by these contacts.

Each of the deposition methods has at least two of the three required characteristics summarised above, but none have emerged as a clear favourite. Sputtered gold is currently the preferred choice of deposition due to its good electrical and adhesive properties, reasonably high interface reflectivity of 70% and its reproducibility. For a double-pass modulator device this reduced back mirror reflectivity does not impact on the device reflectivity change as seriously as it does for a Fabry-Perot device. In this case a back mirror reflectivity of 70% is not sufficient. The main conclusion from the current results is that the function of the metal-semiconductor p+ contact should be split into separate functions and not used as both an optical mirror and electrical contact. This may involve extra device processing but for operation of Fabry-Perot modulators it is necessary. Due to the unreliable nature of this process the use of Bragg stack mirrors for the back mirror may be a better option. This mirror would also require extra processing steps as well as longer growth times. It must be stressed that these conclusions and problems are specific to this work and other device processors may have already solved this problem; although to the authors knowledge there is very little published literature suggesting a solution to this topic. Due to the finite lifetime of this project the initial work done above could not continue, leaving much work involving this issue uncompleted.

4.6 Conclusions

In this chapter the validity of the transfer matrix model developed and presented in chapter 3 is tested against experimental reflectivity measurements taken from various devices and various interfaces along these device structures. The results of this comparison have confirmed the main assumptions reached for device operation at low voltages. When reducing the MQWs from 95 to 59 the absorption coefficient can be extrapolated; the absorption spectrum and QCSE shift at a particular electric field can be extracted for 95 MQWs and similar results are achieved at similar electric fields for 59 MQWs. Even with sample to sample variation, the modulation achieved is very similar to the model prediction. It is expected at much lower voltage operation that there may possibly be some deviation of the above from what is predicted by our model. This is due to such effects as the built-in voltage having stronger influence (removing the need

for an electrical bias line to the modulator) or the electric field dropped across each MQW will have a more uniform value (reducing exciton broadening). These effects will mean some small allowances in modulator design but the data presented in this chapter strongly indicates that the principal idea for low voltage operation holds true.

Data from the various interfaces without the gold mirror shows a good fit to the model predictions and data from the full Fabry-Perot device gives a good prediction of the coupling between the exciton and Fabry-Perot and thus the modulation achievable. Working with a bias voltage appears to be a good choice minimising errors introduced by refractive index changing effects not accounted for in our model, the model predictions when using a bias voltage show good accuracy. The model has only been tested for a relatively low finesse cavity and front mirror reflectivity. Higher finesse cavities will be required at lower voltage operation. At higher finesses the Fabry-Perot resonance dominates the reflectivity spectra and becomes more sensitive to refractive indices changes. The model is operating where these refractive indices changes are minimised and the MQW absorption at the resonance wavelength should be predicted with reasonable accuracy. Taking these into account and the proven record of the transfer matrix model at predicting cavity reflectivity [10,11,12], the modulation predicted at higher finesse cavities should have an acceptable level of accuracy.

Measurements from gold/semiconductor interfaces for various gold deposition methods have shown the unreliable nature of our deposition/device fabrication process. Communication with various other people and semiconductor laboratories from around the world concludes that this is a common problem. The optimum solution to this problem may be to split the interface functions and use two separate interfaces, one deposited for the optical mirror and the other for the electrical contact. Measurements and modelling results show that the back mirror reflectivity is critical to Fabry-Perot modulator devices, the higher the cavity finesse, the more serious its impact on device operation. For low voltage operation this is a serious problem because of the high finesse cavities required, here a high reflectivity reproducible mirror such as a Bragg stack is required for use in large arrays or possibly a Bragg/metal mirror combination. In chapter 5 the ideal low voltage modulator design is investigated and the importance of the back mirror reflectivity to these Fabry-Perot modulator devices is addressed in detail.

4.7 References

- [1] LIVESCU G, BOYD GD, MORGAN RA, CHIROVSKY LMF, FOX AM, LEIBENGUTH RE, ASOM MT, FOCHT MW, 'ROLE OF ELECTROREFRACTION IN QUANTUM-WELL FABRY-PEROT MODULATORS', APPLIED PHYSICS LETTERS, 60: (12) 1418-1420 MAR 23 1992
- [2] 'INTRODUCTION TO OPTICS', PEDROTTI F.L. AND PEDROTTI L.S., PRENTICE HALL INTERNATIONAL INC, NEW JERSEY, 1993
- [3] E.D. PALIK, ' HANDBOOK OF OPTICAL CONSTANTS OF SOLIDS I-III', ACADEMIC PRESS, BOSTON, 1998

[4] PRIVATE COMMUNICATION WITH PROF. COLIN STANLEY, DEPARTMENT OF ELECTRONIC AND ELECTRICAL ENGINEERING, UNIVERSITY OF GLASGOW, SCOTLAND, UK.

[5] 'PROPERTIES OF LATTICE MATCHED AND STRAINED INDIUM GALLIUM ARSENIDE', EDITED BY PALLAB BHATTACHARYA, INSPEC EMIS DATAREVIEW SERIES NO.8, THE INSTITUTION OF ELECTRICAL ENGINEERS, LONDON, 1993

[6] ZOUGANELI P, PARRY G, 'EVALUATION OF THE TOLERANCE OF ASYMMETRIC FABRY-PEROT MODULATORS WITH RESPECT TO REALISTIC OPERATING-CONDITIONS', IEEE JOURNAL OF QUANTUM ELECTRONICS, 31: (6) 1140-1151 JUN 1995

[7] 'OPTICAL PROPERTIES OF AU: SAMPLE EFFECTS', ASPENES DE, KINSBRON E, BACON DD, BELL LAB., MURRAY HILL, NJ, USA, PHYSICAL REVIEW B-CONDENSED MATTER, VOL.21, NO 8,15 APRIL 1980,P3290-9

[8] 'SPECTRO-ELLIPSOMETRIC STUDIES OF GROWTH TEMPERATURE DEPENDENT OPTICAL PROPERTIES OF THIN AU FILMS ', SOONIL LEE, JUNEGIE HONG, SOO-GHEE OH, DEPT OF PHYSICS, ANJOU UNIVERSITY, SUWON, SOUTH KOREA JOURNAL OF THE KOREAN PHYSICAL SOCIETY, VOL. 31,NO 6,DEC 97 P.887-93.

[9] G. PENNELLI, C.R. STANLEY, A.R. BOYD, J. PEARSON "GROWTH AND FABRICATION OF IN(AL,GA)AS-GAAS MODULATOR/DETECTOR ARRAYS FOR SMART PIXEL APPLICATIONS" IN SPATIAL LIGHT MODULATORS AND INTEGRATED OPTOELECTRONIC ARRAYS, OSA TECHNICAL DIGEST (OPTICAL SOCIETY OF AMERICA, WASHINGTON DC, 1999), PP. 27-29

[10] LIN CH, MEESE JM, CHANG YC, 'A LOW-VOLTAGE, HIGH-REFLECTANCE-CHANGE NORMALLY OFF REFRACTIVE GAAS/AL_{0.2}GA_{0.8}AS MQW REFLECTION MODULATOR', IEEE JOURNAL OF QUANTUM ELECTRONICS, 30: (5) 1234-1240 MAY 1994

[11] FRITZ IJ, HAMMONS BE, HOWARD AJ, BRENNAN TM, OLSEN JA, 'FABRY-PEROT REFLECTANCE MODULATOR FOR 1.3 MU-M FROM (INALGA)AS MATERIALS GROWN AT LOW-TEMPERATURE', APPLIED PHYSICS LETTERS, 62: (9) 919-921 MAR 1 1993

[12] FRITZ IJ, BRENNAN TM, HAMMONS BE, HOWARD AJ, WOROBAY W, VAWTER GA, MYERS DR, 'LOW-VOLTAGE VERTICAL-CAVITY TRANSMISSION MODULATOR FOR 1.06 MU-M', APPLIED PHYSICS LETTERS, 63: (4) 494-496 JUL 26 1993

Chapter 5: Alternative modulator structure

5.1 Introduction

In this chapter the reduced modulation value (ΔR) predicted at lower voltage operation in Chapter 3 for the Fabry-Perot device structure using a back gold mirror is investigated further. Modelling indicates that the fixed reflectivity of the gold / semiconductor interface (94%) results in a reduced modulation at lower voltage, higher finesse cavities. Higher back mirror reflectivities having values between 95 to 99.9% are found to make a critical difference to the modulation achievable at low voltage operation. Modelling results using higher back mirror reflectivities predict that modulation of 58% is possible at all voltages modelled for voltages from 5V to 1V. The increasing cavity finesse of these Fabry-Perot devices has a serious impact on the critical device operating tolerances. Tolerances such as the spectral bandwidth, acceptance angle and MBE growth non-uniformities are investigated in detail. The impact on device speed, optical power saturation and temperature sensitivity is also addressed. Taking account of the above characteristics, the lowest possible operating voltage for this current device structure and material system for practical operation in an optical interconnect is determined.

5.2 Back mirror reflectivity

Modelling results summarised in table 3.1 predict that the modulation value (ΔR) decreases significantly at lower voltage operation for a Fabry-Perot device structure incorporating a back gold mirror and front Bragg stack no matter how high the front mirror reflectivity is. Comparison of experimental results and modelling predictions in Chapter 4 have demonstrated the validity of our model. It is now used to investigate in further detail this reduced modulation and to evaluate whether a larger modulation is possible and if these devices can be used in optical interconnects, at very low voltage operation.

5.2.1 Limited Gold mirror reflectivity

The preferred device structure previously modelled in Chapter 3 incorporates a front Bragg mirror and a back gold mirror. Figure 5.1 shows how the reflectivity of this Fabry-Perot cavity changes with increasing front mirror reflectivity, when there is no absorption in the cavity. As the reflectivity of the front Bragg mirror increases relative to the back gold mirror, the Fabry-Perot dip appears and drops in reflectivity, going to zero when the front and back mirror have equal reflectivities allowing total destructive interference to take place.

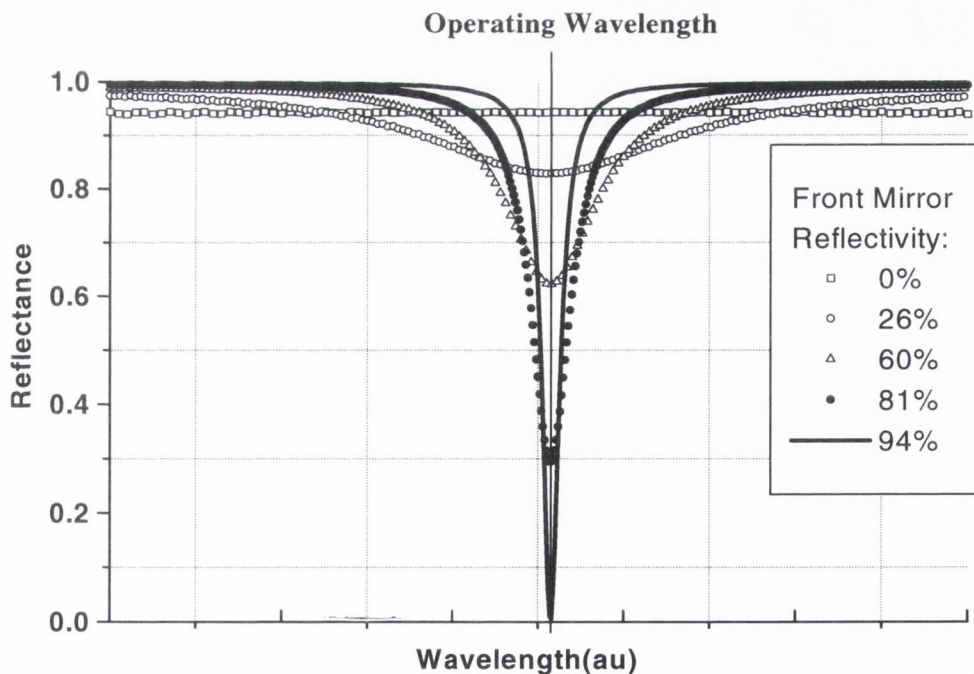


Figure 5.1: Typical plot of reflectivity for a device with a gold back mirror as the reflectivity of the front mirror increases when there is no absorption in the cavity.

In the optimised designs at each of the operating voltages shown in Table 3.1 (Chapter 3), the front mirror reflectivity is increasing as the operating voltage is decreasing. This increasing front mirror reflectivity has a detrimental effect on modulation as it lowers the Fabry-Perot resonance reflectivity and limits the ultimate reflectivity change possible. Figure 5.2 shows the actual reflectivity for the optimally designed 5V and 2V modulator structures in chapter 3. Looking at the 5V modulator R_{on} curves, this curve represents the reflectivity before the device is turned on, the curve is a convolution of the Fabry-Perot dip at 1077nm and exciton absorption at ~ 1065 nm. When the voltage is turned on, the QCSE shifts the exciton absorption peak towards the Fabry-Perot resonance and the resultant reflectivity is shown by the 5V R_{off} curve.

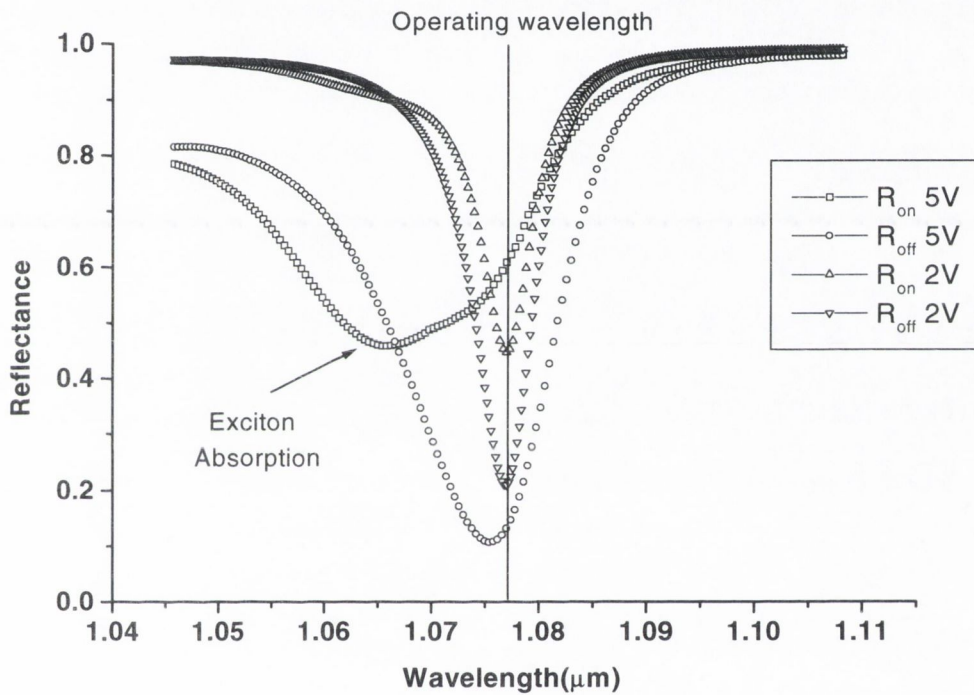


Figure 5.2: Reflectivity for the optimally designed 5V and 2V-modulator structure.

The relatively lower finesse cavity of this 5V structure shows how strongly the exciton absorption influences the reflectivity spectra, ‘pulling’ the cavity resonance towards it. The R_{off} curve shows how the Fabry-Perot resonance appears to be closer to 1075nm than its true design position 1077nm. The reflectivity at the operating wavelength changes from 60% to 14% giving $\Delta R = 46\%$ as presented in Table 3.1. In direct contrast the 2V-modulator device has a higher finesse cavity and the Fabry-Perot resonance dominates more the reflectivity spectra. The Fabry-Perot resonance is at the operating wavelength of 1077nm in both the R_{off} and R_{on} curves, the reflectivity changes from 44% to 20% giving $\Delta R = 24\%$. The important point to note here is the reduced starting R_{on} reflectivity value at the operating wavelength for both devices. For the 5V device it has already dropped to 60% due to a combination of the front mirror

reflectivity and some residual α_0 exciton absorption. For the 2V device it has dropped to 44% due to the higher again front mirror reflectivity. Since the reflectivity change is given by $(R_{\text{on}}-R_{\text{off}})$, these numbers represent the maximum R_{on} value and maximum modulation potentially achievable for a “normally on” device. This upper value is difficult to actually achieve. To maximise the $\Delta R = (R_{\text{on}}-R_{\text{off}})$ value the R_{off} value must be minimised. Thus in the case of the 5V device above, the ΔR value can be increased if R_{off} can be reduced further from 14%. Increasing the front mirror reflectivity can do this but this also reduces the starting R_{on} value. The spectra shown above are for the optimum front mirror reflectivities for these operating voltages, thus there is no net increase in the reflectivity change ΔR when the front mirror reflectivity is increased further. This is also clearly illustrated in Figure 3.10 for the 5V-modulator design.

In summary the reduced R_{on} value as the front mirror reflectivity increases relative to the fixed back gold mirror reflectivity of 94% at lower voltage operation consequentially reduces the modulation $\Delta R=(R_{\text{on}}-R_{\text{off}})$ achievable.

5.2.2 Higher reflectivity back mirror

To avoid limiting the modulation in this way the back mirror reflectivity must be increased. A higher mirror reflectivity than 94% can be achieved by using either a combination of an Au and Bragg stack mirror, or a sole Bragg stack mirror. Figure 5.3 shows the modelled reflectivity achievable for a Bragg stack InAlAs / InGaAs mirror and a mirror consisting of a combination of Au and InAlAs / InGaAs Bragg stack periods, for increasing numbers of Bragg periods. The realistic refractive index values for the periodic Bragg stack layers InAlAs / InGaAs extrapolated from the experimental measurement in Chapter 4 Section 4.4.2.2 is used in this calculation. The refractive index step per period (Δn) is 0.3 and thus a high number of Bragg periods is required to achieve reflectivities greater than 99%. This Bragg stack layer structure is chosen particularly for this current structure because the layer composition matches the lattice constant requirements for this particular complex structure. The small refractive index step per period is unfortunate and will be seen to have a serious impact on device tolerances. This subject is investigated in detail in Chapter 6 when very high contrast/reflectivity Bragg mirrors with only a few periods are explored. For now the limits of the current device structure/material system are investigated.

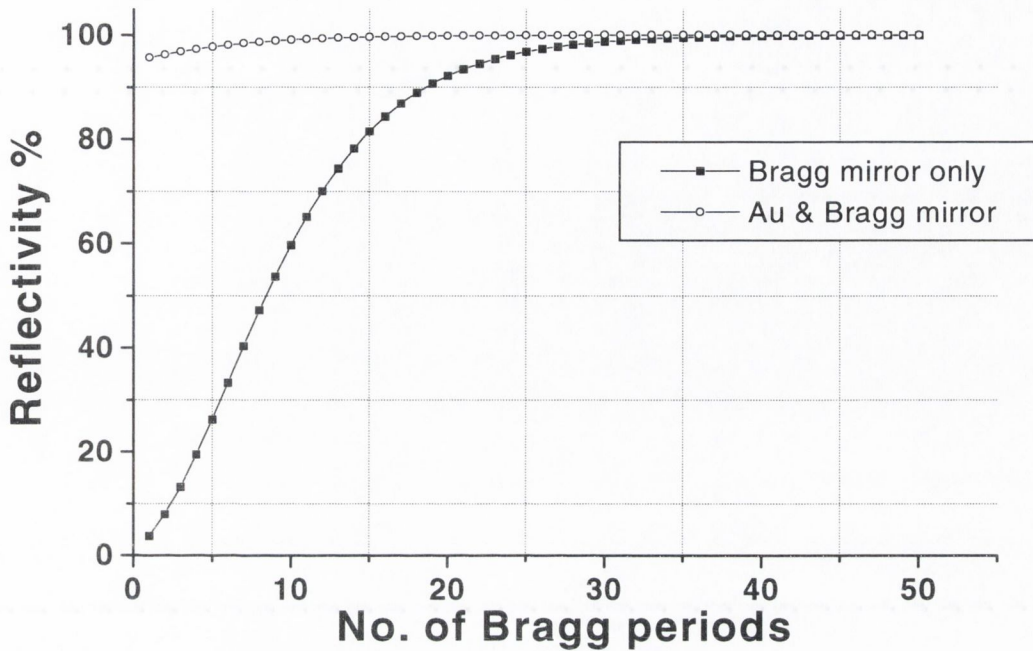


Figure 5.3: Reflectivity of a Bragg stack InAlAs / InGaAs mirror ($\Delta n=0.3$) and a mirror consisting of a combination of Au and an InAlAs / InGaAs Bragg stack, for increasing numbers of Bragg periods

For the combination mirror of Au and Bragg stack it can be seen that the reflectivity increases as expected from that of bare gold (~94%) approaching 100% as more and more Bragg periods are added. More than 30 periods of the sole Bragg mirror are required to achieve a reflectivity value of 99%. While only 10 periods are required in combination with the gold mirror. The unreliable nature of the gold mirror deposition was highlighted in Chapter 4 and thus applies here, but if a reliable and predictable fabrication process were developed, using a Bragg and gold combination would be ideal and has been used successfully in other devices. Using either of these mirrors as the back mirror in the existing structure would require even longer MBE growth times and alternative and/or extra device processing. The Bragg stack would either have to be doped if it is also to perform as the P-contact, or the electrical contact would be made directly to the p-region by etching away part of the Bragg layers. Both approaches do require additional fabrication and/or processing but have been achieved successfully for previous modulator structures. The additional growth time, although undesirable, is not foreseen to be a major problem.

5.2.3 Impact on cavity resonance reflectivity

The impact of the back mirror reflectance on the overall cavity resonance reflectance can be shown using the Fabry-Perot equations presented in chapter 2. When operating at the resonance wavelength and assuming normal incidence Equation 2.19 reduces simply to

$$R = R_0 \tag{5.1}$$

Where

$$R_0 = R_F \left[\frac{1 - \frac{R_\alpha}{R_F}}{1 - R_\alpha} \right] \tag{5.2}$$

And

$$R_\alpha = \sqrt{R_F R_B} e^{-\alpha L} \tag{5.3}$$

Equation 5.1 thus evaluates the reflectance of the Fabry-Perot resonance at normal incidence and at the resonance wavelength. This is plotted for increasing front mirror reflectance R_F and for various back mirror reflectance values R_B when there is no absorption in the cavity in Figure 5.4. The behaviour of the cavity reflectance is unexpected. The closer the back mirror reflectance is to 1, the higher the front mirror reflectance needs to be for significant destructive interference to take place. This unexpected behaviour is only significant at extremely high reflectance values of R_B ($>\approx 97\%$). At $R_B = 0.94$ the cavity reflectance behaves in a more ‘traditional manner’ where changes in the front mirror reflectance results in significant changes in the cavity resonance reflectance value. These results also show that when the effective back mirror reflectance ($R_{B(\text{eff})} = R_B e^{-2\alpha L}$) can only be changed by a small amount due to the available absorption being low (e.g. from $R_B = 0.998$ to $R_{B(\text{eff})} = 0.977$ in Figure 5.4) the cavity reflectance changes most when the front and back mirror reflectance are very high in value. This situation is typical of the low voltage operation condition where the available absorption is low and the effective back mirror reflectance can only be reduced by a small amount. This result suggests that increasing the back mirror reflectance will allow better modulation when the front mirror reflectance is high, as is the case at low voltage operation (Table 3.1).

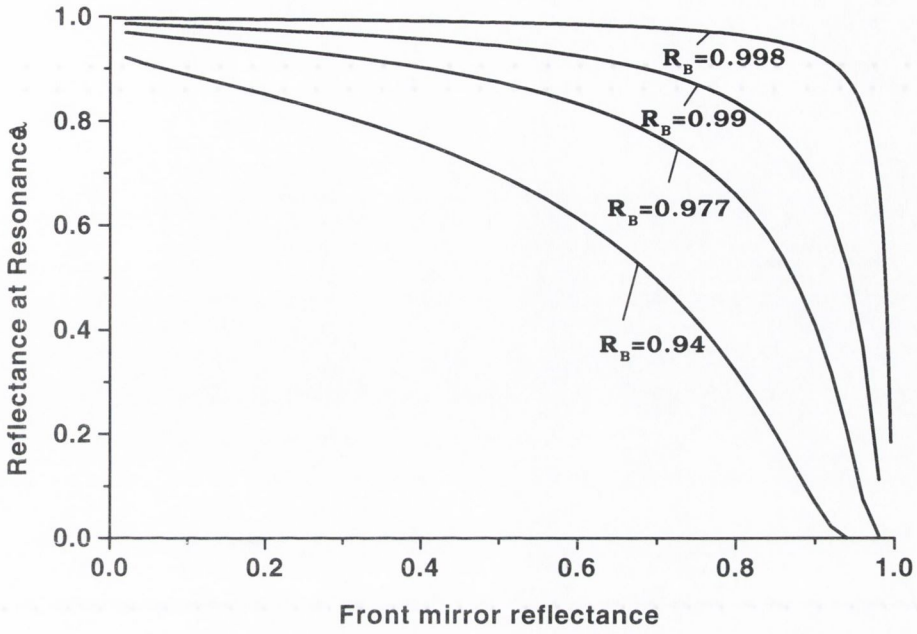


Figure 5.4: Fabry-Perot resonance reflectance for increasing front mirror reflectivity for various back mirror reflectance values calculated using the Fabry-Perot equations.

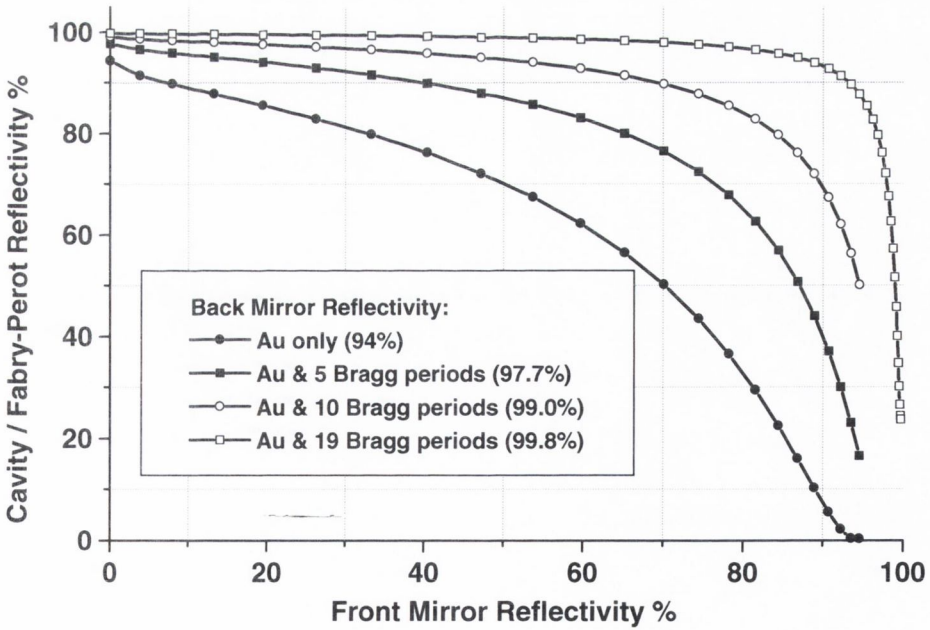


Figure 5.5: Reflectivity of Fabry-Perot resonance for increasing front mirror reflectivity calculated using the transfer matrix model.

As expected identical results are obtained using the transfer matrix model. Referring back to Figure 5.1, if the reflectivity at the Fabry-Perot resonance wavelength is plotted as a function of increasing front mirror reflectivity, the plot shown in Figure 5.5 is obtained for different back mirror reflectivities using the transfer matrix model. These modelling results show once again the sensitivity to the reflectivity of the back mirror. Small changes in its reflectivity can dramatically alter the behaviour of the cavity. In Figure 5.5 when the back mirror consists of Au only, this curve is represented of Figure 5.1. The resonance reflectivity is 0% when the front mirror reflectivity matches the back Au reflectivity (94%). The reflectivity of the Fabry-Perot resonance decreases rapidly as the reflectivity of the front mirror increases and approaches the impedance matching value. This is the reason why the modulation achievable in our initial modulator design was diminishing at lower operating voltages when the front mirror reflectivity was increasing relative to the fixed reflectivity value of the Au mirror. The reflectivity value of the Fabry-Perot resonance (R_{on}) sets the maximum modulation value achievable for any particular structure working as a “normally on” device. For the 1V modulator design the reflectivity of the front mirror is approaching 90% which meant the Fabry-Perot reflectivity R_{on} was close to 10% (see Figure 5.5) and the predicted modulation was 9% (Table 3.1). To avoid limiting the modulation in this way, the back mirror reflectivity must be increased. When the reflectivity of the back mirror is increased as shown in Figure 5.5, the Fabry-Perot reflectivity does not decrease as rapidly, remaining at higher values until the front and back mirror reflectivities are much closer in value. This result means the starting reflectivity value R_{on} can have a high value and reflectivity change ($R_{on}-R_{off}$) can thus have a large value. The loss in absorption due to the fewer numbers of MQWs at lower voltage operation can be compensated by a higher finesse cavity and good modulation should be achieved by using a higher reflectivity back mirror.

5.3 Modelled Fabry-Perot modulator results

The Fabry-Perot modulator structures (Figure 4.1(b)) modelled in Chapter 3 with a back gold mirror were remodelled now incorporating a higher back mirror reflectivity. Figure 5.6 shows the predicted modulation for increasing back mirror reflectivity at each operating voltage. The front mirror reflectivity shown is the optimum reflectivity for maximum reflectivity change.

As expected the 5V modulator gives a modulation of 46% when there are no back Bragg periods in front of the Au and the back mirror reflectivity is 94%. The modulation can be increased to 58% by adding Bragg stack periods to the Au mirror, increasing its reflectivity as seen in Figure 5.3. The interesting result here is for structures designed to operate at lower voltages. For all operating voltages, right down to 1V, a recovery in modulation can clearly be seen as the back mirror reflectivity increases. The lower the operating voltage the stronger this recovery is. An upper limit of 58% modulation can be achieved at all operating voltages, the lower the operating voltage, the more back Bragg periods are required to achieve this upper limit. This is consistent with the results presented in Figure 5.5. Lower voltage devices have higher reflectivity front mirrors which require larger numbers of back Bragg periods to keep a high R_{on}

starting reflectivity. The reflectivity of the back mirror is found to be extremely important for these Fabry-Perot devices. Small changes in reflectivity from 94% for that of Au to 99.9% can increase the modulation at 2V and 1V by a factor of 2.5 (24%→58%) and 6.5 (9%→58%) respectively.

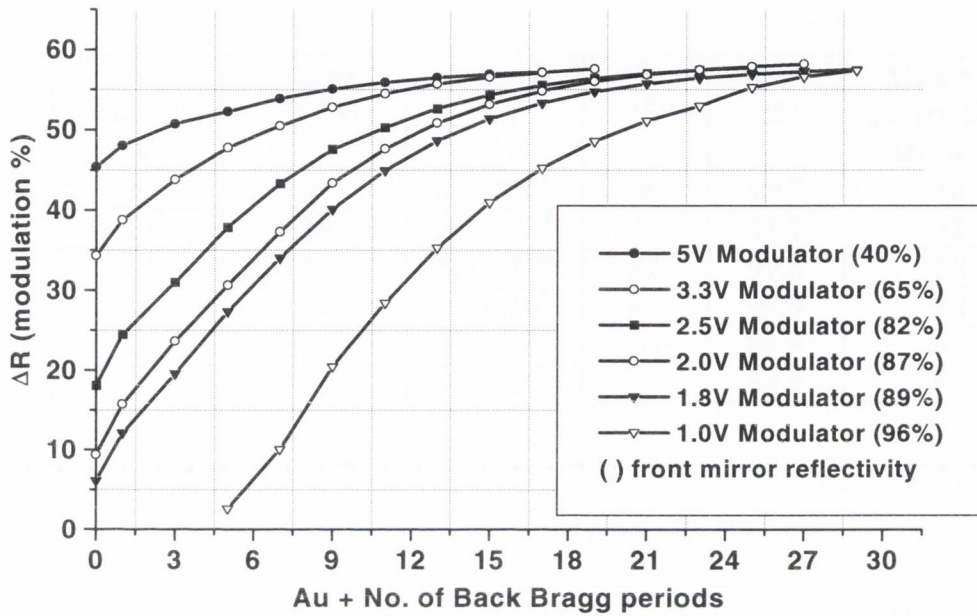


Figure 5.6: Modulation predictions for optimised structures as the reflectivity of the back mirror increases by increasing the number of Bragg periods in front of the gold mirror.

The modulation performance of these devices is measured by the reflectivity change because they are optimally designed for differential operation, and it is this parameter that device modelling has sought to maximise. Differential operation is specific to certain applications and interconnect architectures such as the SPOEC interconnect, other architectures may require individual modulator operation and in this case device contrast can be a useful measure of modulation performance. The reflectivity for the optimised devices shown in Figure 5.6 generally falls from $R_{on} = 67\%$ to $R_{off} = 9\%$. This is generally true for each operating voltage from 5V to 1V and gives a device contrast usually close to 7.5:1. Although the device design for maximum contrast requires a different design as discussed in Section 3.2.1, the contrast attainable using the current reflectivity change designed structures is relatively good [1].

5.3.1 Summary of results

Modelling results and device structure details presented above in Figure 5.6 for the ideal Fabry-Perot modulator structure for the current device and material system are summarised in Table 5.1. These structure details are for maximum modulation and include the mirror reflectivities required at each operating voltage.

Voltage (and bias) V	No. of MQWs	E-Field Vm^{-1}	R_f %	R_B %	Max ΔR Fabry-Perot Device %
5	56	5.77×10^6	40	99.7	58
3.3	38	5.84×10^6	65	99.7	58
2.5	28	5.73×10^6	82	99.8	58
2	24	5.71×10^6	87	99.9	58
1.8	22	5.61×10^6	89	99.9	58
1	12	5.63×10^6	96	99.9	58

Table 5.1: Summary of the modelling results for operating voltages from 5V to 1V showing the reflectivity of the front and back mirrors required to achieve **maximum** modulation at these operating voltages.

The main difference between the earlier results in Table 3.1 for the structure using a gold back mirror and these results is the increased back mirror reflectivity and thus the 58% modulation achievable at all voltages. The back mirror reflectivity values are very high but are typical of the values required and used in VCSEL devices. Achieving a mirror reflectivity of 99.9% is not a trivial task but current VCSEL structures already use good quality, high reflectivity mirrors of this magnitude that are produced in large arrays [2]. The ideal very low voltage modulator structure resembles very much a typical VCSEL device structure. The impressive progress and results achieved in fabrication of VCSEL devices [3] should be adaptable to Fabry-Perot modulator devices for device fabrication of these low voltage structures.

The optimum numbers of MQWs are identical to the structure that used a gold back mirror only in Chapter 3. This result is not unexpected. As we have just seen, the back Au mirror reflectivity was limiting the R_{on} value. When there is no absorption in the cavity, the R_{on} value will have a definite value for a fixed R_f and R_B value. So when different numbers of MQWs are introduced into the cavity, the relative difference in reflectivity change ΔR for different numbers of MQWs would be expected to be the same when the gold mirror was used and when the higher reflectivity back mirror is used. The optimum number of MQWs for whatever back mirror reflectivity is used should give the best modulation and modelling results in Table 3.1 and 5.1 have shown this to be true.

5.3.2 Optical cavity formed using a Bragg stack front and back mirror

The device modelling for the 5V-modulator design, but in the case that both front and back mirrors are Bragg stacks are shown in Figure 5.7.

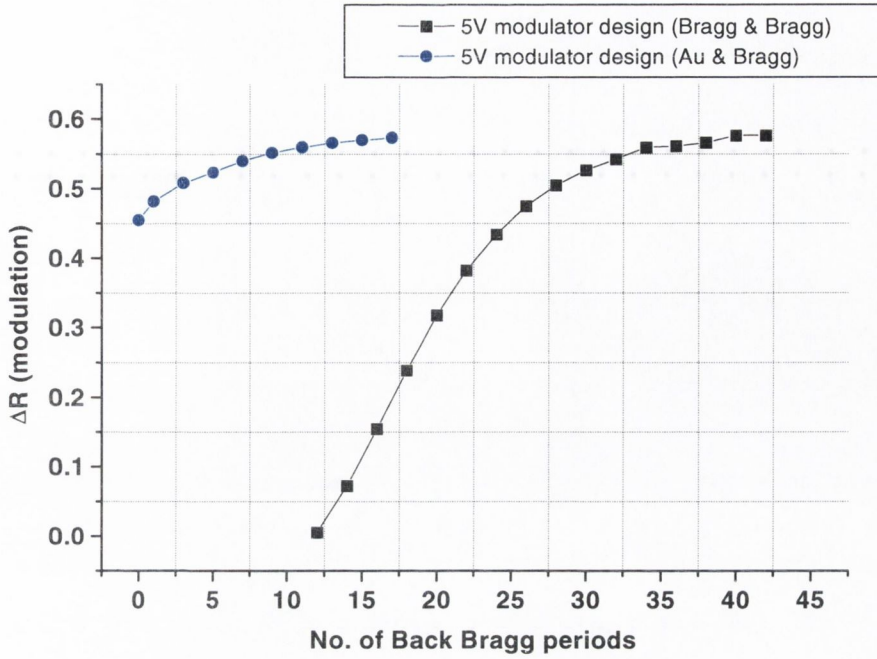


Figure 5.7: Resulting reflectivity change (ΔR) for the 5V optimised structure where the front and back mirrors are Bragg stack only.

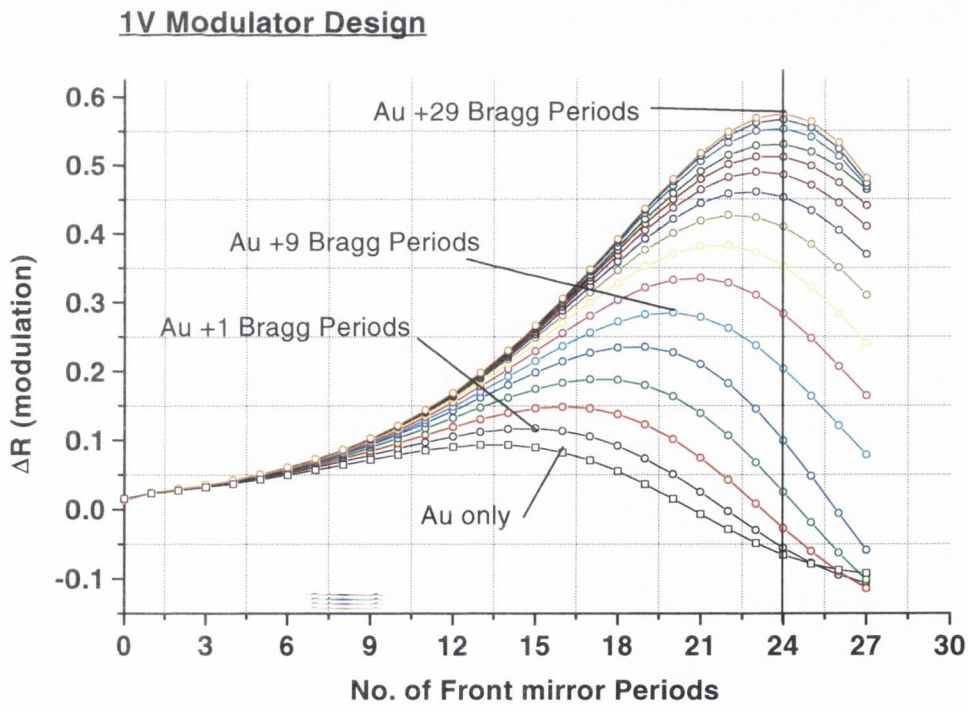


Figure 5.8: The complete picture of the modulation achievable for the 1V modulator for different numbers of front and back Bragg periods (Back mirror Bragg & Au).

In this case gold is not used in the back mirror. The result from the previous Figure 5.5 is also included for comparison. Once again 58% modulation can be achieved but when using a Bragg stack solely for the back mirror, a lot more periods are needed to reach this upper limit, as might be expected from Figure 5.3. This result shows that the recovery in modulation is due to the Fabry-Perot cavity reflectivities and not due to unusual phase changes or any other hidden effects associated with combining a Bragg and Au mirror. It also shows that these modulators could be designed using Bragg stack mirrors only for the front and back mirrors. The number of periods required can be reduced if the refractive index contrast Δn could be increased. The effect on the strain balancing process in the MQWs (section 2.8) must of course be considered in this case.

5.3.3 Modulation map of 1V modulator device

Designing a Fabry-Perot structure to achieve a specific modulation value e.g. 30% can be done in more than one way. Figure 5.8 shows the complete picture of the results presented in Figure 5.6 for the 1V modulation achievable for different combinations of front and back Bragg periods (Back mirror Bragg & Au). The maximum modulation can be reached by using a front mirror consisting of 24 periods and a back mirror consisting of an Au mirror and 29 Bragg periods as seen already in Figure 5.6. To achieve 30% modulation, the minimum numbers of back mirror periods required are 20 and 9 front mirror periods as seen in Figure 5.8. It could alternatively be achieved in a number of other ways e.g. using 17 front Bragg periods and 13 back Bragg periods. To maximise device tolerances, previous results have shown that it is better to design a structure with a modulation value somewhat higher than the required value. Device tolerance results for the 2.5V modulator presented in Section 3.4.1 demonstrated this point. The modulation achievable was $\approx 30\%$ but this resulted in a poor spectral and angular tolerance and practical operation was not possible if a minimum 30% modulation is required. This is a consequence of the unique spectral shape of the Fabry-Perot resonance as explained in Section 3.4.1. Device tolerances of the current devices in Table 5.1 above are addressed in Section 5.5.

5.4 Maximum attainable reflectivity change

A maximum reflectivity change (ΔR) of 58% is achieved at all operating voltages. Since the electric field applied across the MQWs is similar (Table 5.1) at each operating voltage this means that the absorption spectrum at each operating voltage is similar. The difference between devices as the operating voltage is reduced is simply that the overall absorption value is decreasing. The reduced overall absorption is compensated for by a higher finesse cavity that stores the light in the cavity allowing increased interaction with the reduced number of MQWs, effectively increasing the overall absorption. This has been seen experimentally for GaAs/AlGaAs quantum wells/barriers. Whitehead et al. used 15 MQWs and obtained $\Delta R \approx 40\%$ for a 3.5V swing [4]. The device was operating at the hh exciton peak and thus a normally ‘off’

device. The same author later showed a normally ‘on’ device operating to the longer wavelength side of the hh exciton peak with 24 MQWs ($R_B=99\%$, $R_F=76\%$) and demonstrated $\Delta R \approx 55\%$ for 3V operation [5]. Yan et al. [6] measured $\Delta R=47\%$ for a 2V swing also using 24 MQWs with $R_F=80\%$. The measured data in this case shows a low R_{on} value and the ΔR value, although good, appears to be limited by a low back mirror reflectivity in this device. Progress in low voltage operation for InGaAs wells operating around 1000nm has not been as good. The best results come from Fabry Perot strained layer superlattice structures where $\Delta R \approx 40\%$ is achieved at 0 to -4V operation [7,8]. Other Fabry Perot devices having InGaAs MQW active regions typically show reflectivity change values ranging from 40% up to 77% [9,10,11,12] but these devices all have large operating voltages (8V to 22V). The modelling results in Table 5.1 indicate that lower voltage operation should be possible.

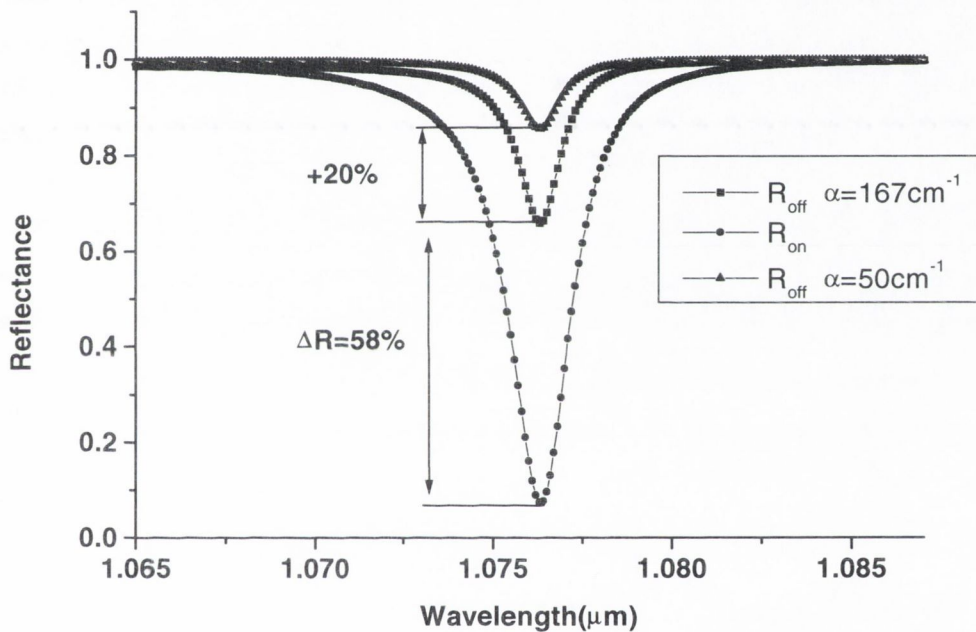


Figure 5.9: Reflectivity spectra of the optimum 2V-modulator structure. This device has a residual absorption value $\alpha_0=167\text{cm}^{-1}$. If the residual absorption is reduced to $\alpha_0=50\text{cm}^{-1}$ the R_{off} value and the reflectivity change increase by 20%.

To maximise the reflectivity change $\Delta R = (R_{on}-R_{off})$, R_{on} is the critical value and this is dependent on the relative front and back mirror reflectivities as shown in Figure 5.2. At lower operating voltages where high reflectivity front mirrors are required to compensate for the reduced total absorption, the back mirror reflectivity is increased accordingly to maintain a high R_{on} starting reflectivity value and a large modulation. As mentioned previously the reflectivity for the optimised devices shown in Figure 5.5 generally falls from $R_{on} = 67\%$ to $R_{off} = 9\%$ and is true for each operating voltage from 5V to 1V. The

residual absorption value α_0 (Figure 3.9) and back mirror reflectivity sets the upper $R_{on} = 67\%$ value and the absorption change $\Delta\alpha$ then changes this value to $R_{off} = 9\%$. If the modulation is to be improved it is clear that the residual absorption needs to be reduced, as this is where the majority of potential modulation is lost (33%). If thought of in terms of mirror reflectivities, the R_{on} value is high when the effective back mirror reflectivity $R_{B(eff)} = R_B e^{-2\alpha L}$ is as large as possible. Since R_B already has a value >0.99 , decreasing the absorption value (α) can only increase the $R_{B(eff)}$ value and thus the R_{on} value. The high residual absorption value, α_0 , is a consequence of the InGaAs material system and its relatively broad exciton linewidth as discussed in section 3.3.1. To achieve the ideal modulator structure the AlGaAs/GaAs system should possibly be better. Here the exciton linewidth is considerably reduced, resulting in a lower α_0 value (Figure 2.5) [13]. This allows a larger R_{on} value to be achieved. This point is illustrated in Figure 5.9, which shows the reflectivity spectra of the optimum 2V-modulator structure. This device has a residual absorption value $\alpha_0 = 167\text{cm}^{-1}$ at the operating wavelength. If the residual absorption is reduced to $\alpha_0 = 50\text{cm}^{-1}$ the increase in the R_{off} value is dramatic and is shown also in Figure 5.9. There is a 20% increase in reflectivity and thus and 20% increase in reflectivity change. The device spectral bandwidth (see Section 5.5.1) also increases by 0.5nm.

The exciton absorption coefficient is larger in this material system compared to the InGaAs because of the larger effective hole and electron masses [14] and the flexibility allowed in lattice matched quantum well design (Section 2.6). This brings the possibility of a larger absorption change $\Delta\alpha$ value and thus the R_{off} value may also be reduced further than the 9% achievable above. This allows the R_{on} and R_{off} values to be maximised and minimised respectively, thus maximising the modulation $\Delta R = (R_{on} - R_{off})$ achievable. Previous work on Fabry-Perot modulator devices with the AlGaAs/GaAs material system has already demonstrated that very high reflectivity changes $>90\%$ are possible [15]. Our modelling results indicate that the AlGaAs/GaAs material system has the potential to produce the largest modulation values and may be the best semiconductor material to use in future low voltage interconnect systems. As we will see in Section 5.5 large modulation values also give good device tolerances due to the inherent shape of the Fabry-Perot spectrum.

These modulation results are very promising. These results show that amplitude modulation that is of sufficient value can be achieved by Fabry-Perot modulator devices at operating voltages that are compatible with current and future CMOS voltages. The possibility of low voltage operation requires the use of very high finesse cavities. Traditionally high finesse cavities have proved difficult to work with due to their poor practical operating tolerances. These and other critical operational tolerances are investigated in detail in Section 5.5 for the above devices.

5.5 Operating tolerances

For practical operation in an interconnect system these Fabry-Perot modulator devices must have good tolerances to MBE growth lateral non-uniformities, have a broad spectral bandwidth and operation must be possible over a reasonable range of incident angles. The high finesse cavities required at lower voltage operation seriously impacts on these operational parameters. The longer effective cavity length due the use of Bragg stack mirrors also deteriorates the growth tolerance. The transfer matrix model is used to investigate these tolerances in detail to see if these devices could be used in a real working system. The impact of lower voltage operation on device modulation bandwidth, increased sensitivity to optical power saturation and ambient temperature change is also presented.

5.5.1 Spectral Bandwidth

The device spectral bandwidth is the wavelength range over which a desired reflectivity change is achievable. A reflectivity change value of 30% corresponding specifically to the minimum modulation value required for the SPOEC interconnect system is used as the benchmark in this work. For a more general comparison between operation at different operating voltages the full width half maximum (FWHM) value is used.

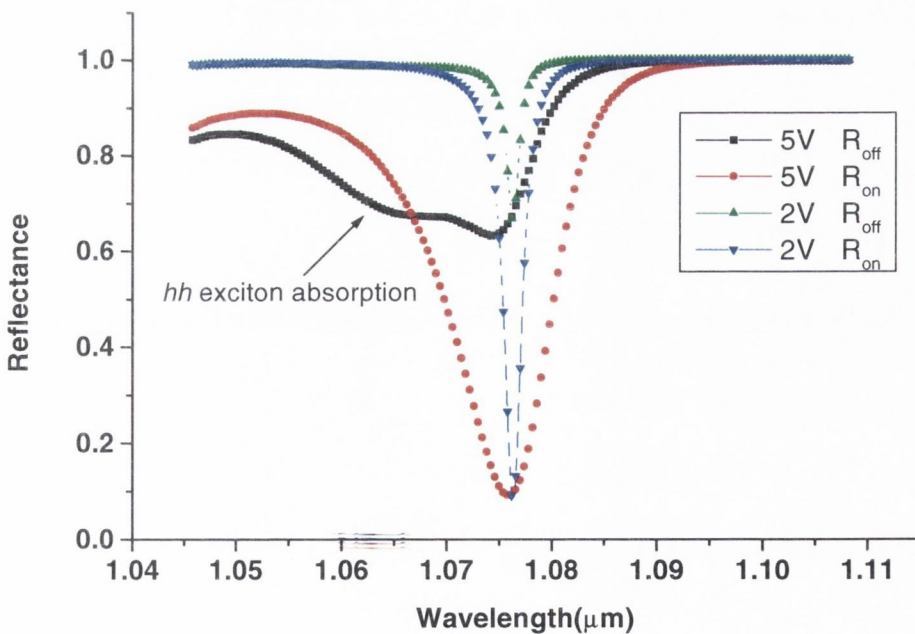


Figure 5.10: Reflectivity spectra for the optimum 5V and 2V modulator devices whose structure is outlined in Table 5.1, giving a maximum reflectivity change of 58%.

From Table 5.1 the modulation achievable at each operating voltage is 58% thus the spectral bandwidth value at FWHM and our benchmark are equivalent. The spectral bandwidth is calculated by subtracting the R_{off} spectrum from the R_{on} spectrum. The reflectivity spectra for the optimum 5V and 2V modulator devices giving 58% reflection change are shown in Figure 5.10. These can be directly compared to Figure 5.2, which shows the same spectra but where the device structures in Figure 5.2 use a back mirror consisting of gold only. This comparison will give an insight into how simply increasing the back mirror allows the reflectivity change to be improved and then the device spectral bandwidth is examined. The first noticeable difference between Figure 5.10 and 5.2 is the stronger influence on the reflectivity spectra of the cavity finesse. The Fabry-Perot resonance in the 5V R_{off} curves is more defined around the resonance wavelength although the exciton absorption can still be seen around 1065nm and the resonance is being 'pulled' to shorter wavelengths, but not as strongly as in Figure 5.2. The increased back mirror reflectivity of 99.7% increases the R_{on} value to 66% from 60% as expected from Figure 5.5 above. The higher back mirror reflectivity permits a higher front mirror reflectivity to be used compared to Figure 5.2 and the R_{off} value thus decreases from 14% to 8% giving a final reflectivity change of 58%. The most dramatic change is in the 2V R_{off} curve. The higher back mirror reflectivity of 99.9% allows the R_{on} value to increase to 66% from 44% and a higher front mirror reflectivity allows the R_{off} value to fall to 8% from 20% giving a dramatic increase in modulation from 24% to 58%.

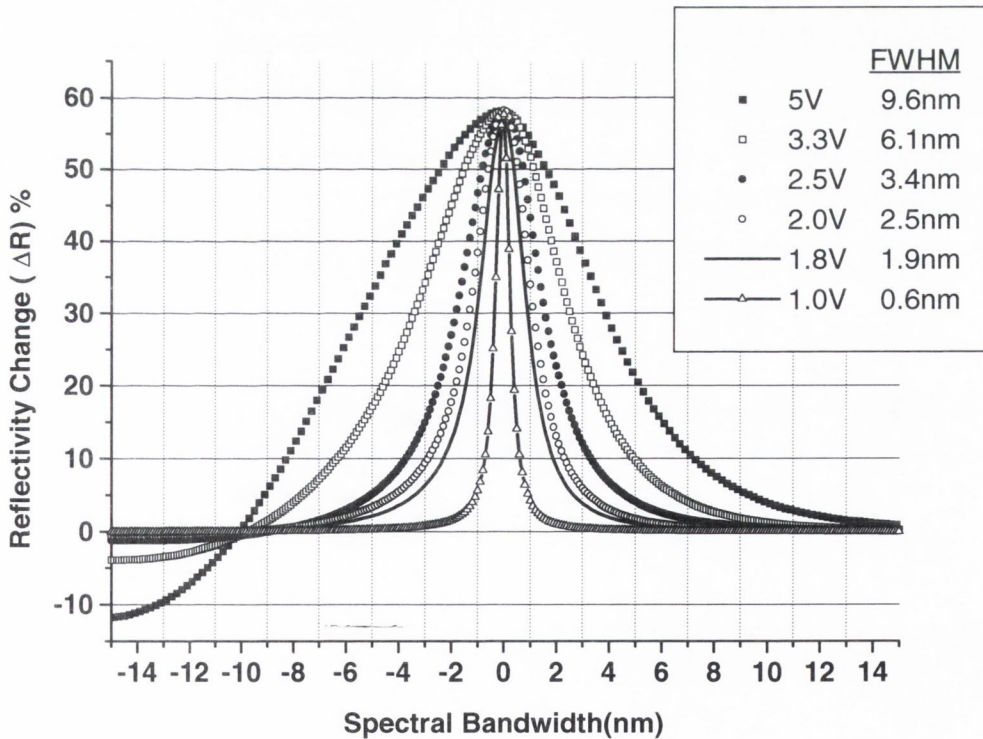


Figure 5.11: Spectral bandwidth for the optimum 5V and 2V modulator devices whose structure is outlined in Table 5.1, giving a maximum reflectivity change of 58%.

The most noticeable feature that stands out when comparing Figure 5.9 and 5.2, is how the reflectivity spectra have narrowed. Higher finesse cavities result in spectrally more narrow Fabry-Perot resonances (Chapter 2) and thus much reduced spectral bandwidth when the R_{off} and R_{on} values are subtracted. For operation at lower voltages Table 5.1 shows how the front and back mirror reflectivities increase and thus the cavity finesse increases as the operating voltage decreases. The narrowing of the Fabry-Perot resonance at lower voltage operation is expected to result in reduced spectral bandwidth. The spectral bandwidth for the device structures summarised in Table 5.1 is calculated and presented in Figure 5.11. In each case the physical cavity thickness has been reduced to a minimum size while keeping the Fabry-Perot resonance at the required wavelength. Shorter cavity thicknesses produce broader resonance widths and thus more spectral bandwidth, an issue which is addressed in detail in Chapter 6. In this case the results presented at each operating voltage give the maximum spectral bandwidth possible for the current device structure. The FWHM spectral bandwidth at each operating voltage is shown on the right hand side of Figure 5.11. The 0nm spectral bandwidth on the x-axis corresponds to the operating wavelength. At 5V on average there is a half-width of 4.8nm either side of the operating wavelength within which greater than 29% reflectivity change is achievable. The spectral bandwidth goes to negative values to the left of the 0nm spectral bandwidth mark, this is due to operation as a ‘normally-on’ device at these shorter wavelengths as can be seen in Figure 5.9 above for 5V operation. This becomes less pronounced at lower voltage operation where the cavity absorption is much reduced and cavity finesse higher. The expected reduction in bandwidth as the operating voltage is reduced is clear. It becomes more serious as the operating voltage gets smaller. A factor of 2 change in operating voltage from 5V→2.5V results in only a factor of 3 reduction in spectral bandwidth but a factor of 5 change in operating voltage from 5V→1V results in a factor of 16 reduction in spectral bandwidth. At operating voltages lower than 2V the spectral bandwidth decreases rapidly to very small values, making practical operation of these devices in a real system difficult.

The increasing cavity finesse required at lower voltage operation results in a reduction in the Fabry-Perot resonance width and thus a reduction in the device spectral bandwidth. If a device is required to operate with a specific modulation value, such as 30% in the SPOEC system, the excess modulation can be exchanged for some spectral bandwidth by decreasing the finesse of the optical cavity. Figure 5.12 shows the modelled spectral bandwidth for the optimum 2V-modulator structure with decreasing front mirror reflectivity values. For a required operation of 30% modulation the spectral bandwidth increases from 2.5nm to 3nm for a reduction in front mirror reflectivity from 87% to 65%. Much larger gains are made at lower reflectivity change values. For a required operation of 20% modulation the spectral bandwidth increases from 3.3nm to 5.2nm for a reduction in front mirror reflectivity from 87% to 54%. At 10% modulation the spectral bandwidth increases from 5.1nm to 9.3nm when the front mirror reflectivity is decreased from 87% to 26%. The shape of the spectral bandwidth curve is a consequence of the shape of the Fabry-Perot resonance curve, which narrows sharply at higher reflectivity values.

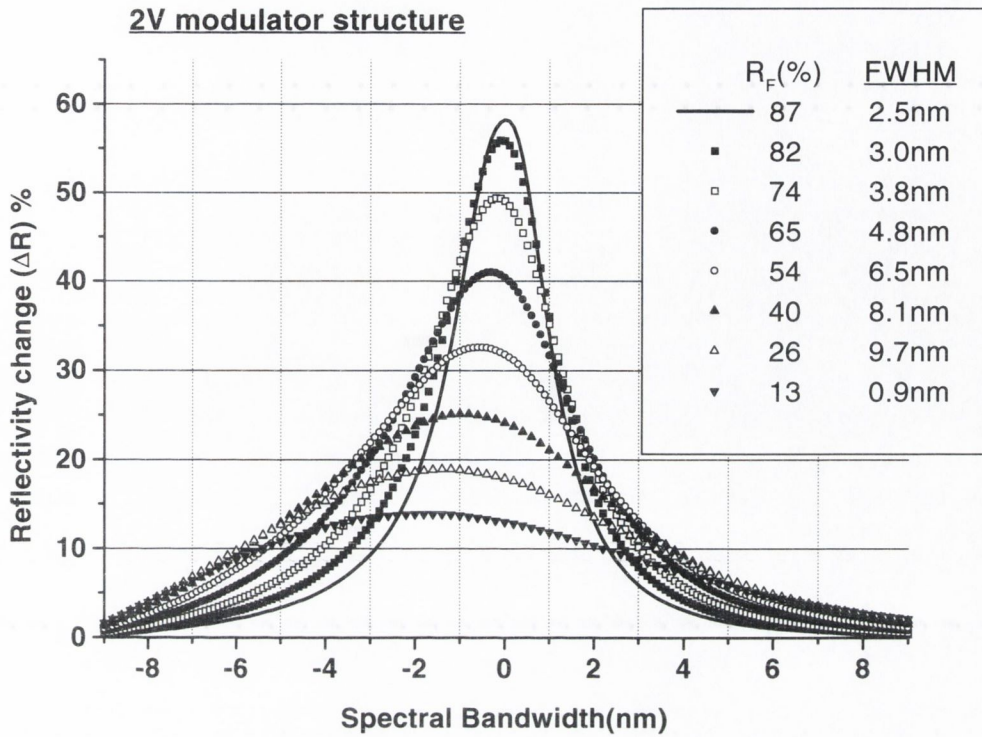


Figure 5.12: Modelled spectral bandwidth for the optimum 2V-modulator structure with decreasing front mirror reflectivity values.

Thus the resultant spectral bandwidth curve, which is calculated from $\Delta R = (R_{on} - R_{off})$, narrows at high reflectivity change values but becomes a lot broader at lower values and broadens further as the cavity finesse is lowered. Thus in going from a 30% modulation value to 10% the spectral bandwidth increases from 2.5nm to 9.3nm. These modelling results show that the modulation value required can be reduced and traded for spectral bandwidth. The modulation value required for a particular system must be given careful consideration. If this value is chosen optimally the device can be designed so it also operates with maximum spectral bandwidth. Similar modelling for operation at 5V to 1.0V shows gains in spectral bandwidth when the front mirror reflectivity is optimised but the largest gains are made at higher operating voltages, which already have lower finesse cavities. Figure 5.10 shows how poor the bandwidth of the 1V modulator is at 0.6nm. When the front mirror reflectivity is reduced at 30% modulation this value increases only to 0.8nm. At 10% modulation the change is from 1.3nm to 3.2nm. The very high finesse cavity required for this very low voltage operation narrows the resonance width to such an extent that its spectral bandwidth is extremely small and small reductions in the front mirror reflectivity do not improve the spectral bandwidth significantly. Operation of these devices at 1V operation looks difficult. A spectral bandwidth of 0.8nm is very small and the resulting tolerances of the above factors are expected to be poor as will soon be seen. The use of a semiconductor laser coupled to an external cavity was suggested to

stabilise the wavelength of the modulator read laser but stability to 0.8nm may limit the use of this method. A large spectral tolerance makes MBE growth of these devices easier. MBE growth tolerance modelling results are examined in the next section. Here a minimum required spectral bandwidth value is suggested which will ultimately set a value on the lowest operating voltage for these current devices.

In Section 5.5.1 the spectral bandwidth of the modulator devices has been examined for the current device and material system. Modelling results have shown the bandwidth to reduce dramatically at lower voltage operation. The spectral bandwidth can be increased somewhat by designing the optical cavity to have the optimum reflectivity mirrors to achieve a required modulation value. The shape of the Fabry-Perot resonance has shown that the reflectivity change value for a particular system must be chosen carefully. Values between 30% to 10% have dramatically increasing spectral bandwidth values, and thus choosing an excessive the modulation value results in much poorer spectral bandwidth tolerances. Having a large spectral bandwidth is beneficial in many ways but most importantly to the device fabrication. The device MBE growth tolerances are now examined in detail.

5.5.2 MBE growth tolerances

A major concern with Fabry-Perot modulator structures is their tolerance to changes in cavity thickness. The thickness of the device structure changes from the centre of the wafer to the edge as discussed in Chapters 3 and 4. This causes the Fabry-Perot resonance to shift in wavelength from the desired operating wavelength. A large device tolerance to this thickness change is required to allow the fabrication of large device arrays and to ensure a large area of the wafer can be used for device processing. As discussed in Section 3.4 for structures grown by molecular beam epitaxy (MBE) or MOVPE there are two issues. One is the absolute accuracy of the thickness grown in the centre of the wafer. This can be addressed by in-situ growth monitoring and/or post-growth processing of the wafer. The second is non-uniformity across a wafer, resulting from growth geometry as seen in Figure 4.15 for wafer B814. This generally cannot be removed and must be tolerated. In this section operation at a fixed wavelength is discussed where the structure is designed and grown to a fixed specified wavelength such as the 1047nm Nd:Ylf laser line. This modulator read wavelength is not tuneable around this wavelength and thus it is critical that the modulator devices are grown correctly to this wavelength. The second case discussed is where the read wavelength is tuneable around a central wavelength, in this case device growth is targeted at this wavelength and if grown slightly wrong the read laser can be tuned to the required wavelength. We will primarily consider operation at a fixed wavelength as the current and foreseeable wide spread use of diffractive optics in interconnect systems imposes this requirement.

5.5.2.1 Absolute growth accuracy

The absolute accuracy of the thickness grown at the centre of the wafer was discussed in Section 3.4.3. Here it was concluded that in-situ growth monitoring was essential to achieve high accuracy of the absolute growth thickness at the wafer centre. It was also concluded from previous results for VCSEL and modulator growth that the minimum allowed device spectral bandwidth is 4nm. The larger the spectral bandwidth the better, but any smaller than this and it is most probable that device operation at the centre of a wafer at the desired operating wavelength would not be possible. This leads us to conclude from Figure 5.11 that the minimum operating voltage for the current modulator structure is $\approx 2.5\text{V}$ since it has a spectral bandwidth of 3.4nm. The other important point made in Section 3.4.3 is related to the thickness non-uniformity across a wafer. Figure 4.15 shows the percentage change in cavity thickness across the wafer for wafer B814. The cavity thickness generally decreases moving away from the centre of the wafer. Thus for this reason and for these devices it is advantageous to growth the cavity thickness too large, to a thickness which will still give the required modulation value of 29% at λ_{op} . In doing this there will be a larger part of the wafer from which to process devices as the cavity thickness will decrease moving towards the edge of the wafer with the modulation simultaneously increasing to 58% and then decreasing again. The larger the spectral bandwidth, the more area of the wafer devices can be used. Reducing the finesse of the cavity can

also increase the spectral bandwidth of the device. The resulting improvement to lateral growth non-uniformities from using a lower finesse cavity to the 2V-modulator device is shown later in Figure 5.18. This allows a greater percentage of the wafer to be processed and the possibility of larger device arrays.

5.5.2.2 Growth non-uniformity across a wafer

To study the modulator growth tolerance, the modulation was calculated when the actual physical thickness deviated from the ideal optical cavity thickness for each modulator structure. The modulation changes because the curves shown in Figure 5.11 above shift in wavelength from the fixed operating wavelength, as the cavity thickness increases or decreases from the ideal thickness. Thickness fluctuations across the wafer also change the $\lambda/4$ layer thickness of the Bragg mirror. In terms of mirror reflectivity this has only the minor effect of shifting only the central wavelength of the Bragg mirror. The Bragg mirror stop-band has sufficient spectral bandwidth so the mirror reflectivity is relatively unchanged at the operating wavelength. Figure 5.13 shows the resulting calculated modulation when the actual thickness deviated from the ideal cavity thickness for each modulator structure.

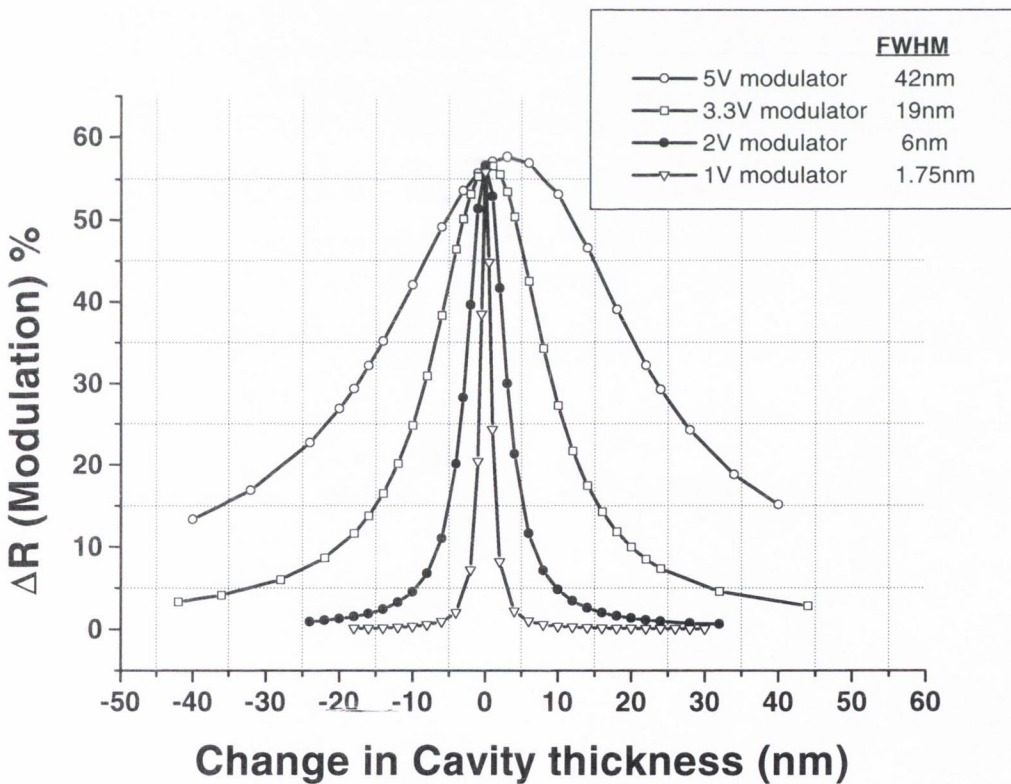


Figure 5.13: Resulting calculated modulation when the actual thickness deviated from the ideal cavity thickness for each modulator structure.

These results show that as might be expected, the lower voltage cavities are more sensitive to cavity thickness changes and thus is reflected in the FWHM values shown in Figure 5.13. There are a number of factors that influence the resulting curves in Figure 5.13 and that were not discussed in Section 3.4 but are dealt with here. The shift $\Delta\lambda$ in wavelength from the fixed operating wavelength λ when the cavity thickness t changes by Δt is given by

$$\frac{\Delta\lambda}{\lambda} = \frac{\Delta t}{t} \quad (5.4)$$

According to this equation the percentage change in cavity thickness causes the same percentage change in the resonance position wavelength from the operating wavelength λ . This equation means that shorter cavities are more sensitive to thickness changes. Using equation 5.4 above if a 1λ cavity in air of thickness 1000nm changes by 10nm, the resulting shift in resonance wavelength from 1000nm will be 10nm (1%). But if a 1λ cavity in semiconductor ($n=3.5$) is used which has a shorter cavity thickness of $(1000/3.5)$ 285.7nm and it also changes by 10nm, then the resulting shift in resonance wavelength from 1000nm will be 35nm (3.5%). This equation has a devastating effect on short optical cavities, resulting in much larger wavelength shifts. But this is not the complete picture. When the optical cavity gets shorter the spectral bandwidth of the Fabry-Perot resonance broadens. This is true at all thicknesses but is most dramatic when the cavity thickness is of wavelength size, this is the so called ‘microcavity effect’ and its benefits to these modulator devices are dealt with in detail in Chapter 6. If the resonance curves and thus the spectral bandwidth curves (Figure 5.11) are broader, then the modulation value will remain high for a greater thickness change. We now have the interesting situation of two competing factors. The shorter optical cavity shifts the resonance faster in wavelength (equation 5.2) reducing the modulation value more quickly. The increased spectral bandwidth due to this shorter cavity will keep the modulation value high for larger thickness changes.

To look more closely at these competing factors the transfer matrix model was used to model the tolerance to thickness change (as done in Figure 5.13) of the 2V-modulator structure for different physical cavity thicknesses. This was done by increasing the thickness of the **p** and **n** doped layers which are effectively used as spacers, but have the required thickness to operate at the device operating wavelength. The results for a physical cavity thickness of $\approx 750\text{nm}$ (24MQW and 400nm spacer) and a cavity thickness 15 times larger of $\approx 11.6\mu\text{m}$ (24MQW and 11.3 μm spacer) for the 2V-modulator are shown in Figure 5.14. The resulting tolerances to changes in cavity thickness are very similar for both cavity sizes. Thus the two competing factors above are effectively cancelling each other out. An interesting outcome of MBE growth of these devices is that the thickness change across a wafer is normally a percentage change of the centre wafer thickness (see Chapter 4). Previously Figure 4.15 showed the percentage change in centre thickness across wafer B814. A truer picture of the tolerance to thickness change across a wafer is produced if the thickness change in Figure 5.14 is represented as a percentage change in cavity thickness and is presented in Figure 5.15. It is clear from Figure 5.15 that having the shortest cavity thickness gives the greatest tolerance to percentage thickness change across a wafer.

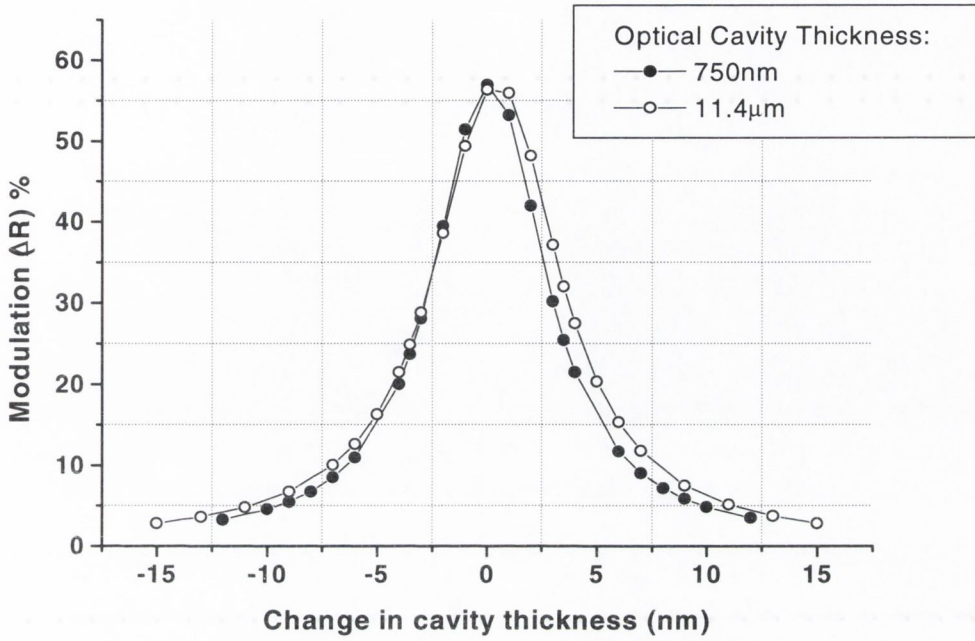


Figure 5.14: Modelling results for a cavity thickness of $\approx 750\text{nm}$ (24MQW and 400nm spacer) and a cavity thickness 15 times larger of $\approx 11.6\mu\text{m}$ (24MQW and 11.3 μm spacer) for the 2V-modulator.

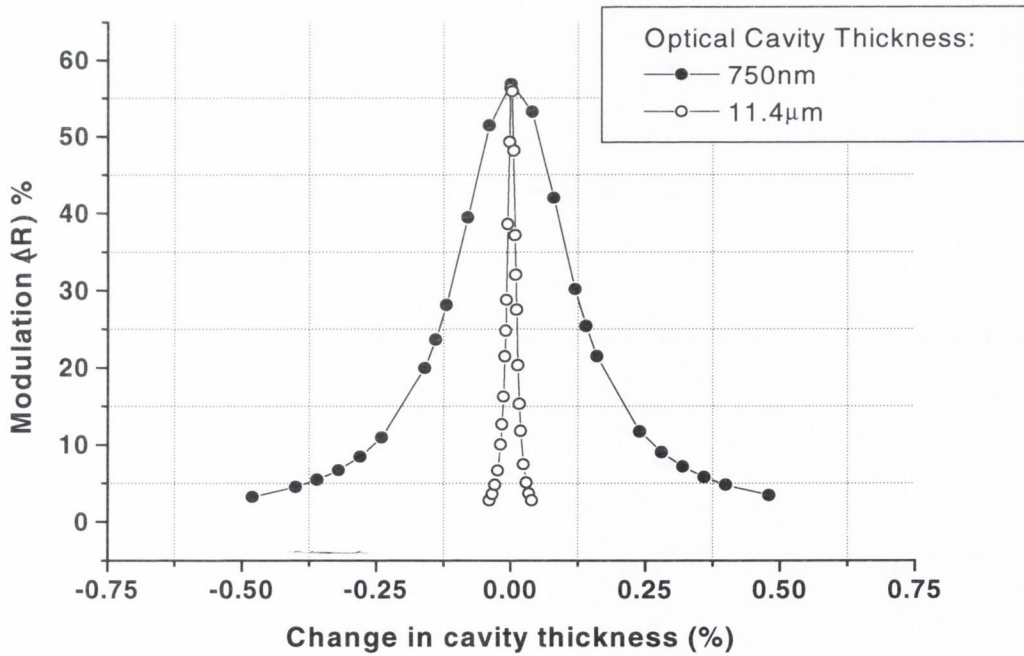


Figure 5.15: Tolerance to thickness change across a wafer when the thickness change in Figure 5.14 is represented as a percentage change in cavity thickness

The maximum tolerance to thickness change across a wafer is achieved when the cavity length is minimised. The other factor that influences the device tolerance to thickness fluctuations across a wafer is the cavity finesse. Reducing the cavity finesse will also allow the growth tolerance to be improved. Devices are normally processed from the full wafer area but the portion of the wafer where the thickness change is typically 1%-1.5% of the centre thickness. A clearer picture of the device tolerances to thickness change across the wafer is given if the thickness change in Figure 5.13 is represented as a percentage change in their optical cavity thickness. Figure 5.16 shows the resulting calculated modulation when the thickness change is plotted as a percentage deviation from the ideal cavity thickness for each modulator structure. The tolerances for the 5V and 3.3V modulator devices show a much poor tolerance to thickness variation across the wafer compared to the tolerances achieved with an Au back mirror in Figure 3.19. The 2V-modulator device has a full width half-maximum value of 0.25%, which is quite poor, only the very centre of the wafer could be used for processing as is commonly done with VCSEL device processing.

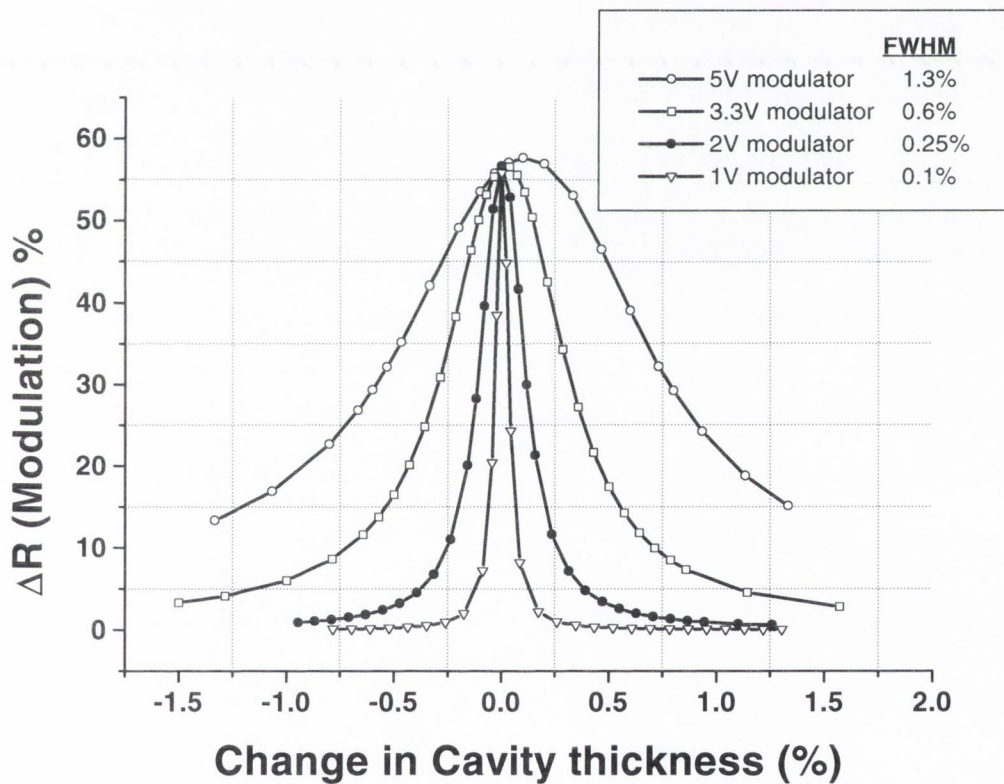


Figure 5.16 shows the resulting calculated modulation when the thickness change is plotted as a percentage deviation from the ideal cavity thickness for each modulator structure.

The poor tolerance shown here are a result of the poor contrast of the Bragg mirrors that results in a large penetration depth and makes up around 70% of the total effective cavity length. Thus the tolerance shown

in Figure 5.16 could be dramatically improved by reducing the penetration depth. This issue is addressed in full detail in Chapter 6 where modelling shows these tolerances can be much improved. Removing the **p** and **n** doped layers and using doped p-type and n-type Bragg mirrors would allow the cavity to be minimised but also introducing absorption into the Bragg mirrors reducing their reflectivity. The modulation achievable is already in excess of the 30% required, so this is possible, the slightly reduced cavity finesse due to this absorption will also have a positive effect on the spectral bandwidth and thus the growth tolerance. We will now briefly consider device operation assuming a tuneable read wavelength adjusted to match an operating wavelength that arises due to growth error. Such operation is problematic due to the wavelength sensitivity of diffractive optics in interconnect systems.

It is common to operate Fabry-Perot devices at wavelengths where a high power laser wavelength is available, especially if large arrays are involved and optical fan-out to the array is being used to read the modulators. A lot of progress has been made in high power semiconductor laser diodes [16]. It is possible in the future that these lasers could be considered for use in optical interconnects. A tuneable laser source allows the possibility of changing the operating wavelength if an error occurs in device growth and operation does not fall at the targeted wavelength at the centre of the wafer.

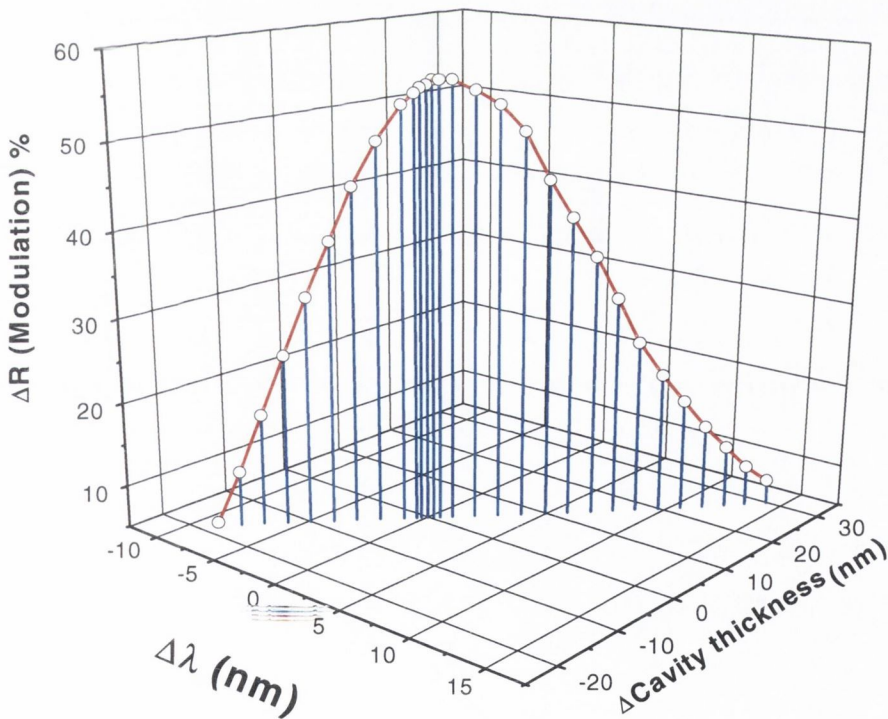


Figure 5.17: Detuning required from the design wavelength to recover modulation for different cavity thickness variations for 1V operation.

The tolerance to cavity thickness variation for the 1V-modulator device shown in Figure 5.13 is very poor at the modulator design wavelength. Variations in cavity thickness shift the optimum operating wavelength to longer or shorter wavelengths depending on whether the cavity is grown too short or too long. The spectral bandwidth curve shown in Figure 5.11 moves away from the fixed operating wavelength but at the resonance wavelength itself, good modulation is still achieved. When this curve shifts in wavelength it is possible to get good modulation at a large range of wavelengths, this wavelength range mostly depends only on the spectral range of the absorption change for the MQWs. Once the absorption change is large over a wide spectral range, good modulation will be achieved at the wavelength the resonance shifts to. This spectral range turns out to be quite large for the InGaAs/(Al)GaAs system as material effects result in a broad exciton absorption. Figure 5.17 shows how much detuning of the read wavelength from the design wavelength is required to recover the modulation for different cavity thickness variations, at 1V modulation. For 30% modulation there is a tuning range of 13nm(-5 to +8nm) for a thickness variation of 26nm(-10 to +16nm) which is a $\pm 2.2\%$ fluctuation in the thickness of the optical cavity. This gives a good tolerance to incorrect growth of the absolute thickness at the centre of the wafer, which usually has growth accuracy well inside this $\pm 2.2\%$ fluctuation in thickness.

5.5.2.3 Summary

The sensitivity of the Fabry-Perot modulator structure to optical cavity thickness changes at the centre of the wafer and across the wafer has been examined. To ensure accurate centre thickness growth of these devices, in-situ monitoring of the device wafer growth is necessary. Based on VCSEL growth accuracy using in-situ monitoring, a minimum required spectral bandwidth of 4nm FWHM was determined. Based on this value of 4nm, the lowest operating voltage possible for the current device structure is around 2.5V having a maximum spectral bandwidth of 3.4nm. The low voltage modulator structures were found to be most sensitive to optical thickness fluctuations. This is due to the higher finesse cavity required at lower voltage operation, which reduces their spectral bandwidth dramatically. Due to the fact that the change in cavity thickness across a wafer is a percentage of the centre wafer thickness, this allows the growth tolerance to be maximised when the optical cavity length is minimised. The cavity size needs to be minimised to maximise the area of the wafer to be processed.

5.5.3 Angular acceptance

As discussed in section 3.4.2 electro-absorption modulators traditionally operate at normal incidence. When large arrays with device sizes of the order of $35\mu\text{m}$ are used in interconnect systems fast converging beams are required to focus the incident light onto the device. The lenses used to focus the light on the modulator devices in the SPOEC system have an angular width of $\pm 9^\circ$. This requires the modulator device to operate over this angular range. As outlined in Chapter 3, the angular response for the devices in Table 5.1 is calculated using the transfer matrix model. Figure 5.18 shows the modulation response for the optimum modulator designs at each operating voltage plotted in a polar format.

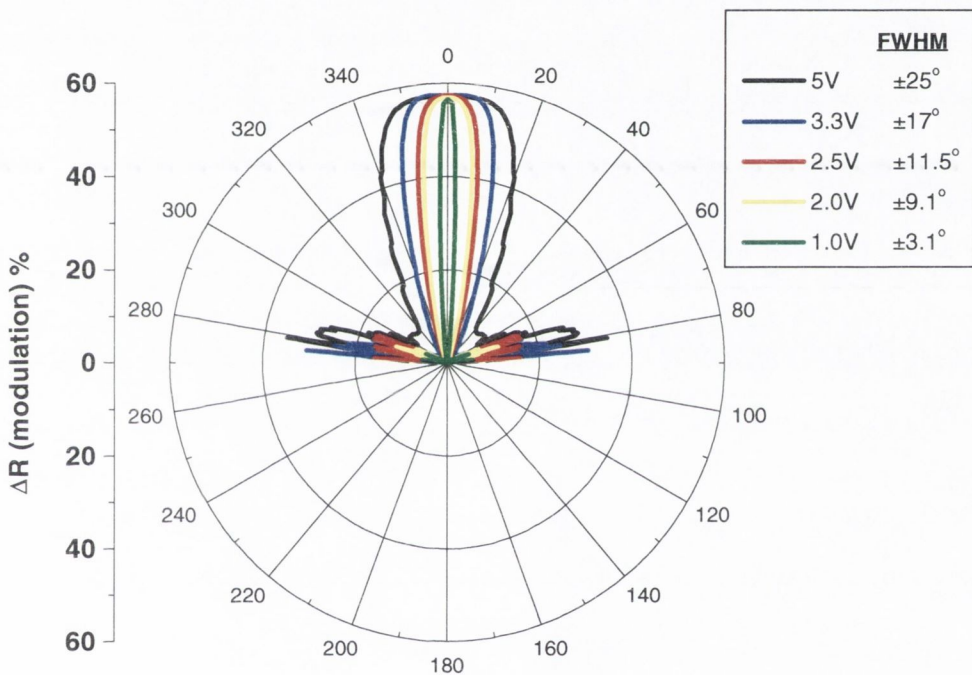


Figure 5.18: Modulation response for the optimum modulator designs at each voltage, a polar format is used with the reflectance change increasing radially from the centre.

The angular tolerance values are calculated where the physical length of the cavity is minimised. Good angular tolerance is found for 5V operation, modelling predicts a FWHM acceptance angle of $\pm 25^\circ$. The modulation value stays very flat for initial angle values to $\pm 10^\circ$ and then starts to rapidly fall off. At operating voltages down to as low as 2V good spectral bandwidth is predicted with the 2V device having a FWHM angular tolerance of $\pm 9^\circ$, which is equal to the angular spread of the incident angles of the current SPOEC interconnect system. The angular tolerance reduces at lower voltage operation due to the higher finesse cavity and the reduced spectral bandwidth in Figure 5.11. For 1V operation the angular acceptance

is $\pm 3.1^\circ$, this tolerance is very small and this would require lenses of long focal length and small angular spread. For operation in a real system this value is too small for practical operation. In Section 5.5.1 reducing the front mirror reflectivity of the optical cavity increased the spectral bandwidth of the devices. If the spectral bandwidth is increased the angular tolerance will also increase. Figure 5.19 shows the modelling results for the angular acceptance of the 2V-modulator device when the front mirror reflectivity is decreased.

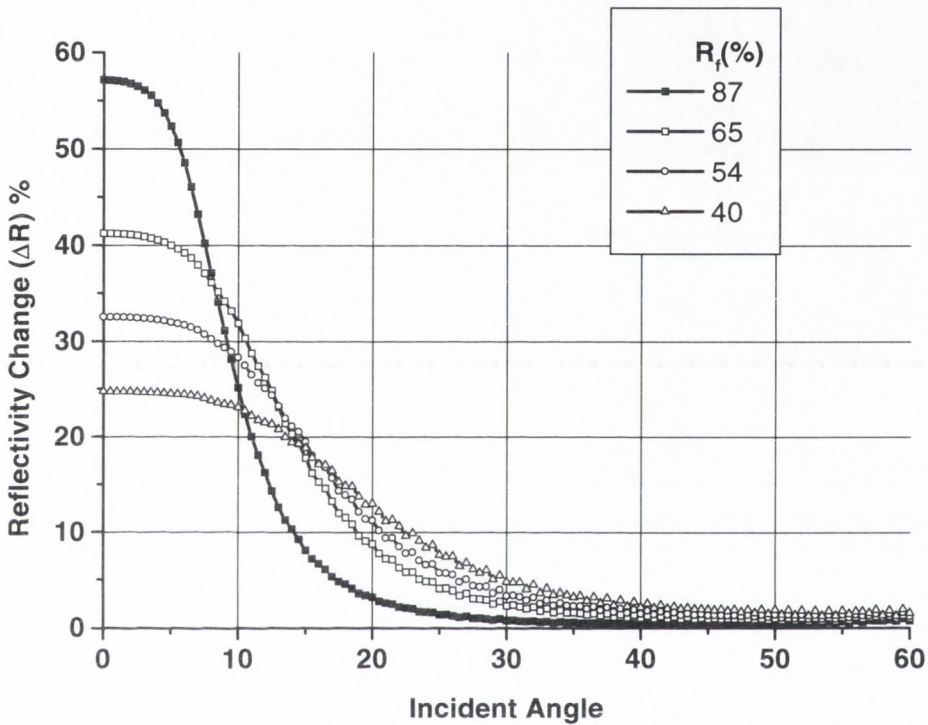


Figure 5.19 shows the modelling results for the angular acceptance of the 2V-modulator device when the front mirror reflectivity is decreased.

At 30% modulation the angular acceptance increases from 9° to 10.5° for a front mirror reflectivity change from 87% to 65%. At 20% modulation the angular acceptance increases from 11° to 15° for a front mirror reflectivity change from 87% to 54%. At 10% modulation the angular acceptance increases from 14° to 23° for a front mirror reflectivity change from 87% to 40%. As we have seen previously in the case of the growth and spectral bandwidth tolerances and now with the angular acceptance, the devices are most sensitive to increases in these tolerances in the 30% to 10% modulation range. The tolerance values must also be considered when choosing the modulation value required for the interconnect system. The angular acceptance values for modulator devices to be used in a real system such as the SPOEC system are

acceptable for operation down to 2V. Devices operating at less than 2V operation require increased values to be used in a practical system.

The microcavity benefits to these devices are explored in Chapter 6 and the benefits to the angular acceptance of these devices are examined in detail. Here we will see how the device angular tolerance can be increased a short cavity orders and by cavity detuning. The temperature sensitivity of these devices is presented next

5.5.4 Temperature sensitivity

The factors that influence the behaviour of the Fabry-Perot modulator device when the ambient temperature changes as presented in Section 3.4.4. Similar modelling using the data summarised in Section 3.4.4 was done to explore the temperature sensitivity of the devices summarised in Table 5.1. The modelling results are presented in Figure 5.20 below for devices with various operating voltages.

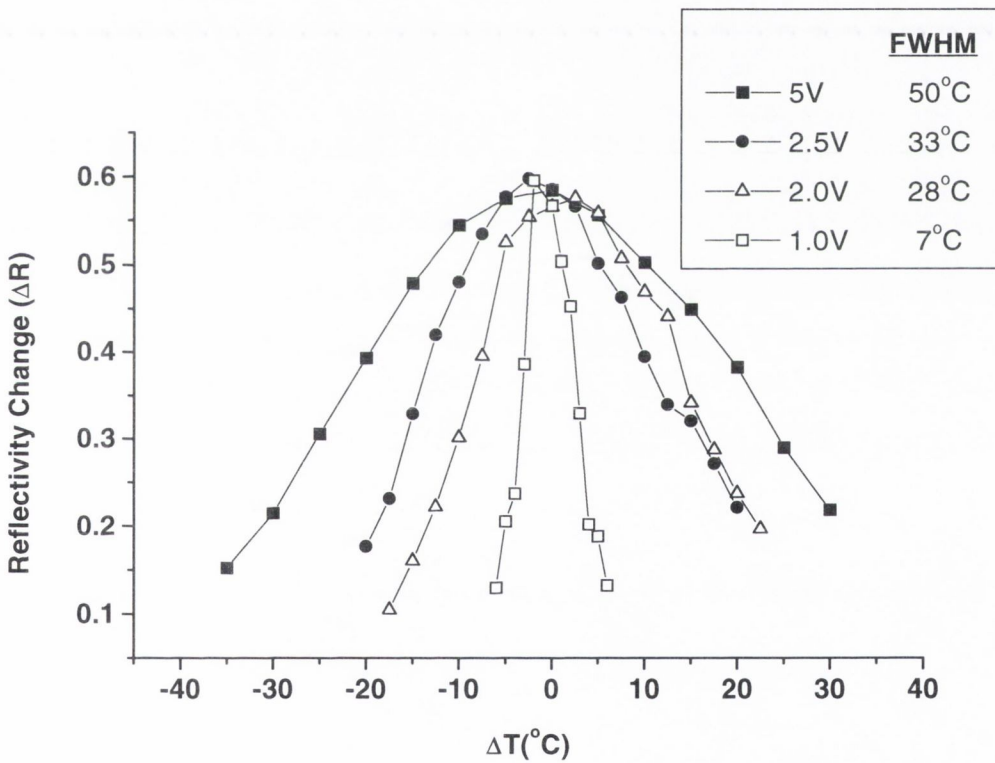


Figure 5.20: Modelled modulation change at the device operation wavelength due to changing ambient temperature for 5V to 1V operation.

In Figure 3.20 when temperature sensitivity of the 5V double-pass modulator was presented and the influence of the shape of the exciton absorption on the curve was clear. This influence can be still seen in the above curves but to a lesser degree, as the cavity finesse increases at lower voltage operation and the

Fabry-Perot resonance dominates more. Temperature changes shift the wavelength of the exciton absorption and the Fabry-Perot resonance (Chapter 3). At lower voltage operation the reduced spectral width of the resonance means that these devices will be more sensitive to temperature changes when operating at a fixed wavelength and voltage. The modelling results in Figure 5.20 verify this, the FWHM reduces from 50°C at 5V operation to 7°C at 1V operation. As discussed in Section 3.6.4 these results are not fully accurate but do give an insight into the behaviour of these devices at lower voltage operation. At 1V operation the FWHM value of 7°C is comparable to the tolerance of the double-pass modulator structure for 30% modulation in Figure 3.20. Previous work in [17] extended the operating temperature range of the modulator device by changing the reverse bias voltage on the modulator in correspondence to the change in temperature. At low voltage operation and operation at CMOS compatible voltages this option is not available to us. In optical interconnect systems these devices are expected to operate with some form of temperature stabilisation such as a Peltier-cooler due to the integration of these Opto-electronic devices with silicon CMOS. Current and future silicon CMOS integrated circuits require a lot of waste heat energy to be dissipated away from the integrated circuit itself [18]. This generated heat is much greater than that currently generated by Opto-electronic devices and is expected to stay this way in future technology. Thus temperature control systems are expected to be a required component in the interconnect architecture to remove this excess heating. The relative increase in device sensitivity at lower voltage operation is thus not foreseen to be a major problem for these devices, as their operating temperature will be controlled in the interconnect system. If these devices are temperature stabilised so the device continually operates at the optimum temperature then the spectral bandwidth and angular tolerance prediction previously hold true. Otherwise the device must be considered as a dynamic system and more rigorous and complex modelling is required to examine the device spectral and angular tolerances.

5.5.5 Optical saturation

The MQW exciton absorption in these Fabry-Perot modulator devices is saturated or 'bleached' at lower laser intensities compared to devices operating in transmission or a double-pass modulator. This is due to the increase in the intensity of the incident light inside the optical cavity. The impact on the Fabry-Perot device operation was discussed earlier in Section 3.4.5. The increase in electric field intensity inside the optical cavity can be calculated using Equation 3.2 and using the transfer matrix model as discussed also in Section 3.4.5. Table 5.2 shows the calculated ratio of the electric field intensity inside the optical to the electric field outside the cavity. From this the resulting reduction in the optical saturation limit for the devices summarised in Table 5.1 above is calculated. A saturation irradiance value of 80 kW/cm² for GaAs MQWs is again used [19] and the focussed beam spot size is taken to be 60µm².

Voltage (and bias) V	Cavity Finesse	I_{Cavity} / I_0	Saturation Limit (mW)
5	6.7	11	4.55
3.3	14.5	20.4	2.45
2.5	31.3	40.6	1.23
2	44.8	58	0.86
1.8	53.4	69.2	0.72
1	154	193.2	0.26

Table 5.2: Details of the reduction in optical saturation power as the optical cavity finesse increases at low voltage operation for a device area of $60\mu\text{m}^2$.

The finesse of these cavities is high, especially at less than 2V operation. This results in a large build-up in electric field intensity inside the optical cavity and the corresponding large reduction in the saturation limit. The reduction of a factor of 194 at 1V operation is a significant change in the saturation limit. As mentioned in Section 3.4.5 the current SPOEC system has an optical power of 2.12mW incident on the modulator devices. Looking at the above values this value would exceed the minimum allowed value at 2.5V operation or less. The predicted changes to modulator device area and array size in future systems [20] cancel each other out and the above table remains relatively unchanged. In Section 3.4.5 based on data from the SPOEC interconnect system, a minimum value of incident optical power on the modulator of **61 μW** was calculated. Thus once the optical incident power is larger than **61 μW** and less than the values shown in Table 5.2, device and system operation is possible. In conclusion, to avoid exciton saturation in the MQWs and to allow operation of these low voltage Fabry-Perot to be possible, the incident optical power would have to reduce from the current SPOEC system value. Reducing the optical power of the read beam is not foreseen to impact negatively on device or system operation and thus optical saturation is not seen as a significant problem for Fabry-Perot modulators used in future low voltage interconnect systems.

5.5.6 Device speed

The reduced number of MQWs at lower voltage operation effects the device capacitance and thus the modulation bandwidth. The required numbers of MQWs at lower voltage operation in Table 5.1 are identical to the devices in Table 3.1. The impact of the reduction in MQWs on modulation bandwidth is presented in Section 3.4.6.

5.6 Conclusions

In this chapter the diminishing modulation achievable at lower voltage operation from the device structure studied in Chapter 3 was examined. Modelling has revealed the limiting factor to be the finite reflectivity of the back Au mirror. An alternative structure was then investigated in which the mirror reflectivity could be varied by using a Bragg and Au mirror combination allowing reflectivities up to 99.9%. Modelling revealed the reflectivity range between 95% and 99.9% to be extremely critical for low voltage operation of Fabry-Perot modulator structures. Modelling results predict 58% modulation at operation voltages down to 1V to be possible for this particular MQW material and structure. Modelling results predict expected superior performance in the AlGaAs material system and this is verified in many publications. The increased finesse of these devices impacts unfavourably on the device operating tolerances that are required for system operation. For the current structure being investigated in this chapter a lower limit of 2.5V operation maybe possible after considering all these factors. The required reflectivity change has been shown to be achievable in this chapter but the poor device tolerance is impeding their use in interconnect systems, and the poor tolerance to growth non-uniformities prevents the fabrication of very large arrays. Chapter 6 investigates how these tolerances may be improved and the impact of an optical cavity having a short cavity order on these tolerances, using currently available technology.

5.7 References

- [1] LAW KK, MERZ JL, COLDREN LA, 'EFFECT OF LAYER THICKNESS VARIATIONS ON THE PERFORMANCE OF ASYMMETRIC FABRY-PEROT REFLECTION MODULATORS' JOURNAL OF APPLIED PHYSICS, 72: (3) 855-860 AUG 1 1992
- [2] M.K HIBBS-BRENNER, R.A.MORGAN, R.A. WALTERSON, J.A. LEHMAN, E.L.KALWEIT, S. BOUNNAK, T. MARTA AND R. GIESKE, 'PERFORMANCE, UNIFORMITY, AND YIELD OF 850-NM VCSEL'S DEPOSITED BY MOVPE', IEEE PHOTONICS TECHNOLOGY LETTERS, 8: (1) 7-9 JAN 1996
- [3] H.Q. HOU, H.C. CHUI, K.D. CHOQUETTE, B.E. HAMMONS, W.G. BREILAND AND K.M. GEIB, 'HIGHLY UNIFORM AND REPRODUCIBLE VERTICAL-CAVITY SURFACE-EMITTING LASERS GROWN BY METALORGANIC VAPOR PHASE EPITAXY WITH IN-SITU REFLECTOMETRY', IEEE PHOTONICS TECHNOLOGY LETTERS, 8: (10) 1285-1287 OCT 1996
- [4] WHITEHEAD M, RIVERS A, PARRY G, ROBERTS JS, 'VERY LOW-VOLTAGE, NORMALLY-OFF ASYMMETRIC FABRY-PEROT REFLECTION MODULATOR', ELECTRONICS LETTERS, 26: (19) 1588-1590 SEP 13 1990
- [5] LAW KK, WHITEHEAD M, MERZ JL, COLDREN LA, 'SIMULTANEOUS ACHIEVEMENT OF LOW INSERTION LOSS, HIGH CONTRAST AND LOW OPERATING VOLTAGE IN ASYMMETRIC FABRY-PEROT REFLECTION MODULATOR', ELECTRONICS LETTERS, 27: (20) 1863-1865 SEP 26 1991

- [6] R.H. YAN, R.J. SIMES AND L.A. COLDREN, 'EXTREMELY LOW VOLTAGE FABRY-PEROT REFLECTION MODULATORS', IEEE PHOTONICS TECHNOLOGY LETTERS, 2: (2) 118-119 FEB 1990
- [7] FRITZ IJ, MYERS DR, VAWTER GA, BRENNAN TM, HAMMONS BE., 'NOVEL REFLECTANCE MODULATOR EMPLOYING AN INGAAS/ALGAAS STRAINED-LAYER SUPERLATTICE FABRY-PEROT CAVITY WITH UNSTRAINED INGAAS/INALAS MIRRORS', APPLIED PHYSICS LETTERS, 58: (15) 1608-1610 APR 15 1991
- [8] FRITZ IJ, OLSEN JA, HOWARD AJ, BRENNAN TM, HAMMONS BE, VAWTER GA, 'STRAINED-LAYER-SUPERLATTICE TECHNOLOGY FOR VERTICAL-CAVITY OPTOELECTRONIC MODULATORS AT NEAR-INFRARED WAVELENGTHS', IEEE JOURNAL OF QUANTUM ELECTRONICS, 30: (2) 452-458 FEB 1994
- [9] HU KZ, CHEN L, MADHUKAR A, CHEN P, KYRIAKAKIS C, KARIM Z, TANGUAY AR, 'INVERTED CAVITY GAAS/INGAAS ASYMMETRIC FABRY-PEROT REFLECTION MODULATOR', APPLIED PHYSICS LETTERS, 59: (14) 1664-1666 SEP 30 1991
- [10] CHEN L, KAPRE RM, HU KZ, MADHUKAR A, 'HIGH-CONTRAST OPTICALLY BISTABLE OPTOELECTRONIC SWITCH BASED ON INGAAS/GAAS (100) ASYMMETRIC FABRY-PEROT MODULATOR, DETECTOR, AND RESONANT TUNNELING DIODE', APPLIED PHYSICS LETTERS, 59: (13) 1523-1525 SEP 23 1991
- [11] HU KZ, CHEN L, MADHUKAR A, CHEN P, RAJKUMAR KC, KAVIANI K, KARIM Z, KYRIAKAKIS C, TANGUAY AR, 'HIGH CONTRAST RATIO ASYMMETRIC FABRY-PEROT REFLECTION-LIGHT MODULATOR BASED ON GAAS/INGAAS MULTIPLE QUANTUM-WELLS', APPLIED PHYSICS LETTERS, 59: (9) 1108-1110 AUG 26 1991
- [12] B.PEZESHKI, S.M. LORD AND J.S. HARRIS JR., 'ELECTROABSORPTIVE MODULATORS IN INGAAS/ALGAAS', APPLIED PHYSICS LETTERS, 59: (8) 888-890 AUG 19 1991
- [13] CUNNINGHAM JE, 'RECENT DEVELOPMENTS AND APPLICATIONS IN ELECTROABSORPTION SEMICONDUCTOR MODULATORS', MATERIALS SCIENCE & ENGINEERING R-REPORTS, 25: (5-6) 155-194 AUG 31 1999
- [14] 'PROPERTIES OF LATTICE MATCHED AND STRAINED INDIUM GALLIUM ARSENIDE', EDITED BY PALLAB BHATTACHARYA, INSPEC EMIS DATAREVIEW SERIES NO.8, THE INSTITUTION OF ELECTRICAL ENGINEERS, LONDON, 1993
- [15] TREZZA JA, PEZESHKI B, LARSON MC, LORD SM, HARRIS JS, 'HIGH-CONTRAST ASYMMETRIC FABRY-PEROT ELECTROABSORPTION MODULATOR WITH ZERO PHASE-CHANGE', APPLIED PHYSICS LETTERS, 63: (4) 452-454 JUL 26 1993
- [16] A.AL-MUHANNA, L.J.MAWST, D. BOTEZ, D.Z. GARBUZOV, R.U. MARTINELLI, AND J.C. CONNOLLY, 'HIGH POWER (>10W) CONTINUOUS-WAVE OPERATION FROM 100- μ M-TEMPERATURE 0.97- μ M-EMITTING AL-FREE DIODE LASERS', APPLIED PHYSICS LETTERS, 73:(9) 1182-1184 31 AUG 1998
- [17] GOOSSEN KW, CUNNINGHAM JE, JAN WY, LEIBENGUTH R, 'ON THE OPERATIONAL AND MANUFACTURING TOLERANCES OF GAAS-ALAS MQW MODULATORS', IEEE JOURNAL OF QUANTUM ELECTRONICS, 34: (3) 431-438 MAR 1998
- [18] SEMICONDUCTOR INDUSTRY ASSOCIATION: THE NATIONAL TECHNOLOGY ROADMAP FOR SEMICONDUCTORS: TECHNOLOGY NEEDS', 1997 EDITION.

[19] GOOSSEN KW, CUNNINGHAM JE, JAN WY, 'GAAS 850-NM MODULATORS SOLDER-BONDED TO SILICON', IEEE PHOTONICS TECHNOLOGY LETTERS, 5: (7) 776-778 JUL 1993

[20] MEL-ARI TECHNOLOGY ROADMAP: OPTOELECTRONIC INTERCONNECTS FOR INTEGRATED CIRCUITS, EUROPEAN COMMISSION IST PROGRAMME: FUTURE AND EMERGING TECHNOLOGIES, 2ND EDITION SEPT 1999

Chapter 6:

Impact of Microcavity regime on Fabry-Perot Modulators

6.1 Introduction

In this chapter we investigate the so called ‘microcavity effect’, exploring the potential benefits to the modulator device of using a short optical cavity having a size approaching the operating wavelength. Work to date has concentrated on the benefits to LED (light emitting diode) emission brought about by the inclusion of the active area in a short optical cavity are first summarised. The same characteristics of a short optical cavity are found to benefit Fabry-Perot modulators as those that benefit devices operating in emission. These characteristics are presented, along with transfer matrix modelling results showing the increased spectral bandwidth, angular acceptance and temperature tolerance achievable at shorter cavity orders. The impact of a short cavity order on the device growth tolerances is also discussed further. From these results and the modulation results predicted in Chapter 5, a more complete overall picture of the optimal Fabry-Perot modulator structure for low voltage operation can be concluded. This device will have good modulation capability with sufficient device tolerances for operation in an optical interconnect.

6.2 Benefits of a short optical cavity to LED emission

The modification of the spatial emission pattern and the rate of spontaneous emission when an emitting dipole is placed in an optical cavity having dimensions the order of the emission wavelength was investigated by Purcell [1] in 1946. He showed theoretically that altering the number of photon modes using a short optical cavity could alter the spontaneous emission rate, a field of study known as cavity quantum electrodynamics. Much of the basic theory was confirmed using Langmuir-Blodgett thin films [3]. The definition of a microcavity used here is adopted from the approach of Benisty et al. [10] and occurs when the cavity order $m < 2n^2$ (n being the cavity refractive index) and the cavity order is the number of half-wavelengths that fit into a cavity. Due to technological restrictions it is only in recent times [2] that the microcavity idea has been investigated in semiconductor light emitters. Since then placing an active region in a short optical cavity has shown that the LED linewidth can be narrowed, its brightness increased and more recently a considerable improvement in the light extraction efficiency [4] (light extracted from inside the optical cavity to the outside). The main benefits to light emission are now briefly discussed.

6.2.1 Spontaneous emission rate

An increased spontaneous emission rate is desirable in an emitter as the reduced electron-hole recombination time allows the device electrical modulation bandwidth to be increased. It also increases the emission efficiency as the non-radiative carrier lifetime becomes relatively less important. When an emitter is placed in a planar optical cavity there is optical confinement in one direction resulting in only two full degrees of freedom and a limited number of states in the confined dimension compared to the bulk semiconductor case. This results in an alteration of the normal free space density of photon states that can be emitted into, which can alter the spontaneous emission rate W governed by Fermi's golden rule

$$W = \frac{2\pi}{h} |\langle f | H | i \rangle|^2 \rho(E) \quad (6.1)$$

Where $|i\rangle$ is the initial state with no photons and $|f\rangle$ the final state with one photon, H is the Hamiltonian interaction operator. $\rho(E)$ is the density of final photon states, in this case the density of optical modes available to the emitted photon. The modification of the spontaneous emission rate has been demonstrated for atoms in planar microcavities in [5] and a maximum enhancement of three times the free space emission rate is predicted to occur for the optimum $\lambda/2$ cavity with ideal mirrors [6]. The mirrors used in semiconductor structures are either metal mirror and/or Bragg stack mirrors. Reflectivities greater than 95% are difficult to achieve at optical frequencies with metal mirrors and losses occur due to absorption in the metal. Although Bragg stack mirrors give higher reflectivities, the strong angular dependence of the mirror reflectivity results in mirror losses, making the above cavity with ideal mirrors difficult to achieve in reality. Thus the three dimensional density of optical modes available to the emitted photon is not fully altered to being entirely two dimensional. The predicted spontaneous emission enhancement for

semiconductor microcavity structures is at best estimated to be $\pm 20\%$ [7]. More significant increases in the spontaneous emission rate are predicted and measured from structures with optical confinement in two or three dimensional structures [2,8].

6.2.2 Antinode factor

Although the two dimensional density of optical modes is not changed significantly in a semiconductor microcavity, the emission is also influenced by the standing optical wave set up along the normal of the cavity which is accounted for by the matrix element in Fermi's golden rule (Eqn.6.1). The standing electromagnetic wave inside the cavity produces nodes where there is no coupling of the optical electric field to the emitter and antinodes where there is optimum coupling to the emitter. A standing wave produced in an optical cavity is shown in Chapter 3 in Figure 3.22. In this case it is a standing optical wave produced by our modulator structure but the situation is identical in emission. The antinode factor can generally be described by [9]

$$\zeta_m(z) = 2 \sin^2(kz) \quad (6.2)$$

Where \mathbf{k} is the wavevector in the z -direction normal to the cavity of length L given by $\mathbf{k}=\pi\mathbf{m}/L$ and \mathbf{m} is the cavity order i.e. the number of half-wavelengths ($\lambda/2$) in the optical cavity. The maximum antinode value is 2 and minimum is zero. For large cavities the (\mathbf{kz}) value in Eqn.6.2 will span more than π within in the layer and the averaged antinode factor in the z -direction is 1. The emission in a microcavity is believed to be redistributed among the number of cavity orders \mathbf{m} according to the antinode factor ζ_m . Once the cavity order $m \geq 3$ the antinode factor averages out to 1 and $\sum \zeta_m \approx m$. It is only at cavity orders ≤ 3 (of the order of the emission wavelength) that the antinode factor can differ from 1 and emission can be favoured into these cavity modes. The fraction of emission η_i radiated into a given cavity mode \mathbf{i} is then given by

$$\eta_i = \frac{\zeta_i}{\sum \zeta_m} \approx \frac{\zeta_i}{m} \quad (6.3)$$

Thus the fraction of emission η_i radiated into a given cavity mode \mathbf{i} is the antinode factor / cavity order. Further analysis [9] leads to the conclusion that the overall extraction efficiency η (light extracted from inside the optical cavity to the outside) of a semiconductor optical cavity is given by $\eta=\zeta_o/m$. Where ζ_o is the antinode factor of the extracted mode. (We will return to this point shortly) Thus the smaller the cavity order, \mathbf{m} , the greater the extraction efficiency giving a maximum extraction efficiency of $2/m$. For an emitter the microcavity regime is defined as the cavity order where the optical cavity extraction efficiency surpasses the extraction efficiency possible when only a single back mirror is used. The extraction efficiency for a single mirror is given by [10] $1/2n^2$ thus the microcavity regime is defined by

$$m \leq 2n^2 \quad (6.4)$$

assuming an average antinode factor value of 1 and n is the refractive index of the cavity medium.

6.2.3 Extraction efficiency

When an emitter is placed in an optical cavity there is also a spatial redistribution of the emitted light due to interference from light reflected from the back mirror interfering with light exiting the front mirror. The situation is illustrated in Figure 6.1. The back mirror amplitude reflectance is given by r_b and front mirror given by r_f . The cavity thickness $L=m\lambda/2n$ where n is the refractive index of the cavity medium, m the cavity order and λ the resonant wavelength of the optical cavity at normal incidence. If the emission source is assumed to be an emitting dipole, its emission pattern into free space is typically given by $E_v=E_0\sin^2(\theta)$. If this emitting dipole is positioned at a distance d from the back mirror in the Fabry-Perot cavity in figure 6.1 the resultant emission far field intensity is found by summing the series of reflected waves yielding [10]

$$|E_{res}| = |E_v|^2 (\zeta) \frac{1 - r_f^2}{|1 - r_f r_b e^{2ik_z L}|^2} \quad (6.5)$$

Where the wavevector in the z -direction is given by $k_z=2\pi n \cos(\theta)/\lambda_e$, λ_e being the emission wavelength and the antinode factor $\zeta=1+r_b^2 \pm 2r_b \cos(2\phi)$ where $\phi=k_z d$.

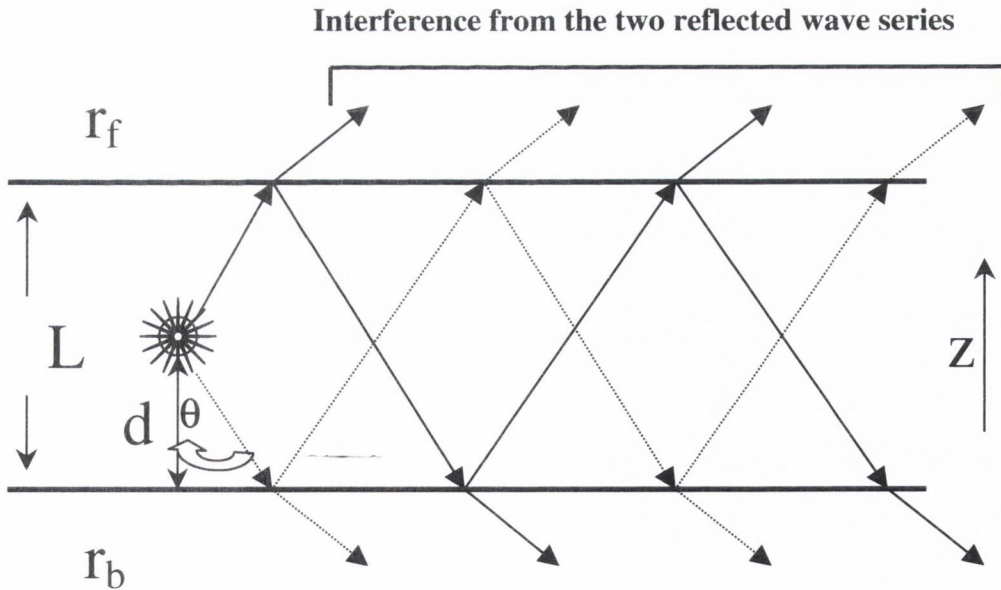


Figure 6.1: Optical cavity containing an emitting dipole. The far-field emission pattern is a result of interference between the two series of reflections indicated.

The antinode factor takes account of the position of the emitter in the optical cavity and is a maximum when \mathbf{d} corresponds to an antinode position. The \pm term accounts for the reflectance phase of the back mirror and is taken to be positive and in the case considered below will introduce a phase shift of $\pi/2$. The final term in equation 6.5 is just the airy factor seen earlier in Chapter 2, which accounts for the influence of the optical cavity on the emitted radiation.

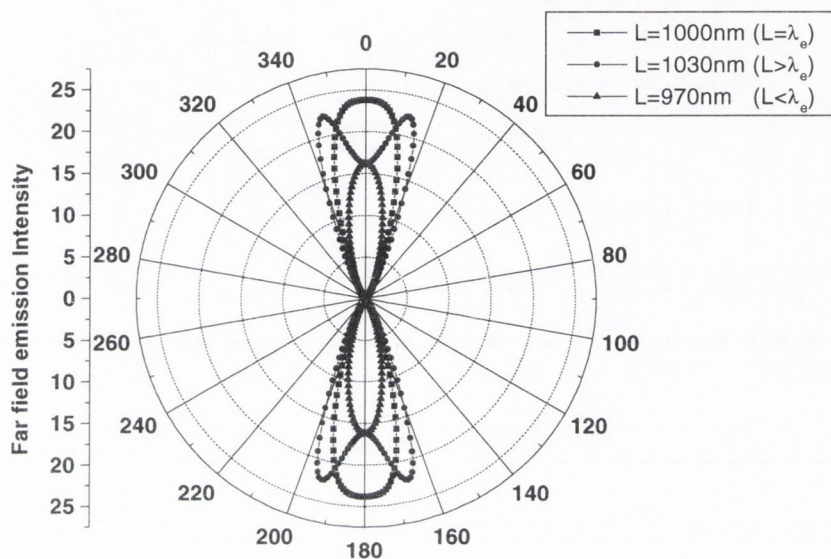


Figure 6.2: Emission far fields intensity calculated using equation 6.5 for three different cavity thicknesses.

This value is a maximum when the cavity thickness $L = m\lambda_c/2n$ is chosen so that constructive interference occurs between the reflected series of waves shown in Figure 6.1. The emission far field intensity is calculated using equation 6.5 and presented in Figure 6.2 for three different cavity thicknesses with the emitter placed at an antinode $\mathbf{d} = m\lambda_c/4n$. The dipole emission value E_v is normalised to 1 so the intensity values presented in Figure 6.2 represent the enhancement over the free space emission value. The front mirror reflectivity used was 80% and a back mirror reflectivity of 95%. The dipole emission was assumed to be at $\lambda_c = 1000\text{nm}$ and for simplicity the cavity refractive index was taken to be 1, the cavity order $m=2$. The plotted intensity values in Figure 6.2 solely represent the redistribution of the free space emission when an emitter is placed in an optical cavity due to interference effects. This representation is very simplistic but extremely useful when explaining the improvement in extraction efficiency due to an optical cavity. The results in Figure 6.2 shows that, when $L = \lambda_c = 1000\text{nm}$, maximum constructive interference occurs and is centred on the cavity axis at 0° . The intensity has been enhanced in this direction by a factor $4 \times 1 - r_f^2 / (1 - r_f r_b)^2 = 25$. The intensity reduces with increasing angle due to the $\text{Cos}(\theta)$ dependence of the phase

difference $\phi = 2\mathbf{k}_z \mathbf{d} = 2(2\pi n \cos(\theta) / \lambda_e) \mathbf{d} = (2\pi n L \cos(\theta) / \lambda_e)$ between the two series of reflected waves shown in Figure 6.1. For the case where the cavity length $L > \lambda_e$ a doubled lobed pattern is predicted and maximum intensity occurs at an angle. These lobes occur at an angle $\theta = \cos^{-1}(\lambda_e / nL) = 13.8^\circ$ because the phase difference $\phi = (2\pi n L \cos(\theta) / \lambda_e)$ at this angle becomes an integer multiple of π at this angle and constructive interference occurs (positive phase change of $\pi/2$ from the back mirror). For the case of $L < \lambda_e$ the $\cos(\theta)$ is < 1 and thus the phase difference ϕ can never be an integer multiple of 2π and the resulting emission is suppressed along the axis of the optical cavity as seen in Figure 6.2. This simple illustration shows how an optical cavity redistributes the light emitted into discrete angles and it is this property, as will be shown shortly, that allows the light extraction efficiency η to be increased.

6.2.3.1 Emission in bulk material

Total internal reflection is the source of poor extraction efficiencies from bare semiconductor material. For emission in GaAs ($n=3.54$), the light extraction to air is only possible through an angular range given by the critical angle $\theta_c = \sin^{-1}(1/3.54) = 16.4^\circ$. If the emitter is assumed to be isotropic the extraction efficiency can be defined as the ratio of the solid angle that escapes through the critical angle to the overall emission solid angle.

$$\Omega_{SA}(\theta) = \frac{A_{surface}}{r^2} = \frac{\int_0^\theta \int_0^{2\pi} r^2 \sin(\theta) d\psi d\theta}{r^2} = 2\pi \int_0^\psi \sin(\theta) d\psi = 2\pi(1 - \cos(\theta)) \quad (6.6)$$

Thus the extraction efficiency is given by

$$\eta = \frac{\Omega_{SA}(16.4^\circ)}{\Omega_{SA}(180^\circ)} = 0.02 \quad (6.7)$$

Only 2% of the light is extracted from GaAs but the light also undergoes $\approx 30\%$ reflection at the GaAs/air interface so even less than 2% is extracted. Commercial devices use a highly reflecting back mirror which doubles the emission in the forward direction and cover the device in a dome of epoxy having roughly a refractive index of 1.5. This increases the critical angle and the interface reflection achieving efficiencies of $\approx 9.5\%$.

6.2.3.2 Optical cavity extraction

The redistribution of the emitted light by the optical cavity was shown in Figure 6.2 above. The extraction efficiency can be increased by an optical cavity due to the light being redirected into the critical angular range or the escape cone between 0 and θ_c . The wavevector scheme of Figure 6.3 presented in [10] is useful when explaining light extraction. The elemental solid angle (ring) subtended by $d\theta$ around an emission angle θ is given by $d\Omega = 2\pi \times d(\cos(\theta))$ from equation 6.6 and is proportional to $dk_z = k \times d(\cos(\theta))$. Thus the amount of emission in the escape cone 0 to θ_c to be extracted is proportional to the shaded integral below the Airy function in Figure 6.3 between $k_z=k$ and $k_z=k\cos(\theta_c)$.

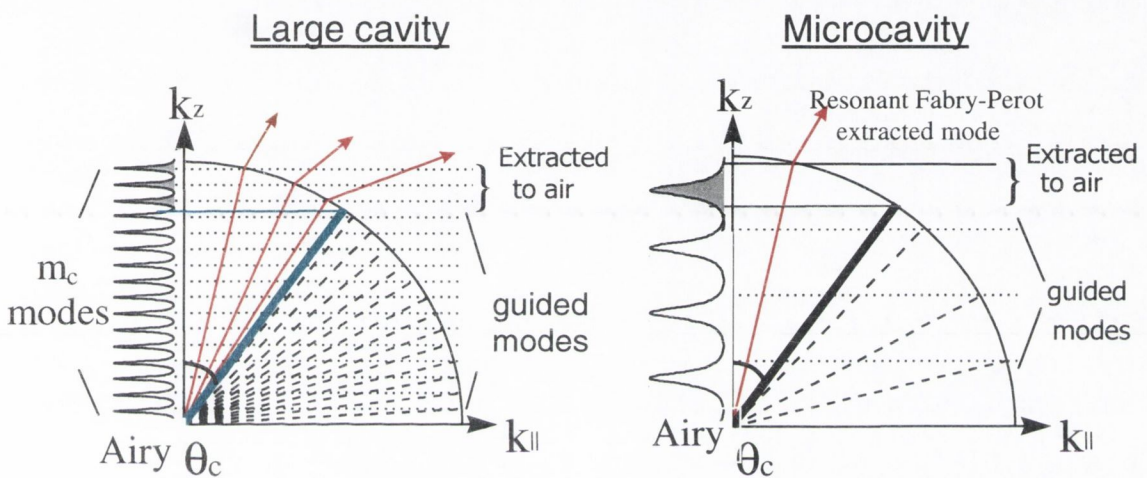


Figure 6.3: k-space plot showing the cavity modes, critical angle and the Airy factor as a function of k_z [10] for a large cavity order and a cavity having a small order and few modes.

The fraction of emission η_i radiated into a given cavity mode i is the antinode factor / cavity order (eqn.6.3). In the large cavity case in Figure 6.3 three cavity modes are extracted and emission in the remaining cavity modes is guided inside the semiconductor and probably reabsorbed. The ratio of the number of modes escaping to the number guided is small and most of the emission is lost to guided modes and not extracted. In the short microcavity case this ratio is much improved and thus a greater fraction of emission is extracted increasing the extraction efficiency. As mentioned previously the overall extraction efficiency η of a semiconductor optical cavity is given by $\eta = \zeta_0 / m$. Where ζ_0 is the antinode factor of the extracted mode. Thus the smaller the cavity order m the greater the extraction efficiency giving a maximum extraction efficiency of $2/m$.

The amount of emission in the escape cone, 0 to θ_c , to be extracted is proportional to the shaded integral below the Airy function in Figure 6.3 between $k_z=k$ and $k_z=k\cos(\theta_c)$. For maximum extraction there is typically one cavity mode in the escape cone. An optimised microcavity LED does not have its

emission maximum at 0° (Figure 6.2) due to the fact that when light is emitted at larger angles, only half the Airy function would appear in the escape cone. Instead maximum extraction occurs when the emission maximum is detuned to oblique angles as seen in the case where $L > \lambda_e$ in Figure 6.2. This occurs when the Airy peak is centred in the escape window as shown in Figure 6.3 for the microcavity case and the shaded integral below the Airy factor in the escape cone is maximised. The resulting far field emission pattern is doubled lobed and is shown in figure 6.4 for a detuned microcavity LED [11]. A monochromatic source has of course been assumed in the above analysis. In reality exciton emission will have a spectral width but the above approach is still valid. The narrower the spectral width the larger the extraction efficiency possible due to the wavelength dependence of the Airy factor. Extraction efficiencies for semiconductor emitters as high as 20% have been reported using this approach [12].

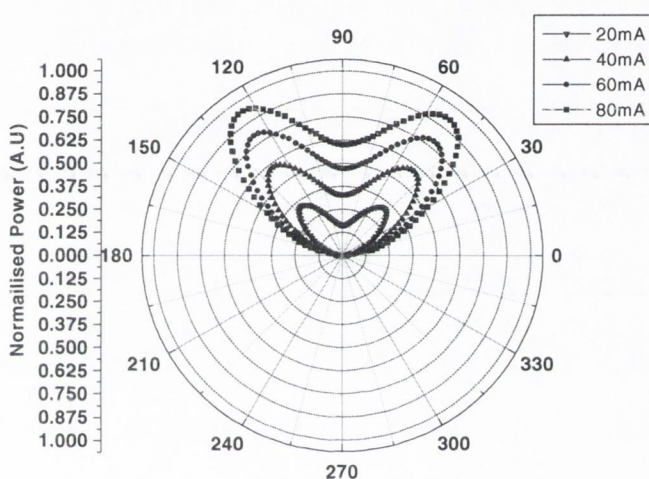


Figure 6.4: Measured far field emission pattern from a microcavity LED [11] whose optical cavity is detuned (cavity thickness slightly longer than $L = m\lambda/2n$ where λ is the emission wavelength) to achieve large extraction efficiency.

As well as improving the extraction efficiency an optical cavity also produces directional emission which can improve device coupling to optical fibre [4]. The optical cavity also leads to spectral filtering of the emission. This reduction in the emission linewidth is beneficial to the achievable transmission bandwidth in optical fibre due to the reduction in chromatic dispersion [13].

So far in this chapter the benefits to LED emission of using a short optical cavity have been summarised. The principle benefit of a short optical cavity to a realistic semiconductor device is the improvement in extraction efficiency. The situation is quite different with respect to Fabry-Perot modulator devices since the light is incident upon the device and not originating from the high index medium and thus these devices do not suffer from total internal reflection limitation. The benefits of a short optical cavity to Fabry-Perot modulator devices are presented next which reveal similarities to emission case.

6.3 Impact of short optical cavity on Fabry-Perot modulators

The factors presented previously that impact on the properties of light emission in a microcavity are expected, by a symmetrical argument, to have an impact on the absorption properties of the semiconductor material.

6.3.1 Absorption rate

The increase in the spontaneous emission rate predicted when an emitter is placed in a short optical cavity would also benefit modulator devices, as this increase in oscillator strength would in turn be expected to result in an increase in the absorption rate. Unfortunately this effect is small for semiconductor optical cavities and no significant change in absorption is expected for microcavity modulator devices. Due to technological difficulties, progress has been slower in devices with optical confinement in two and three dimensions. However any enhancements to the spontaneous emission rate by these structures may also lead to an interest in these structures for use as low voltage modulator devices, due to the possible enhancement of absorption in these structures.

6.3.2 Antinode factor

The antinode factor must also be considered with respect to the modulator structure. The 1V-modulator structure has the lowest number of MQWs (12) in the active region, which interacts with the standing wave optical field intensity. These 12 MQWs make up a total thickness of $(12 \times (8.8 + 5.54)) + 5.54 = 177.6 \text{ nm}$. One wavelength inside the optical cavity corresponds to $\lambda/n = 1076 \text{ nm} / 3.5 = 307 \text{ nm}$, thus the 12 MQWs occupy a thickness roughly $\lambda/2$ in size. In this case the antinode factor averages to 1 no matter where the group of 12 MQWs is placed in the optical cavity. This is also the case for operation at larger voltages. To benefit from the antinode factor the number of MQWs needs to be reduced to ≈ 3 and the MQW absorption would increase by a factor of 2 equivalent to 6 MQWs. In the InGaAs material system the absorption coefficient is not large enough for sufficient modulation to be achieved with 6 MQWs at 1V operation, thus for the current InGaAs Fabry-Perot modulator there is no benefit from the antinode factor. The larger absorption coefficient in the GaAs material system may allow operation to be possible at 1V with 6 MQWs. Using 3 MQWs positioned at the antinode (equivalent to 6 MQWs) the device would benefit from possibly lower voltage operation due to the reduction in active layer thickness and the reduced cavity order.

6.3.3 Spectral and spatial properties

The main benefits from a short cavity order come from changes to the spectral and spatial properties as in the emission case.

6.3.3.1 Cavity order

The calculated reflectivity from a Fabry-Perot cavity over a broad wavelength range, calculated using equation 2.19 is presented in Figure 6.5 below. The cavity refractive index is taken to be $n=1$ and the cavity is designed to be resonant at $\lambda=1000\text{nm}$ for normal incidence and has a cavity thickness of $L=1500\text{nm}$.

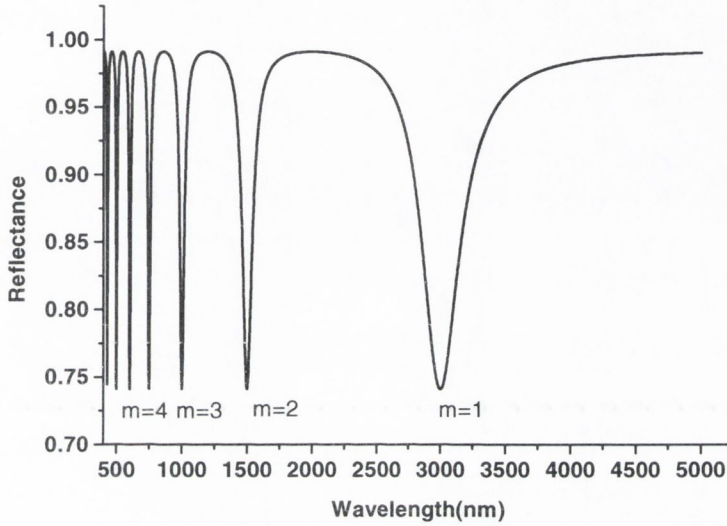


Figure 6.5: Calculated reflectivity from a Fabry-Perot cavity over a broad wavelength range, calculated using equation 2.19. The refractive index of the cavity $n=1$ and the cavity is designed to be resonant at $\lambda=1000\text{nm}$ for normal incidence and has a cavity thickness of $L=1500\text{nm}$. The front and back mirror reflectivities are 50% and 95% respectively.

The cavity order m can be found using equation (2.27)

$$m = \frac{nL \cos \vartheta_1}{\lambda/2} \quad (6.8)$$

Thus the cavity order can be thought of as the number of half-wavelengths that will fit into the optical cavity (and $m=3$ in the case of the example in Figure 6.5). Fabry-Perot resonances also occur at longer wavelengths $\lambda=3000\text{nm}$ in the cavity corresponding to $m=1$, and at $\lambda=1500\text{nm}$ corresponding to $m=2$. Cavity orders greater than $m=3$ all occur at shorter wavelengths, $\lambda=750\text{nm}$ corresponding to $m=4$ etc. The interesting point here is the spectral bandwidth of each cavity order. The cavity resonance clearly narrows as the cavity order increases. This is a result of the $\text{Sin}^2(\delta)$ dependence of the cavity reflectivity in Equation 2.19. A resonance (minimum) occurs every time $\delta=(\pi) \times [nL/(\lambda/2)]$ cycles through an integer multiple of π i.e. every cavity order (Eqn.6.8). The $1/\lambda$ dependence means that at smaller wavelength values this cycle occurs more often as seen in Figure 6.5 above. This results in the spectral bandwidth at higher orders being much reduced compared to low cavity orders. The Fabry-Perot reflectivity is now plotted in Figure 6.6 at wavelengths around the wavelength of interest $\lambda=1000\text{nm}$ for cavity thicknesses $L=m\lambda/2n$ corresponding to different cavity orders m . The increase in

spectral bandwidth at low cavity orders is dramatic. The FWHM spectral bandwidth at $\lambda=1000\text{nm}$ initially increases slowly as the cavity order decreases from $m=30$ to 15, but as the cavity order reduces from $m=15$ to 1 the spectral bandwidth dramatically increases. The full width half-maximum (FWHM) spectral bandwidth value in Figure 6.6 is plotted in Figure 6.7 for different cavity orders and clearly shows the dramatic increase at cavity orders $m<15$. From the above discussion regarding the resonance minima dependence on cavity order m (Figure 6.5), the equation $y=A/x$ is found to give a good fit to the data. A is a constant found to be equal to the spectral bandwidth value for $m=1$. Also presented in Figure 6.7 is similar data for the optical cavity shown in Figure 6.6 but having a higher finesse with $R_f=90\%$ and $R_b=95\%$. In this case the increase in spectral bandwidth at low cavity orders is not as dramatic. Once again the equation $y=A/x$ gives a good fit to the data when reduced by a factor F_R . F_R turns out to be equal to the ratio of the cavity finesse (equation 2.23) for the two cavities considered here and $F_R = 40.1/8.4 = 4.7$. In Chapter 5 modelling of the device operating tolerances have showed that a large spectral bandwidth is necessary to have good tolerance to off axis operation, good MBE growth tolerances and increased temperature sensitivity. The above results indicate that these tolerances can be maximised by having the shortest possible cavity order.

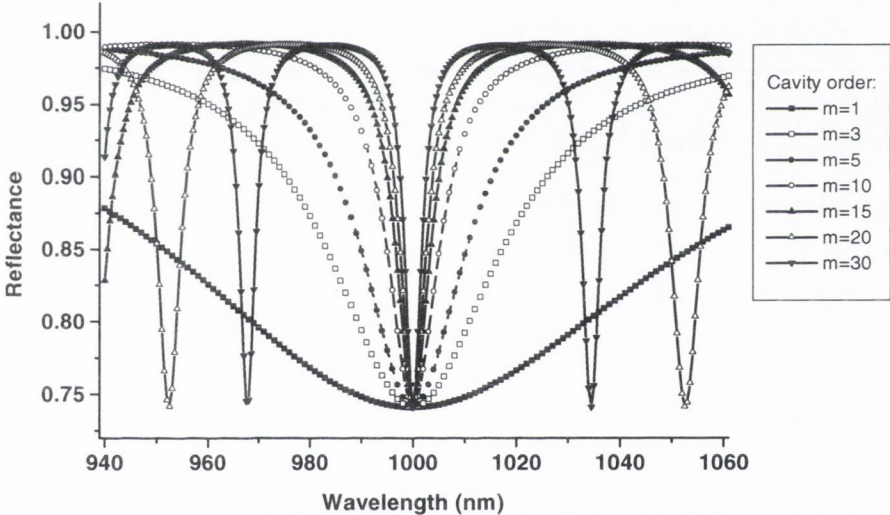


Figure 6.6: Fabry-Perot reflectivity plotted at wavelengths around the wavelength of interest $\lambda=1000\text{nm}$ for cavity thicknesses $L=m\lambda/2n$ corresponding to different orders m .

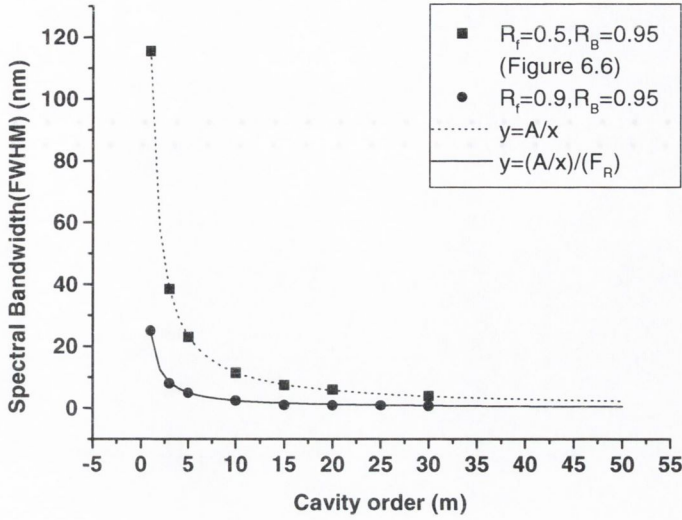


Figure 6.7: FWHM spectral bandwidth at different cavity orders for the optical cavity presented in the previous figure having $R_f=50\%$ and $R_b=95\%$. Also presented is data for a similar optical cavity but having a higher finesse with $R_f=90\%$ and $R_b=95\%$. The equation $y=A/x$ gives a good fit to the data in each case, A is a constant found to be equal to the spectral bandwidth value for $m=1$.

6.3.3.2 Fabry-Perot modulator cavity order

In the above simple analysis the cavity order is calculated using equation 6.8 but this equation assumes that there is no penetration into the cavity mirrors and the cavity order is solely determined by the actual physical cavity thickness. In reality only a metal mirror approaches such as mirror, having very small penetration depths typically a few nanometers. Unfortunately as we have seen in Chapter 3 the reflectivities achievable with metal mirrors do not exceed 95% and are accompanied by significant absorption. For higher reflectivities Bragg mirror are required. When a Bragg stack mirror is used its operation principle depends on the summation of Fresnel reflections as the incident light penetrates the mirror. Thus the penetration of the incident light into the mirror must be accounted for when considering the cavity length/order. If the physical or bare cavity order is defined as $m_o=nL/(\lambda/2)$ and the additional cavity order due to the penetration length L_p into the Bragg mirror is $\Delta m_c=nL_p/(\lambda/2)$ the total cavity order for front and back Bragg stack mirrors is

$$m_o + 2\Delta m_c = \frac{nL}{\lambda/2} + \frac{2nL_p}{\lambda/2} \quad (6.9)$$

the penetration length can be calculated from [15]

$$L_p = \frac{\lambda}{2} \frac{n_L}{n_L n_H \Delta n} \quad (6.10)$$

where n_L , n_H are the refractive indices of the low and high Bragg mirror layers and $\Delta n = n_H - n_L$ the mirror refractive index step, thus:

$$\Delta m_c = \frac{n_L n_H}{n_H n_L \Delta n} \approx \frac{n}{2\Delta n} \quad (6.11)$$

Equation 6.11 shows that the Bragg mirror refractive index step $\Delta n = n_H - n_L$ plays a major role in determining the penetration depth into the mirror and the additional cavity order.

In the Fabry-Perot modulator case, the devices modelled in Chapter 5 at each operating voltage were modelled with a minimum cavity thickness. At each operating voltage the minimum amount of P+ layer thickness was used to place the Fabry-Perot resonance at the required operating wavelength. The modulator cavity order is given by $m = m_0 + 2\Delta m_c$ since Bragg mirrors are used for the front and back cavity mirrors. The physical cavity order m_0 is reduced at lower voltage operation due to the reduced number of MQWs in the optical cavity. This is only reduced by a small amount from $m_0 = 4$ at 5V to $m_0 = 2$ at 1V operation due to the quantum well and barrier thicknesses being only 8.8nm and 5.54nm respectively and a cavity order being of thickness $\lambda/2n \approx 150$ nm. The contribution from the Bragg mirrors to the total cavity order is given by equation 6.11 and for the current device structure modelling in Chapter 5 $n_L = 3.1$, $n_H = 3.42$, $\Delta n = 0.32$ giving a penetration order of $m_c = 5.4$ per Bragg mirror. The total cavity order is $m = 17$ at 5V reducing to $m = 14.9$ at 1V. Thus the Bragg mirrors contribution to the total cavity order $\approx 70\%$. In order to take advantage of the benefits of a short cavity order to the device spectral bandwidth, (Figure 6.5) the choice of mirrors for the optical cavity needs careful consideration. The *InAlAs* / *InGaAs* Bragg mirror composition, used in the MBE grown modulator device in Chapter 4 and whose experimentally verified refractive indices values were used in the optimum device modelling in Chapter 5, was chosen to fulfil lattice matching conditions and to cooperate with strain balancing layers. At this time the importance of the cavity order was not realised and not considered. The use of a higher refractive index contrast/step Bragg mirrors would reduce the cavity order and benefit the device tolerances. The benefits to the device operation tolerances are investigated using the transfer matrix model and presented in the next section.

6.4 Impact of short cavity order

The improved spectral bandwidth predicted above is firstly investigated using the transfer matrix model for the 1V and 2V modulator (see Table 5.1) whose spectral bandwidth (Figure 5.12) is the poorest for the current device structure having values of 0.6nm and 2.1nm respectively. Improvements in spectral bandwidth also benefit the device angular acceptance, MBE growth tolerance and temperature sensitivity. The benefits to these tolerances are also examined

6.4.1 Spectral bandwidth

The improvement in modulator spectral bandwidth is investigated using the transfer matrix model for various cavity orders. The cavity order for the current modulator structure modelled in Chapter 5 is m

≈ 15 . The contribution to this from the bare cavity is already minimised. To reduce the total cavity order the refractive indices values of the Bragg mirror layers are altered to achieve a larger refractive index step thus reducing the cavity order (eqn. 6.11). In reality the material composition and thus the refractive index values of the Bragg mirror are decided by such factors as lattice matching and constraints minimising strain in the device; and thus can not be varied unlike parameters in this modelling. The layers chosen do coincide with current Bragg mirror technology and these modelling results are in general applicable to all material systems. In our modelling the cavity order is increased from the current cavity order ($m \approx 15$) by fixing the Bragg mirror parameters and increasing the physical cavity thickness and cavity order m_0 . Modelling has shown identical results regardless of whether the cavity order is accounted for principally by m_0 or Δm_c . Modelling results are presented in Figure 6.8 for the 1V and 2V modulator structure. As in Chapter 5 the spectral bandwidth is calculated for the reflectivity change ΔR at FWHM ($\approx 30\%$).

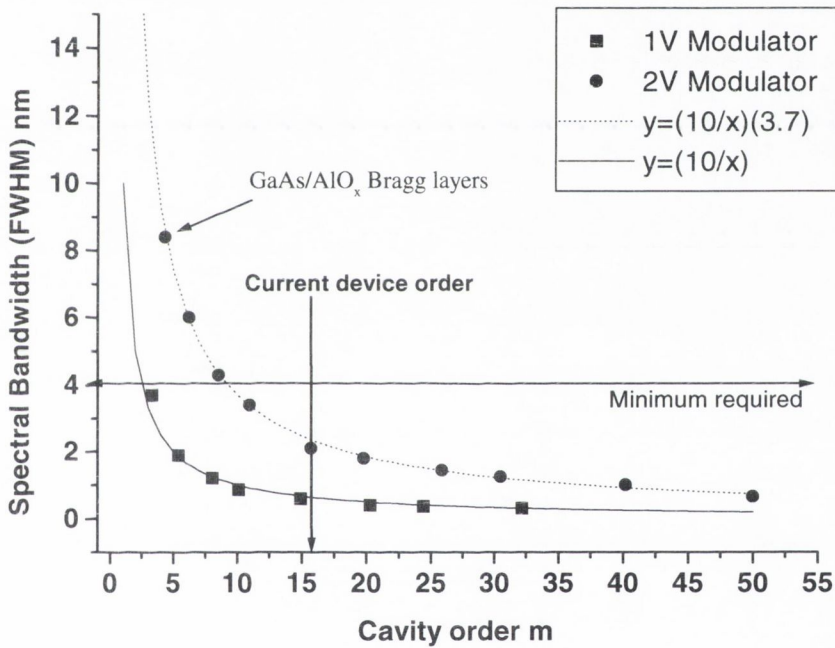


Figure 6.8: Modelling results for the 1V and 2V modulator structure whose spectral bandwidth for the current device (Figure 5.14) is 0.6nm and 2.1nm respectively. The spectral bandwidth is calculated for the reflectivity change at FWHM ($\approx 30\%$).

As expected from Figure 6.7 the spectral bandwidth increases as the cavity order reduces and the 2V modulator benefits more due to its lower finesse cavity. The lowest cavity order (with current technology) is achieved when the Bragg mirror consists of GaAs/AlO_x layers [15] (data points). The refractive index layers are taken to be 3.47 and 1.75 respectively [16] giving a $\Delta m_c = 0.7$ per Bragg mirror. The total cavity order in this case is $m_{1V} = 3.3$ at 1V and $m_{2V} = 4.3$ at 2V and the resulting spectral bandwidth is much improved to 3.7nm and 8.4nm respectively. For a GaAs/AlAs Bragg mirror $m_{1V} = 10.1$ and $m_{2V} = 11$ and the resulting spectral bandwidth improves only slightly to 0.87nm at 1V;

but to 3.4nm at 2V which is approaching the required absolute growth tolerance value of 4nm as discussed in Chapter 5. The equation $y=Ax$ is fitted to the data at 1V as done previously in Figure 6.7. The best fit was found when $A=10$ indicating that if a microcavity order of $m=1$ was attainable the maximum spectral bandwidth achievable for the 1V modulator is 10nm. When multiplied by a factor equal to the ratio of the 1V modulator finesse to the 2V modulator finesse ($F_R=3.7$) the fit shown in Figure 6.8 is obtained for the 2V device. Thus a microcavity order of $m=1$ would yield a spectral bandwidth achievable for the 2V modulator of $10 \times 3.7 = 37\text{nm}$. This relationship is useful as it allows us to predict spectral bandwidth values at shorter cavity orders than it is possible to model using the transfer matrix model. The approach of reducing the cavity order by increasing the refractive index step is eventually limited, as the optimum reflectivity of the Bragg mirror cannot be achieved due to large increase in reflectivity per Bragg period. As mentioned above (Section 5.5.1) the minimum spectral bandwidth required concurring with current absolute growth accuracy is ($\pm 2\text{nm}$) 4nm. From the above predictions this would require a cavity order $m=9$ for 2V operation, which is realistically possible. Unfortunately for 1V operation a cavity order of $m=2$ would be required to attain the required spectral bandwidth. Achieving a cavity order this small is currently not possible for our modulator structure. This will make device growth at 1V operation very difficult and improbable without undesirable post-growth processing.

6.4.2 Angular acceptance

The angular acceptance of these devices was modelled as described in Chapter 3 at different cavity orders, as outlined in Section 6.4.1 above. The angular acceptance at different cavity orders for the optimum 1V and 2V modulators in Table 5.1 is presented in Figure 6.9. The angular acceptance value plotted is the half width half maximum (HWHM) value of the device reflectivity change ΔR ($\approx 30\%$).

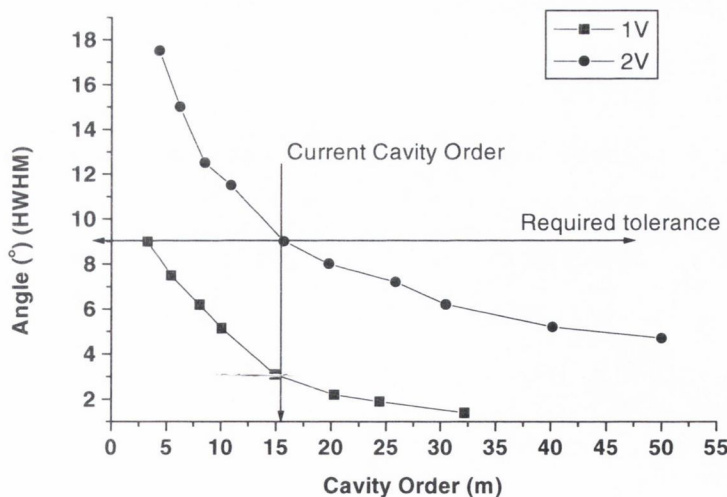


Figure 6.9: Calculated angular acceptance at different cavity orders for the 1V and 2V modulators.

The angular tolerance of the devices also improves at shorter cavity orders as expected from Figure 6.6. As previously stated the 1V and 2V devices modelled in Chapter 5 have a cavity order $m \approx 15$ and in this case the 2V-modulator structure actually meets the required angular tolerance of $\pm 9^\circ$. The increase in angular acceptance at lower cavity orders is always beneficial and may allow more freedom in the design of the systems optics. At 1V operation the required tolerance of $\pm 9^\circ$ is achieved at the limits of the lowest cavity order currently achievable of $m=3.3$.

The angular acceptance can also be increased by detuning of the cavity resonance from the optimum operating wavelength to longer wavelengths. This approach is also used in microcavity LED emission to maximise light extraction as outlined in Section 6.2 above. The angular acceptance of the 2V modulator device modelled in Section 5.5.3 is shown in figure 6.10 represented by the 0nm detuning curve. Here the optical cavity thickness is chosen so as the Fabry-Perot resonance is placed at the optimum operation wavelength (λ_{op}) at which maximum reflectivity change occurs (about 23nm from the 0V *hh* exciton peak as outlined in Chapter 3).

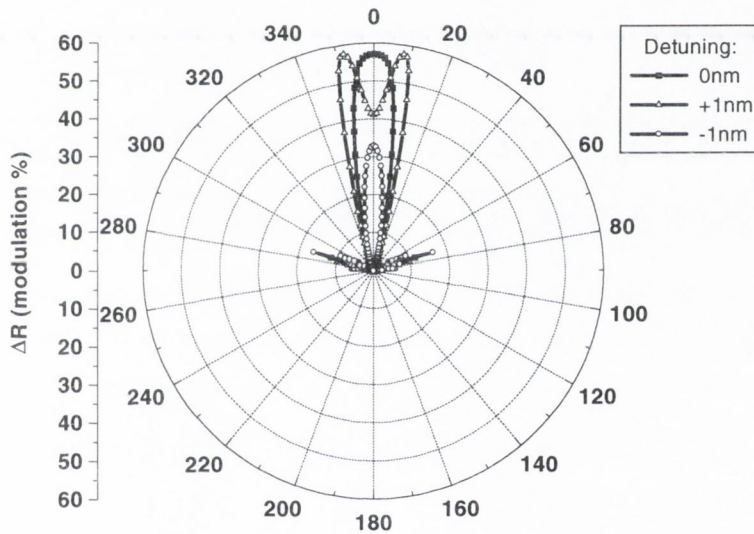


Figure 6.10: Calculated angular acceptance for the 2V-modulator device as modelled in section 5.5.3. Data are also presented for the case where the optical cavity thickness is adjusted so the Fabry-Perot resonance occurs 1nm longer and shorter than the optimum operating wavelength.

When the optical cavity thickness is increased so as the cavity resonance is placed 1nm to the longer wavelength side of λ_{op} the angular acceptance curve contains a doubled lobed feature often seen in emission for microcavity LEDs (Figure 6.4). The double lobed feature is again due to the $\text{Cos}(\theta)$ dependence of the phase difference $\phi = 2\pi[\text{Ln}\text{Cos}(\theta_1)/\lambda_{op}]$ (for each traversal of the cavity) between the two series of reflected waves that interfere as outlined in Chapter 2. In this case when the cavity thickness $L = \lambda_{op}$ **destructive** interference occurs between the two series of reflected waves and the Fabry-Perot resonance has a minima at $\lambda = \lambda_{op}$. For the case where $L > \lambda_{op}$ a doubled lobed pattern is predicted and these lobes or interference minima occur at an internal angle $\theta_1 = \text{Cos}^{-1}(\lambda_{op}/\text{Ln})$ which is

related to the external incident angle through Snells law. At this angle the phase difference $\phi = 2\pi[L\text{Cos}(\theta_1)/\lambda_{op}]$ becomes an integer multiple of π allowing full destructive interference to occur. Again for the case of $L < \lambda_{op}$ the $\text{Cos}(\theta)$ value is always < 1 and thus the phase difference ϕ can never be an integer multiple of π and the destructive interference minima cannot occur resulting in the overall reflectivity change being reduced as seen in Figure 6.10. This result shows a number of important points. Cavity detuning to longer wavelengths allows the angular acceptance to be increased. The angular range increases from $\pm 9^\circ$ at 0nm detuning to $\pm 13^\circ$ for +1nm detuning at the FWHM value. The modulation value does decrease along the cavity axis at 0° but remains above the required minimum value of 30%. These results are for a cavity order $m=15.5$ and at lower cavity orders the angular acceptance values can also be increased from the 0nm detuning values shown in Figure 6.9 above. The final point here concerns MBE growth of these devices. The above data shows that it is always better from an angular tolerance point of view to grow the optical cavity too long. Growing the cavity shorter than the optimum thickness will have a detrimental effect on the angular tolerance as seen for the -1nm detuning in Figure 6.10. The above results also must be considered when processing large arrays from a grown wafer as different areas of the wafer although yielding the required modulation may have different angular tolerances.

6.4.3 MBE Growth non-uniformities

To study the modulator growth tolerance, the modulation is calculated when the actual physical cavity thickness deviated from the ideal optical cavity thickness for each modulator structure as before. The modulation changes because the curves shown in Figure 5.11 shift in wavelength from the fixed operating wavelength, as the cavity thickness increases or decreases from the ideal thickness. The tolerance to non-uniform growth across a wafer was dealt with in detail in Section 5.5.2.2. The main factors that influence the growth tolerance across a wafer were the shift $\Delta\lambda$ in wavelength from the fixed operating wavelength λ when the cavity thickness t changes by Δt is given by

$$\frac{\Delta\lambda}{\lambda} = \frac{\Delta t}{t} \quad (6.12)$$

and the cavity finesse, which reduces the spectral bandwidth at lower voltage operation giving poorer growth tolerances to changes in cavity thickness. From modelling results in section 5.5.2.2 and the fact that due to growth conditions the wafer thickness changes radially as a percentage of the centre wafer thickness, it was concluded that the tolerance to non-uniform growth was optimised when the cavity thickness is minimised. This means shorter cavities will have a smaller thickness difference between the wafer centre and wafer edge (eqn.6.12) and much improved tolerance to cavity thickness changes across the wafer.

One would initially expect the increase in spectral bandwidth as the cavity order m is reduced to benefit the tolerance to cavity thickness fluctuations. Spectrally wider curves (Figure 5.11) should allow the modulation value to remain at large values (above the FWHM value of 29%) for larger thickness changes than summarised in Figure 5.13. Thus the 2V-modulator structure was used to investigate the benefits of a short cavity order. As before, the cavity order is reduced by changing the

refractive index step of the Bragg mirror and the modulator growth tolerance is examined by calculating the modulation when the actual physical cavity thickness deviated from the ideal optical cavity thickness. Modelling results are presented in Figure 6.11. For comparison data is shown for the 2V structure of cavity order $m=15.5$ modelled in Chapter 5 (Figure 5.13). The modelling results at shorter cavity orders in Figure 6.11 show no improvement in tolerance to absolute cavity thickness fluctuations. A closer look at the modelling results revealed that as the cavity order is reduced the device spectral bandwidth increased as expected but the resonance wavelength position was found to shift more in wavelength cancelling the benefit of the increased spectral bandwidth. This behaviour is identical to modelling results in Figure 5.14 where changing the actual physical cavity thickness and thus m_0 produced nearly identical tolerances to cavity thickness changes. The results in Figure 5.14 are governed by Equation 6.12. When the total cavity order is changed by changing Δm_c in fact what is being changed is the penetration depth into the Bragg mirror. The cavity length L in Equation 6.12 consists of the physical cavity length L_0 and the penetration depth into each Bragg mirror L_p given by Equation 6.10. Thus it is not surprising that identical results to Figure 5.14 were obtained as in both cases it is just the effective cavity length that is being changed. Thus the conclusions made in Chapter 5 to obtain maximum tolerance to thickness fluctuations still hold. To maximise these tolerances the cavity thickness L or order m , which must be minimised. If the results in Figure 6.11 are plotted as a percentage change of the total cavity thickness taking the reduced effective cavity length for the higher contrast Bragg mirrors into account the improvement to growth tolerance can be seen. These results are plotted in Figure 6.12.

The improvement to growth non-uniformities is clear to see. The cavity order of $m=4.2$ is the lowest currently possible. It assumes the $p+$ and $n+$ layers currently contained inside the optical cavity were removed and the Bragg mirrors doped p -type and n -type as done with current VCSEL structures. It also assumes the Bragg mirrors consist of high contrast GaAs/ AlO_x layers. This minimises the physical cavity thickness L . The tolerance increases to a FWHM value of 1.2%, which is a more acceptable value. For the production of very large arrays of these devices the reduction of the cavity length is essential.

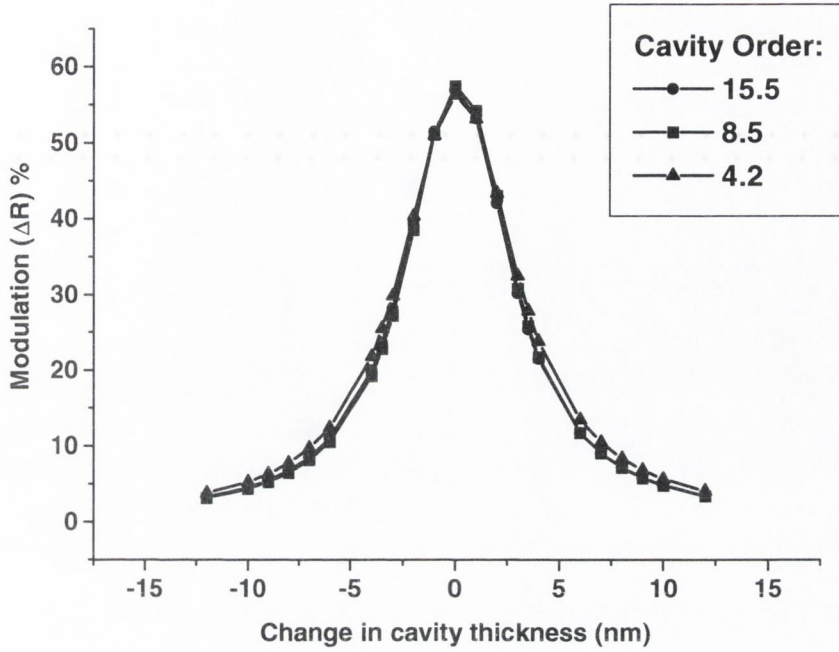


Figure 6.11: Modelling results for the 2V-modulator device showing changes in the device modulation as the optimum cavity thickness changes, for different cavity orders.

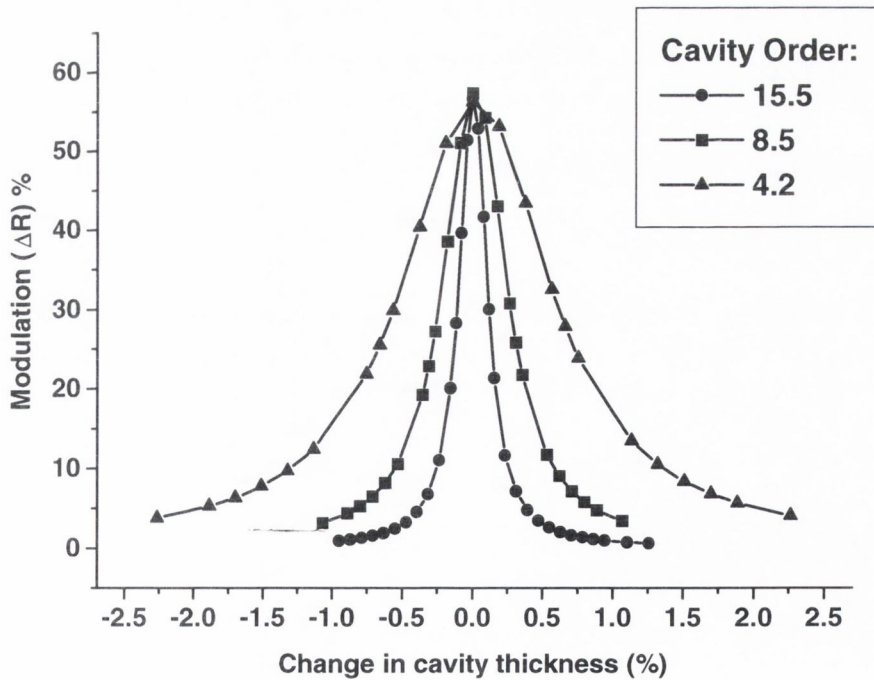


Figure 6.12: Modelling results presented in Figure 6.11 but plotted as a percentage change in the total cavity thickness (physical cavity length and mirror penetration lengths).

If we assume the physical cavity thickness to be principally made up of the number of MQWs in the optical cavity and thus $L_o \approx 24(8.8+5.54) = 344\text{nm}$. The modulator cavity size is about 1λ typically the size of the VCSEL optical cavity and thus the modulator and VCSEL devices should have similar absolute thickness changes across the wafer assuming they will use identical doped Bragg mirrors. This is where the modulator structure gains an advantage over VCSEL devices. The FWHM $\pm 3\text{nm}$ thickness change in Figure 6.11 represents the allowed change in thickness across a wafer, any greater thickness changes will mean the modulation achievable at the operating wavelength drops below a specific system value of 30%. The important point here is the operating wavelength remains unchanged for modulator device. In the VCSEL case assuming a similar 1λ cavity (344nm), a $\pm 3\text{nm}$ thickness change will change the emission wavelength by $\pm [(3\text{nm}/L_o+L_p) \times 100] \approx 0.6\%$. (from eqn.6.12) e.g. if the emission wavelength is 1000nm then $\Delta\lambda=\pm 6\text{nm}$. A change of this magnitude is intolerable to the system optics in the SPOEC system where a tolerance specification of $\Delta\lambda=\pm 1.0\text{nm}$ is required [17]. From this reasoning, much larger arrays should be possible using modulator devices. To get an idea of the array size possible from Figure 4.13 a cavity thickness change of $\pm 0.6\%$ corresponds a distance from the centre of $25.4\text{mm}-12.5\text{mm}=12.9\text{mm}$. Assuming the change in cavity thickness to be symmetric radially from the wafer centre. Taking the device pitch used in the SPOEC routing chip of $150\mu\text{m}$ and a square wafer area of $(12.9) \times (12.9) \times 2$ (for full wafer area) a simplistic calculation gives an array size of $\approx 170 \times 170$ devices ideally all operating with 30% modulation at 2V operation. This array size is compatible with the required array size at this operating voltage as predicted by the optical interconnect roadmap [18].

6.4.4 Temperature sensitivity

The effect of changing ambient temperature on the exciton absorption and Fabry-Perot resonance is outlined in Chapter 3 Section 3.4.4. The temperature sensitivity at each operating voltage is presented in Figure 5.23. The reduced spectral bandwidth at lower voltage operation is believed to produce the poorer temperature tolerance predicted at low voltage operation. A broader spectral bandwidth is thus expected to give an improved tolerance to changes in ambient temperature. The cavity order of the 2V-modulator was reduced by increasing the refractive index step of its Bragg mirror to a cavity order of $m=6$. The temperature tolerance was then calculated as described in section 3.4.4 and the resulting tolerance to temperature changes is plotted in figure 6.12. The temperature tolerance for the 2V cavity order of $m=15.5$ modelled in Chapter 5 is also presented for comparison. The temperature range at which 30% modulation is possible increase from 26°C at $m=15.5$ to 40°C at $m=6$. The reflectivity change for $m=6$ is smaller than $m=15.5$ due to the large index step of the Bragg mirror for cavity order $m=6$ and the resulting difficulty is achieving the optimum Bragg mirror reflectivity. These results are promising although these devices would still require some form of temperature control for operation in a real system as discussed in section 5.5.4.

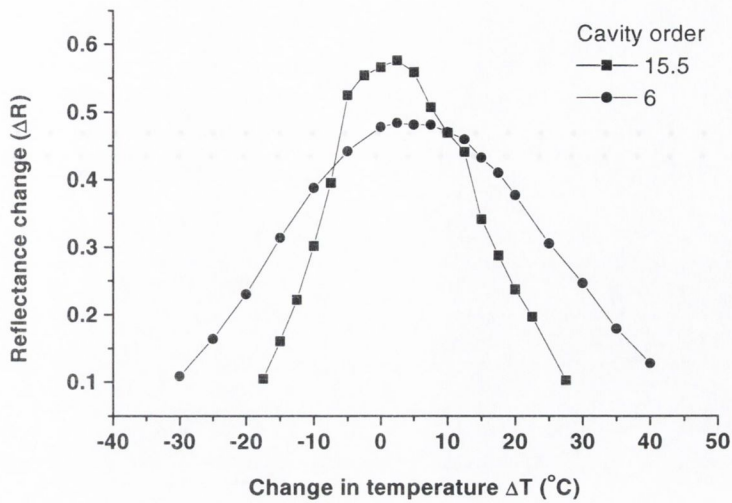


Figure 6.12: Calculated temperature tolerance for the 2V-modulator device at cavity orders $m=15.5$ and at reduced cavity order $m=6$. The reduced cavity order shows an increased tolerance to temperature changes.

6.5 Conclusions

In this section the benefits of a short optical cavity to the operation of a Fabry-Perot modulator have been presented. Modelling has shown how the device spectral bandwidth increases as the optical cavity order decreases. The spectral bandwidth is proportional to $1/\text{cavity order}$, thus a cavity order $m=10$ has a spectral bandwidth 10 times smaller than a cavity order of $m=1$. The angular acceptance range is also increased at shorter cavity orders. The angular range can be increased even further by ‘detuning’ where the cavity resonance is placed at a longer wavelength to the optimum operating wavelength but with a reduction in modulation along the cavity axis. Modelling results also showed that detuning to the shorter wavelength results in a reduced angular tolerance. The increased spectral bandwidth will result in more tolerance to error in the absolute growth thickness at the wafer centre. Regarding growth non-uniformities a short physical cavity order m_0 is necessary to maximise the device tolerance to optical cavity thickness changes across a wafer and allow the production of large area arrays. Modelling has also predicted that the increased spectral bandwidth also improves the temperature sensitivity of these devices. It is difficult to compare devices in the literature to the modelled devices above due to devices have different finesses, structures and operating voltages. The devices that show the largest spectral bandwidths (and thus tolerances) operating at low voltages are devices that have high contrast doped Bragg mirrors and short cavity lengths [19,20,21,22]. The other important point is that normally ‘on’ devices operating with maximum reflectivity change having better tolerances relative to device operation with maximum contrast. The higher finesse cavity required at lower voltage operation narrows the R_{off} curve and makes it more sensitive to environmental changes [19]. Since the device contrast is most sensitive to this value it results in poorer tolerances.

At this point the principle factors that govern and influence the operation of this modulator device have been studied to a level that allows us to conclude the limits of operation possible with the current InGaAs/(Al)GaAs material system we have been working with. The majority of these results have general application and the principal findings and conclusions can be brought together to produce an overall picture of the main factors which impact on the device structure and operation in any material system. From these findings an optimum structure can be predicted and concluded in Chapter 7.

6.6 References

- [1] E.M. PURCELL, 'SPONTANEOUS EMISSION PROBABILITIES AT RADIO FREQUENCIES', PHYSICAL REVIEW 69, 681 1946
- [2] C. WEISBUCH, H. BENISTY, R.HOUDRE, 'OVERVIEW OF FUNDAMENTALS AND APPLICATIONS OF ELECTRONS, EXCITONS AND PHOTONS IN CONFINED STRUCTURES', JOURNAL OF LUMINESCENCE, 85 271-293 2000
- [3] E.F. SCHUBERT, N.E.J HUNT, R.J. MALIK, M. MICOVIC, D.L.MILLER, 'TEMPERATURE AND MODULATION CHARACTERISTICS OF RESONANT CAVITY LIGHT EMITTING DIODES' JNL. OF LIGHTWAVE TECHNOLOGY VOL. 14, NO. 7 (P1721), JULY 1996.
- [4] H. DE NEVE, J.BLONDELLE, P. VAN DEALE, P. DEMEESTER, R. BAETS, AND G.BORGHES, 'RECYCLING OF GUIDED MODE LIGHT EMISSION IN PLANAR MICROCAVITY LIGHT EMITTING DIODES',APPLIED PHYSICS LETTERS, 70: (7) P799 1997
- [5] D.J. HEINZEN, J.J. CHILDS, J.E. THOMAS AND M.S. FELD, 'ENHANCED AND INHIBITED SPONTANEOUS EMISSION BY ATOMS IN A CONFOCAL RESONATOR', PHYSICAL REVIEW LETTERS 58, 1320 1987
- [6] G.BJORK, Y. YAMAMOTO AND H. HEITMANN, 'SPONTANEOUS EMISSION CONTROL IN SEMICONDUCTOR MICROCAVITIES, CONFINED ELECTRONS AND PHOTONS: NEW PHYSICS AND APPLICATIONS' PLENUM, NEW YORK, 1995
- [7] G.BJORK AND Y. YAMAMOTO, 'SPONTANEOUS EMISSION IN PLANAR DIELECTRIC MICROCAVITIES', CRC PRESS 1995
- [8] J.M. GERARD, B. SERMAGE, B. GAYRAL, B.LEGRAND, E.COSTARD, V. THIERRY-MIEG, 'ENHANCED SPONTANEOUS EMISSION BY QUANTUM BOXES IN A MONOLITHIC OPTICAL MICROCAVITY', PHYSICAL REVIEW LETTERS, 81: (5) 1110-1113 AUG 3 1998
- [9] H. BENISTY, 'PHYSICS OF LIGHT EXTRACTION EFFICIENCY IN PLANAR MICROCAVITY LIGHT-EMITTING DIODES', FUNDAMENTALS AND APPLICATIONS OF CONFINED PHOTON SYSTEMS, H. BENISTY, J-M. GERARD, R.HOUDRE, J.RARITY, AND C. WEISBUCH EDS., HEIDELBURG: SPRINGER, 1999.
- [10] H. BENISTY, H. DE NEVE AND C. WEISBUCH, 'IMPACT OF PLANAR MICROCAVITY EFFECTS ON LIGHT EXTRACTION – PART I: BASIC CONCEPTS AND ANALYTICAL TRENDS', IEEE JOURNAL OF QUANTUM ELECTRONICS, 34: (9) 1612-1631 SEPT 1998
- [11] T. KAVANAGH, 'DIRECTIONAL EMISSION CONTROL IN MICROCAVITY LIGHT EMITTING DIODES:ITS EFFECT ON FIBRE COUPLING AND SYSTEMS PERFORMANCE', MSC. THESIS, PHYSICS DEPARTMENT, TRINITY COLLEGE DUBLIN, AUG 2000.

- [12] H. DE NEVE, J. BLONDELLE, P. VAN DAELE, P. DEMEESTER, R. BAETS 'RECYCLING OF GUIDED MODE LIGHT EMISSION IN PLANAR MICROCAVITY LIGHT EMITTING DIODES' APPL. PHYS. LETT. VOL. 70 NO. 7 (P799) FEBRUARY 1997.
- [13] N.E.J. HUNT, E.F. SCHUBERT, R.F. KOPF, D.L. SIVCO, A.Y. CHO AND G.J. ZYDZIK, 'INCREASED FIBRE COMMUNICATIONS BANDWIDTH FROM A RESONANT CAVITY LIGHT EMITTING DIODE EMITTING AT 940NM', APPLIED PHYSICS LETTERS, 63: (19) P2600 1993
- [14] MACLEOD H.A., 'THIN FILM OPTICAL FILTERS', ADAM HILGER LTD, BRISTOL, 1986
- [15] M.H. MACDOUGAL, H.ZHAO, P.D. DAPKUS, M.ZARI AND W.H. STEIER, 'WIDE-BANDWIDTH DISTRIBUTED BRAGG REFLECTORS USING OXIDE/GAAS MULTILAYERS', ELECTRONICS LETTERS, 30:(14), 1147-1148, 1994
- [16] E.D. PALIK, ' HANDBOOK OF OPTICAL CONSTANTS OF SOLIDS I-III', ACADEMIC PRESS, BOSTON, 1998
- [17] A.C. WALKER, M.P.Y. DESMULLIEZ, M.G. FORBES, S.J. FANCEY, G.S. BULLER, M.R. TAGHIZADEH, J.A.B. DINES, C.R. STANLEY, G. PENNELLI, A.R. BOYD, P. HORAN, D. BYRNE, J. HEGARTY, S. EITEL, H.-P. GAUGGEL, K.-H. GULDEN, A. GAUTHIER, P. BENABES, J.L. GUTZWILLER, AND M. GOETZ, 'DESIGN AND CONSTRUCTION OF AN OPTOELECTRONIC CROSSBAR SWITCH CONTAINING A TERABIT/S FREE-SPACE OPTICAL INTERCONNECT', IEEE J. SELECTED TOPICS IN QUANT. ELECTRON. SPECIAL ISSUE ON SMART PHOTONIC COMPONENTS, INTERCONNECTS AND PROCESSING, VOL. 5, NO. 2, PP 236-249 (1999).
- [18] MEL-ARI TECHNOLOGY ROADMAP: 'OPTOELECTRONIC INTERCONNECTS FOR INTEGRATED CIRCUITS, EUROPEAN COMMISSION IST PROGRAMME: FUTURE AND EMERGING TECHNOLOGIES' ,2ND EDITION SEPT 1999
- [19] LAW KK, MERZ JL, COLDREN LA, 'EFFECT OF LAYER THICKNESS VARIATIONS ON THE PERFORMANCE OF ASYMMETRIC FABRY-PEROT REFLECTION MODULATORS', JOURNAL OF APPLIED PHYSICS, 72: (3) 855-860 AUG 1 1992
- [20] WHITEHEAD M, RIVERS A, PARRY G, ROBERTS JS, 'VERY LOW-VOLTAGE, NORMALLY-OFF ASYMMETRIC FABRY-PEROT REFLECTION MODULATOR', ELECTRONICS LETTERS, 26: (19) 1588-1590 SEP 13 1990
- [21] ZOUGANELI P, STEVENS PJ, ATKINSON D, PARRY G, 'DESIGN TRADE-OFFS AND EVALUATION OF THE PERFORMANCE ATTAINABLE BY GAAS-AL_{0.3}GA_{0.7}AS ASYMMETRIC FABRY-PEROT MODULATORS', IEEE JOURNAL OF QUANTUM ELECTRONICS, 31: (5) 927-943 MAY 1995
- [22] K-K LAW, WHITEHEAD M, MERZ JL, COLDREN LA, 'SIMULTANEOUS ACHIEVEMENT OF LOW INSERTION LOSS, HIGH CONTRAST AND LOW OPERATING VOLTAGE IN ASYMMETRIC FABRY-PEROT REFLECTION MODULATOR', ELECTRONICS LETTERS, 27: (20) 1863-1865 SEP 26 1991

Chapter 7 Conclusions

7.1 Conclusions

This thesis has discussed and presented work related to the Fabry-Perot modulator device with respect to the device physics and its development for compatible operation in current and future digital optical interconnect systems. The results presented relate to low voltage operation compatible with future CMOS voltages while simultaneously achieving operating tolerances that are compatible in a working system. At this point the principal factors that govern and influence the operation of a modulator device have been studied to a level that firstly, allows us to conclude the probable limits of operation possible with the InGaAs/(Al)GaAs material system we have been working with and produces a set of design guidelines that should permit the fabrication of an operational low voltage device. The principal findings and conclusions from the previous 4 chapters are now brought together to produce an overall picture of the main factors which impact on the device structure and operation. These factors have been discussed and optimised individually throughout this thesis while considering the impact on other device performance parameters. Here they will be addressed in general terms. From these findings an optimum structure can be concluded.

The first key point modelling of InGaAs/(Al)GaAs Fabry Perot modulator structures in this study has revealed, is that there is an optimum electric field across a given number of MQWs that gives the maximum reflectivity change. Thus, for a fixed operating voltage, the optimum operation is achieved when the number of MQWs is altered to obtain that optimum electric field. This consequently means that an optical cavity of increasing finesse will be required for decreasing operating voltages.

The fact that an optical cavity is essential, the intimate relationship between the absorption available from the MQWs and the resulting mirror reflectivities required to produce maximum reflectivity change (amplitude modulation) was examined. Regarding the active MQW region the most important parameters at the optimum operating wavelength are the absorption α_{on} and the residual absorption α_o and the absorption change $\Delta\alpha = \alpha_{on} - \alpha_o$, which determine the achievable reflectivity change. The R_{on} value is largely influenced by α_o and the R_{off} value by α_{on} where the reflectivity change $\Delta R = R_{on} - R_{off}$. The α_{on} value determines the front mirror reflectivity required to reduce the reflectivity R_{off} value to a value close to zero. The chosen front mirror reflectivity (R_F) value along with the residual absorption α_o , then determine the R_{on} reflectivity value which can be increased by increasing the back mirror reflectivity R_B and thus maximising $\Delta R = R_{on} - R_{off}$ (the R_F value may require some further small increases to obtain maximum ΔR). At lower voltage operation the α_{on} value is reduced due to the lower number of MQWs and thus R_F is required to increase, thereby having a knock-on effect of increasing R_B , to maximise the reflectivity change possible and increasing, the overall cavity finesse. From the offset the MQW absorption determines the optical cavity and device structure. The optical cavity finesse determines many of the device operational parameters such as its spectral bandwidth and the angular range the device will operate at, its tolerance to epitaxial growth and its temperature sensitivity. The optical saturation power is also determined by the cavity finesse but modelling has found it not to be of critical concern. The device electrical bandwidth is the sole operational parameter not directly determined by the optical cavity. Thorough modelling has shown how the above mentioned parameters deteriorate as the optical cavity finesse increases at lower voltage operation. The above conclusions are true regardless of the optical cavity length and minimising the cavity finesse is a key to low voltage operation. Due to the intimate relationship with the MQW absorption, this can be accomplished by minimising the α_o value and maximising the α_{on} value. This currently makes the GaAs material system the optimum choice.

The other key factor for low voltage operation of these devices is the use of a short cavity size to produce a 'microcavity modulator'. The material system used will set the cavity finesse required for a given operating voltage. The device tolerances set by this finesse can be improved by using the shortest optical cavity length possible. A critical issue is the cavity mirrors used and it is most likely Bragg mirrors will be used due to the >95% reflectivities required. It is essential this mirror has a high refractive index step per period to minimise the penetration length into the mirror. Ideally these mirrors should be doped to also minimise the physical cavity length. This technology is standard in VCSEL fabrication and can readily be adapted to Fabry-Perot modulator devices. Much of the previously published work on GaAs/AlGaAs modulators used this approach. In minimising the cavity length the key issue regarding these devices, the tolerances to growth variations across a wafer, can dramatically be improved allowing the production of large arrays of devices. As the VCSEL and modulator

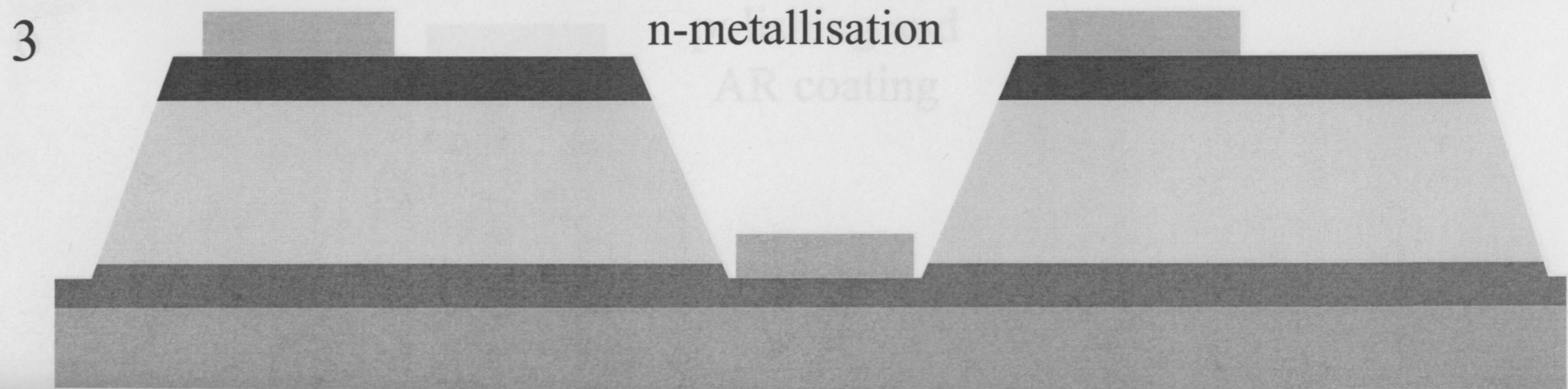
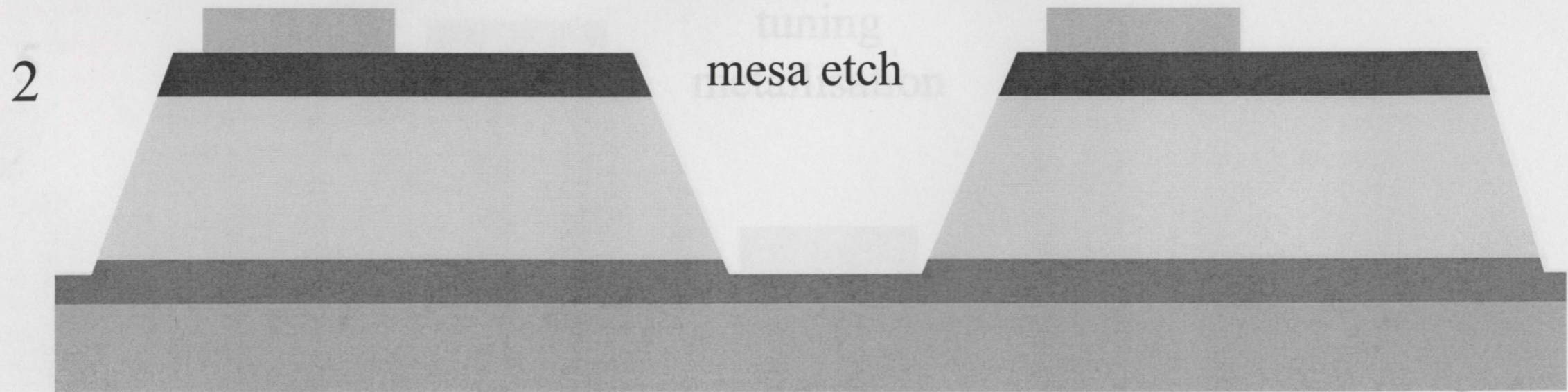
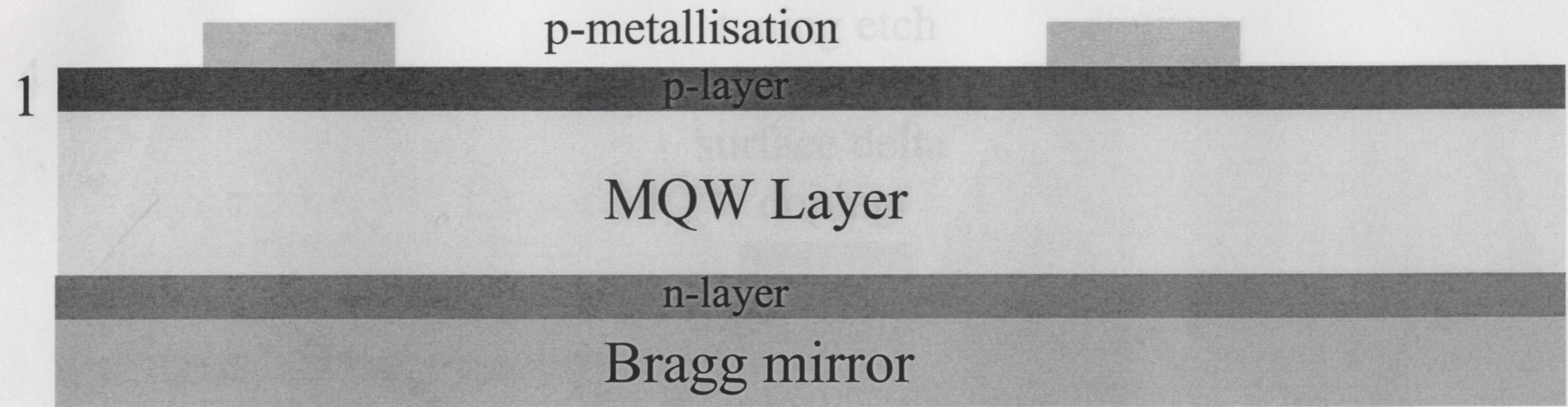
structures are almost identical, modulators should achieve the same non-uniformity tolerances currently shown by VCSEL devices, and even larger modulator arrays should be possible as outlined in Chapter 6.

The limitations of the double-pass reflection modulator were verified with results showing the poor modulation response at operation voltages below 5V voltage swings and thus the motivation for investigating an alternative structure. The Fabry-Perot structure incorporating a gold back mirror and a front Bragg stack was investigated. The use of a back Au mirror allows the existing modulator structure in the SPOEC system to be used. With only a minor modification, the growth of an additional number of front Bragg periods. Modelling results revealed lower voltage operation to be possible down to 2.5V while still achieving the required 30% reflectivity change. At lower voltage operation the reflectivity change achievable from this structure reduced dramatically, no matter how high a front mirror reflectivity was used, and this was found to be due to the limited reflectivity of the Au/semiconductor mirror. An analysis of the device tolerance revealed good tolerances at 5V and 3.3V operation with good tolerances to MBE growth non-uniformities due to the short optical cavity length achievable using a metal mirror. The tolerances at these voltages compared well to the double-pass structure (for 5V operation) and certainly show the potential for operation in a real system. Based on the predicted results for 5V operation Fabry-Perot device structures were fabricated. The measured results produced a lot of useful information validating earlier assumptions made as to device behaviour at lower voltage operation. Reflectivity measurements were used to improve the device layer parameters used in the transfer matrix model and device measurements confirmed the validity of using this approach to model these structures. Measurements also revealed the unpredictability of using gold deposition on semiconductor simultaneously as a mirror and electrical contact. Separating these functions when using a metal coating may be a better approach.

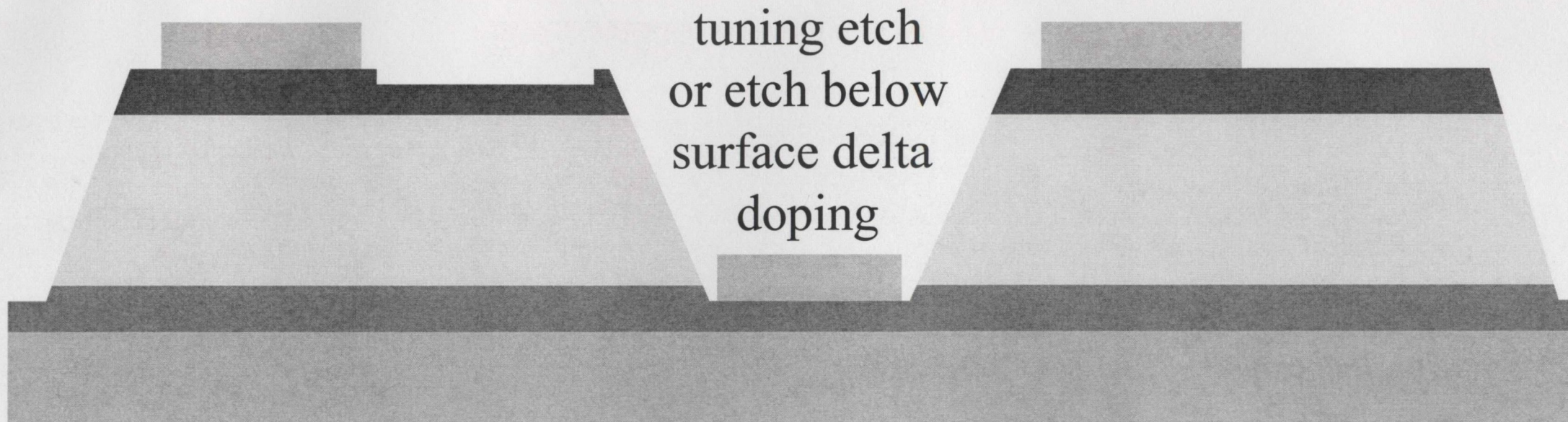
The use of a Bragg mirror or Bragg/gold mirror for the back mirror of the Fabry-Perot device revealed how critical the reflectivity of this mirror is to low voltage operation. Although low voltage operation was predicted to be possible with reflectivity changes of almost 60% down to 1V operation, the high finesse cavities required seriously impacts on the operating tolerances. Of most concern is the large effective cavity length, which results in poor tolerances to the production of large device arrays using epitaxial growth largely due to the poor contrast of the chosen Bragg mirror structure. Equal reflectivity changes were predicted at all operating voltages and thus it is the device operating parameters that determine the lowest possible operating voltage for device operation in an optical interconnect system. The most important of these being the tolerance to the current epitaxial growth absolute thickness accuracy and non-uniformity across a wafer. Taking this and the other practical operational tolerance into account, 2V operation is probably the lowest operation voltage currently possible for InGaAs/(Al)GaAs Fabry Perot modulators, assuming the cavity length can be further reduced by using higher contrast Bragg mirrors improving the device growth tolerance. The relatively low α_o value and the α_{on} value require finesse that are too high at lower than 2V operation, and the shortest cavity lengths currently achievable cannot compensate. One possible solution maybe to use a coupled cavity structure that previous work has shown to improve the spectral bandwidth of Fabry-Perot devices. Although not pursued here, it may present another means to improve the device

Appendix A: Processing steps for Fabry-Perot modulators

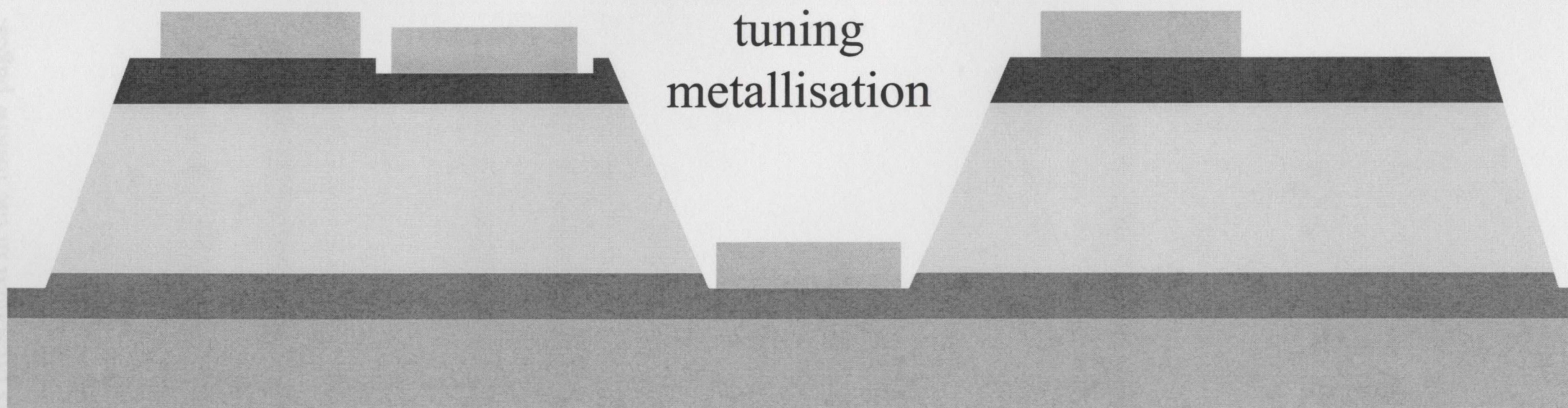
The following diagrams show the processing steps for the semiconductor structures presented in chapter 4.



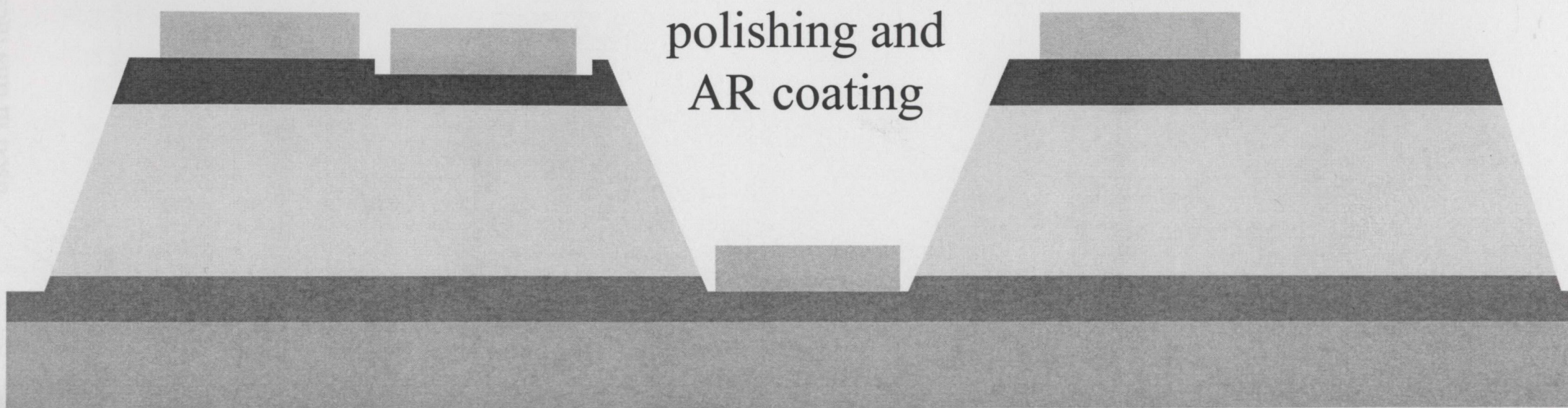
4



5



6



Appendix B: MATLAB code for transfer matrix model

The programming code written in MATLAB for the transfer matrix model used in this thesis is presented in the follow pages.

```
program to calculate reflectivity of multilayer modulator structure
clear;
% Parameters
lambda=0.6328; % wavelength in micrometers
n0=1; % refractive index of incident medium
n1=1.47; % refractive index of layer 1
n2=1.4739; % refractive index of layer 2
n3=1.4739; % refractive index of layer 3
n4=1.4739; % refractive index of layer 4
n5=1.4739; % refractive index of layer 5
n6=1.4739; % refractive index of layer 6
n7=1.4739; % refractive index of layer 7
n8=1.4739; % refractive index of layer 8
n9=1.4739; % refractive index of layer 9
n10=1.4739; % refractive index of layer 10
n11=1.4739; % refractive index of layer 11
n12=1.4739; % refractive index of layer 12
n13=1.4739; % refractive index of layer 13
n14=1.4739; % refractive index of layer 14
n15=1.4739; % refractive index of layer 15
n16=1.4739; % refractive index of layer 16
n17=1.4739; % refractive index of layer 17
n18=1.4739; % refractive index of layer 18
n19=1.4739; % refractive index of layer 19
n20=1.4739; % refractive index of layer 20
n21=1.4739; % refractive index of layer 21
n22=1.4739; % refractive index of layer 22
n23=1.4739; % refractive index of layer 23
n24=1.4739; % refractive index of layer 24
n25=1.4739; % refractive index of layer 25
n26=1.4739; % refractive index of layer 26
n27=1.4739; % refractive index of layer 27
n28=1.4739; % refractive index of layer 28
n29=1.4739; % refractive index of layer 29
n30=1.4739; % refractive index of layer 30
n31=1.4739; % refractive index of layer 31
n32=1.4739; % refractive index of layer 32
n33=1.4739; % refractive index of layer 33
n34=1.4739; % refractive index of layer 34
n35=1.4739; % refractive index of layer 35
n36=1.4739; % refractive index of layer 36
n37=1.4739; % refractive index of layer 37
n38=1.4739; % refractive index of layer 38
n39=1.4739; % refractive index of layer 39
n40=1.4739; % refractive index of layer 40
n41=1.4739; % refractive index of layer 41
n42=1.4739; % refractive index of layer 42
n43=1.4739; % refractive index of layer 43
n44=1.4739; % refractive index of layer 44
n45=1.4739; % refractive index of layer 45
n46=1.4739; % refractive index of layer 46
n47=1.4739; % refractive index of layer 47
n48=1.4739; % refractive index of layer 48
n49=1.4739; % refractive index of layer 49
n50=1.4739; % refractive index of layer 50
n51=1.4739; % refractive index of layer 51
n52=1.4739; % refractive index of layer 52
n53=1.4739; % refractive index of layer 53
n54=1.4739; % refractive index of layer 54
n55=1.4739; % refractive index of layer 55
n56=1.4739; % refractive index of layer 56
n57=1.4739; % refractive index of layer 57
n58=1.4739; % refractive index of layer 58
n59=1.4739; % refractive index of layer 59
n60=1.4739; % refractive index of layer 60
n61=1.4739; % refractive index of layer 61
n62=1.4739; % refractive index of layer 62
n63=1.4739; % refractive index of layer 63
n64=1.4739; % refractive index of layer 64
n65=1.4739; % refractive index of layer 65
n66=1.4739; % refractive index of layer 66
n67=1.4739; % refractive index of layer 67
n68=1.4739; % refractive index of layer 68
n69=1.4739; % refractive index of layer 69
n70=1.4739; % refractive index of layer 70
n71=1.4739; % refractive index of layer 71
n72=1.4739; % refractive index of layer 72
n73=1.4739; % refractive index of layer 73
n74=1.4739; % refractive index of layer 74
n75=1.4739; % refractive index of layer 75
n76=1.4739; % refractive index of layer 76
n77=1.4739; % refractive index of layer 77
n78=1.4739; % refractive index of layer 78
n79=1.4739; % refractive index of layer 79
n80=1.4739; % refractive index of layer 80
n81=1.4739; % refractive index of layer 81
n82=1.4739; % refractive index of layer 82
n83=1.4739; % refractive index of layer 83
n84=1.4739; % refractive index of layer 84
n85=1.4739; % refractive index of layer 85
n86=1.4739; % refractive index of layer 86
n87=1.4739; % refractive index of layer 87
n88=1.4739; % refractive index of layer 88
n89=1.4739; % refractive index of layer 89
n90=1.4739; % refractive index of layer 90
n91=1.4739; % refractive index of layer 91
n92=1.4739; % refractive index of layer 92
n93=1.4739; % refractive index of layer 93
n94=1.4739; % refractive index of layer 94
n95=1.4739; % refractive index of layer 95
n96=1.4739; % refractive index of layer 96
n97=1.4739; % refractive index of layer 97
n98=1.4739; % refractive index of layer 98
n99=1.4739; % refractive index of layer 99
n100=1.4739; % refractive index of layer 100
% Thicknesses
d1=0.01; % thickness of layer 1
d2=0.01; % thickness of layer 2
d3=0.01; % thickness of layer 3
d4=0.01; % thickness of layer 4
d5=0.01; % thickness of layer 5
d6=0.01; % thickness of layer 6
d7=0.01; % thickness of layer 7
d8=0.01; % thickness of layer 8
d9=0.01; % thickness of layer 9
d10=0.01; % thickness of layer 10
d11=0.01; % thickness of layer 11
d12=0.01; % thickness of layer 12
d13=0.01; % thickness of layer 13
d14=0.01; % thickness of layer 14
d15=0.01; % thickness of layer 15
d16=0.01; % thickness of layer 16
d17=0.01; % thickness of layer 17
d18=0.01; % thickness of layer 18
d19=0.01; % thickness of layer 19
d20=0.01; % thickness of layer 20
d21=0.01; % thickness of layer 21
d22=0.01; % thickness of layer 22
d23=0.01; % thickness of layer 23
d24=0.01; % thickness of layer 24
d25=0.01; % thickness of layer 25
d26=0.01; % thickness of layer 26
d27=0.01; % thickness of layer 27
d28=0.01; % thickness of layer 28
d29=0.01; % thickness of layer 29
d30=0.01; % thickness of layer 30
d31=0.01; % thickness of layer 31
d32=0.01; % thickness of layer 32
d33=0.01; % thickness of layer 33
d34=0.01; % thickness of layer 34
d35=0.01; % thickness of layer 35
d36=0.01; % thickness of layer 36
d37=0.01; % thickness of layer 37
d38=0.01; % thickness of layer 38
d39=0.01; % thickness of layer 39
d40=0.01; % thickness of layer 40
d41=0.01; % thickness of layer 41
d42=0.01; % thickness of layer 42
d43=0.01; % thickness of layer 43
d44=0.01; % thickness of layer 44
d45=0.01; % thickness of layer 45
d46=0.01; % thickness of layer 46
d47=0.01; % thickness of layer 47
d48=0.01; % thickness of layer 48
d49=0.01; % thickness of layer 49
d50=0.01; % thickness of layer 50
d51=0.01; % thickness of layer 51
d52=0.01; % thickness of layer 52
d53=0.01; % thickness of layer 53
d54=0.01; % thickness of layer 54
d55=0.01; % thickness of layer 55
d56=0.01; % thickness of layer 56
d57=0.01; % thickness of layer 57
d58=0.01; % thickness of layer 58
d59=0.01; % thickness of layer 59
d60=0.01; % thickness of layer 60
d61=0.01; % thickness of layer 61
d62=0.01; % thickness of layer 62
d63=0.01; % thickness of layer 63
d64=0.01; % thickness of layer 64
d65=0.01; % thickness of layer 65
d66=0.01; % thickness of layer 66
d67=0.01; % thickness of layer 67
d68=0.01; % thickness of layer 68
d69=0.01; % thickness of layer 69
d70=0.01; % thickness of layer 70
d71=0.01; % thickness of layer 71
d72=0.01; % thickness of layer 72
d73=0.01; % thickness of layer 73
d74=0.01; % thickness of layer 74
d75=0.01; % thickness of layer 75
d76=0.01; % thickness of layer 76
d77=0.01; % thickness of layer 77
d78=0.01; % thickness of layer 78
d79=0.01; % thickness of layer 79
d80=0.01; % thickness of layer 80
d81=0.01; % thickness of layer 81
d82=0.01; % thickness of layer 82
d83=0.01; % thickness of layer 83
d84=0.01; % thickness of layer 84
d85=0.01; % thickness of layer 85
d86=0.01; % thickness of layer 86
d87=0.01; % thickness of layer 87
d88=0.01; % thickness of layer 88
d89=0.01; % thickness of layer 89
d90=0.01; % thickness of layer 90
d91=0.01; % thickness of layer 91
d92=0.01; % thickness of layer 92
d93=0.01; % thickness of layer 93
d94=0.01; % thickness of layer 94
d95=0.01; % thickness of layer 95
d96=0.01; % thickness of layer 96
d97=0.01; % thickness of layer 97
d98=0.01; % thickness of layer 98
d99=0.01; % thickness of layer 99
d100=0.01; % thickness of layer 100
% Transfer matrix calculation
M=eye(2); % identity matrix
for i=1:100
    k=2*pi*n(i)/lambda; % wave number
    A=cos(k*d(i)); % cos(k*d)
    B=sin(k*d(i)); % sin(k*d)
    C=-i*n(i)*B; % -i*n(i)*sin(k*d)
    D=i*n(i)*B; % i*n(i)*sin(k*d)
    M=[A B; C D]; % transfer matrix for layer i
end
% Input and output fields
Ei=1; % incident electric field
Hi=1; % incident magnetic field
% Output fields
[Eo, Ho]=M*[Ei; Hi]; % output fields
% Reflectivity and transmittivity
R=abs(Eo)/abs(Ei)^2; % reflectivity
T=abs(Ho)/abs(Hi)^2; % transmittivity
% Plotting
figure;
plot(R, T);
xlabel('Reflectivity (R)');
ylabel('Transmittivity (T)');
title('Transfer Matrix Model Results');
end
```

```

% Program to calculate reflectivity of multilayer modulator structure
% Declan Byrne
% program to calculate reflectivity for diferent incident angles
% Ref. calculated for TE and TM and averaged
% Trinity College Dublin
% Transfer matrix model
clear
tic
disp('working')
INANGLE=0;
BK=17;%:2:30
NW=59:59;
NW=input('Enter number of wells ? ');
WP=7;% set to 10 for finding minimum
BK=3;%
load 'b499d4'
ALPHA2(:,252)=0;
NO=1;
tPl=2.7120e-007;for 65 adjusted
while (NO~=203) & (NO~=202) & (NO~=204)
WS=1045.8+(0);%WS=input('ENTER STARTING WAVELENGTH IN NANOMETRES ?');

WF=1108.3+(0);%WF=input('ENTER FINISHING WAVELENGTH IN NANOMETRES ?');
WF=WF*0.000000001;
WI=.1;%WI=input('ENTER INCREMENT IN NANOMETRES ?');
BW=1076;%1003.5;%BW=input('ENTER DESIGN WAVELENGTH IN NANOMETRES ?');
INANGLE=0;%INANGLE=input('ENTER INCIDENT ANGLE IN DEGREES ?');
INANGLERAD=INANGLE*2*pi/360;%convert to radians
% REFRACTIVE INDICES INFORMATION
RIGD=0.2903-i*7.463;
RIRL=3.510;
RIGB=3.473;
RIA11=3.1278;%3.01+0.09;; % layer InAlAs
RIB11=3.4295; % layer InGaAs
RISUB1=3.4739;
RIAR=RISUB1;%sqrt(RISUB1);
RRIAR=1.86;
RIIM=RISUB1;
RIEM=1;

% LAYER THICKNESS INFORMATION
tB=BW/(4*RIB11);
tA=BW/(4*RIA11);
tGD=180e-9;
tP11=10e-9;
tnl=300*1e-9
tRL=1.0e-6;
tGB=2.0e-6;
tSUB=200e-6;
tAR=BW/(4*RIAR);
*****

% load in the dispersion data

load 'diswelladj'
dispersionwells(1,626);

load 'disbarrieradj'
dispersionbarriers(1,626);

load 'disdopingadj'
dispersiondopings(1,626);

load 'disgaasadj'
dispersiongaases(1,626);

load 'disinalasadj'
dispersioninalases(1,626);

hold on
BIAS=252;%11; % OUR BIAS VOLTAGE 5V
% starting to load in the data

%load 'b706d2'
A1=ALPHA2;
[Q,W]=size(A1);

```

```

% loop here for no. of front mirror periods

for FT = NP % # 4
%figure(FT+200)
for Y1=BIAS;%:APPLIEDV-BIAS:APPLIEDV; % #1 *****NOTE 'V' HERE HAS TO BE DEFINED TO BE > THAN 1
% TO PLOT FABRY PEROT MODE LET V=32
WAVELENGTH1(1,:) = WS:WI:WF;
ALPHA499(:,Y1) = A1(:,Y1);

SCALING = (1.0e+4/95)*NW; %
% complex refractive index of well
K(:,1) = ((ALPHA499(:,Y1).*WAVELENGTH1(1,:))*1e+2) / (4*pi))*SCALING;
K(X) = ((ALPHA*WAVELENGTH) / (4*pi));
CRIQW1(:,1) = RIQW - i*K(:,1);
% dispersion values for wells and barriers

RIW = dispersionwells(1,:);
RIBR = dispersionbarriers(1,:);
tW = 8.8e-9;
tBR = 5.54e-9;
RIQW = sqrt(((RIW.^2).*tW + (RIBR.^2).*tBR)/(tBR+tW));
tQW = (NW*tW) + (NW*tBR)+tBR;
tCAV = tP11+tP1+tN1+tQW;
CRIQW1(:,1) = RIQW - i*K(:,1);

RIPl1 = dispersiondopings(1,:)' - 0.08;
RIPl = dispersiondopings(1,:)' - 0.08;
RIInl = dispersiondopings(1,:)' - 0.08;
RISUB = dispersiongaases(1,:);
RIA = dispersioninalases(1,:)' + 0.09;
RIB = dispersiondopings(1,:)' - 0.08;

% *****
K(:,1) = 0; % ((ALPHA499(:,Y1).*WAVELENGTH1(1,:))*1e+2) / (4*pi))*SCALING; %1e+2 IS STILL SCALING TO BRIANS VALUES
K(X) = ((ALPHA*WAVELENGTH) / (4*pi));
CRIQW1(:,1) = RIQW - i*K(:,1);
KW(:,1) = (K(:,1).*tQW) / (NW.*tW); % abs in wells only
CRIW(:,1) = RIW - i*KW(:,1);
% CALCULATE BETA - INTERNAL ANGLES
BETAGD = asin(RIIM*sin(INANGLERAD)/RIGD);
BETAP11 = asin(RIIM.*sin(INANGLERAD)./RIPl1);
BETAP1 = asin(RIIM.*sin(INANGLERAD)./RIPl);
BETAN1 = asin(RIIM.*sin(INANGLERAD)./RIInl);
BETARL = asin(RIIM.*sin(INANGLERAD)/RIRL);
BETAGB = asin(RIIM.*sin(INANGLERAD)/RIGB);
BETAA = asin(RIIM.*sin(INANGLERAD)./RIA);
BETAB = asin(RIIM.*sin(INANGLERAD)./RIB);
BETASUB = asin(RIIM.*sin(INANGLERAD)./RISUB);
BETAAR = asin(RIIM.*sin(INANGLERAD)/RIAR);
BETAQW = asin(RIIM.*sin(INANGLERAD)./CRIQW1(:,1));
BETAW = asin(RIIM.*sin(INANGLERAD)./CRIW(:,1));
BETABR = asin(RIIM.*sin(INANGLERAD)./RIBR);
% SET POLARISATION - S-POLARISATION
UGD = RIGD*cos(BETAGD);
UP11 = RIPl1*cos(BETAP11);
UP1 = RIPl*cos(BETAP1);
UN1 = RIInl*cos(BETAN1);
URL = RIRL*cos(BETARL);
UGB = RIGB*cos(BETAGB);
UA = RIA*cos(BETAA);
UB = RIB*cos(BETAB);
USUB = RISUB*cos(BETASUB);
UAR = RIAR*cos(BETAAR);
UQW = CRIQW1(:,1).*cos(BETAQW(:,1));
UW = CRIW(:,1).*cos(BETAW(:,1));
UBR = RIBR*cos(BETABR);
% CALCULATE DELTA - PATH DIFFERENCES
DELTAGD = (2*pi*RIGD*tGD*cos(BETAGD))./WAVELENGTH1(1,:);
DELTAP11 = (2.*pi.*RIPl1.*tP11.*cos(BETAP11))./WAVELENGTH1(1,:);
DELTAP1 = (2.*pi.*RIPl.*tP1.*cos(BETAP1))./WAVELENGTH1(1,:);
DELTAN1 = (2.*pi.*RIInl.*tN1.*cos(BETAN1))./WAVELENGTH1(1,:);
DELTARL = (2*pi*RIRL*tRL*cos(BETARL))./WAVELENGTH1(1,:);
DELTAGB = (2*pi*RIGB*tGB*cos(BETAGB))./WAVELENGTH1(1,:);
DELTAAR = (2.*pi.*RIAR.*tAR.*cos(BETAAR))./WAVELENGTH1(1,:);
DELTAA = (2.*pi.*RIA.*tA.*cos(BETAA))./WAVELENGTH1(1,:);
DELTAB = (2.*pi.*RIB.*tB.*cos(BETAB))./WAVELENGTH1(1,:);
DELTASUB = (2.*pi.*RISUB.*tSUB.*cos(BETASUB))./WAVELENGTH1(1,:);
DELTAAR = (2*pi*RIAR*tAR*cos(BETAAR))./WAVELENGTH1(1,:);
DELTAQW = (2*pi.*CRIQW1(:,1).*tQW.*cos(BETAQW(:,1)))./WAVELENGTH1(1,:);
DELTAW = (2.*pi.*CRIW(:,1).*tW.*cos(BETAW(:,1)))./WAVELENGTH1(1,:);
DELTABR = (2.*pi.*RIBR.*tBR.*cos(BETABR))./WAVELENGTH1(1,:);
% CALCULATE MATRIX
MGD1 = cos(DELTAGD(:,1));
MGD2 = (i./UGD).*sin(DELTAGD(:,1));

```

```

MGD3=i.*UGD.*sin(DELTAGD(:,1));
MGD4=cos(DELTAGD(:,1));

MP11=cos(DELTAP11(:,1));
MP12=(i./UP11).*sin(DELTAP11(:,1));
MP13=i.*UP11.*sin(DELTAP11(:,1));
MP14=cos(DELTAP11(:,1));

MP1=cos(DELTAP1(:,1));
MP2=(i./UP1).*sin(DELTAP1(:,1));
MP3=i.*UP1.*sin(DELTAP1(:,1));
MP4=cos(DELTAP1(:,1));

Mn1=cos(DELTAN1(:,1));
Mn2=(i./Un1).*sin(DELTAN1(:,1));
Mn3=i.*Un1.*sin(DELTAN1(:,1));
Mn4=cos(DELTAN1(:,1));

MRL1=cos(DELTARL(:,1));
MRL2=(i./URL).*sin(DELTARL(:,1));
MRL3=i.*URL.*sin(DELTARL(:,1));
MRL4=cos(DELTARL(:,1));

MGB1=cos(DELTAGB(:,1));
MGB2=(i./UGB).*sin(DELTAGB(:,1));
MGB3=i.*UGB.*sin(DELTAGB(:,1));
MGB4=cos(DELTAGB(:,1));

MA1=cos(DELTAAR(:,1));
MA2=(i./UAR).*sin(DELTAAR(:,1));
MA3=i.*UAR.*sin(DELTAAR(:,1));
MA4=cos(DELTAAR(:,1));

MB1=cos(DELTAB(:,1));
MB2=(i./UB).*sin(DELTAB(:,1));
MB3=i.*UB.*sin(DELTAB(:,1));
MB4=cos(DELTAB(:,1));

MSUB1=cos(DELTASUB(:,1));
MSUB2=(i./USUB).*sin(DELTASUB(:,1));
MSUB3=i.*USUB.*sin(DELTASUB(:,1));
MSUB4=cos(DELTASUB(:,1));

MAR1=cos(DELTAAR(:,1));
MAR2=(i./UAR).*sin(DELTAAR(:,1));
MAR3=i.*UAR.*sin(DELTAAR(:,1));
MAR4=cos(DELTAAR(:,1));

MQW1=cos(DELTAQW(:,1));
MQW2=(i./UQW).*sin(DELTAQW(:,1));
MQW3=i.*UQW.*sin(DELTAQW(:,1));
MQW4=cos(DELTAQW(:,1));

MW1=cos(DELTAW(:,1));
MW2=(i./UW).*sin(DELTAW(:,1));
MW3=i.*UW.*sin(DELTAW(:,1));
MW4=cos(DELTAW(:,1));

MBR1=cos(DELTABR(:,1));
MBR2=(i./UBR).*sin(DELTABR(:,1));
MBR3=i.*UBR.*sin(DELTABR(:,1));
MBR4=cos(DELTABR(:,1));

```

```

% Transfer Matrix
%*****

```

```

if FT==0

M1=(MAR1.*MSUB1)+(MAR2.*MSUB3);
M2=(MAR1.*MSUB2)+(MAR2.*MSUB4);
M3=(MAR3.*MSUB1)+(MAR4.*MSUB3);
M4=(MAR3.*MSUB2)+(MAR4.*MSUB4);

M11=(M1.*MGB1)+(M2.*MGB3);
M21=(M1.*MGB2)+(M2.*MGB4);
M31=(M3.*MGB1)+(M4.*MGB3);
M41=(M3.*MGB2)+(M4.*MGB4);

M12=(M11.*MRL1)+(M21.*MRL3);
M22=(M11.*MRL2)+(M21.*MRL4);
M32=(M31.*MRL1)+(M41.*MRL3);
M42=(M31.*MRL2)+(M41.*MRL4);

```

```
M13=(M12.*Mnl1)+(M22.*Mnl3);
M23=(M12.*Mnl2)+(M22.*Mnl4);
M33=(M32.*Mnl1)+(M42.*Mnl3);
M43=(M32.*Mnl2)+(M42.*Mnl4);
```

```
M14=(M13.*MQW1)+(M23.*MQW3);
M24=(M13.*MQW2)+(M23.*MQW4);
M34=(M33.*MQW1)+(M43.*MQW3);
M44=(M33.*MQW2)+(M43.*MQW4);
```

```
M15=(M14.*MPl1)+(M24.*MPl3);
M25=(M14.*MPl2)+(M24.*MPl4);
M35=(M34.*MPl1)+(M44.*MPl3);
M45=(M34.*MPl2)+(M44.*MPl4);
```

```
M16=(M15.*MPl11)+(M25.*MPl13);
M26=(M15.*MPl12)+(M25.*MPl14);
M36=(M35.*MPl11)+(M45.*MPl13);
M46=(M35.*MPl12)+(M45.*MPl14);
```

```
% ***** Back Bragg
```

```
MBMirror1(:,1)=(M16.*MA1)+(M26.*MA3);
MBMirror2(:,1)=(M16.*MA2)+(M26.*MA4);
MBMirror3(:,1)=(M36.*MA1)+(M46.*MA3);
MBMirror4(:,1)=(M36.*MA2)+(M46.*MA4);
```

```
for loop=2:BK*2
```

```
if mod(loop,2)==0 % B
    MBMirror1(:,loop)=(MBMirror1(:,loop-1).*MB1)+(MBMirror2(:,loop-1).*MB3);
    MBMirror2(:,loop)=(MBMirror1(:,loop-1).*MB2)+(MBMirror2(:,loop-1).*MB4);
    MBMirror3(:,loop)=(MBMirror3(:,loop-1).*MB1)+(MBMirror4(:,loop-1).*MB3);
    MBMirror4(:,loop)=(MBMirror3(:,loop-1).*MB2)+(MBMirror4(:,loop-1).*MB4);
end
```

```
if mod(loop,2)==1 % A
    MBMirror1(:,loop)=(MBMirror1(:,loop-1).*MA1)+(MBMirror2(:,loop-1).*MA3);
    MBMirror2(:,loop)=(MBMirror1(:,loop-1).*MA2)+(MBMirror2(:,loop-1).*MA4);
    MBMirror3(:,loop)=(MBMirror3(:,loop-1).*MA1)+(MBMirror4(:,loop-1).*MA3);
    MBMirror4(:,loop)=(MBMirror3(:,loop-1).*MA2)+(MBMirror4(:,loop-1).*MA4);
end
```

```
end
```

```
% extra A
```

```
MBMirror1(:,BK*2+1)=(MBMirror1(:,BK*2).*MA1)+(MBMirror2(:,BK*2).*MA3);
MBMirror2(:,BK*2+1)=(MBMirror1(:,BK*2).*MA2)+(MBMirror2(:,BK*2).*MA4);
MBMirror3(:,BK*2+1)=(MBMirror3(:,BK*2).*MA1)+(MBMirror4(:,BK*2).*MA3);
MBMirror4(:,BK*2+1)=(MBMirror3(:,BK*2).*MA2)+(MBMirror4(:,BK*2).*MA4);
```

```
% ***** end of Back Bragg
```

```
%MF1=MBMirror1(:,BK*2+1);
%MF2=MBMirror2(:,BK*2+1);
%MF3=MBMirror3(:,BK*2+1);
%MF4=MBMirror4(:,BK*2+1);
```

```
MF1=(MBMirror1(:,BK*2+1).*MGD1)+(MBMirror2(:,BK*2+1).*MGD3);
MF2=(MBMirror1(:,BK*2+1).*MGD2)+(MBMirror2(:,BK*2+1).*MGD4);
MF3=(MBMirror3(:,BK*2+1).*MGD1)+(MBMirror4(:,BK*2+1).*MGD3);
MF4=(MBMirror3(:,BK*2+1).*MGD2)+(MBMirror4(:,BK*2+1).*MGD4);
```

```
%MF1=(M16.*MGD1)+(M26.*MGD3);
%MF2=(M16.*MGD2)+(M26.*MGD4);
%MF3=(M36.*MGD1)+(M46.*MGD3);
%MF4=(M36.*MGD2)+(M46.*MGD4);
```

```
else if BK==0
```

```
M1=(MAR1.*MSUB1)+(MAR2.*MSUB3);
M2=(MAR1.*MSUB2)+(MAR2.*MSUB4);
M3=(MAR3.*MSUB1)+(MAR4.*MSUB3);
M4=(MAR3.*MSUB2)+(MAR4.*MSUB4);
M11=(M1.*MGB1)+(M2.*MGB3);
```

```
M21=(M1.*MGB2)+(M2.*MGB4);
M31=(M3.*MGB1)+(M4.*MGB3);
M41=(M3.*MGB2)+(M4.*MGB4);
```

```
M12=(M11.*MRL1)+(M21.*MRL3);
M22=(M11.*MRL2)+(M21.*MRL4);
M32=(M31.*MRL1)+(M41.*MRL3);
M42=(M31.*MRL2)+(M41.*MRL4);
```

```
% mirror layers
```

```
%*****
```

```
MGMirror1(:,1)=(M12.*MA1)+(M22.*MA3);
MGMirror2(:,1)=(M12.*MA2)+(M22.*MA4);
MGMirror3(:,1)=(M32.*MA1)+(M42.*MA3);
MGMirror4(:,1)=(M32.*MA2)+(M42.*MA4);
```

```
for loop=2:FT*2
```

```
if mod(loop,2)==0 % B
    MGMirror1(:,loop)=(MGMirror1(:,loop-1).*MB1)+(MGMirror2(:,loop-1).*MB3);
    MGMirror2(:,loop)=(MGMirror1(:,loop-1).*MB2)+(MGMirror2(:,loop-1).*MB4);
    MGMirror3(:,loop)=(MGMirror3(:,loop-1).*MB1)+(MGMirror4(:,loop-1).*MB3);
    MGMirror4(:,loop)=(MGMirror3(:,loop-1).*MB2)+(MGMirror4(:,loop-1).*MB4);
end
```

```
if mod(loop,2)==1 % A
    MGMirror1(:,loop)=(MGMirror1(:,loop-1).*MA1)+(MGMirror2(:,loop-1).*MA3);
    MGMirror2(:,loop)=(MGMirror1(:,loop-1).*MA2)+(MGMirror2(:,loop-1).*MA4);
    MGMirror3(:,loop)=(MGMirror3(:,loop-1).*MA1)+(MGMirror4(:,loop-1).*MA3);
    MGMirror4(:,loop)=(MGMirror3(:,loop-1).*MA2)+(MGMirror4(:,loop-1).*MA4);
end
```

```
end
```

```
% extra A
```

```
MGMirror1(:,FT*2+1)=(MGMirror1(:,FT*2).*MA1)+(MGMirror2(:,FT*2).*MA3);
MGMirror2(:,FT*2+1)=(MGMirror1(:,FT*2).*MA2)+(MGMirror2(:,FT*2).*MA4);
MGMirror3(:,FT*2+1)=(MGMirror3(:,FT*2).*MA1)+(MGMirror4(:,FT*2).*MA3);
MGMirror4(:,FT*2+1)=(MGMirror3(:,FT*2).*MA2)+(MGMirror4(:,FT*2).*MA4);
```

```
M18=(MGMirror1(:,FT*2+1).*Mnl1)+(MGMirror2(:,FT*2+1).*Mnl3);
M28=(MGMirror1(:,FT*2+1).*Mnl2)+(MGMirror2(:,FT*2+1).*Mnl4);
M38=(MGMirror3(:,FT*2+1).*Mnl1)+(MGMirror4(:,FT*2+1).*Mnl3);
M48=(MGMirror3(:,FT*2+1).*Mnl2)+(MGMirror4(:,FT*2+1).*Mnl4);
```

```
% MQWs layers
```

```
%*****
```

```
MGQW1(:,1)=(M18.*MBR1)+(M28.*MBR3);
MGQW2(:,1)=(M18.*MBR2)+(M28.*MBR4);
MGQW3(:,1)=(M38.*MBR1)+(M48.*MBR3);
MGQW4(:,1)=(M38.*MBR2)+(M48.*MBR4);
```

```
for loop=2:NW*2
```

```
if mod(loop,2)==0 % B
    MGQW1(:,loop)=(MGQW1(:,loop-1).*MW1)+(MGQW2(:,loop-1).*MW3);
    MGQW2(:,loop)=(MGQW1(:,loop-1).*MW2)+(MGQW2(:,loop-1).*MW4);
    MGQW3(:,loop)=(MGQW3(:,loop-1).*MW1)+(MGQW4(:,loop-1).*MW3);
    MGQW4(:,loop)=(MGQW3(:,loop-1).*MW2)+(MGQW4(:,loop-1).*MW4);
end
```

```
if mod(loop,2)==1 % A
    MGQW1(:,loop)=(MGQW1(:,loop-1).*MBR1)+(MGQW2(:,loop-1).*MBR3);
    MGQW2(:,loop)=(MGQW1(:,loop-1).*MBR2)+(MGQW2(:,loop-1).*MBR4);
    MGQW3(:,loop)=(MGQW3(:,loop-1).*MBR1)+(MGQW4(:,loop-1).*MBR3);
    MGQW4(:,loop)=(MGQW3(:,loop-1).*MBR2)+(MGQW4(:,loop-1).*MBR4);
end
```

```
end
```

```
% extra BR
```

```
MGQW1(:,NW*2+1)=(MGQW1(:,NW*2).*MBR1)+(MGQW2(:,NW*2).*MBR3);
MGQW2(:,NW*2+1)=(MGQW1(:,NW*2).*MBR2)+(MGQW2(:,NW*2).*MBR4);
MGQW3(:,NW*2+1)=(MGQW3(:,NW*2).*MBR1)+(MGQW4(:,NW*2).*MBR3);
```

```
MGQW4 (:,NW*2+1) = (MGQW3 (:,NW*2) .*MBR2) + (MGQW4 (:,NW*2) .*MBR4);
```

```
%M19 = (M18 .*MQW1) + (M28 .*MQW3);  
%M29 = (M18 .*MQW2) + (M28 .*MQW4);  
%M39 = (M38 .*MQW1) + (M48 .*MQW3);  
%M49 = (M38 .*MQW2) + (M48 .*MQW4);
```

```
M110 = (MGQW1 (:,NW*2+1) .*MPL1) + (MGQW2 (:,NW*2+1) .*MPL3);  
M210 = (MGQW1 (:,NW*2+1) .*MPL2) + (MGQW2 (:,NW*2+1) .*MPL4);  
M310 = (MGQW3 (:,NW*2+1) .*MPL1) + (MGQW4 (:,NW*2+1) .*MPL3);  
M410 = (MGQW3 (:,NW*2+1) .*MPL2) + (MGQW4 (:,NW*2+1) .*MPL4);
```

```
M111 = (M110 .*MPL11) + (M210 .*MPL13);  
M211 = (M110 .*MPL12) + (M210 .*MPL14);  
M311 = (M310 .*MPL11) + (M410 .*MPL13);  
M411 = (M310 .*MPL12) + (M410 .*MPL14);
```

```
MF1 = (M111 .*MGD1) + (M211 .*MGD3);  
MF2 = (M111 .*MGD2) + (M211 .*MGD4);  
MF3 = (M311 .*MGD1) + (M411 .*MGD3);  
MF4 = (M311 .*MGD2) + (M411 .*MGD4);
```

```
else
```

```
M1 = (MAR1 .*MSUB1) + (MAR2 .*MSUB3);  
M2 = (MAR1 .*MSUB2) + (MAR2 .*MSUB4);  
M3 = (MAR3 .*MSUB1) + (MAR4 .*MSUB3);  
M4 = (MAR3 .*MSUB2) + (MAR4 .*MSUB4);
```

```
M11 = (M1 .*MGB1) + (M2 .*MGB3);  
M21 = (M1 .*MGB2) + (M2 .*MGB4);  
M31 = (M3 .*MGB1) + (M4 .*MGB3);  
M41 = (M3 .*MGB2) + (M4 .*MGB4);
```

```
M12 = (M11 .*MRL1) + (M21 .*MRL3);  
M22 = (M11 .*MRL2) + (M21 .*MRL4);  
M32 = (M31 .*MRL1) + (M41 .*MRL3);  
M42 = (M31 .*MRL2) + (M41 .*MRL4);
```

```
% mirror layers
```

```
%*****
```

```
MGMirror1 (:,1) = (M12 .*MA1) + (M22 .*MA3);  
MGMirror2 (:,1) = (M12 .*MA2) + (M22 .*MA4);  
MGMirror3 (:,1) = (M32 .*MA1) + (M42 .*MA3);  
MGMirror4 (:,1) = (M32 .*MA2) + (M42 .*MA4);
```

```
for loop=2:FT*2
```

```
if mod(loop,2)==0 % B  
MGMirror1 (:,loop) = (MGMirror1 (:,loop-1) .*MB1) + (MGMirror2 (:,loop-1) .*MB3);  
MGMirror2 (:,loop) = (MGMirror1 (:,loop-1) .*MB2) + (MGMirror2 (:,loop-1) .*MB4);  
MGMirror3 (:,loop) = (MGMirror3 (:,loop-1) .*MB1) + (MGMirror4 (:,loop-1) .*MB3);  
MGMirror4 (:,loop) = (MGMirror3 (:,loop-1) .*MB2) + (MGMirror4 (:,loop-1) .*MB4);  
end
```

```
if mod(loop,2)==1 % A  
MGMirror1 (:,loop) = (MGMirror1 (:,loop-1) .*MA1) + (MGMirror2 (:,loop-1) .*MA3);  
MGMirror2 (:,loop) = (MGMirror1 (:,loop-1) .*MA2) + (MGMirror2 (:,loop-1) .*MA4);  
MGMirror3 (:,loop) = (MGMirror3 (:,loop-1) .*MA1) + (MGMirror4 (:,loop-1) .*MA3);  
MGMirror4 (:,loop) = (MGMirror3 (:,loop-1) .*MA2) + (MGMirror4 (:,loop-1) .*MA4);  
end
```

```
end
```

```
% extra A
```

```
MGMirror1 (:,FT*2+1) = (MGMirror1 (:,FT*2) .*MA1) + (MGMirror2 (:,FT*2) .*MA3);  
MGMirror2 (:,FT*2+1) = (MGMirror1 (:,FT*2) .*MA2) + (MGMirror2 (:,FT*2) .*MA4);  
MGMirror3 (:,FT*2+1) = (MGMirror3 (:,FT*2) .*MA1) + (MGMirror4 (:,FT*2) .*MA3);  
MGMirror4 (:,FT*2+1) = (MGMirror3 (:,FT*2) .*MA2) + (MGMirror4 (:,FT*2) .*MA4);
```

```
M18 = (MGMirror1 (:,FT*2+1) .*Mnl1) + (MGMirror2 (:,FT*2+1) .*Mnl3);  
M28 = (MGMirror1 (:,FT*2+1) .*Mnl2) + (MGMirror2 (:,FT*2+1) .*Mnl4);  
M38 = (MGMirror3 (:,FT*2+1) .*Mnl1) + (MGMirror4 (:,FT*2+1) .*Mnl3);  
M48 = (MGMirror3 (:,FT*2+1) .*Mnl2) + (MGMirror4 (:,FT*2+1) .*Mnl4);
```

```
% MQWs layers
```

```
*****
```

```
MGQW1(:,1)=(M18.*MBR1)+(M28.*MBR3);  
MGQW2(:,1)=(M18.*MBR2)+(M28.*MBR4);  
MGQW3(:,1)=(M38.*MBR1)+(M48.*MBR3);  
MGQW4(:,1)=(M38.*MBR2)+(M48.*MBR4);
```

```
for loop=2:NW*2
```

```
if mod(loop,2)==0 % B  
MGQW1(:,loop)=(MGQW1(:,loop-1).*MW1)+(MGQW2(:,loop-1).*MW3);  
MGQW2(:,loop)=(MGQW1(:,loop-1).*MW2)+(MGQW2(:,loop-1).*MW4);  
MGQW3(:,loop)=(MGQW3(:,loop-1).*MW1)+(MGQW4(:,loop-1).*MW3);  
MGQW4(:,loop)=(MGQW3(:,loop-1).*MW2)+(MGQW4(:,loop-1).*MW4);  
end
```

```
if mod(loop,2)==1 % A  
MGQW1(:,loop)=(MGQW1(:,loop-1).*MBR1)+(MGQW2(:,loop-1).*MBR3);  
MGQW2(:,loop)=(MGQW1(:,loop-1).*MBR2)+(MGQW2(:,loop-1).*MBR4);  
MGQW3(:,loop)=(MGQW3(:,loop-1).*MBR1)+(MGQW4(:,loop-1).*MBR3);  
MGQW4(:,loop)=(MGQW3(:,loop-1).*MBR2)+(MGQW4(:,loop-1).*MBR4);  
end
```

```
end
```

```
% extra BR
```

```
MGQW1(:,NW*2+1)=(MGQW1(:,NW*2).*MBR1)+(MGQW2(:,NW*2).*MBR3);  
MGQW2(:,NW*2+1)=(MGQW1(:,NW*2).*MBR2)+(MGQW2(:,NW*2).*MBR4);  
MGQW3(:,NW*2+1)=(MGQW3(:,NW*2).*MBR1)+(MGQW4(:,NW*2).*MBR3);  
MGQW4(:,NW*2+1)=(MGQW3(:,NW*2).*MBR2)+(MGQW4(:,NW*2).*MBR4);
```

```
%M19=(M18.*MQW1)+(M28.*MQW3);
```

```
%M29=(M18.*MQW2)+(M28.*MQW4);
```

```
%M39=(M38.*MQW1)+(M48.*MQW3);
```

```
%M49=(M38.*MQW2)+(M48.*MQW4);
```

```
M110=(MGQW1(:,NW*2+1).*MP11)+(MGQW2(:,NW*2+1).*MP13);
```

```
M210=(MGQW1(:,NW*2+1).*MP12)+(MGQW2(:,NW*2+1).*MP14);
```

```
M310=(MGQW3(:,NW*2+1).*MP11)+(MGQW4(:,NW*2+1).*MP13);
```

```
M410=(MGQW3(:,NW*2+1).*MP12)+(MGQW4(:,NW*2+1).*MP14);
```

```
M111=(M110.*MP111)+(M210.*MP113);
```

```
M211=(M110.*MP112)+(M210.*MP114);
```

```
M311=(M310.*MP111)+(M410.*MP113);
```

```
M411=(M310.*MP112)+(M410.*MP114);
```

```
% ***** Back Bragg
```

```
MBMirror1(:,1)=(M111.*MA1)+(M211.*MA3);
```

```
MBMirror2(:,1)=(M111.*MA2)+(M211.*MA4);
```

```
MBMirror3(:,1)=(M311.*MA1)+(M411.*MA3);
```

```
MBMirror4(:,1)=(M311.*MA2)+(M411.*MA4);
```

```
for loop=2:BK*2
```

```
if mod(loop,2)==0 % B  
MBMirror1(:,loop)=(MBMirror1(:,loop-1).*MB1)+(MBMirror2(:,loop-1).*MB3);  
MBMirror2(:,loop)=(MBMirror1(:,loop-1).*MB2)+(MBMirror2(:,loop-1).*MB4);  
MBMirror3(:,loop)=(MBMirror3(:,loop-1).*MB1)+(MBMirror4(:,loop-1).*MB3);  
MBMirror4(:,loop)=(MBMirror3(:,loop-1).*MB2)+(MBMirror4(:,loop-1).*MB4);  
end
```

```
if mod(loop,2)==1 % A  
MBMirror1(:,loop)=(MBMirror1(:,loop-1).*MA1)+(MBMirror2(:,loop-1).*MA3);  
MBMirror2(:,loop)=(MBMirror1(:,loop-1).*MA2)+(MBMirror2(:,loop-1).*MA4);  
MBMirror3(:,loop)=(MBMirror3(:,loop-1).*MA1)+(MBMirror4(:,loop-1).*MA3);  
MBMirror4(:,loop)=(MBMirror3(:,loop-1).*MA2)+(MBMirror4(:,loop-1).*MA4);  
end
```

```
end
```



```

% extra A
MBMirror1(:,BK*2+1)=(MBMirror1(:,BK*2).*MA1)+(MBMirror2(:,BK*2).*MA3);
MBMirror2(:,BK*2+1)=(MBMirror1(:,BK*2).*MA2)+(MBMirror2(:,BK*2).*MA4);
MBMirror3(:,BK*2+1)=(MBMirror3(:,BK*2).*MA1)+(MBMirror4(:,BK*2).*MA3);
MBMirror4(:,BK*2+1)=(MBMirror3(:,BK*2).*MA2)+(MBMirror4(:,BK*2).*MA4);

% ***** end of Back Bragg

%MF1=MBMirror1(:,BK*2+1);
%MF2=MBMirror2(:,BK*2+1);
%MF3=MBMirror3(:,BK*2+1);
%MF4=MBMirror4(:,BK*2+1);

%MF1=(MBMirror1(:,BK*2+1).*MGD1)+(MBMirror2(:,BK*2+1).*MGD3);
%MF2=(MBMirror1(:,BK*2+1).*MGD2)+(MBMirror2(:,BK*2+1).*MGD4);
%MF3=(MBMirror3(:,BK*2+1).*MGD1)+(MBMirror4(:,BK*2+1).*MGD3);
%MF4=(MBMirror3(:,BK*2+1).*MGD2)+(MBMirror4(:,BK*2+1).*MGD4);

MF1=(M111.*MGD1)+(M211.*MGD3);
MF2=(M111.*MGD2)+(M211.*MGD4);
MF3=(M311.*MGD1)+(M411.*MGD3);
MF4=(M311.*MGD2)+(M411.*MGD4);

end
end

% CALCULATE INTENSITY AND REFLECTION

UI=RIIM*cos(INANGLERAD);

% EXIT ANGLE
BETAO=asin(RIIM*sin(INANGLERAD)/RIEM);

UO=RIEM*cos(BETAO);

% INTENSITY
r=(UI.*MF1+UI*UO.*MF2-MF3-UO.*MF4) ./ (UI.*MF1+UI.*UO.*MF2+MF3+UO.*MF4);

% REFLECTION
R=abs((r).^2);

% GRAPH

hold on
figure(200)
plot(WAVELENGTH1(1,:),R,'r')
xlabel('Wavelength(m)');
ylabel('Reflectance');
grid on
zoom on
pause(0.001)

%for n=1:length(R)
R1(FT+1,Y1,1:length(R))=R(1:length(R),1);
%end

end % from #1

disp('Processed data for front mirror period ');disp(FT)

end % from #4 end of front mirror loop

t=BIAS;
% check for min position
% check for min position

f1=193:1:213; % cutting down on the spectral range to scan over for minima
R2=R1(FT+1,t,f1);

SIZE=size(R2);
min=2;

```

```
for D=1:SIZE(1,3)
    if R2(1,1,D)< min;
        min=R2(1,1,D);
        NO=D+193;          % Add back the 203 so the program continues as normal
    end
end
% adjusting thickness of graded buffer layer

if NO < 203;
    if NO <= 175
        tPl=tPl+1e-8;
    end
    if NO <= 194
        tPl=tPl+1e-9;
    end
    if NO <= 199
        tPl=tPl+1e-10;
    end
    if NO <= 201
        tPl=tPl+1e-11;
    end
    if NO <= 202
        tPl=tPl+1e-12;
    end
end

if NO > 203;
    if NO >=226
        tPl=tPl-1.5e-8;
    end
    if NO >=217
        tPl=tPl-1.5e-9;
    end
    if NO >= 207
        tPl=tPl-1.5e-10;
    end
    if NO >=205
        tPl=tPl-1.5e-11;
    end
    if NO >=204
        tPl=tPl-1.5e-12;
    end
end

NO
tPl
end % end of while statement

*****
*****
TEST=1

for polarisation=0:1;
count=0;
for INANGLE=0;%:1:90;%:1:90;

    INANGLERAD=INANGLE*2*pi/360 ;%convert to radians

    count=count+1;
    store2(3,count)=INANGLE;

for BK=17;%:2:30

for NW=95:95

NP=1;
```



```
6,12.4788e-6,12.8459e-6,13.2129e-6,13.5799e-6,13.9470e-6,14.3140e-6,14.6810e-6,15.0480e-6,15.4151e-6,15.7821e-6,16.1491e-6,16.5161e-6,16.8832e-6,17.2502e-6,17.6172e-6,17.9842e-6,18.3513e-6];
```

```
%EFIELD=[  
0,0.0429,0.0859,0.1288,0.1717,0.2146,0.2576,0.3005,0.3434,0.3864,0.4293,0.4722,0.5152,0.5581,0.6010,0.6439,0.6869,0.7298,0.7727,0.8157,0.8586,0.9015,0.9444,0.9874,1.0303,1.0732,1.1162,1.1591,1.2020,1.2450,1.2879]*1e+7;
```

```
SIZE1=size(EFIELD);  
MAX=VOLT2/(NW*Length); %can go to 110nm and still get 44% reflectivity change  
% 64 nm is what we think the real value is at 10^18 doping  
% so i think this will give us 46% reflectivity change
```

```
for S=1:SIZE1(1,2)
```

```
if MAX <= EFIELD(1,S);  
MAX=EFIELD(1,S);  
NO(1,S)=S;  
break  
end
```

```
if MAX > EFIELD(1,S);
```

```
disp('No absorption curve found');  
end
```

```
end  
%NO(1,S)=31;  
NUMBER=NO(1,S);  
DIFF1=EFIELD(1,NUMBER)-(VOLT2/(NW*Length));  
DIFF2=(VOLT2/(NW*Length))-EFIELD(1,NUMBER-1);
```

```
if DIFF1<DIFF2;  
VOLTAGE2=NUMBER;  
disp('Absorption curve found');  
VOLTAGE2;
```

```
end  
if DIFF2<DIFF1;  
VOLTAGE2=NUMBER-1;  
disp('Absorption curve found');  
VOLTAGE2;
```

```
end
```

```
VOLTAGE2
```

```
*****
```

```
disp('Starting to calculate Reflectance spectra now')
```

```
disp(' ');  
disp('New run');  
disp(date);  
time=clock;  
disp(' time :');  
disp(time(1,4)),disp(time(1,5))
```

```
WS=1045.8-(0);%WS=input('ENTER STARTING WAVELENGTH IN NANOMETRES ?');  
WS=WS*0.000000001;  
WF=1108.3-(0);%WF=input('ENTER FINISHING WAVELENGTH IN NANOMETRES ?');  
WF=WF*0.000000001;  
WI=.1;%WI=input('ENTER INCREMENT IN NANOMETRES ?');  
WI=WI*0.000000001;  
%BW=1003.5;%BW=input('ENTER DESIGN WAVELENGTH IN NANOMETRES ?');  
BW=BW*0.000000001;
```

```
%INANGLE=0;%INANGLE=input('ENTER INCIDENT ANGLE IN DEGREES ?');  
%INANGLERAD=INANGLE*2*pi/360;%convert to radians
```

```
hold on
```

```
% ENTER VOLTAGE SPECIFICATIONS HERE  
% FOR APPLIED VOLTAGE ADD REAL BIAS VOLTAGE AND REAL APPLIED VOLTAGE TOGETHER  
% AND ENTER THE CORRESPONDING VALUE FOR THE TOTAL.  
% ENTER THE BIAS AS NORMAL  
BIAS1=VOLTAGE1;% OUR BIAS VOLTAGE 0V  
APPLIEDV1=VOLTAGE2+(BIAS1-1);% 5V DIFFERENCE
```

```
%load 'b706d2'  
A1=ALPHA2;
```

```

[Q,W]=size(A1);
% loop here for no. of front mirror periods

for FT =NP;% 0:NP    % # 4
%figure(FT+1)

for Y1=BIAS1:APPLIEDV1-BIAS1:APPLIEDV1; % #1 *****NOTE 'V' HERE HAS TO BE DEFINED TO BE > THAN 1

    WAVELENGTH1(1,:)=WS:WI:WF;

    ALPHA499(:,Y1)=A1(:,Y1);

SCALING=(1.0e+4/95)*NW; %
% complex refractive index of well
K(:,1)=(ALPHA499(:,Y1).*WAVELENGTH1(1,:)'*1e+2) / (4*pi))*SCALING;
%K(X)=(ALPHA*WAVELENGTH) / (4*pi));

CRIQW1(:,1)=RIQW-i*K(:,1);

KW(:,1)=(K(:,1).*tQW)./(NW.*tW);    % abs in wells only
CRIW(:,1)=RIW-i*KW(:,1);

% CALCULATE BETA - INTERNAL ANGLES
BETAGD=asin(RIIM*sin(INANGLERAD)/RIGD);
BETAP11=asin(RIIM.*sin(INANGLERAD)./RIP11);
BETAP1=asin(RIIM.*sin(INANGLERAD)./RIP1);
BETAN1=asin(RIIM.*sin(INANGLERAD)./RIN1);
BETARL=asin(RIIM*sin(INANGLERAD)/RIRL);
BETAGB=asin(RIIM*sin(INANGLERAD)/RIGB);
BETAA=asin(RIIM.*sin(INANGLERAD)./RIA);
BETAB=asin(RIIM.*sin(INANGLERAD)./RIB);
BETASUB=asin(RIIM.*sin(INANGLERAD)./RISUB);
BETAAR=asin(RIIM*sin(INANGLERAD)/RIAR);
BETAQW=asin(RIIM*sin(INANGLERAD)./CRIQW1(:,1));

BETAW=asin(RIIM.*sin(INANGLERAD)./CRIW(:,1));
BETABR=asin(RIIM.*sin(INANGLERAD)./RIBR);

% SET POLARISATION
if polarisation==0

    disp('TE polarisation')

UGD=RIGD*cos(BETAGD);
UP11=RIP11.*cos(BETAP11);
UP1=RIP1.*cos(BETAP1);
Un1=RIN1.*cos(BETAN1);
URL=RIRL*cos(BETARL);
UGB=RIGB*cos(BETAGB);
UA=RIA.*cos(BETAA);
UB=RIB.*cos(BETAB);
USUB=RISUB.*cos(BETASUB);
UAR=RIAR*cos(BETAAR);
UQW=CRIQW1(:,1).*cos(BETAQW(:,1));
UW=CRIW(:,1).*cos(BETAW(:,1));
UBR=RIBR.*cos(BETABR);
UI=RIIM*cos(INANGLERAD);

% EXIT ANGLE
BETAO=asin(RIIM*sin(INANGLERAD)/RIEM);

UO=RIEM*cos(BETAO);
end

if polarisation==1

    disp('TM polarisation')

UGD=RIGD./cos(BETAGD);
UP11=RIP11./cos(BETAP11);
UP1=RIP1./cos(BETAP1);
Un1=RIN1./cos(BETAN1);
URL=RIRL/cos(BETARL);
UGB=RIGB/cos(BETAGB);
UA=RIA./cos(BETAA);
UB=RIB./cos(BETAB);
USUB=RISUB./cos(BETASUB);
UAR=RIAR/cos(BETAAR);
UQW=CRIQW1(:,1)./cos(BETAQW(:,1));

```

```

W=CRIW(:,1)/cos(BETAW(:,1));
RBR=RIBR./cos(BETABR);

UI=RIIM/cos(INANGLERAD);

% EXIT ANGLE
BETAO=asin(RIIM*sin(INANGLERAD)/RIEM);

UO=RIEM/cos(BETAO);

end

% CALCULATE DELTA - PATH DIFFERENCES

DELTA GD=(2*pi*RIGD*tGD*cos(BETAGD))./WAVELENGTH1(1,:);
DELTA P11=(2.*pi.*RIPl1.*tPl1.*cos(BETAP11))./WAVELENGTH1(1,:);
DELTA P1=(2.*pi.*RIPl.*tPl.*cos(BETAP1))./WAVELENGTH1(1,:);
DELTA n1=(2.*pi.*RIInl.*tnl.*cos(BETAn1))./WAVELENGTH1(1,:);
DELTA RL=(2*pi*RIRL*tRL*cos(BETARL))./WAVELENGTH1(1,:);
DELTA GB=(2*pi*RIGB*tGB*cos(BETAGB))./WAVELENGTH1(1,:);
DELTA A=(2.*pi.*RIA.*tA.*cos(BETAA))./WAVELENGTH1(1,:);
DELTA B=(2.*pi.*RIB.*tB.*cos(BETAB))./WAVELENGTH1(1,:);
DELTA SUB=(2.*pi.*RISUB.*tSUB.*cos(BETASUB))./WAVELENGTH1(1,:);
DELTA AR=(2*pi*RIAR*tAR*cos(BETAAR))./WAVELENGTH1(1,:);
DELTA QW=(2*pi.*CRIQW1(:,1).*tQW.*cos(BETAQW(:,1)))./WAVELENGTH1(1,:);

DELTA W=(2.*pi.*CRIW(:,1).*tW.*cos(BETAW(:,1)))./WAVELENGTH1(1,:);
DELTA BR=(2.*pi.*RIBR.*tBR.*cos(BETABR))./WAVELENGTH1(1,:);

% CALCULATE MATRIX
MGD1=cos(DELTA GD(:,1));
MGD2=(i./UGD).*sin(DELTA GD(:,1));
MGD3=i.*UGD.*sin(DELTA GD(:,1));
MGD4=cos(DELTA GD(:,1));

MP111=cos(DELTA P11(:,1));
MP112=(i./UP11).*sin(DELTA P11(:,1));
MP113=i.*UP11.*sin(DELTA P11(:,1));
MP114=cos(DELTA P11(:,1));

MP11=cos(DELTA P1(:,1));
MP12=(i./UP1).*sin(DELTA P1(:,1));
MP13=i.*UP1.*sin(DELTA P1(:,1));
MP14=cos(DELTA P1(:,1));

Mn11=cos(DELTA n1(:,1));
Mn12=(i./Un1).*sin(DELTA n1(:,1));
Mn13=i.*Un1.*sin(DELTA n1(:,1));
Mn14=cos(DELTA n1(:,1));

MRL1=cos(DELTA RL(:,1));
MRL2=(i./URL).*sin(DELTA RL(:,1));
MRL3=i.*URL.*sin(DELTA RL(:,1));
MRL4=cos(DELTA RL(:,1));

MGB1=cos(DELTA GB(:,1));
MGB2=(i./UGB).*sin(DELTA GB(:,1));
MGB3=i.*UGB.*sin(DELTA GB(:,1));
MGB4=cos(DELTA GB(:,1));

MA1=cos(DELTA A(:,1));
MA2=(i./UA).*sin(DELTA A(:,1));
MA3=i.*UA.*sin(DELTA A(:,1));
MA4=cos(DELTA A(:,1));

MB1=cos(DELTA B(:,1));
MB2=(i./UB).*sin(DELTA B(:,1));
MB3=i.*UB.*sin(DELTA B(:,1));
MB4=cos(DELTA B(:,1));

MSUB1=cos(DELTA SUB(:,1));
MSUB2=(i./USUB).*sin(DELTA SUB(:,1));
MSUB3=i.*USUB.*sin(DELTA SUB(:,1));
MSUB4=cos(DELTA SUB(:,1));

MAR1=cos(DELTA AR(:,1));
MAR2=(i./UAR).*sin(DELTA AR(:,1));
MAR3=i.*UAR.*sin(DELTA AR(:,1));
MAR4=cos(DELTA AR(:,1));

MQW1=cos(DELTA QW(:,1));
MQW2=(i./UQW).*sin(DELTA QW(:,1));
MQW3=i.*UQW.*sin(DELTA QW(:,1));

```

```

MQW4=cos(DELTAQW(:,1));
MW1=cos(DELTAW(:,1));
MW2=(i./UW).*sin(DELTAW(:,1));
MW3=i.*UW.*sin(DELTAW(:,1));
MW4=cos(DELTAW(:,1));

MBR1=cos(DELTABR(:,1));
MBR2=(i./UBR).*sin(DELTABR(:,1));
MBR3=i.*UBR.*sin(DELTABR(:,1));
MBR4=cos(DELTABR(:,1));

% Transfer Matrix
%*****
if FT==0
M1=(MAR1.*MSUB1)+(MAR2.*MSUB3);
M2=(MAR1.*MSUB2)+(MAR2.*MSUB4);
M3=(MAR3.*MSUB1)+(MAR4.*MSUB3);
M4=(MAR3.*MSUB2)+(MAR4.*MSUB4);

M11=(M1.*MGB1)+(M2.*MGB3);
M21=(M1.*MGB2)+(M2.*MGB4);
M31=(M3.*MGB1)+(M4.*MGB3);
M41=(M3.*MGB2)+(M4.*MGB4);

M12=(M11.*MRL1)+(M21.*MRL3);
M22=(M11.*MRL2)+(M21.*MRL4);
M32=(M31.*MRL1)+(M41.*MRL3);
M42=(M31.*MRL2)+(M41.*MRL4);

M13=(M12.*Mnl1)+(M22.*Mnl3);
M23=(M12.*Mnl2)+(M22.*Mnl4);
M33=(M32.*Mnl1)+(M42.*Mnl3);
M43=(M32.*Mnl2)+(M42.*Mnl4);

M14=(M13.*MQW1)+(M23.*MQW3);
M24=(M13.*MQW2)+(M23.*MQW4);
M34=(M33.*MQW1)+(M43.*MQW3);
M44=(M33.*MQW2)+(M43.*MQW4);

M15=(M14.*MP11)+(M24.*MP13);
M25=(M14.*MP12)+(M24.*MP14);
M35=(M34.*MP11)+(M44.*MP13);
M45=(M34.*MP12)+(M44.*MP14);

M16=(M15.*MP111)+(M25.*MP113);
M26=(M15.*MP112)+(M25.*MP114);
M36=(M35.*MP111)+(M45.*MP113);
M46=(M35.*MP112)+(M45.*MP114);

% ***** Back Bragg

MBMirror1(:,1)=(M16.*MA1)+(M26.*MA3);
MBMirror2(:,1)=(M16.*MA2)+(M26.*MA4);
MBMirror3(:,1)=(M36.*MA1)+(M46.*MA3);
MBMirror4(:,1)=(M36.*MA2)+(M46.*MA4);

for loop=2:BK*2

if mod(loop,2)==0 % B
MBMirror1(:,loop)=(MBMirror1(:,loop-1).*MB1)+(MBMirror2(:,loop-1).*MB3);
MBMirror2(:,loop)=(MBMirror1(:,loop-1).*MB2)+(MBMirror2(:,loop-1).*MB4);
MBMirror3(:,loop)=(MBMirror3(:,loop-1).*MB1)+(MBMirror4(:,loop-1).*MB3);
MBMirror4(:,loop)=(MBMirror3(:,loop-1).*MB2)+(MBMirror4(:,loop-1).*MB4);
end

if mod(loop,2)==1 % A
MBMirror1(:,loop)=(MBMirror1(:,loop-1).*MA1)+(MBMirror2(:,loop-1).*MA3);
MBMirror2(:,loop)=(MBMirror1(:,loop-1).*MA2)+(MBMirror2(:,loop-1).*MA4);
MBMirror3(:,loop)=(MBMirror3(:,loop-1).*MA1)+(MBMirror4(:,loop-1).*MA3);
MBMirror4(:,loop)=(MBMirror3(:,loop-1).*MA2)+(MBMirror4(:,loop-1).*MA4);
end
end

% extra A

```

```
MBMirror1(:,BK*2+1)=(MBMirror1(:,BK*2).*MA1)+(MBMirror2(:,BK*2).*MA3);
MBMirror2(:,BK*2+1)=(MBMirror1(:,BK*2).*MA2)+(MBMirror2(:,BK*2).*MA4);
MBMirror3(:,BK*2+1)=(MBMirror3(:,BK*2).*MA1)+(MBMirror4(:,BK*2).*MA3);
MBMirror4(:,BK*2+1)=(MBMirror3(:,BK*2).*MA2)+(MBMirror4(:,BK*2).*MA4);
```

```
% ***** end of Back Bragg
```

```
%MF1=MBMirror1(:,BK*2+1);
%MF2=MBMirror2(:,BK*2+1);
%MF3=MBMirror3(:,BK*2+1);
%MF4=MBMirror4(:,BK*2+1);
```

```
%MF1=(MBMirror1(:,BK*2+1).*MGD1)+(MBMirror2(:,BK*2+1).*MGD3);
%MF2=(MBMirror1(:,BK*2+1).*MGD2)+(MBMirror2(:,BK*2+1).*MGD4);
%MF3=(MBMirror3(:,BK*2+1).*MGD1)+(MBMirror4(:,BK*2+1).*MGD3);
%MF4=(MBMirror3(:,BK*2+1).*MGD2)+(MBMirror4(:,BK*2+1).*MGD4);
```

```
MF1=(M16.*MGD1)+(M26.*MGD3);
MF2=(M16.*MGD2)+(M26.*MGD4);
MF3=(M36.*MGD1)+(M46.*MGD3);
MF4=(M36.*MGD2)+(M46.*MGD4);
```

```
else
```

```
M1=(MAR1.*MSUB1)+(MAR2.*MSUB3);
M2=(MAR1.*MSUB2)+(MAR2.*MSUB4);
M3=(MAR3.*MSUB1)+(MAR4.*MSUB3);
M4=(MAR3.*MSUB2)+(MAR4.*MSUB4);
```

```
M11=(M1.*MGB1)+(M2.*MGB3);
M21=(M1.*MGB2)+(M2.*MGB4);
M31=(M3.*MGB1)+(M4.*MGB3);
M41=(M3.*MGB2)+(M4.*MGB4);
```

```
M12=(M11.*MRL1)+(M21.*MRL3);
M22=(M11.*MRL2)+(M21.*MRL4);
M32=(M31.*MRL1)+(M41.*MRL3);
M42=(M31.*MRL2)+(M41.*MRL4);
```

```
% mirror layers
```

```
%*****
```

```
MGMirror1(:,1)=(M12.*MA1)+(M22.*MA3);
MGMirror2(:,1)=(M12.*MA2)+(M22.*MA4);
MGMirror3(:,1)=(M32.*MA1)+(M42.*MA3);
MGMirror4(:,1)=(M32.*MA2)+(M42.*MA4);
```

```
for loop=2:FT*2
```

```
if mod(loop,2)==0 % B
MGMirror1(:,loop)=(MGMirror1(:,loop-1).*MB1)+(MGMirror2(:,loop-1).*MB3);
MGMirror2(:,loop)=(MGMirror1(:,loop-1).*MB2)+(MGMirror2(:,loop-1).*MB4);
MGMirror3(:,loop)=(MGMirror3(:,loop-1).*MB1)+(MGMirror4(:,loop-1).*MB3);
MGMirror4(:,loop)=(MGMirror3(:,loop-1).*MB2)+(MGMirror4(:,loop-1).*MB4);
end
```

```
if mod(loop,2)==1 % A
MGMirror1(:,loop)=(MGMirror1(:,loop-1).*MA1)+(MGMirror2(:,loop-1).*MA3);
MGMirror2(:,loop)=(MGMirror1(:,loop-1).*MA2)+(MGMirror2(:,loop-1).*MA4);
MGMirror3(:,loop)=(MGMirror3(:,loop-1).*MA1)+(MGMirror4(:,loop-1).*MA3);
MGMirror4(:,loop)=(MGMirror3(:,loop-1).*MA2)+(MGMirror4(:,loop-1).*MA4);
end
```

```
end
```

```
% extra A
MGMirror1(:,FT*2+1)=(MGMirror1(:,FT*2).*MA1)+(MGMirror2(:,FT*2).*MA3);
MGMirror2(:,FT*2+1)=(MGMirror1(:,FT*2).*MA2)+(MGMirror2(:,FT*2).*MA4);
MGMirror3(:,FT*2+1)=(MGMirror3(:,FT*2).*MA1)+(MGMirror4(:,FT*2).*MA3);
MGMirror4(:,FT*2+1)=(MGMirror3(:,FT*2).*MA2)+(MGMirror4(:,FT*2).*MA4);
```

```
M18=(MGMirror1(:,FT*2+1).*Mnl1)+(MGMirror2(:,FT*2+1).*Mnl3);
M28=(MGMirror1(:,FT*2+1).*Mnl2)+(MGMirror2(:,FT*2+1).*Mnl4);
M38=(MGMirror3(:,FT*2+1).*Mnl1)+(MGMirror4(:,FT*2+1).*Mnl3);
```



```
M48=(MGMirror3(:,FT*2+1).*Mnl2)+(MGMirror4(:,FT*2+1).*Mnl4);
```

```
% MQWs layers
```

```
*****
```

```
MGQW1(:,1)=(M18.*MBR1)+(M28.*MBR3);  
MGQW2(:,1)=(M18.*MBR2)+(M28.*MBR4);  
MGQW3(:,1)=(M38.*MBR1)+(M48.*MBR3);  
MGQW4(:,1)=(M38.*MBR2)+(M48.*MBR4);
```

```
for loop=2:NW*2
```

```
if mod(loop,2)==0 % B  
MGQW1(:,loop)=(MGQW1(:,loop-1).*MW1)+(MGQW2(:,loop-1).*MW3);  
MGQW2(:,loop)=(MGQW1(:,loop-1).*MW2)+(MGQW2(:,loop-1).*MW4);  
MGQW3(:,loop)=(MGQW3(:,loop-1).*MW1)+(MGQW4(:,loop-1).*MW3);  
MGQW4(:,loop)=(MGQW3(:,loop-1).*MW2)+(MGQW4(:,loop-1).*MW4);  
end
```

```
if mod(loop,2)==1 % A  
MGQW1(:,loop)=(MGQW1(:,loop-1).*MBR1)+(MGQW2(:,loop-1).*MBR3);  
MGQW2(:,loop)=(MGQW1(:,loop-1).*MBR2)+(MGQW2(:,loop-1).*MBR4);  
MGQW3(:,loop)=(MGQW3(:,loop-1).*MBR1)+(MGQW4(:,loop-1).*MBR3);  
MGQW4(:,loop)=(MGQW3(:,loop-1).*MBR2)+(MGQW4(:,loop-1).*MBR4);  
end
```

```
end
```

```
% extra BR
```

```
MGQW1(:,NW*2+1)=(MGQW1(:,NW*2).*MBR1)+(MGQW2(:,NW*2).*MBR3);  
MGQW2(:,NW*2+1)=(MGQW1(:,NW*2).*MBR2)+(MGQW2(:,NW*2).*MBR4);  
MGQW3(:,NW*2+1)=(MGQW3(:,NW*2).*MBR1)+(MGQW4(:,NW*2).*MBR3);  
MGQW4(:,NW*2+1)=(MGQW3(:,NW*2).*MBR2)+(MGQW4(:,NW*2).*MBR4);
```

```
%M19=(M18.*MQW1)+(M28.*MQW3);  
%M29=(M18.*MQW2)+(M28.*MQW4);  
%M39=(M38.*MQW1)+(M48.*MQW3);  
%M49=(M38.*MQW2)+(M48.*MQW4);
```

```
M110=(MGQW1(:,NW*2+1).*MP11)+(MGQW2(:,NW*2+1).*MP13);  
M210=(MGQW1(:,NW*2+1).*MP12)+(MGQW2(:,NW*2+1).*MP14);  
M310=(MGQW3(:,NW*2+1).*MP11)+(MGQW4(:,NW*2+1).*MP13);  
M410=(MGQW3(:,NW*2+1).*MP12)+(MGQW4(:,NW*2+1).*MP14);
```

```
M111=(M110.*MP111)+(M210.*MP113);  
M211=(M110.*MP112)+(M210.*MP114);  
M311=(M310.*MP111)+(M410.*MP113);  
M411=(M310.*MP112)+(M410.*MP114);
```

```
% ***** Back Bragg
```

```
MBMirror1(:,1)=(M111.*MA1)+(M211.*MA3);  
MBMirror2(:,1)=(M111.*MA2)+(M211.*MA4);  
MBMirror3(:,1)=(M311.*MA1)+(M411.*MA3);  
MBMirror4(:,1)=(M311.*MA2)+(M411.*MA4);
```

```
for loop=2:BK*2
```

```
if mod(loop,2)==0 % B  
MBMirror1(:,loop)=(MBMirror1(:,loop-1).*MB1)+(MBMirror2(:,loop-1).*MB3);  
MBMirror2(:,loop)=(MBMirror1(:,loop-1).*MB2)+(MBMirror2(:,loop-1).*MB4);  
MBMirror3(:,loop)=(MBMirror3(:,loop-1).*MB1)+(MBMirror4(:,loop-1).*MB3);  
MBMirror4(:,loop)=(MBMirror3(:,loop-1).*MB2)+(MBMirror4(:,loop-1).*MB4);  
end
```

```
if mod(loop,2)==1 % A  
MBMirror1(:,loop)=(MBMirror1(:,loop-1).*MA1)+(MBMirror2(:,loop-1).*MA3);  
MBMirror2(:,loop)=(MBMirror1(:,loop-1).*MA2)+(MBMirror2(:,loop-1).*MA4);  
MBMirror3(:,loop)=(MBMirror3(:,loop-1).*MA1)+(MBMirror4(:,loop-1).*MA3);  
MBMirror4(:,loop)=(MBMirror3(:,loop-1).*MA2)+(MBMirror4(:,loop-1).*MA4);  
end
```

```
end
```

```

% extra A
MBMirror1(:,BK*2+1)=(MBMirror1(:,BK*2).*MA1)+(MBMirror2(:,BK*2).*MA3);
MBMirror2(:,BK*2+1)=(MBMirror1(:,BK*2).*MA2)+(MBMirror2(:,BK*2).*MA4);
MBMirror3(:,BK*2+1)=(MBMirror3(:,BK*2).*MA1)+(MBMirror4(:,BK*2).*MA3);
MBMirror4(:,BK*2+1)=(MBMirror3(:,BK*2).*MA2)+(MBMirror4(:,BK*2).*MA4);

% ***** end of Back Bragg

%MF1=MBMirror1(:,BK*2+1);
%MF2=MBMirror2(:,BK*2+1);
%MF3=MBMirror3(:,BK*2+1);
%MF4=MBMirror4(:,BK*2+1);

%MF1=(MBMirror1(:,BK*2+1).*MGD1)+(MBMirror2(:,BK*2+1).*MGD3);
%MF2=(MBMirror1(:,BK*2+1).*MGD2)+(MBMirror2(:,BK*2+1).*MGD4);
%MF3=(MBMirror3(:,BK*2+1).*MGD1)+(MBMirror4(:,BK*2+1).*MGD3);
%MF4=(MBMirror3(:,BK*2+1).*MGD2)+(MBMirror4(:,BK*2+1).*MGD4);

MF1=(M111.*MGD1)+(M211.*MGD3);
MF2=(M111.*MGD2)+(M211.*MGD4);
MF3=(M311.*MGD1)+(M411.*MGD3);
MF4=(M311.*MGD2)+(M411.*MGD4);

end

% CALCULATE INTENSITY AND REFLECTION

%UI=RIIM*cos(INANGLERAD);

% EXIT ANGLE
%BETAO=asin(RIIM*sin(INANGLERAD)/RIEM);

%UO=RIEM*cos(BETAO);

% INTENSITY
r=(UI.*MF1+UI*UO.*MF2-MF3-UO.*MF4) ./ (UI.*MF1+UI.*UO.*MF2+MF3+UO.*MF4);

% REFLECTION
R=abs((r).^2);

% GRAPH
hold on
figure(FT+1)
plot(WAVELENGTH1(1,:),R,'b')
xlabel('Wavelength(m)');
ylabel('Reflectance');
grid on
zoom on

%for n=1:length(R)
R1(FT+1,Y1,1:length(R))=R(1:length(R),1);
%end

end % from #2
pause(0.0001)

disp('Processed data for front mirror period ');disp(FT)

end % from #4 end of front mirror loop

% plot REFLECTIVITY CHANGE HERE

for FT = 0:NP
if FT==0
%DELTAR(0+1,0+1,:)=(R1(0+1,BIAS1,:))-(R1(0+1,APPLIEDV1,:));
DELTAR(0+1,0+1,:)=(R1(0+1,BIAS1,:))-(R1(0+1,APPLIEDV1,:));
end
if FT~=0
%DELTAR(1+FT,1+FT,:)=(R1(FT+1,BIAS1,:))-(R1(FT+1,APPLIEDV1,:));
DELTAR(1+FT,1+FT,:)=(R1(FT+1,BIAS1,:))-(R1(FT+1,APPLIEDV1,:));
store(1,count)=(R1(FT+1,BIAS1,302));
store(2,count)=(R1(FT+1,APPLIEDV1,302));
store1(1,polarisation+1,count)=(R1(FT+1,BIAS1,302));
store1(2,polarisation+1,count)=(R1(FT+1,APPLIEDV1,302));
end

```

```

end
for FT = 0:NP
    if FT==0
        for fifille=1:626
            dec(1,fifille)=DELTAR(1,1,fifille);
        end
    end
    if FT~=0
        for fifille=1:626
            dec(1+FT,fifille)=DELTAR(1+FT,1+FT,fifille);
        end
    end
end

end
NW
for FT = 0:NP
    if FT==0
        dis(1,1)=DELTAR(1,1,NO(1,1));
    end
    if FT~=0
        dis(1,1+FT)=DELTAR(1+FT,1+FT,NO(1,1));
    end
end

data1(1,NW-(NW-1))=NW;

for FT = 0:NP
    if FT==0
        data2(1,BK-(BK-1))=dis(1,1);
    end
    if FT~=0
        data2(1+FT,BK-(BK-1))=dis(1,1+FT);
    end
end

data10(1,NW)=NW;

for FT = 0:NP
    if FT==0
        data30(1,count)=dis(1,1);
    end
    if FT~=0
        data30(1+FT,count)=dis(1,1+FT);
    end
end

figure(BK+2)
hold on
xlabel('Angle');
ylabel('TE & TM Reflectivity');
grid on
zoom on

plot(INANGLE, [(store1(1,polarisation+1,count)+store1(1,polarisation+1,count))./2], 'or')
plot(INANGLE, [(store1(2,polarisation+1,count)+store1(2,polarisation+1,count))./2], '*b')

end
end

% plot alpha here

Y1=BIAS1:APPLIEDV1-BIAS1:APPLIEDV1;
figure(99)
hold on
plot(WAVELENGTH1(1,:),ALPHA499(:,BIAS1))
plot(WAVELENGTH1(1,:),ALPHA499(:,APPLIEDV1))
xlabel('Wavelength(m)');
ylabel('alpha');
grid on

hold on
plot(WAVELENGTH1(1,:),(ALPHA499(:,APPLIEDV1)-ALPHA499(:,BIAS1)))
xlabel('Wavelength(m)');

```

```
ylabel('alpha');
grid on

end % angle loop

end % polarisation loop

store2(1,:) = [(store1(1,1,:) + store1(1,2,:)) ./ 2];
store2(2,:) = [(store1(2,1,:) + store1(2,2,:)) ./ 2];

figure(BK+3)
hold on
xlabel('Angle');
ylabel('Average Reflectivity');
grid on
zoom on

plot(store2(3,:), store2(1,:), 'ok') % Bias V
plot(store2(3,:), store2(2,:), '*k') % applied V

store5(1,:) = (store2(1,:) - store2(2,:));

figure(BK+4)
hold on
xlabel('Angle');
ylabel('Average Modulation');
grid on
zoom on

plot(store2(3,:), store5(1,:), 'ob') % Bias V

toc
```